FAILURE PROCESSES IN SOFT AND QUASI-BRITTLE MATERIALS WITH NONHOMOGENEOUS MICROSTRUCTURES

BY

DANIEL W. SPRING

DISSERTATION

Submitted in partial fulfillment of the requirements
for the degree of Doctor of Philosophy in Civil Engineering
in the Graduate College of the
University of Illinois at Urbana-Champaign, 2015

Urbana, Illinois

Doctoral Committee:

Professor Glaucio H. Paulino, Chair and Director of Research
Professor Iwona Jasiuk
Professor William G. Buttlar
Professor Oscar Lopez-Pamies
Professor Ahmed E. Elbanna
Professor Kyoungsoo Park, Yonsei University

Abstract

Material failure pervades the fields of materials science and engineering; it occurs at various scales and in various contexts. Understanding the mechanisms by which a material fails can lead to advancements in the way we design and build the world around us. For example, in structural engineering, understanding the fracture of concrete and steel can lead to improved structural systems and safer designs; in geological engineering, understanding the fracture of rock can lead to increased efficiency in oil and gas extraction; and in biological engineering, understanding the fracture of bone can lead to improvements in the design of bio-composites and medical implants. In this thesis, we numerically investigate a wide spectrum of failure behavior; in soft and quasi-brittle materials with nonhomogeneous microstructures considering a statistical distribution of material properties.

The first topic we investigate considers the influence of interfacial interactions on the macroscopic constitutive response of particle reinforced elastomers. When a particle is embedded into an elastomer, the polymer chains in the elastomer tend to adsorb (or anchor) onto the surface of the particle; creating a region in the vicinity of each particle (often referred to as an interphase) with distinct properties from those in the bulk elastomer. This interphasial region has been known to exist for many decades, but is primarily omitted in computational investigations of such composites. In this thesis, we present an investigation into the influence of interphases on the macroscopic constitutive response of particle filled elastomers undergoing large deformations. In addition, at large deformations, a localized region of failure tends to accumulate around inclusions. To capture this localized region of failure (often referred to as interfacial debonding), we use cohesive zone elements which follow the Park-Paulino-Roesler traction-separation relation. To account for friction, we present a new, coupled cohesive-friction relation and detail its formulation and implementation. In the process of this investigation, we developed a small library of cohesive elements for use with a commercially available finite element analysis software package.

Additionally, in this thesis, we present a series of methods for reducing mesh dependency in two-dimensional dynamic cohesive fracture simulations of quasi-brittle materials. In this setting, cracks are only permitted to propagate along element facets, thus a poorly designed

discretization of the problem domain can introduce artifacts into the fracture behavior. To reduce mesh induced artifacts, we consider unstructured polygonal finite elements. A randomly-seeded polygonal mesh leads to an isotropic discretization of the problem domain, which does not bias the direction of crack propagation. However, polygonal meshes tend to limit the possible directions a crack may travel at each node, making this discretization a poor candidate for dynamic cohesive fracture simulations. To alleviate this problem, we propose two new topological operators. The first operator we propose is adaptive element-splitting, and the second is adaptive mesh refinement. Both operators are designed to improve the ability of unstructured polygonal meshes to capture crack patterns in dynamic cohesive fracture simulations. However, we demonstrate that element-splitting is more suited to pervasive fracture problems, whereas, adaptive refinement is more suited to problems exhibiting a dominant crack.

Finally, we investigate the use of geometric and constitutive design features to regularize pervasive fragmentation behavior in three-dimensions. Throughout pervasive fracture simulations, many cracks initiate, propagate, branch and coalesce simultaneously. Because of the cohesive element method's unique framework, this behavior can be captured in a regularized manner. In this investigation, unstructuring techniques are used to introduce randomness into a numerical model. The behavior of quasi-brittle materials undergoing pervasive fracture and fragmentation is then examined using three examples. The examples are selected to investigate some of the significant factors influencing pervasive fracture and fragmentation behavior; including, geometric features, loading conditions, and material gradation.

To my family

Acknowledgments

I would like to sincerely thank my research adviser, Professor Glaucio H. Paulino, for his guidance, willingness to teach, and continued support and encouragement. His appreciation for advancing students not only academically, but also professionally has been inspiring. I am also indebted to Professor Kyoungsoo Park for his early role as my mentor. His assistance and the example he set were building blocks that laid the foundation for my graduate education. Professor Lopez-Pamies and Professor Roesler were invaluable collaborators who enriched my experience with discussion and expanded my knowledge into fields of engineering previously unknown to me. I very gratefully thank Professor Iwona Jasiuk, Professor William G. Buttlar, and Professor Ahmed E. Elbanna for their valuable contributions as members of my dissertation committee.

Although my formal mentoring occurred through professor-student relationships, much of my knowledge comes from the students I've had the privilege of sharing this experience with. I was honored to be able to collaborate with many great students, including Armen Amirkhanian, Sofie Léon, and Taha Goudarzi. The work we did together was diverse and exciting. I am also very grateful to the colleagues who have provided insight, and spurred discussions throughout my graduate education. I would like to thank Arun L. Gain, Evgueni Filipov, Heng Chi, Tomas Zegard, Oliver Giraldo-Londoño, Cameron Talischi, Lauren Beghini, Junho Song, Xiaojia (Shelly) Zhang, Ke (Chris) Liu, Tuo Zhao, Emily Daniels, Yang Jiang, Will Colletti, Tam Nguyen, Eshan Dave, Rodrigo Espinha, Ludimar Lima de Aguiar, Marco Alfano, Luis Arnaldo, Peng Wei, Hélio Emmendoerfer Junior, Rejane Canha, and Leonardo Duarte for their valuable comments and inspiration.

Without the support of the Natural Sciences and Engineering Research Council of Canada, I would not have been given the flexibility to do the varied research that I did. Their financial support throughout my Doctorate degree has been a blessing. I gratefully recognize the financial support of the National Science Foundation through projects CMMI 1321661 and 1437535. Additionally, I would like to thank the University of Illinois at Urbana-Champaign for welcoming me into their program, and challenging me academically, professionally and personally. Finally, I would like to thank my family for their quiet and constant support.

Table of Contents

Chapter 1

Introduction

Material failure pervades the fields of materials science and engineering; it occurs at various scales and in various contexts. Understanding the mechanisms by which a material fails can lead to advancements in the way we design and build the world around us. For example, in structural engineering, understanding the fracture of concrete and steel can lead to improved structural systems and safer designs; in geological engineering, understanding the fracture of rock can lead to increased efficiency in oil and gas extraction; and in biological engineering, understanding the fracture of bone can lead to improvements in the design of bio-composites and medical implants. Some examples of material failure influencing an engineering application are illustrated in Figure 1.1.

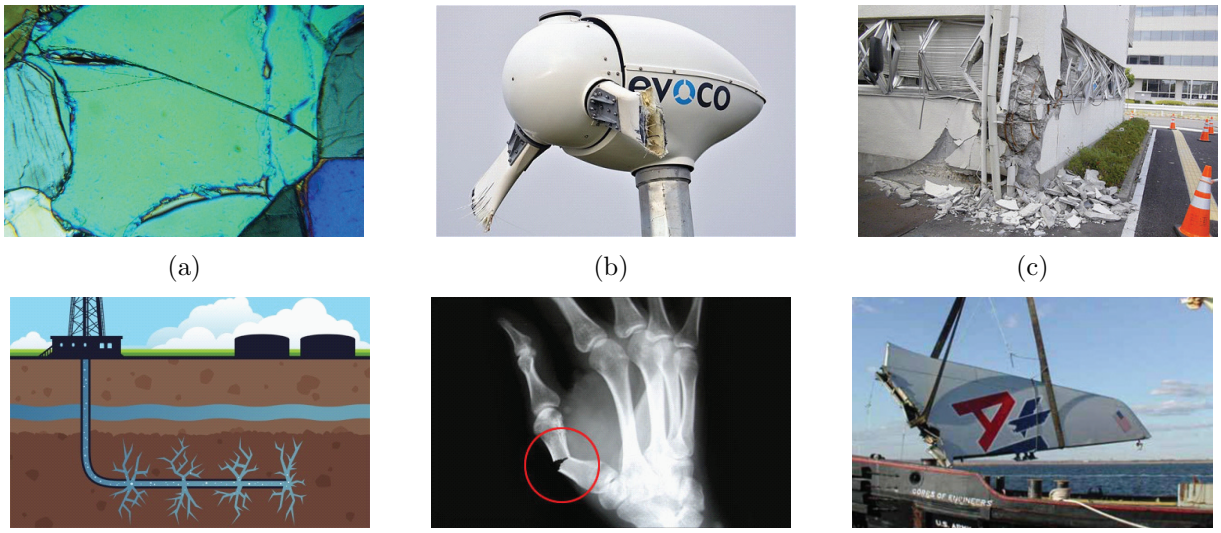

(a) (b) (c)

(d) (e) (f)

Figure 1.1: Some examples of material failure in the fields of materials science and engineering: (a) transgranular fracture in a crystalline material (und.nodak.com), (b) turbine failure due to extreme weather (telegraph.co.uk), (c) seismic collapse (nrc.gov), (d) fracking to increase efficiency in gas extraction (mlive.com), (e) bone fracture (pixshark.com), and (f) structural failure resulting in loss of life (comsol.com).

In addition to the prevalence of failure, there is also a wide range of failure mechanisms. In some cases, failure occurs due to a dominant crack, while in other cases, failure is catas-

trophic, causing pervasive damage to occur throughout a material. Between these two ends of the failure spectrum, crack branching and crack coalescence mechanisms arise, as illustrated in Figure 1.2. In this thesis we discuss the full spectrum of fracture behavior; in both two and three dimensions; in both quasi-static and dynamic loading conditions; and in both soft and quasi-brittle materials.

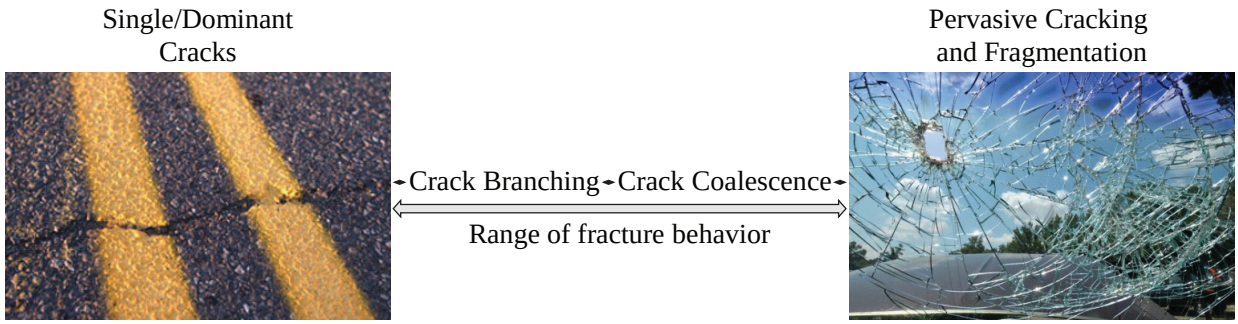

Figure 1.2: Range of fracture behavior. From problems dominated by a single crack, through crack branching and coalescence, to pervasive cracking and complete fragmentation.

In this introductory chapter, we briefly describe the fracture processes of materials, and discuss some of the prevalent methods for simulating fracture. Additionally, we situate and motivate the particular problems investigated in this thesis. At the conclusion of this chapter, we outline the scope of the current work and the organization of the topics in each of the remaining chapters.

1.1 Characterization of fracture

Fracture mechanics refers to the modeling of the singular stress fields present in the equilibrium solutions for cracked homogeneous linear elastic isotropic materials. The assumption of linear elastic fracture mechanics (LEFM) is useful in some applications; however, physically realistic fracture mechanics is not linear. In real material microstructures, microcracks and voids form, developing an inelastic zone of damage in front of the crack-tip, as illustrated in Figure 1.3(a). The size and extent of this zone of inelastic damage dictates the fracture process, and ultimately the manner in which the structure may fail.

In general, the fracture of all materials can be classified as either brittle, quasi-brittle, or ductile. The specific classification depends on the ratio of the relative size of the fracture process zone (or nonlinear softening zone), and the nonlinear hardening zone, with respect to the specimen size, as illustrated in Figure 1.3(b). In brittle materials, both the fracture process zone and the nonlinear hardening zone are small, and LEFM principals are often

applicable. In quasi-brittle materials, the fracture process zone is much larger than the nonlinear hardening zone. Finally, in ductile materials, the nonlinear hardening zone is much larger than the fracture process zone, and elasto-plastic fracture mechanics principals are often applicable.

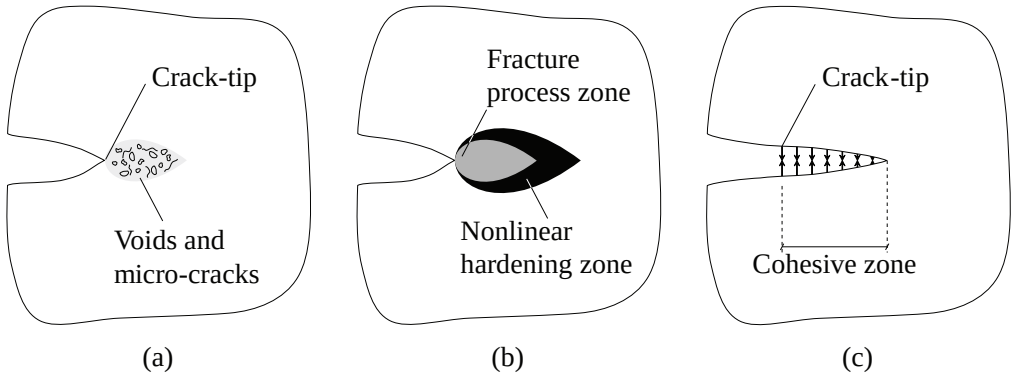

Figure 1.3: Schematics of: (a) the inelastic zone of damage in front of the crack-tip; (b) the softening fracture process zone and nonlinear hardening zone; and (c) the cohesive zone used to represent the inelastic zone of damage.

In the fracture process zone, the material softens, as a result of void growth and microcrack formation. Conceptually, the fracture process zone can be approximated by a cohesive zone [1, 2], as illustrated in Figure 1.3(c). The constitutive relation of the material in the cohesive zone can be described by a traction-separation relation (otherwise referred to as a cohesive zone model). The particular shape of the traction-separation relation defines the characteristics of the fracture process zone, thus, it is material dependent.

1.2 Summary of numerical methods for simulating fracture

Analytical solutions to fracture problems are often limited in application. Most analytical solutions are tabulated for specific geometries with specific boundary conditions [3, 4], and often rely on the assumption that the crack lies in an infinite domain. To model fracture in an arbitrary geometry with arbitrary boundary conditions (prominent in real world applications), numerical simulation is the method of choice. While fracture has been simulated in complicated, realistic structures for decades, many of the prevalent methods still suffer limitations in computational ease of use, speed, accuracy, and physical resolution. Moreover, many of the prominent methods cannot readily handle inhomogeneous composite structures, or nonlinear materials. As a consequence, in this thesis, we focus on the finite element method; which is intrinsically able to handle heterogeneity and nonlinearity. Although we

focus on the finite element method to simulate fracture, numerous alternative approaches have been proposed in the literature. In this section, we give an overview of some of the more prevalent numerical methods for simulating fracture. First, we give a general overview of the finite element method, then discuss a sampling of the many alternative methods.

1.2.1 Finite Element Method

The finite element method (FEM) computes the approximate solution to a partial differential or integral equation. When complex materials, boundary condition or geometries are modeled, these equations become difficult to solve analytically. The FEM is able to solve these complex problems in a regularized manner, in a reasonable amount of time, and with a relatively small amount of work. The basis for the finite element method can be derived from the principle of virtual work, expressed in the linear setting as:

$$\int_{\Omega} \delta\boldsymbol{\varepsilon}^{\mathrm{T}}\boldsymbol{\sigma} d\Omega = \int_{\Gamma} \delta\mathbf{u}^{\mathrm{T}}\mathbf{T} d\Gamma + \int_{\Omega} \delta\mathbf{u}^{\mathrm{T}}\mathbf{b} d\Omega, \tag{1.1}$$

where Ω is an arbitrary domain, subjected to surface tractions, $\mathbf{T}$, along its boundary, Γ. Moreover, $\boldsymbol{\sigma}$ denotes the stresses, $\mathbf{b}$ denotes the body forces; $\mathbf{u}$ is the displacement, $\delta\mathbf{u}$ is the virtual displacement, and $\delta\boldsymbol{\varepsilon}$ is the virtual strain.

The idea behind the finite element method is that the integral over the entire domain is approximately equivalent to the sum of the integrals taken over a finite number of smaller sub-domains known as "elements". Each element is defined by a set of nodes, connectivities, and element shape functions. The discretization of the principle of virtual work (1.1), using the standard Galerkin approximation [5], takes the following form:

$$\left(\int_{\Omega_e} \mathbf{B}_e^{\mathrm{T}}\mathbf{D}\mathbf{B}_e\mathbf{u}_e \mathrm{d}\Omega_e - \int_{\Omega_e} \mathbf{N}_e^{\mathrm{T}}\mathbf{b}_e \mathrm{d}\Omega_e - \int_{\Gamma_e} \mathbf{N}_e^{\mathrm{T}}\mathbf{t}_e \mathrm{d}\Gamma_e\right) \delta\mathbf{u}_e^{\mathrm{T}} = 0, \tag{1.2}$$

where Ω_e is the element domain, $\mathbf{N}_e$ is a matrix containing local element shape functions, $\mathbf{B}_e$ is a matrix relating the element strains to the element displacements, $\mathbf{D}$ is an elasticity matrix, and $\mathbf{u}_e$ and $\delta\mathbf{u}_e$ are the nodal displacement and virtual displacement vectors, respectively. Since Equation 1.2 holds for any virtual displacement, the first term must be equal to zero. We can then define the element-wise components of the stiffness matrix and force vector as:

$$\mathbf{K}_e = \int_{\Omega_e} \mathbf{B}_e^{\mathrm{T}}\mathbf{D}\mathbf{B}_e \mathrm{d}\Omega_e, \tag{1.3}$$

$$\mathbf{F}_e = \int_{\Omega_e} \mathbf{N}_e^{\mathrm{T}} \mathbf{b}_e \mathrm{d}\Omega_e + \int_{\Gamma_e} \mathbf{N}_e^{\mathrm{T}} \mathbf{t}_e \mathrm{d}\Gamma_e. \tag{1.4}$$

The element level components of the stiffness matrix and force vector can be assembled, which leads to a global system of algebraic equations for the unknown displacements over the entire domain [5, 6].

To capture fracture within the finite element method, special purpose cohesive elements are included within the formulation to describe the constitutive relation in the cohesive zone ahead of the crack-tip, as illustrated in Figure 1.3(c). Each cohesive element is inserted along the facet joining two bulk finite elements in the direction of potential crack propagation. Thus, the cohesive elements are one dimension smaller than the bulk elements (i.e. in 2D, cohesive elements are 1D, and in 3D, cohesive elements are 2D). A further discussion on cohesive elements will be included in Section 1.3.

1.2.2 Extended or Generalized Finite Element Method

The extended FEM (XFEM) or generalized FEM (GFEM) enriches the solution space of the standard finite element method. In particular, discontinuous enrichment functions are used to represent the crack surface and singular enrichment functions are used to represent the crack-tip. A key advantage of the extended FEM is that the bulk finite element mesh does not need to be updated to track the crack path. However, the discontinuity in the element shape functions effectively splits the element; which requires a lot of heuristic manipulations, and can present numerical integration and time-stepping issues in dynamic fracture simulations [7]. To avoid this, some researchers recommend applying restrictions to the locations at which an element can be split. For example, Remmers et al. [8] require that the element can not be split if it causes the split element to be less than 10% the area of the original element. In three dimensions, the extended FEM has proven useful in modeling fracture problems dominated by a single crack [9, 10, 11]. However, when faced with the full spectrum of fracture behavior, the extended FEM can become prohibitively complicated [12].

1.2.3 Boundary Element Method

The boundary element method (BEM) [13, 14] eliminates the need to discretize the interior of the domain, but instead represents the domain with a mesh around the boundary. In doing so, it requires fewer elements, resulting in a cost efficient method. The BEM has shown great promise in solving linear elastic, isotropic problems, but is not an effective

method for modeling anisotropic or nonlinear problems [11, 15]. Techniques have been proposed to overcome the difficulties in solving problems containing anisotropic materials [16], however, the efficiency of the BEM is lost due to the complex nature of these solutions. Within dynamic fracture simulations, multiple cracks initiate, branch, coalesce and fragment; characteristics which the BEM is currently unable to capture [11].

1.2.4 Discontinuous Galerkin Methods

The discontinuous Galerkin (DG) method seeks an elementwise-continuous polynomial approximation of the field variables over the chosen discretization [17]. Consequently, the approximation of the field variables is discontinuous across element interfaces. The main idea of the DG method is to use numerical flux terms to address the inter-element discontinuities. There have been a variety of proposed numerical flux terms in the literature, a review of many of the prominent flux terms, and their influence on numerical consistency and stability, can be found in [18].

The DG framework has been extended to account for dynamic fracture behavior [17]. In a similar fashion to that used in the FEM, to capture fracture within the DG framework, cracks are nucleated at the interface between two bulk elements. Upon the nucleation of a crack, the DG flux terms are no longer present in the formulation, and are replaced with a traction-separation relation which governs the fracture process of the material. This approach has shown to be scalable [19], and suitable for simulating pervasive fragmentation problems in three-dimensions [17]; much like the finite element method [20]. An extension of the DG method considers the discretization of spacetime domains and the use of basis functions that are fully discontinuous across all spacetime element boundaries [21]. This extension, known as the spacetime discontinuous Galerkin (SDG) method, has been used to investigate problems in dynamic cohesive fracture [22, 23].

1.2.5 Meshless Methods

The previously discussed methods discretize the problem domain into elements, and interpolate the unknown fields using element-based shape functions. Alternatively, meshless methods represent the unknown fields with nodal information [24]. By increasing the number of nodes dispersed in a region, a higher resolution of information in that region is obtained. Thus, nodes are typically clustered around the critical portions of the domain; which, in fracture problems, is the crack-tip. Each node is contained within a nodal-support region,

and a weight function is defined over each nodal-support region. The spacing of the nodes is such that each point in the domain is covered by at least three distinct weight functions. The resulting global fields are then interpolated from nodal information using a Moving Least Squares fitting procedure [25].

Examples of meshless methods include the Diffuse Element Method [26], the Element Free Galerkin method [27, 28, 29], the Reproducing Kernel Method [30], the Meshless Local Petrov-Galerkin method [31], the cracked particles method [32], and the Material Point Method [33]. Although meshless methods have shown some promise in modeling problems where fracture is dominated by a single crack, many of them still suffer from volume deletion during pervasive fracture and fragmentation problems. As the continuum material fragments, it evolves into a collection of spheres; which have a theoretical maximum packing limit of 74% [12], leading to a nonphysical loss of volume in the model.

1.2.6 Peridynamics

Peridynamics is a model which represents a material by a network of nodes [34]. Each node interacts with every other node located within a local neighborhood called a horizon. The pair-wise force interactions between nodes contain all the constitutive properties of the material being modeled. Damage is incorporated into a pair-wise force function by allowing the bonds to break once a certain critical elongation is reached. Once a bond is broken, the force is distributed to the other bonds. This process of bond breaking and load redistribution is the mechanism by which cracks initiate and propagate in the peridynamics model. The peridynamics model has been used to simulate dynamic cracks in brittle materials [35, 36], and is capable of capturing crack branching behavior consistent with experiments.

Recently, criticism has been raised on the use and applicability of the peridynamics model [37]. One criticism arises from the use of pair-wise force functions, analogous to interatomic potentials, to describe the interactions between particles which are not nearest neighbors. In heterogeneous materials, at scales larger than $3nm$, these interactions are inconsequential [37]. Instead, at these larger scales, interactions between particles which are not nearest neighbors occur through normal and shear forces in the contacts, not through potential-based pair-wise forces [37]. However, peridynamics is frequently applied to problems at these larger scales [38, 39, 40]. An additional criticism arises when a node is close to the boundary of the domain, and its horizon extends outside the boundary. To account for this in the peridynamics model, a non-physical adjustment is incorporated which results in an effectively softer material near the boundary [37, 36]. This issue is so well recognized that

it has been termed the "skin effect" in peridynamics models [36].

1.3 Classification and characterization of cohesive fracture

As discussed in the previous sections, in this thesis, we investigate failure processes using the finite element method, and use cohesive zone elements to represent the inelastic zone of damage in the region of failure. The constitutive response of a cohesive element follows a cohesive model. The cohesive model should be compatible with, but is selected independently of, the constitutive model of the bulk elements. This section describes the primary classification subsets of the prevalent cohesive models in the literature.

1.3.1 Potential-based vs. non-potential-based cohesive models

There are two distinct groups of cohesive zone models proposed in the literature. The first group consists of non-potential-based models. These models do not require the development of a symmetric system, thus they are relatively easy to develop [41]. Some examples of non-potential-based models are the linear [42], bilinear [43], trilinear [44], and trapezoidal [45] softening models. Alternatively, potential-based models are derived from a potential function; which completely characterizes the fracture behavior. The first derivatives of the potential correspond to the normal and shear component of traction, whereas the second derivatives correspond to the components of the material tangent modulus for the selected potential. In this case, since the tangent stiffness matrix is derived from a potential function, it is symmetric. There have been many potential functions proposed in the literature, including some with specific polynomial orders [46, 47], some with exponential expressions [48, 49, 50], and even one with general polynomial order [51].

1.3.2 Intrinsic vs. extrinsic cohesive models

Within each group of cohesive zone models (potential-based and non-potential-based) there are two subsets of traction-separation relations. Elements with intrinsic cohesive models are inserted, a priori, into a mesh and have a traction-separation relation which consists of both an initial elastic range and a softening range. This initial elastic range can create an artificial compliance in the mesh and may lead to non-physical results [52, 53, 54], thus they are primarily used in problems where the location of material failure is known, or specified, beforehand. On the other hand, extrinsic cohesive elements are inserted adaptively into a

mesh [55, 56, 57], and are useful in problems where the fracture path is not known prior to the start of the simulation. The traction-separation relation corresponding to an extrinsic cohesive model does not contain an initial elastic range and thus does not cause issues of artificial compliance. Sample intrinsic and extrinsic traction-separation relations, derived from the potential-based Park-Paulino-Roesler cohesive model [51], are illustrated in Figure 1.4.

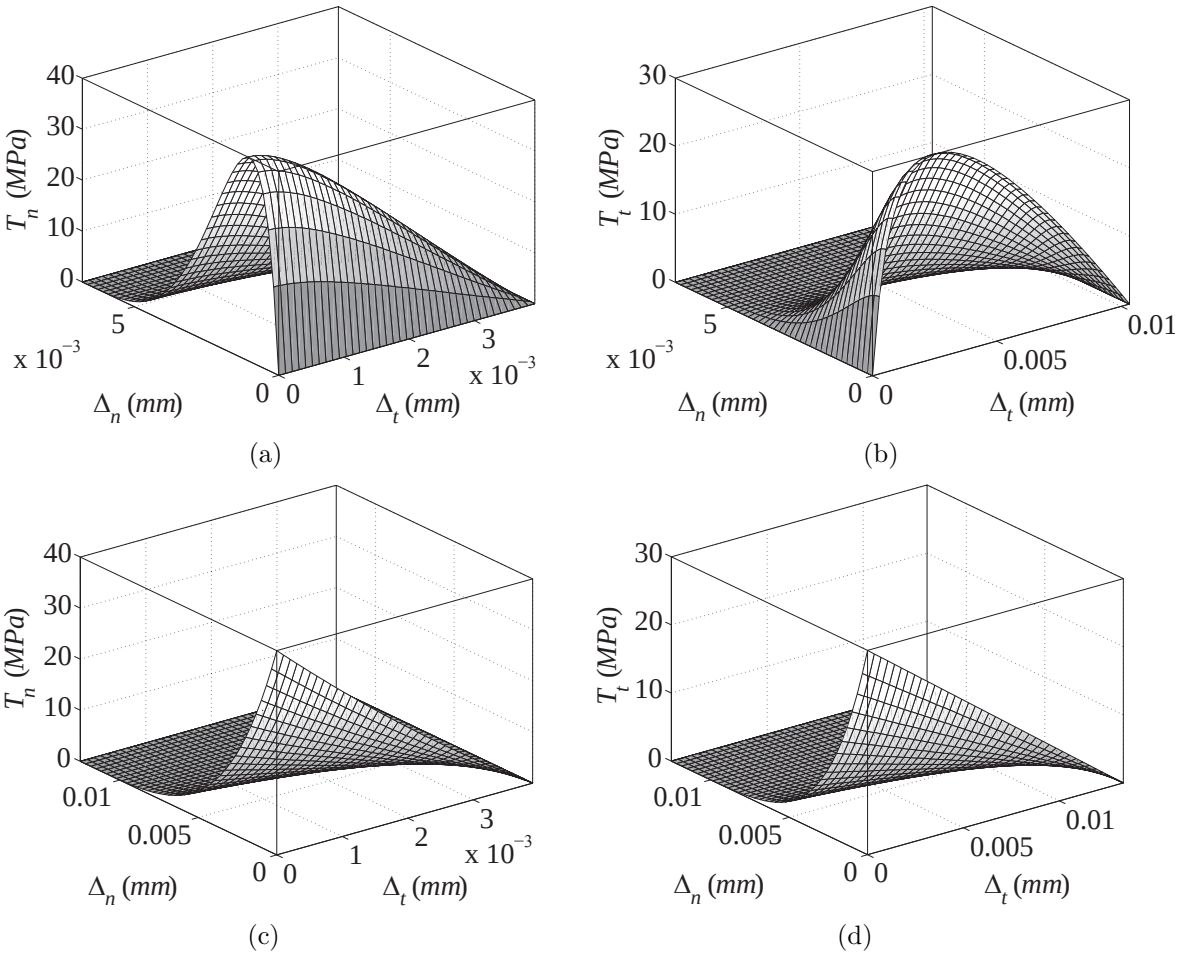

Figure 1.4: Cohesive models representative of: (a) intrinsic softening in the normal direction; (b) intrinsic softening in the tangential direction; (c) extrinsic softening in the normal direction; and (d) extrinsic softening in the tangential direction. The models are derived from the Park-Paulino-Roesler cohesive model [51] with the following fracture properties: normal energy = $100N/m$, strength = $40MPa$, shape parameter = 5, and initial slope indicator = 0.15; and tangential energy = $200N/m$, strength = $30MPa$, shape parameter = 2, and initial slope indicator = 0.25.

1.3.3 Mesh dependency

One of the primary critiques of the cohesive element method is its inherent mesh dependency [58]. Since cohesive elements are only permitted to be inserted along facets joining two bulk finite elements, if the initial mesh is designed poorly it may artificially influence the fracture behavior. In some instances, when fracture paths are known a priori, cohesive elements may be used to represent failure without influence from the mesh. For example, in this thesis, we use intrinsic cohesive elements to model particle debonding. In this example, failure only occurs between a particle and the matrix, or interphase, surrounding the particle; therefore, the size and extent of the region of failure is not influenced by the bulk mesh. However, in the dynamic fracture of brittle materials, fracture patterns are not known beforehand. In this instance, the underlying mesh can significantly influence the fracture behavior. Since this is an important issue in the cohesive element approach to fracture, we will investigate the influence of mesh dependency in dynamic fracture simulations in both two- and three-dimensions in Chapters 5 and 6, respectively.

1.4 Interface and interphase effects in particle reinforced composites

One of the topics we explore in depth in this thesis is that of particle reinforced composites. There are four primary factors which influence the macroscopic constitutive response of particle reinforced composites: component properties, component concentrations, interphases, and interfacial debonding. Interphases are often a byproduct of surface treatments applied to the particles to control agglomeration. Alternatively, in polymer based materials such as carbon-black reinforced rubber, an interphase or "bound rubber" phase often occurs at the particle-matrix interface. For example, when an inclusion is embedded into an elastomeric matrix, the polymer chains in the elastomer tend to adsorb (or anchor) onto the surface of the inclusion. This behavior results in an interphasial region in the vicinity of each particle wherein the mobility of the polymer chains is restricted, as illustrated in Figure 1.5. The composition and extent of this region is influenced by a number of factors; including the surface area and surface treatment of the inclusion phase, as well as the level of mixing and age of the composite [59, 60]. For example, Ramier et al. [61, 62] recently conducted a series of experiments on consistently prepared specimens, with different surface treatments applied to the particles in each specimen. Their investigation focused on the influence of the different surface treatments on the cross-linking in the matrix. Their results indicated that

treating the surface of the particles significantly alters the large deformation constitutive response of the composite. Representative results from their investigation are depicted in Figure 1.6.

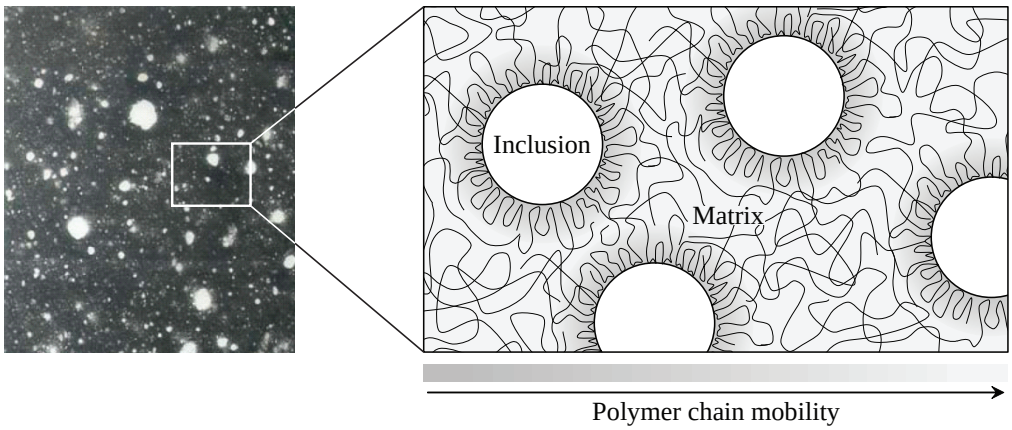

Figure 1.5: Schematic of the polymer chain mobility in an elastomeric matrix with particle inclusions. Experimental image extracted from Ramier [62].

Additionally, studies on the failure of particle reinforced composites indicate that, at large strains, a localized region of failure (or interfacial debonding) forms around particle inclusions [63, 64, 65, 66, 67]. Ramier et al. also observed this interfacial debonding behavior in many of their experiments [61, 62]. Globally, interfacial debonding is seen to significantly soften the response of the composite, as illustrated in Figure 1.6(b). In this thesis, we use computational homogenization techniques to develop a fully three-dimensional computational framework capable of capturing these microscale features, and investigate their influence on the macroscale constitutive response of particle reinforced composites. In this framework, we model interphases explicitly and use cohesive elements to capture interfacial debonding.

The numerical investigation of interfacial debonding using the cohesive element method was pioneered by Needleman in 1987 [46]. In his investigation, *intrinsic* cohesive elements were used to capture the full range of particle debonding behavior, from void nucleation to full decohesion. To date, most investigations of interfacial debonding have been conducted using two-dimensional and simplified three-dimensional models. In two dimensions, the plain strain assumption is often employed to model fiber inclusions. Zhong and Knauss [68, 69] used linear softening cohesive elements to investigate debonding in fiber-reinforced composites with structured microstructures. They focused on the tensile response of the composites, and studied the influence of various factors; including particle size, shape and distribution. Moraleda et al. [70] used a linear softening cohesive relation to study the influence of interfacial debonding on the tensile response of fiber-reinforced elastomers. They considered both a

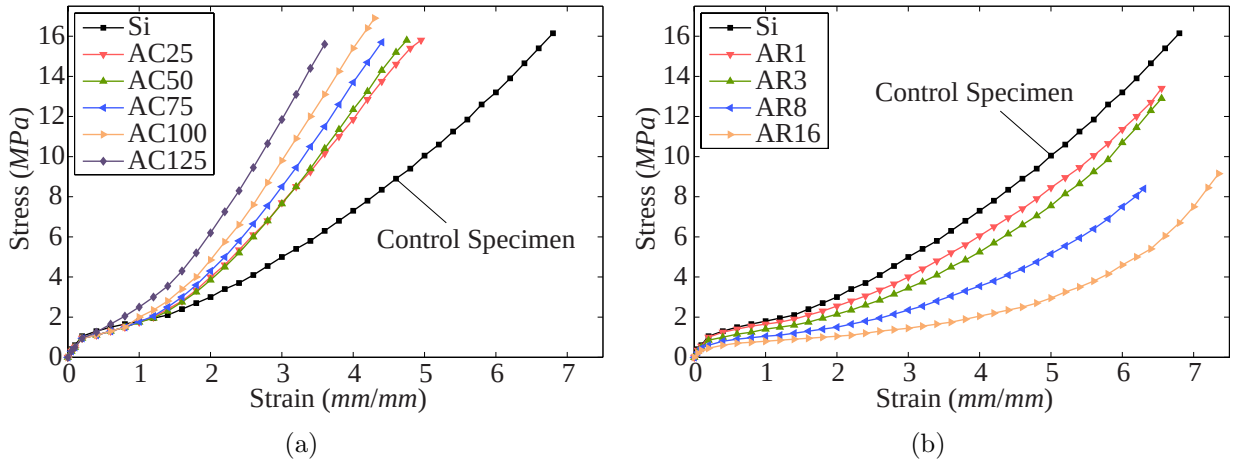

Figure 1.6: Experimentally obtained uniaxial stress-strain response of styrene-butadiene rubber filled with a 20% concentration of silica particles with different surface treatments (Si, AC25, AC50, AC75, AC100, AC125, AR1, AR3, AR8, and AR16); which results in different types of interphases, and hence different macroscopic constitutive responses. (a) Perfectly bonded interphases, and (b) interphases with interfacial debonding. Data extracted from Ramier [62].

single particle microstructure and a microstructure with a random distribution of monodisperse particles. Inglis et al. [71] used two-dimensional models to investigate debonding in polydisperse microstructures containing a high concentration of particulates. Brassart et al. [72] used the same numerical framework as Inglis et al. to capture the debonding of rigid inclusions under axisymmetric tension. They considered periodic unit cells with a random distribution of up to ten monodisperse particles.

However, to accurately capture the effect of spherical particle inclusions, fully three-dimensional modeling is necessary. Matouš and Geubelle [73, 74] used an effective displacement, exponential softening, cohesive relation to study the debonding of spherical particles. In their fully three-dimensional investigation, they considered both a single particle microstructure and a four-particle microstructure. In their investigation of the four-particle microstructure, they used a slight perturbation in the position of the particles. Through these simplified microstructures they were able to demonstrate the significant influence of interfacial debonding on the macroscopic constitutive response of these composites.

One common feature among all of the investigations mentioned above is that none of them consider the influence of interphases. While it has been shown experimentally that interphases significantly alter the macroscopic response of particle reinforced composites, their inclusion in computational models is widely omitted. There are four primary factors which influence the macroscopic response of particle reinforced composites: component properties, component concentrations, interphases, and interfacial debonding. In this thesis, we investigate the interplay between the four factors and attempt to quantify their influence on the

macroscopic constitutive response of these composite materials under both small and large deformations in both linear elastic and hyperelastic materials.

1.5 Thesis scope and organization

The objective of this thesis is to investigate the full spectrum of failure behavior, using the cohesive element method. First, we develop a computational framework to investigate the constitutive response of particle reinforced composites, considering the influence of physically meaningful interphases and interfacial debonding. Next, we develop two new topological operators for unstructured polygonal discretizations, to reduce mesh induced artifacts in dynamic cohesive fracture simulations in two-dimensions. Finally, in three-dimensions, we use unstructuring methods to investigate and regularize the pervasive fracture and fragmentation of quasi-brittle materials under extreme loading scenarios.

The remainder of the thesis is organized as follows. Chapter 2 discusses the significance of perfectly bonded, microscale interphases on the macroscale constitutive response of particle reinforced elastomers. We first discuss the relevant theoretical frameworks which have been proposed to capture the large deformation response of these composites; giving particular attention to a recently developed framework by Goudarzi et al. [75]. We then develop a computational framework capable of capturing the influence of interphases. The computational framework is verified and validated with theoretical and experimental results available in the literature. Chapter 3 presents the formulation and implementation of a small library of three-dimensional cohesive elements for use in a commercial finite element analysis software package. This contribution was written from an educational perspective, and, for wider dissemination, is accompanied with a sample source code in Appendix B. Next, we combine the three-dimensional cohesive elements with the computational framework developed in Chapter 2 to investigate the role of interphases and interfacial debonding on the constitutive response of particle reinforced composites in Chapter 4.

In the remaining chapters of the thesis, we switch our focus from quasi-static failure with intrinsic cohesive elements to dynamic failure with adaptively inserted, extrinsic cohesive elements. First, in Chapter 5, we explore the benefits of using polygonal finite elements for simulating dynamic cohesive fracture. In order to reduce mesh induced bias in the geometrically restrictive polygonal meshes, we develop two new topological operators. We discuss the implementation of the new operators, and quantify their improvement on fracture behavior through a geometric study and five numerical examples. The examples are selectively chosen to represent the full range of fracture behavior in quasi-brittle materials; from problems

failing due to a dominant crack to problems failing due to pervasive fragmentation. Finally, in Chapter 6, we use both geometric and constitutive unstructuring methods to investigate and regularize the pervasive fracture and fragmentation of quasi-brittle materials under extreme loading conditions in three-dimensions. Additionally, in this chapter, we present a new meshing strategy which addresses many of the outstanding mesh induced issues observed while conducting the work in this thesis. Finally, a summary of the main conclusions of this work, and a number of directions in which this work could be extended, is presented in Chapter 7.

Chapter 2

Particle Reinforced Elastomers and the Significance of Interphases

The objective of the next three chapters is to develop and implement a computational framework for modeling the constitutive response of particle reinforced elastomers, considering the influence of both interphases and interfacial debonding. In this chapter, we limit our investigation to the influence of perfectly bonded interphases. In the subsequent chapter, we develop a small library of cohesive elements suitable for capturing the behavior of interfacial debonding. In Chapter 4, we combine the work in this chapter and the next, to investigate the combined influence of both interphases and interfacial debonding on the macroscopic constitutive response of particle reinforced elastomers.

This chapter motivates the inclusion of interphases in the numerical analysis of particle reinforced elastomers. The presence of interphases surrounding particle inclusions is a well established occurrence; however, their incorporation in both theoretical and computational frameworks which aim to capture the full range of behavior of these composites, is often omitted. In this chapter, we provide a brief summary of the experimental and theoretical work that has been done on this topic. Additionally, we outline a recently developed, fully nonlinear theoretical framework which accounts for the presence of perfectly bonded interphases in particle reinforced elastomers. Finally, we present a computational framework capable of capturing the behavior of such composites, and investigate the influence of many significant microstructural features; including, constituent properties and concentrations. For the most generality, we consider both monodisperse and polydisperse microstructures in both the small deformation and large deformation regimes. The computational framework is verified and validated with theoretical and experimental results available in the literature.

2.1 Introduction

When a particle is embedded into an elastomeric matrix, the polymer chains in the elastomer tend to adsorb (or anchor) onto the surface of the particle; either by means of a chemical reaction or by an act of interdiffusion of the component materials [59, 76]. This behavior

results in an interphasial region in the vicinity of each particle with distinct properties from both those of the matrix and those of the particle. This interphase region plays a key role in all particulate filled composites, regardless of the type, or structure, of the components. In some cases, interphases are concluded to be the primary factor controlling the properties of a composite [76, 77]; thus, their investigation is of utmost importance to the future development and advancement of such composites.

While interphases have been known to exist for many decades [78, 79, 80, 81, 82], their visualization and experimental characterization has only recently become possible. In 2004, Mäder and Gao [83] used scanning force microscopy to observe the modulus profile in the interphasial region surrounding fibers embedded in an elastomeric matrix. They demonstrated that the stiffness of the interphase depends on the composition and surface treatment of the fiber. More recently, Qu et al. [84] experimentally visualized and characterized the behavior of the material at the particle-elastomer interface. They used atomic force microscopy to conduct in-situ imaging of particle-elastomer interactions. They demonstrated that the macroscopic properties (in particular, the stiffness and scratch resistance) of the composite can be tailored, by selectively designing the surface chemistry of the particles. Typical results from their investigation are illustrated in Figure 2.1.

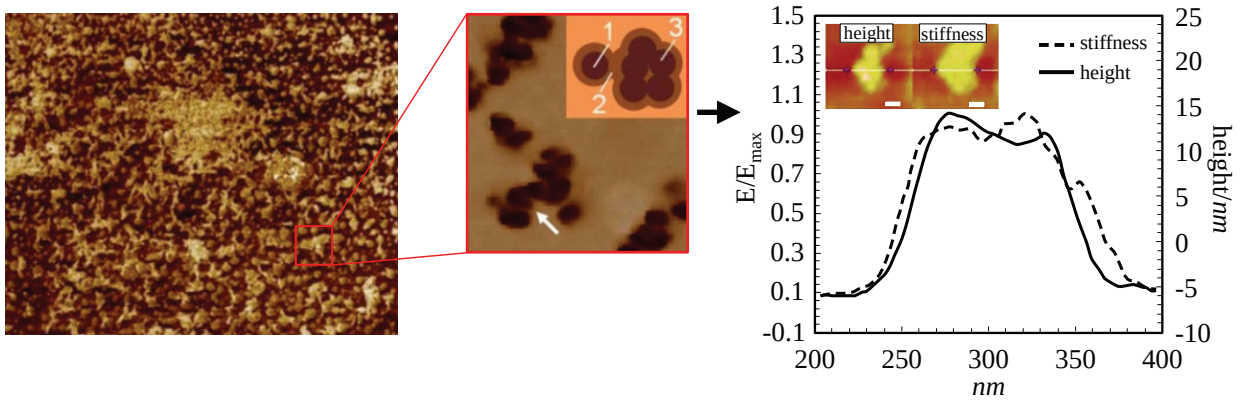

Figure 2.1: Experimental evidence of interphases showing the normalized particle profiles measured on torsional harmonic atomic force microscopy height and stiffness maps (scale bar = $50nm$). Images extracted from Qu et al. [84].

To capture the full effect of spherical particle reinforced elastomers in a computational framework, three-dimensional modeling is necessary. An early investigation of particle reinforced elastomers can be found in the limited study of Bergström and Boyce [85]. They investigated the influence of perfectly bonded particle inclusions on the macroscopic compressive stiffness of elastomers. Using very coarse finite element models, they demonstrated that the addition of particles leads to stiffening behavior in line with experimental observations. Later, Segurado and Llorca [86] conducted a numerical investigation into the influence of

particle inclusions and voids on the effective modulus of an elastomeric matrix. They demonstrated that a representative unit cell, with randomly distributed monodisperse particles and periodic boundary conditions, can capture behavior in line with analytical solutions available in the literature. Alternatively, Galli et al. [87] investigated the influence of polyhedral inclusions on the elasto-plastic response of particle reinforced composites. By assuming polyhedral inclusions, they were able to use the same mesh discretization for each concentration of particles they considered, by simply assigning a larger number of finite elements to the properties of the particles. More recently, Lopez-Pamies et al. [88, 89] developed an approximate analytical solution for isotropic hyperelastic materials reinforced by an infinitely polydisperse distribution of rigid particles. They verified their analytical solution with full 3D finite element simulations, the first of their kind to extend to the finite deformation regime. Their investigation found good correlation between theoretically derived and numerically simulated results. The contributions of Lopez-Pamies et al. significantly influenced and motivated the contributions in this chapter. Even though their investigation omitted the inclusion of interphases, they did comment on the known, significant contribution of interphases to the overall constitutive response of such composite materials.

The objective of this chapter is to motivate the inclusion of interphases when modeling heterogeneous multiphase materials. To the best of the author's knowledge, their has been no computational framework proposed for the investigation of particle reinforced elastomers; which includes the influence of interphases, in the finite deformation regime. We aim to show that the inclusion of interphases in particle reinforced elastomers can lead to behavior which is more consistent with that obtained experimentally. To do this, we investigate the influence of interphases in both the small-deformation and large-deformation regimes, and attempt to demonstrate the key interphasial properties which influence the global constitutive response. In the following section, we provide some background information on the history of this problem. In Section 2.3, we briefly outline the theoretical framework developed in conjunction with this work; the extended details of the theoretical formulation may be found in the accompanying publication [75]. Section 2.4, proposes a computational framework for the full 3D simulation of these composites; wherein we explicitly model homogeneous interphases at the particle-matrix interface. In Section 2.5, we compare our computational framework with both theoretical and experimental results in the small deformation regime; and, in Section 2.6, we compare our computational framework with both theoretical and experimental results in the large deformation regime. Finally, we provide some concluding remarks and discuss the extension of this work in Section 2.7.

2.2 History

In 1906, Einstein [90] derived a solution for the effective viscosity of a dilute suspension of rigid particles in a viscous solvent, assuming perfect adhesion between the phases. He determined that the effective viscosity of the solvent, $\bar{\eta}$ is given as:

$$\bar{\eta} = \eta \left(1 + 2.5c\right), \tag{2.1}$$

where η is the viscosity of the solvent, and c is the concentration of the particles. By exploiting the analogy between Stokes-flow and small-strain linear elasticity, Smallwood extended the Einstein solution to linear elasticity. In this case, the resulting effective shear modulus, $\bar{\mu}$, of an isotropic incompressible elastomer reinforced with a dilute concentration of rigid spherical particles is similarly calculated as:

$$\bar{\mu} = \mu_m \left(1 + 2.5c\right), \tag{2.2}$$

where μ_m is the modulus of the elastomeric matrix. Subsequently, Guth [91] extended the Einstein-Smallwood solution, to account for a finite concentration of particles:

$$\bar{\mu} = \mu_m \left(1 + 2.5c + 14.1c^2\right), \tag{2.3}$$

where the quadratic term accounts for the mutual interaction of pairs of particles. In this setting of linear elasticity, many authors have made contributions; accounting for non-spherical inclusions and non-dilute concentrations (for example, see [92, 93] and the references therein).

As opposed to the early attention given to the small-strain problem, the first formal framework capable of describing the finite strain response of filled elastomers was proposed by Hill [94] in 1972. Despite the presence of an applicable framework, however, little progress has been made in its application [89, 95]. In the following section, we will discuss a recently proposed, fully nonlinear, closed-form solution for the overall response of filled elastomers under finite strains - developed by Goudarzi et al. [75]. In their formulation, they consider the influence of perfectly bonded interphases. Their solution procedure consists of three steps. In the first step, a closed-form solution is developed for a dilute suspension of rigid particles, bonded to a neo-Hookean matrix through interphases of finite size. In the second step, an iterated dilute homogenization technique is used to extend the dilute solution to one for a finite concentration of particles in a Gaussian elastomer. Finally, in the third step, a nonlinear comparison medium method is used to develop a solution for a finite concentration of particles in a non-Gaussian elastomer.

2.3 Theoretical framework

In this section, we briefly outline the theoretical solution developed by Goudarzi et al. [75, 95]; which describes the macroscopic response of particle reinforced elastomers with perfectly bonded interphases. The extended details of the solution may be found in the principal publication [75]; we just highlight a few critical details for completeness, and maintain the notation of [75] for consistency. In subsequent sections, we will use this theoretical framework to verify the computational framework developed in this chapter.

2.3.1 The problem

The problem under consideration is that of a filled elastomer occupying a domain Ω, with boundary $\partial\Omega$, in its undeformed state, as illustrated in Figure 2.2. The composite material consists of a random dispersion of rigid particles, bonded to an elastomeric matrix through interphases of finite size [95]. The elastomeric matrix is assumed to be isotropic and incompressible. The particles are assumed to be spherical, and their random dispersion is assumed to result in an isotropic material. Additionally, the interphases are assumed to be of constant thickness and constituted of a Gaussian elastomer. The matrix, particles and interphases occupy domains Ω_m, Ω_p and Ω_i, respectively; such that $\Omega = \Omega_m + \Omega_p + \Omega_i$. Thus, the concentrations of the respective components are given by $c_m \equiv |\Omega_m| \,/\, |\Omega|$, $c_p \equiv |\Omega_p| \,/\, |\Omega|$, and $c_i \equiv |\Omega_i| \,/\, |\Omega|$.

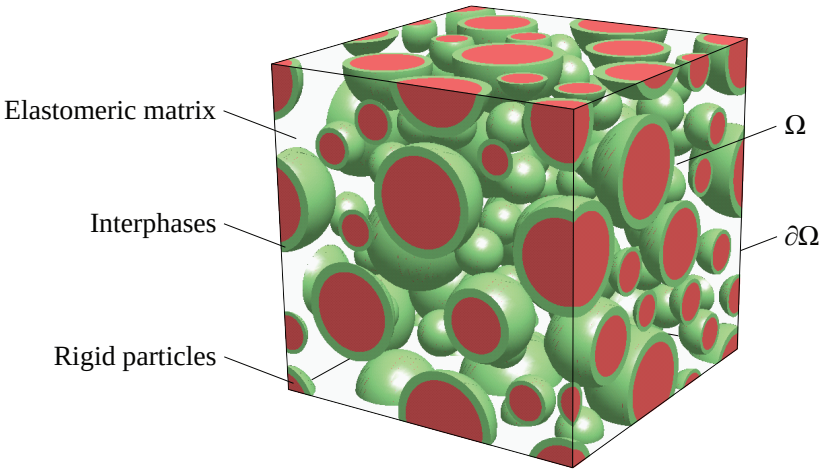

Figure 2.2: A schematic of the composite filled elastomer considered in this investigation. The composite consists of a random dispersion of rigid particles, bonded to an elastomeric matrix through constant-thickness interphases of finite size.

2.3.2 A *dilute* concentration of particles in the *small*-deformation regime

Goudarzi et al. [75] developed a series of solutions for the macroscopic response of particle filled elastomers considering the influence of interphases. First, they assumed a *dilute* concentration of rigid particles bonded to a Gaussian matrix through constant-thickness interphases. The Gaussian matrix is assumed to follow a neo-Hookean material model, with stored-energy function:

$$\Psi\left(I_1\right) = \left\{ \begin{array}{ll} \frac{\mu_m}{2}\left[I_1 - 3\right] & \text{if } J = \lambda_1\lambda_2\lambda_3 = 1 \\ +\infty & \text{otherwise} \end{array} \right\}, \tag{2.4}$$

where μ_m is the initial shear modulus of the matrix, $I_1 = \mathbf{F}\cdot\mathbf{F}$ is the first principal invariant of the right Cauchy-Green tensor, and $\mathbf{F}$ is the deformation gradient. A *dilute* concentration of particles assumes that particles are well separated (i.e. they do not interact with one another). With this assumption, it is expected that the effective stored-energy function for a dilute suspension of particles in a finite-sized matrix will agree identically with that for a single particle suspended in an infinite matrix [75]. In the limit of small deformations, Goudarzi et al. [75] demonstrate that this problem has an exact solution, wherein the effective stored-energy function is described as:

$$\overline{\Psi}\left(\bar{I}_1, \bar{I}_2, c_p, c_i\right) = \mu_m \mathrm{tr}\bar{\boldsymbol{\varepsilon}}^2 + \frac{5\mu_m}{2}\mathrm{tr}\bar{\boldsymbol{\varepsilon}}^2 c_p + \frac{5\left(\mu_i - \mu_m\right)\left(q_1\mu_i + q_4\mu_m\right)\mu_m}{2\left(q_1\mu_i^2 + q_2\mu_i\mu_m + q_3\mu_m^2\right)}\mathrm{tr}\bar{\boldsymbol{\varepsilon}}^2 c_i, \tag{2.5}$$

where $\bar{\boldsymbol{\varepsilon}} = (\overline{\mathbf{F}} + \overline{\mathbf{F}} - 2\mathbf{I})/2$, and $\bar{I}_1 = \bar{\lambda}_1^2 + \bar{\lambda}_2^2 + \bar{\lambda}_1^{-2}\bar{\lambda}_2^{-2}$ and $\bar{I}_2 = \bar{\lambda}_1^{-2} + \bar{\lambda}_2^{-2} + \bar{\lambda}_1^2\bar{\lambda}_2^2$ are the first two principal invariants. Additionally,

$$q_1 = 38k^{10} + 225k^7 - 336k^5 + 200k^3 + 48, \tag{2.6}$$

$$q_2 = 89k^{10} + 75k^7 - 168k^5 + 100k^3 - 96, \tag{2.7}$$

$$q_3 = 48k^{10} - 300k^7 + 504k^5 - 300k^3 + 48, \tag{2.8}$$

$$q_4 = \frac{4\left(k-1\right)^3\left(2k^3+3\right)\left(4k^6 + 16k^5 + 40k^4 + 55k^3 + 40k^2 + 16k + 4\right)}{k^2 + k + 1}, \tag{2.9}$$

with

$$k = \left(1 + \frac{c_i}{c_p}\right)^{1/3}. \tag{2.10}$$

This may also be written in compact form as:

$$\overline{\Psi}\left(\bar{I}_1, \bar{I}_2, c_p, c_i\right) = \overline{\mu}^{\text{dilute}} \text{tr}\overline{\boldsymbol{\varepsilon}}^2, \tag{2.11}$$

where

$$\overline{\mu}^{\text{dilute}} \equiv \mu_m + \frac{5\mu_m}{2} c_p + \frac{5(\mu_i - \mu_m)(q_1\mu_i + q_4\mu_m)\mu_m}{2(q_1\mu_i^2 + q_2\mu_i\mu_m + q_3\mu_3^2)} c_i. \tag{2.12}$$

Notably, this solution is a generalization of the classical Einstein-Smallwood solution (2.2) for the effective shear modulus of a dilute distribution of rigid spherical particles suspended in a matrix (i.e without the inclusion of interphases). For extended details, and features, of the above formulation, the reader is referred to [75].

2.3.3 A *dilute* concentration of particles in the *large*-deformation regime

In general, it is not possible to solve dilute problems in finite elasticity by analytical means. Thus, in order to develop an approximate solution, numerical approaches are necessary. Goudarzi et al. [75] constructed a numerical solution by developing a finite element model of an infinitesimal particle, surrounded by an interphase, embedded in a finite-size block of elastomer. The resulting finite element solution admitted the following asymptotic form:

$$\overline{\Psi}^{\text{FE}}\left(\bar{I}_1, \bar{I}_2, c_p, c_i\right) = \frac{\mu_m}{2}\left[\bar{I}_1 - 3\right] + \mu_m H\left(\bar{I}_1, \bar{I}_2\right) c_p + \mu_m G\left(\bar{I}_1, \bar{I}_2\right) c_i, \tag{2.13}$$

where H and G are correction functions, accounting for the inclusion of the particle and the interphase, respectively. The numerical forms of the correction functions are computed as follows [75]:

$$H\left(\bar{I}_1, \bar{I}_2\right) = \frac{1}{c_p}\left\{\frac{1}{\mu_m}\overline{\Psi}^{\text{FE}}\left(\bar{I}_1, \bar{I}_2, c_p, 0\right) - \frac{1}{2}\left[\bar{I}_1 - 3\right]\right\}, \tag{2.14}$$

$$G\left(\bar{I}_1, \bar{I}_2\right) = \frac{1}{c_i}\left\{\frac{1}{\mu_m}\overline{\Psi}^{\text{FE}}\left(\bar{I}_1, \bar{I}_2, c_p, c_i\right) - \frac{1}{2}\left[\bar{I}_1 - 3\right] - H\left(\bar{I}_1, \bar{I}_2\right) c_p\right\}. \tag{2.15}$$

After computing the correction functions, Goudarzi et al. [75] deduced the following closed-form analytical approximations:

$$H\left(\bar{I}_1, \bar{I}_2\right) = \frac{5}{4}\left[\bar{I}_1 - 3\right], \tag{2.16}$$

$$G\left(\bar{I}_1, \bar{I}_2\right) = \frac{5(\mu_i - \mu_m)(q_1\mu_i + q_4\mu_m)}{4(q_1\mu_i^2 + q_2\mu_i\mu_m + q_3\mu_3^2)}\left[\bar{I}_1 - 3\right]. \tag{2.17}$$

Substituting the approximations for the correction functions back into the effective stored-energy function (2.13) yields:

$$\overline{\Psi}^{\mathrm{FE}}\left(\bar{I}_1, \bar{I}_2, c_p, c_i\right) = \frac{\mu_m}{2}\left[\bar{I}_1 - 3\right] + \frac{5\mu_m}{4}\left[\bar{I}_1 - 3\right] c_p + \frac{5\left(\mu_i - \mu_m\right)\left(q_1\mu_i + q_4\mu_m\right)\mu_m}{4\left(q_1\mu_i^2 + q_2\mu_i\mu_m + q_3\mu_m^2\right)}\left[\bar{I}_1 - 3\right] c_i \tag{2.18}$$

$$= \frac{\overline{\mu}^{\mathrm{dilute}}}{2}\left[\bar{I}_1 - 3\right] \tag{2.19}$$

where the coefficients, q_1, q_2, q_3, and q_4 are defined by Expressions 2.6 to 2.9.

2.3.4 A *finite* concentration of particles in a *Gaussian* elastomer

The randomly oriented, sparsely cross-linked, long chain molecular structure of elastomers enables these materials to undergo large, nonlinear elastic deformations. As an elastomer undergoes large deformations, its randomly oriented molecular structure becomes preferentially oriented [96]. Thus, the distribution and initial lengths of the individual chains in the molecular structure impacts the manner in which the elastomer stiffens. A single polymer chain is said to contain n links of length l [96]. In a *Gaussian* elastomer, the average initial length of each chain (in the undeformed configuration) is $L_o = \sqrt{n}l$, and the final extended length of each chain, after deformation, is assumed to be much less than the fully extended length, nl [96]. However, at large strains, this assumption is no longer valid, and typical elastomers display strain hardening (behavior that the Gaussian assumption is unable to capture). In this case, we turn to a *non-Gaussian* description of the elastomer, wherein strain hardening behavior can be captured. In this section, we describe the solution for a finite concentration of particles in a Gaussian elastomer and in the next section we describe the corresponding solution for a non-Gaussian elastomer.

In order to obtain the solution for a Gaussian elastomer reinforced by a *finite* concentration of rigid particles, an iterated dilute homogenization method is used [97, 98, 99]. In this method, at each iteration, a dilute concentration of rigid particles is embedded in the matrix. The resulting composite at each iteration is viewed as a homogenous matrix during the next iteration, wherein a dilute concentration of particles of much larger size are embedded in the composite. This procedure is repeated an arbitrarily large number of times, until a finite total concentration of particles is reached. Details of the iterated dilute homogenization method may be found in references [89, 100]. Following this approach, Goudarzi et al. [75]

calculated the following homogenized solution for a finite concentration of rigid particles bonded to a Gaussian matrix through constant-thickness interphases:

$$\overline{\Psi}\left(\bar{I}_1, \bar{I}_2, c_p, c_i\right) = \frac{\overline{\mu}}{2}\left[\bar{I}_1 - 3\right], \tag{2.20}$$

where $\bar{\mu}$ is defined implicitly through the expression:

$$\begin{aligned}
&\mathcal{F}_1\left\{\bar{\mu}, \mu_m\right\} = \frac{c_i\left[q_4^2 - q_4\left(q_1 + 2q_2 + q_3\right) + q_1 q_3\right] + c_p\left[q_3\left(2q_1 + q_2\right) - q_4\left(q_2 + 2q_3\right)\right]}{\sqrt{c_i^2\left(q_1 + q_4\right)^2 + 2c_i c_p\left[q_4\left(2q_1 + q_2\right) - q_1\left(q_2 + 2q_3\right)\right] + c_p^2\left(q_2^2 - 4q_1 q_3\right)}} \times \\
&\left\{\tanh^{-1}\left[\frac{c_i\left(q_4 - q_1\right) + c_p q_2 + 2\left(c_p q_3 - c_i q_4\right)\frac{\overline{\mu}}{\mu_i}}{\sqrt{c_i^2\left(q_1 + q_4\right)^2 + 2c_i c_p\left[q_4\left(2q_1 + q_2\right) - q_1\left(q_2 + 2q_3\right)\right] + c_p^2\left(q_2^2 - 4q_1 q_3\right)}}\right] - \right. \\
&\left.\tanh^{-1}\left[\frac{c_i\left(q_4 - q_1\right) + c_p q_2 + 2\left(c_p q_3 - c_i q_4\right)\frac{\mu_m}{\mu_i}}{\sqrt{c_i^2\left(q_1 + q_4\right)^2 + 2c_i c_p\left[q_4\left(2q_1 + q_2\right) - q_1\left(q_2 + 2q_3\right)\right] + c_p^2\left(q_2^2 - 4q_1 q_3\right)}}\right]\right\} - \\
&\frac{1}{2}\left(q_3 + q_4\right)\ln\left[\frac{c_i\left(\overline{\mu} - \mu_i\right)\left(\mu_i q_1 + q_4\overline{\mu}\right) - c_p\left(\mu_i^2 q_1 + \mu_i q_2\overline{\mu} + q_3\overline{\mu}^2\right)}{c_i\left(\mu_m - \mu_i\right)\left(\mu_i q_1 + q_4\mu_m\right) - c_p\left(\mu_i^2 q_1 + \mu_i q_2\mu_m + q_3\mu_m^2\right)}\right] + \\
&\left(q_4 - \frac{c_p}{c_i}q_3\right)\ln\left[\left(1 - c_i - c_p\right)^{5/2}\frac{\overline{\mu}}{\mu_m}\right] = 0.
\end{aligned} \tag{2.21}$$

and the coefficients, q_1, q_2, q_3, and q_4 are defined by Expressions 2.6 to 2.9.

2.3.5 A *finite* concentration of particles in a *non-Gaussian* elastomer

Finally, using the above solution for a filled Gaussian elastomer, a comparison medium method can be used to develop a corresponding solution for a filled non-Gaussian elastomer [101, 102]. Briefly, the comparison medium method uses a variational framework which permits the construction of an explicit, approximate solution for the effective stored-energy function for a filled non-Gaussian elastomer directly in terms of the "simpler" effective stored-energy function for a filled Gaussian elastomer [89]. Using this method, Goudarzi et al. [75] derive the following explicit form for the effective stored-energy function for a filled non-Gaussian elastomer:

$$\overline{\Psi}\left(\bar{I}_1, \bar{I}_2, c_p, c_i\right) = \left(1 - c_p - c_i\right)\Psi_m\left(\mathcal{I}_1\right) + \frac{\overline{\mu}_0}{2}\left[\bar{I}_1 - 3\right] - \left(1 - c_p - c_i\right)\frac{\mu_0}{2}\left[\mathcal{I}_1 - 3\right], \tag{2.22}$$

where

$$\mathcal{I}_1 = \left(\frac{c_p\bar{\mu}_0 + \frac{(\mu_i-\bar{\mu}_0)(q_1\mu_i+q_4\bar{\mu}_0)}{q_1\mu_i^2+q_2\mu_i\bar{\mu}_0+q_3\bar{\mu}_0^2}c_i\bar{\mu}_0}{c_p\mu_0 + \frac{(\mu_i-\mu_0)(q_1\mu_i+q_4\mu_0)}{q_1\mu_i^2+q_2\mu_i\mu_0+q_3\mu_0^2}c_i\mu_0} \right) \frac{\left[\bar{I}_1 - 3\right]}{1 - c_p - c_i} + 3, \tag{2.23}$$

and $\bar{\mu}_0$ and μ_0 are defined implicitly through the coupled nonlinear equations:

$$\mathcal{F}_1\left\{\bar{\mu}_0, \mu_0\right\} = 0, \quad \text{and} \quad \mathcal{F}_2\left\{\bar{\mu}_0, \mu_0\right\} = \Psi'_m\left(\mathcal{I}_1\right) - \frac{\mu_0}{2} = 0, \tag{2.24}$$

and $\mathcal{F}_1$ is given in Equation 2.21. Once again, for extended details and features of the formulation, the reader is referred to [75].

2.4 Computational framework

To complete our investigation, in this section, we develop a computational framework capable of capturing the macroscopic response of particle reinforced elastomers with perfectly bonded interphases. The computational framework is based on the use of a representative unit cell, and, for broad applicability, uses the commercial finite element analysis software Abaqus [103] to carry out the simulations. A representative unit cell (RUC) is a microstructural model containing the smallest material volume element for which the usual spatially constant macroscopic constitutive representation is accurately captured [104, 105]. The size of the RUC model should be large enough to represent the microstructure without introducing non-existing macroscopic properties (such as anisotropy in a macroscopically isotropic material). The appropriate sizing of our models will be investigated in Section 2.4.5. Alternatively, one may use a representative volume element (RVE) model; which is a microstructural model capable of reproducing the statistical nature of the microstructure in the actual composite. To be statistically representative of the composite (i.e. to effectively include a sampling of all possible microstructural configurations that occur in the composite), the model may need to be sized arbitrarily large. The sizing of the RVE is generally qualitative; thus articles on the topic generally state that the RVE must be sized "sufficiently large" compared to the microstructural size [104]. Additionally, the larger the mismatch in material properties the large the size of the RVE, thus the cases being investigated (a rigid phase in a soft phase) will lead to very large models and could become computationally cumbersome [106].

Representative unit cells are commonly applied in the literature to investigate random, periodic microstructures, as they allow one to obtain the complete microstructure of the material by translating the unit cell in the three ($\pm$) Cartesian directions [107, 108, 109], as illustrated in Figure 2.3. In this investigation, we consider composites with both monodis-

perse and polydisperse distributions of particles; however, our investigation demonstrates that there is little difference between the two distributions, at small particle concentrations.

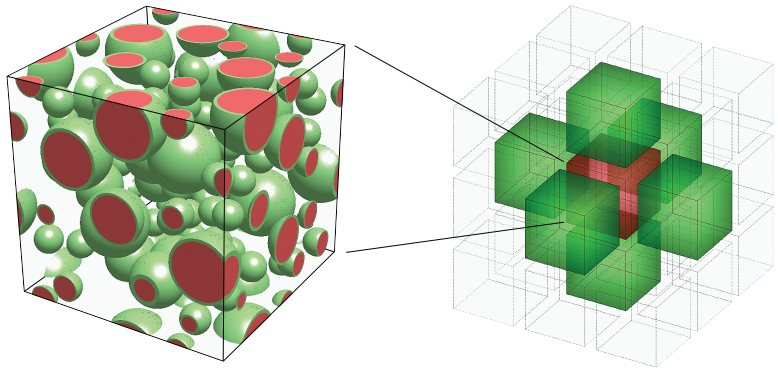

Figure 2.3: Depiction of a periodic geometry. Periodicity ensures that the particles are placed in such a manner that if the cell were to be replicated and placed adjacent, in any of the three ($\pm$) Cartesian directions, it would result in a continuous microstructure.

2.4.1 Microstructures with a monodisperse distribution of particles

The monodisperse microstructures are generated using a constrained random sequential adsorption algorithm [86, 110]. Spherical particles of radius r_p, surrounded by interphases of thickness t, are sequentially added to the microstructure. For ease of modeling, it is assumed that interphases do not overlap. This assumption allows for a higher quality discretization of the problem domain, while permitting a more general behavior analysis. Once a random location for a particle is generated, two necessary criterion are checked for that site to be accepted:

- If the center-to-center distance between the interphase of a newly generated particle and that of a previously accepted one is below a specified constraint value, the new site is rejected. The constraint value, s_1, is calculated as $s_1 = 2\,(1 + d_1)\,(r_p + t)$, where the offset distance is fixed as $d_1 \geq 0.05$. Using notation similar to that of Lopez-Pamies et al. [89], this is compactly written as:

$$\left\|\mathbf{X}^i - \mathbf{X}^j - \mathbf{h}\right\| \geq s_1, \tag{2.25}$$

  where $i,\, j = 1, 2, \ldots N$, $\mathbf{X}^i$ ($\mathbf{X}^j$) denotes the location of the centroid of particle i (j), N is the total number of particles in the microstructure, and $\mathbf{h}$ is a vector composed of 0, L, and $-L$ entries, accounting for the periodicity of the unit cell with dimensions $L \times L \times L$ [89].

- The distance between the boundary of the unit cell, $\partial\Omega$, and any interphase, should be sufficiently great to allow for a high quality discretization to be formed. The distance, s_2, between the boundary and each interphase should satisfy:

$$\left|X_k^i - r_p - t\right| \geq s_2, \qquad \left|X_k^i + r_p + t - L\right| \geq s_2 \qquad (k = 1, 2, 3) \tag{2.26}$$

  where $s_2 = d_2\,(r_p + t)$ and the offset distance is fixed as $d_2 = 0.05$.

Prior investigations have illustrated that the use of $N = 30$ particles is appropriate to capture the overall isotropy of the material [86, 89], and is the number of particles used in this investigation. This assumption is verified in Section 2.4.5. Figure 2.4 illustrates sample monodisperse microstructures generated using the above procedure, for a particle concentration of $c_p = 0.15$. A script incorporating the above procedure for generating monodisperse microstructures is included in Appendix A.

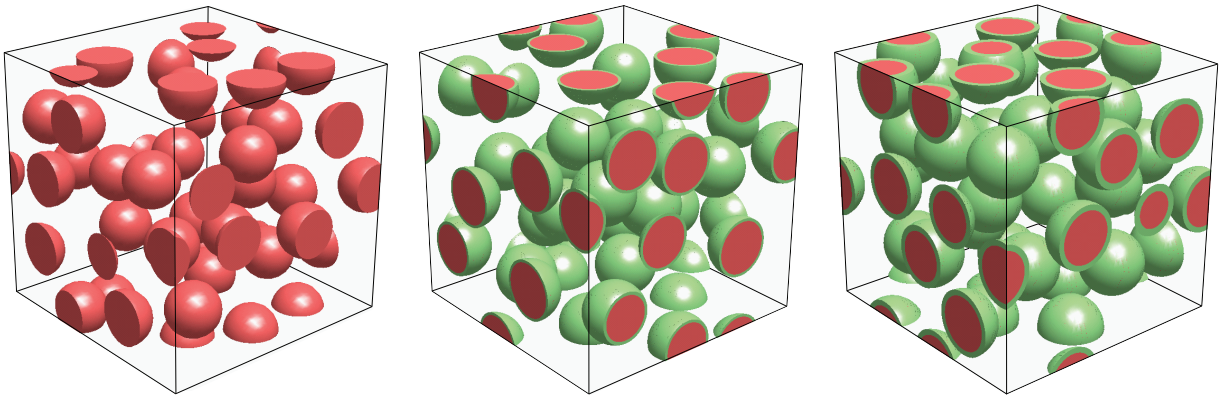

(a) (b) (c)

Figure 2.4: Representative monodisperse microstructures, containing a random distribution of 30 particles. The particles constitute a concentration of $c_p = 0.15$ and are surrounded by (a) no interphase, (b) interphases with a thickness of $t = 0.1r_p$, and (c) interphases with a thickness of $t = 0.2r_p$.

2.4.2 Microstructures with a polydisperse distribution of particles

For the polydisperse microstructures, polydispersity is represented through three families of particle sizes [89]. The particle locations are determined using a similar constrained adsorption algorithm to that used for the monodisperse microstructures [75, 86, 89]. The procedure we use to generate the polydisperse microstructures is as follows:

- Families of particles with three different radii, $r_p^{(i)}$ $(i = 1, 2, 3)$, are selected with concentrations $c_p^{(i)}$; surrounded by interphases with thickness $t^{(i)}$, such that:

$$\left\{r_p^{(1)}, r_p^{(2)}, r_p^{(3)}\right\} \cong \left\{r_p, \frac{7}{9}r_p, \frac{4}{9}r_p\right\} \qquad \text{with} \qquad r_p = L\left(\frac{3c_p^{(1)}}{4\pi N_p}\right)^{1/3}, \tag{2.27}$$

$$\left\{c_p^{(1)}, c_p^{(2)}, c_p^{(3)}\right\} = \{0.5c_p, 0.25c_p, 0.25c_p\} \qquad \text{with} \qquad c_p^{(1)} + c_p^{(2)} + c_p^{(3)} = c_p, \tag{2.28}$$

$$\left\{\frac{t^{(1)}}{r_p^{(1)}}, \frac{t^{(2)}}{r_p^{(2)}}, \frac{t^{(3)}}{r_p^{(3)}}\right\} = \left\{\frac{t}{r}, \frac{t}{r}, \frac{t}{r}\right\} \qquad \text{with} \qquad t = \gamma r, \tag{2.29}$$

where N_p denotes the number of particles with the largest radius and thickest interphase, and γ is a constant multiplier.

- The particles are added sequentially, from the family with the largest particle size to that with the smallest particle size. To guarantee an adequate spatial discretization, each placement of a particle must satisfy constraints analogous to those enforced for the monodisperse microstructures (i.e constraints (2.25) and (2.26)).

In this investigation, we set $N_p = 10$ such that the microstructure contains a total of 80 particles [75]. Figure 2.5 illustrates sample microstructures generated using the above procedure, for a particle concentration of $c_p = 0.15$.

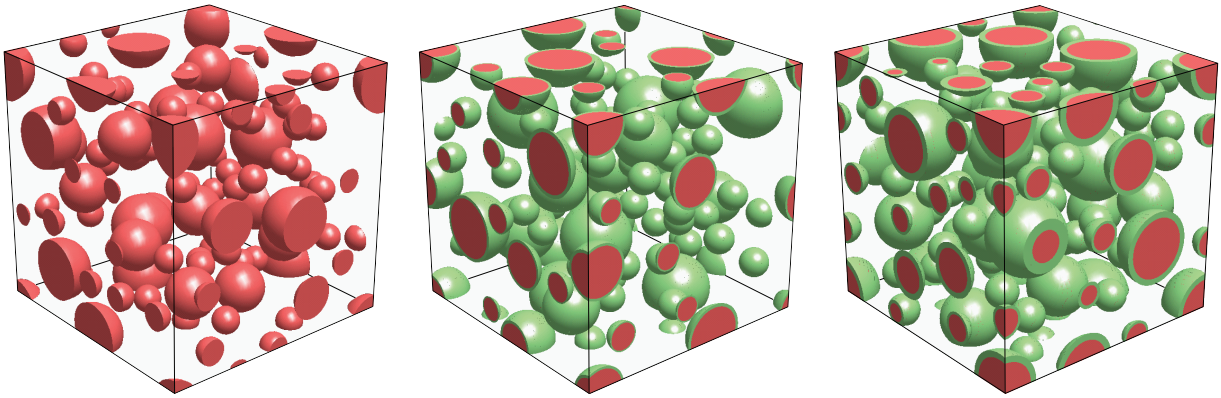

(a) (b) (c)

Figure 2.5: Representative polydisperse microstructures, containing a random distribution of 80 particles of three different radii. The particles constitute a concentration of $c_p = 0.15$ and are surrounded by (a) no interphase, (b) interphases with a thickness of $t = 0.1r_p^{(i)}$, and (c) interphases with a thickness of $t = 0.2r_p^{(i)}$.

2.4.3 Material models

The perfectly rigid behavior of the particles is numerically approximated by setting the stiffness of the particles to be four orders of magnitude ($10,000\times$) greater than that of the

elastomeric matrix [111]. Alternatively, a variational rigid-body constraint could have been implemented, to capture the perfectly rigid behavior of the particles [112]; however, this approach was not pursued here. The elastomeric matrix throughout this investigation is assumed to be hyperelastic and incompressible, and two different models are considered to describe its constitutive response. Initially, we consider an incompressible Gaussian elastomer following the neo-Hookean model; which has the following stored-energy function:

$$\Psi\left(I_1\right) = \left\{ \begin{array}{ll} \frac{\mu}{2}\left[I_1 - 3\right] = \frac{\mu}{2}\left[\lambda_1^2 + \lambda_2^2 + \lambda_3^2 - 3\right] & \text{if } J = \lambda_1\lambda_2\lambda_3 = 1 \\ +\infty & \text{otherwise} \end{array} \right\}, \tag{2.30}$$

where I_1 is the first principal invariant of the right Cauchy-Green deformation tensor, μ is the initial shear modulus of the material, and λ_1, λ_2 and λ_3 are the singular terms of the deformation gradient, $\mathbf{F}$.

For the non-Gaussian elastomer, the constitutive model proposed by Lopez-Pamies [113] is implemented into a UHYPER subroutine of Abaqus [103]. The stored-energy function for this model is expressed as:

$$\Psi\left(I_1\right) = \sum_{r=1}^{M} \frac{3^{1-\alpha_r}}{2\alpha_r}\mu_r\left(I_1^{\alpha_r} - 3^{\alpha_r}\right), \tag{2.31}$$

where M is the number of terms included in the summation and μ_r and α_r are experimentally determined material parameters. This material model accounts for strain hardening, unlike the neo-Hookean material model, but can revert back to a neo-Hookean-equivalent model in the small-deformation regime.

2.4.4 Periodic boundary conditions

To capture the behavior of a truly periodic microstructure, the model considers both a periodic geometry (see Figure 2.3) and periodic boundary conditions. The periodic boundary conditions are expressed as:

$$\begin{array}{l} u_k\left(0, X_2, X_3\right) - u_k\left(L, X_2, X_3\right) = \left(\overline{F}_{k1} - \delta_{k1}\right) L, \\ u_k\left(X_1, 0, X_3\right) - u_k\left(X_1, L, X_3\right) = \left(\overline{F}_{k2} - \delta_{k2}\right) L, \\ u_k\left(X_1, X_2, 0\right) - u_k\left(X_1, X_2, L\right) = \left(\overline{F}_{k3} - \delta_{k3}\right) L, \end{array} \tag{2.32}$$

where X_1, X_2 and X_3 correspond to a Cartesian frame of reference, where the origin is placed at a corner of the cell and the axes are aligned with the edges of the cell. Moreover, k is a constant $(= 1, 2, 3)$, δ_{ki} denotes the Kronecker delta, and $\overline{F}_{ki}$ are the components of the

prescribed average deformation gradient. To impose these periodic boundary conditions, the surface mesh on opposite faces of the cell need to be mirrors of one another. The pairing of the nodes on opposite faces is conducted automatically by Netgen [114], and incorporated into the Abaqus analysis using multi-point constraints [103].

2.4.5 Assessment of microstructure isotropy

In all models containing a finite number of randomly placed particles, the isotropy of the microstructure is only approximate [89]. There are multiple approaches for determining whether the random placement of particles results in an approximately isotropic microstructure. Many authors take a geometric approach, computing the centroid or moment of inertia of the particles [86, 111, 115]. Alternatively, one could take a constitutive approach, by examining the co-axiality between the average Cauchy stress tensor, $\overline{\mathbf{T}} \doteq \overline{\mathbf{S}}\overline{\mathbf{F}}^{\mathrm{T}}$, and the average left Cauchy-Green strain tensor, $\overline{\mathbf{B}} \doteq \overline{\mathbf{F}}\overline{\mathbf{F}}^{\mathrm{T}}$, under three loading conditions: (i) uniaxial tension, (ii) uniaxial compression, and (iii) simple shear [75, 89]. Since the constitutive approach is sufficient, we use this approach for all loading conditions, and particle and interphase concentrations we consider. Each microstructure is tested, and those which result in an angle of co-axiality greater than 0.05 radians are discarded [75, 89]. Representative values of the maximum angle of co-axiality for the microstructures used in this study are presented in Table 2.1.

Interphase Thickness	Interphase Stiffness	θ_X (rad)	θ_Y (rad)	θ_Z (rad)
$0.05r_p^{(i)}$	$\mu_i = 2\mu_m$	0.00350	0.00753	0.00708
	$\mu_i = 5\mu_m$	0.00388	0.00849	0.00779
	$\mu_i = \infty$	0.00428	0.00885	0.00886
$0.10r_p^{(i)}$	$\mu_i = 2\mu_m$	0.00527	0.00747	0.00637
	$\mu_i = 5\mu_m$	0.00615	0.00879	0.00770
	$\mu_i = \infty$	0.00786	0.01013	0.00922
$0.20r_p^{(i)}$	$\mu_i = 2\mu_m$	0.00421	0.00934	0.01131
	$\mu_i = 5\mu_m$	0.00645	0.01031	0.01721
	$\mu_i = \infty$	0.00789	0.01426	0.02344

Table 2.1: Maximum angle of co-axiality for the assessment of microstructure isotropy. θ_I corresponds to the angle of co-axiality computed when the microstructure is extended in uniaxial tension in the I direction. Results are listed for a particle concentration of $c = 0.15$.

Each model is discretized with quadratic, hybrid tetrahedral elements (C3D10H elements in Abaqus), using the open-source mesh generator Netgen [114]. A mesh refinement study was conducted using randomly generated meshes with approximately 60,000, 100,000 and 140,000 elements, as illustrated in Figure 2.6. Meshes with approximately 100,000 elements displayed a sufficient level of accuracy, and is the target mesh size for the results presented in the remainder of the chapter.

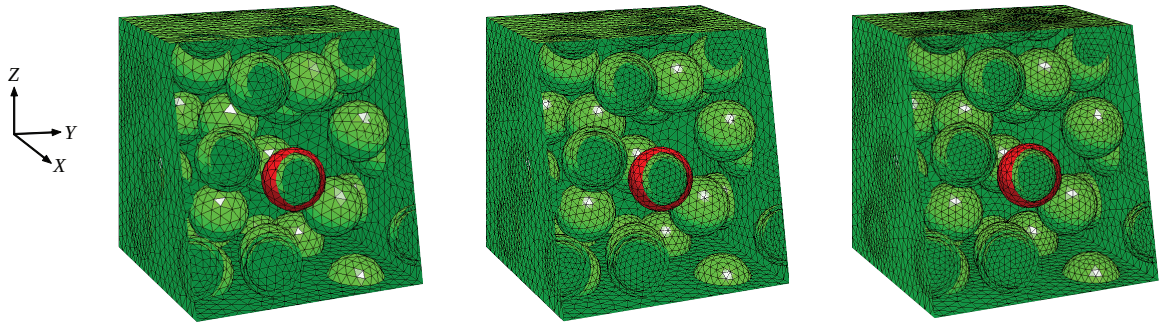

Figure 2.6: Three representative meshes in the undeformed configuration for a distribution of monodisperse particles with a particle concentration of $c_p = 0.15$, and an interphase thickness of $t = 0.2r_p^{(i)}$: (a) a coarse mesh with approximately 60,000 elements, (b) a fine mesh with approximately 100,000 elements, and (c) a very fine mesh with approximately 140,000 elements.

2.5 Small deformation results

In this section, we investigate the influence of; the concentration of particles, the nature of the dispersion (monodisperse or polydisperse), and the interphase thickness and stiffness, on the effective modulus of the composite material. We compare the results from our computational framework with both theoretical and experimental results.

2.5.1 Comparison with theory

In the limit of small deformations, the effective stored-energy function (2.22) reduces asymptotically to [75]:

$$\overline{\Psi}\left(\bar{I}_1, \bar{I}_2, c_p, c_i\right) = \bar{\mu}\mathrm{tr}\bar{\boldsymbol{\varepsilon}}^2, \tag{2.33}$$

where $\bar{\mu}$ is the effective shear modulus of the composite, defined implicitly by:

$$\mathcal{F}_1 \{\bar{\mu}, \mu_m\} = 0, \tag{2.34}$$

and $\mathcal{F}_1$ is defined by Equation 2.21. Thus, the response of the composite is completely characterized by the effective shear modulus $\bar{\mu}$. Figure 2.7 illustrates both numerical and analytical results for the normalized effective shear modulus, $\bar{\mu}/\mu_m$, as a function of the concentration of particles, c_p, for various microstructural configurations. As is well known, the inclusion of stiff particles to a soft elastomer acts to greatly increase the effective overall stiffness of the composite. Notably though, Figure 2.7 demonstrates that the presence of interphases has a comparable influence on the effective stiffness as does the presence of the particles alone.

In Figures 2.7(a) and 2.7(b), we illustrate the influence of the thickness of the interphase on the effective composite stiffness. For thinner interphases ($t/r = 0.05$ and $t/r = 0.1$), both monodisperse and polydisperse microstructures closely approximate the analytical solution. However, when the interphase thickness increases to $t/r = 0.2$, the monodisperse microstructures deviate from the analytical solution at concentrations greater than $c_p = 0.15$. Alternatively, for all values of interphase thickness considered in this investigation, the polydisperse microstructures demonstrate good correlation with the analytical solution. Thus, even though the theoretical formulation considers an infinitely polydisperse microstructure, our results demonstrate that approximating the polydispersity of the microstructure with three families of particle sizes provides sufficiently accurate results.

In Figures 2.7(c) and 2.7(d), we fix the interphase thickness at $t/r = 0.1$, to illustrate the influence of the interphase modulus on the effective composite stiffness. The first thing to note is that the effective composite stiffness is less sensitive to a change in interphase stiffness than it is for a change in interphase thickness. Additionally, both monodisperse and polydisperse microstructures demonstrate good agreement with the analytical solution, even at particle concentrations up to $c_p = 0.25$. We also note that the influence of the stiffness of the interphase culminates rapidly. For instance, the response of composites with an interphase just 5 times stiffer than the matrix ($\mu_i/\mu_m = 5$) is similar to that when the interphase is rigid ($\mu_i \to \infty$).

2.5.2 Comparison with experiments

There have been numerous experimental investigations into the effective modulus of particle reinforced composites in the small-deformation regime. In the early 1940's, Smallwood [116]

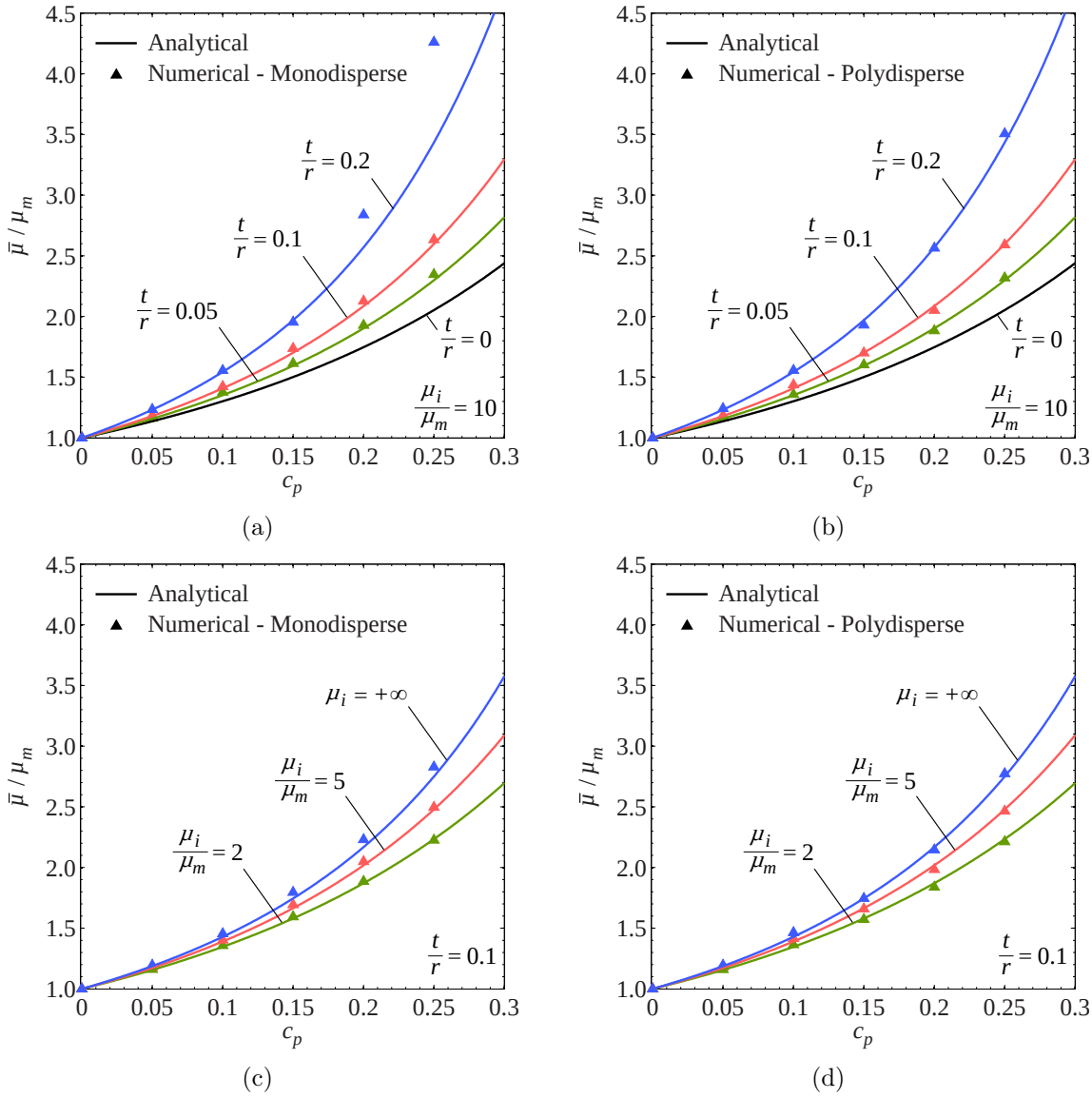

Figure 2.7: Results of the investigation on the effective composite stiffness of particle reinforced elastomers, considering the influence of interphases. Numerical results are compared with those derived theoretically. Results are shown for: (a) a monodisperse distribution with a constant interphase stiffness, (b) a polydisperse distribution with a constant interphase stiffness, (c) a monodisperse distribution with a constant interphase thickness, and (d) a polydisperse distribution with a constant interphase thickness.

conducted an in-depth experimental and theoretical investigation into the influence of different fillers on the effective modulus of such composites. His study demonstrated the variation in the macroscopic response of the composite, based on the variable characteristics of the fillers. Some fillers were shown to alter the elastomeric matrix surrounding the inclusions while others showed preference to flocculate. Smallwood concluded that the effective modulus of the composite depends on the type of filler used, the concentration of the filler, and the

interaction at the filler-elastomer interface. More recently, Omnès et al. [117] investigated the influence of different types of carbon-black particles (N330 and N650) on the response of natural rubber under small strains. Similar to Smallwood's findings, they demonstrate that the response of the composite varies significantly, depending on the type of filler used. Additionally, even when using the same concentration of the same type of filler, the resulting effective modulus of the composite showed some variation. Based on their experimental findings, they hypothesized that the variation they observed was a result of an interphasial region at the particle-elastomer interface. The results of these studies, along with multiple others, are summarized in Figure 2.8.

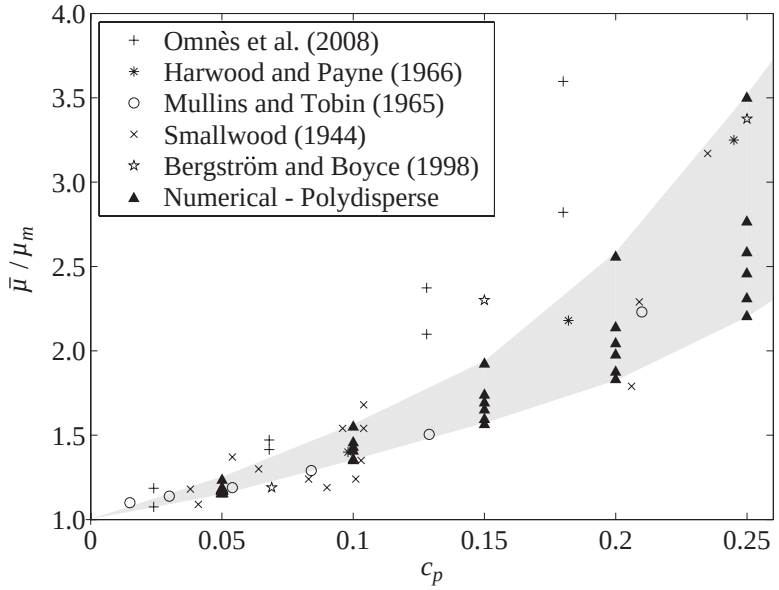

Figure 2.8: Experimental comparison of effective moduli. Numerical results are denoted by solid triangles, and, for each particle concentration, depict all the cases of interphase thickness and stiffness we considered. The gray overlay defines the bounds of the numerically obtained results. Experimental results are extracted from the literature ([85, 116, 117, 118, 119]).

We overlay the numerically computed effective moduli onto the experimental data in Figure 2.8. The comparison demonstrates that a wide range of experimentally obtained effective moduli, for similar concentrations of particles, can be captured by the inclusion of physically realistic interphases. If we were to consider a wider range of values for the interphase thickness, we would capture a wider range of experimental data, however, this becomes numerically challenging at large particle concentrations. This comparison suggests that the inclusion of an interphasial region provides an explanation for the wide range of behavior observed experimentally, and is a crucial component that should not be omitted when modeling particle reinforced elastomers.

2.6 Finite deformation results

In this section, we investigate the influence of the interphase thickness and stiffness on the macroscopic constitutive response of particle reinforced elastomers as they undergo finite strains. For the sake of brevity, we do not present results for all the microstructural configurations we considered. Instead, based on our findings in the small deformation investigation, we focus on monodisperse microstructures and fix the particle concentration at $c_p = 0.15$. While we do not illustrate results for other microstructural configurations, we did an extensive parametric study on all the parameters we consider, with both monodisperse and polydisperse microstructures, and the results discussed below represent typical behavior observed in our investigation. The computations are carried out in the commercial code ABAQUS by following an incremental loading path. We utilize the default dual convergence criterion in abaqus [103], namely, the permissible ratio of the largest solution correction to the largest corresponding incremental solution is set at $|\Delta\mathbf{u}| / |\mathbf{u}_{\max}| = 10^{-2}$, while the permissible ratio of the largest residual to the corresponding average force norm is set at $R_{tol} = 5 \times 10^{-3}$. Whenever one of these criteria is not satisfied the computations are stopped. This typically happens whenever the elements in between two adjacent interphases become exceedingly distorted because of the locally large deformations involved.

2.6.1 Results for Gaussian elastomers: Comparison with theory

We first consider the case of a Gaussian elastomeric matrix, with a neo-Hookean stored-energy function (2.30). Typical results from our investigation are illustrated in Figure 2.9, for: (a) uniaxial compression, (b) uniaxial tension, (c) simple shear, and (d) pure shear loading conditions. The theoretically derived stress-deformation relations for these loading conditions are expressed as:

- Uniaxial loading $\left(\bar{\lambda}_1 = \bar{\lambda},\, \bar{\lambda}_2 = \bar{\lambda}_3 = \bar{\lambda}^{-1/2} \text{ with } \bar{\tau}_2 = \bar{\tau}_3 = 0\right)$:

$$\bar{S}_{un} = \bar{\lambda}^{-1}\bar{\tau}_1 = \frac{\mathrm{d}\bar{\Psi}}{\mathrm{d}\bar{\lambda}} = \bar{\mu}\left[\bar{\lambda} - \bar{\lambda}^{-2}\right], \tag{2.35}$$

- Simple shear $\left(\bar{\lambda}_1 = (\bar{\gamma} + \sqrt{\bar{\gamma}^2 + 4})/2,\, \bar{\lambda}_2 = \bar{\lambda}_1^{-1},\, \bar{\lambda}_3 = 1\right)$:

$$\bar{S}_{ss} = \frac{\mathrm{d}\bar{\Psi}}{\mathrm{d}\bar{\gamma}} = \bar{\mu}\bar{\gamma}, \tag{2.36}$$

- Pure shear $\left(\overline{\lambda}_1 = \overline{\lambda},\, \overline{\lambda}_2 = \overline{\lambda}^{-1},\, \overline{\lambda}_3 = 1 \text{ with } \bar{\tau}_2 = 0\right)$:

$$\overline{S}_{ps} = \overline{\lambda}^{-1}\bar{\tau}_1 = \frac{\mathrm{d}\overline{\Psi}}{\mathrm{d}\overline{\lambda}} = \bar{\mu}\left[\overline{\lambda} - \overline{\lambda}^{-3}\right], \tag{2.37}$$

where $\overline{S}_{un}$, $\overline{S}_{ss}$, and $\overline{S}_{ps}$ are the first Piola-Kirchoff stress measures; and $\bar{\tau}_2$, $\bar{\tau}_2$, and $\bar{\tau}_2$ are the macroscopic principal Cauchy stress measures. As in the case of small deformations, the effective shear modulus, $\bar{\mu}$, is implicitly defined by Equation 2.34. We consider three realizations for the interphase: (i) no interphase, $t/r = 0$; (ii) an interphase with stiffness $\mu_i/\mu_m = 5$ and thickness $t/r = 0.1$; and (iii) a rigid interphase, $\mu_i = \infty$, with thickness $t/r = 0.2$. These interphase configurations are selected to demonstrate the wide variation of behavior which can be attributed to the presence of an interphase of reasonable thickness and stiffness.

From the results in Figure 2.9, it is clear that the computational framework and theoretical framework, while developed independently, demonstrate good agreement under all loading conditions. The overall large deformation response of the Gaussian elastomer is significantly stiffened by the inclusion of rigid particles. Additionally, the results demonstrate that the presence of interphases has a comparable influence on the stiffness of the elastomer as does the presence of the particles alone. The increase in stiffness generated by the presence of interphases is more sensitive to the interphase thickness than it is to the interphase modulus; as was the case in the small deformation investigation. We emphasize that, while these conclusions are drawn based on the results illustrated in Figure 2.9, they are also representative of conclusions drawn for other microstructural configurations and constituent properties under the same loading conditions.

2.6.2 Results for non-Gaussian elastomers: Comparison with theory

Here, we consider the case of a non-Gaussian elastomeric matrix, described by the stored-energy function in Equation 2.31, with $\mu_1 = 0.032MPa$, $\mu_2 = 0.3MPa$, $\alpha_1 = 3.837$, and $\alpha_2 = 0.559$. The values of the parameters in the stored-energy function are selected to correspond to a typical silicone rubber [89]. The corresponding initial shear modulus for this material is $\mu_m = \mu_1 + \mu_2 = 0.332MPa$. For convenience, we write down the explicit form of the effective stored-energy function (2.22), as:

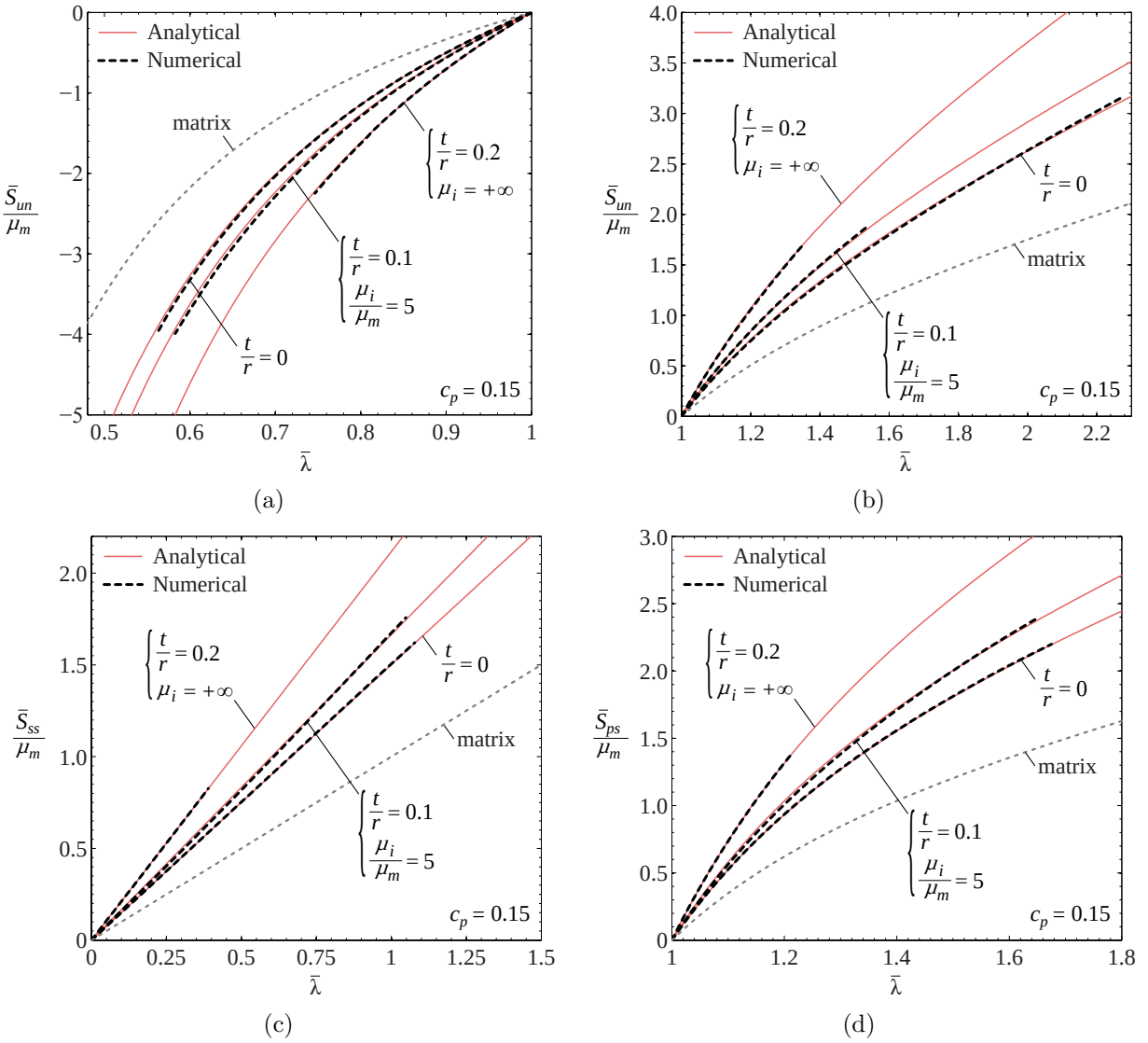

Figure 2.9: Macroscopic constitutive response of a particle reinforced Gaussian elastomer, considering the influence of interphases. Typical results are illustrated for loading under: (a) uniaxial compression, (b) uniaxial tension, (c) simple shear, and (d) pure shear. The particle concentration is fixed at $c_p = 0.15$, and the interphase thickness and stiffness is varied. The solid lines corresponds to the theoretical solution considering an infinitely polydisperse microstructure, and the dashed lines correspond to the numerical results considering a monodisperse microstructure.

$$\overline{\Psi}\left(\bar{I}_1,\bar{I}_2,c_p,c_i\right)=(1-c_p-c_i)\left[\frac{3^{1-\alpha_1}}{2\alpha_1}\mu_1\left(\mathcal{I}_1^{\alpha_1}-3^{\alpha_1}\right)+\frac{3^{1-\alpha_2}}{2\alpha_2}\mu_2\left(\mathcal{I}_1^{\alpha_2}-3^{\alpha_2}\right)\right]$$
$$+\frac{\overline{\mu}_0}{2}\left[\bar{I}_1-3\right]-(1-c_p-c_i)\frac{\mu_0}{2}\left[\mathcal{I}_1-3\right], \quad (2.38)$$

where $\mathcal{I}_1$ is given by Equation 2.23 and the variables $\bar{\mu}_0$ and μ_0 are implicitly defined by the following set of coupled nonlinear equations:

$$\mathcal{F}_1\left\{\bar{\mu}_0, \mu_0\right\} = 0, \quad \text{and} \quad \mathcal{F}_2\left\{\bar{\mu}_0, \mu_0\right\} = \frac{3^{1-\alpha_1}}{2}\mu_1 \mathcal{I}_1^{\alpha_1 - 1} + \frac{3^{1-\alpha_2}}{2}\mu_2 \mathcal{I}_1^{\alpha_2 - 1} - \frac{\mu_0}{2} = 0, \tag{2.39}$$

where $\mathcal{F}_1$ is defined by Equation 2.21.

Typical results from our investigation are illustrated in Figure 2.10, for: (a) uniaxial compression, (b) uniaxial tension, (c) simple shear, and (d) pure shear loading conditions. With this choice of stored-energy function, the theoretically derived stress-deformation relations for these loading conditions are expressed as:

- Uniaxial loading $\left(\bar{\lambda}_1 = \bar{\lambda},\, \bar{\lambda}_2 = \bar{\lambda}_3 = \bar{\lambda}^{-1/2} \text{ with } \bar{\tau}_2 = \bar{\tau}_3 = 0\right)$:

$$\bar{S}_{un} = \bar{\lambda}^{-1}\bar{\tau}_1 = \frac{\mathrm{d}\bar{\Psi}}{\mathrm{d}\bar{\lambda}} = \bar{\mu}_0\left[\bar{\lambda} - \bar{\lambda}^{-2}\right]. \tag{2.40}$$

- Simple shear $\left(\bar{\lambda}_1 = (\bar{\gamma} + \sqrt{\bar{\gamma}^2 + 4})/2,\, \bar{\lambda}_2 = \bar{\lambda}_1^{-1},\, \bar{\lambda}_3 = 1\right)$:

$$\bar{S}_{ss} = \frac{\mathrm{d}\bar{\Psi}}{\mathrm{d}\bar{\gamma}} = \bar{\mu}_0\bar{\gamma}. \tag{2.41}$$

- Pure shear $\left(\bar{\lambda}_1 = \bar{\lambda},\, \bar{\lambda}_2 = \bar{\lambda}^{-1},\, \bar{\lambda}_3 = 1 \text{ with } \bar{\tau}_2 = 0\right)$:

$$\bar{S}_{ps} = \bar{\lambda}^{-1}\bar{\tau}_1 = \frac{\mathrm{d}\bar{\Psi}}{\mathrm{d}\bar{\lambda}} = \bar{\mu}_0\left[\bar{\lambda} - \bar{\lambda}^{-3}\right]. \tag{2.42}$$

Moreover, we consider the same three realizations for the interphase as in the investigation with a Gaussian matrix.

The results in Figure 2.10 demonstrate that the stiffness of the composite is significantly influenced by not only the addition of particles, but also the presence of interphases. At small to moderate deformations, there is good agreement between the numerical and analytical results under all loading conditions. At larger deformations, the numerical results demonstrate a stiffer response than the analytical solution. This behavior is expected, and could be explained by a number of reasons: (*i*) the finite element shape functions present a stiffer space of solutions than in reality; (*ii*) the theoretical solution assumes an infinitely polydisperse microstructure, thus it may approximate a lower bound [75]; (*iii*) at large deformations the particle-to-particle interactions in the monodisperse microstructure tend

to stiffen the composite, and (iv) at large deformations the particles become preferentially oriented in the direction of loading, deviating from the isotropy that the theoretical solution assumes. Regardless, the trends observed for both the numerical and analytical results are consistent (i.e. the increase in stiffness due to the interphases is more sensitive to the interphase thickness than it is to the interphase modulus).

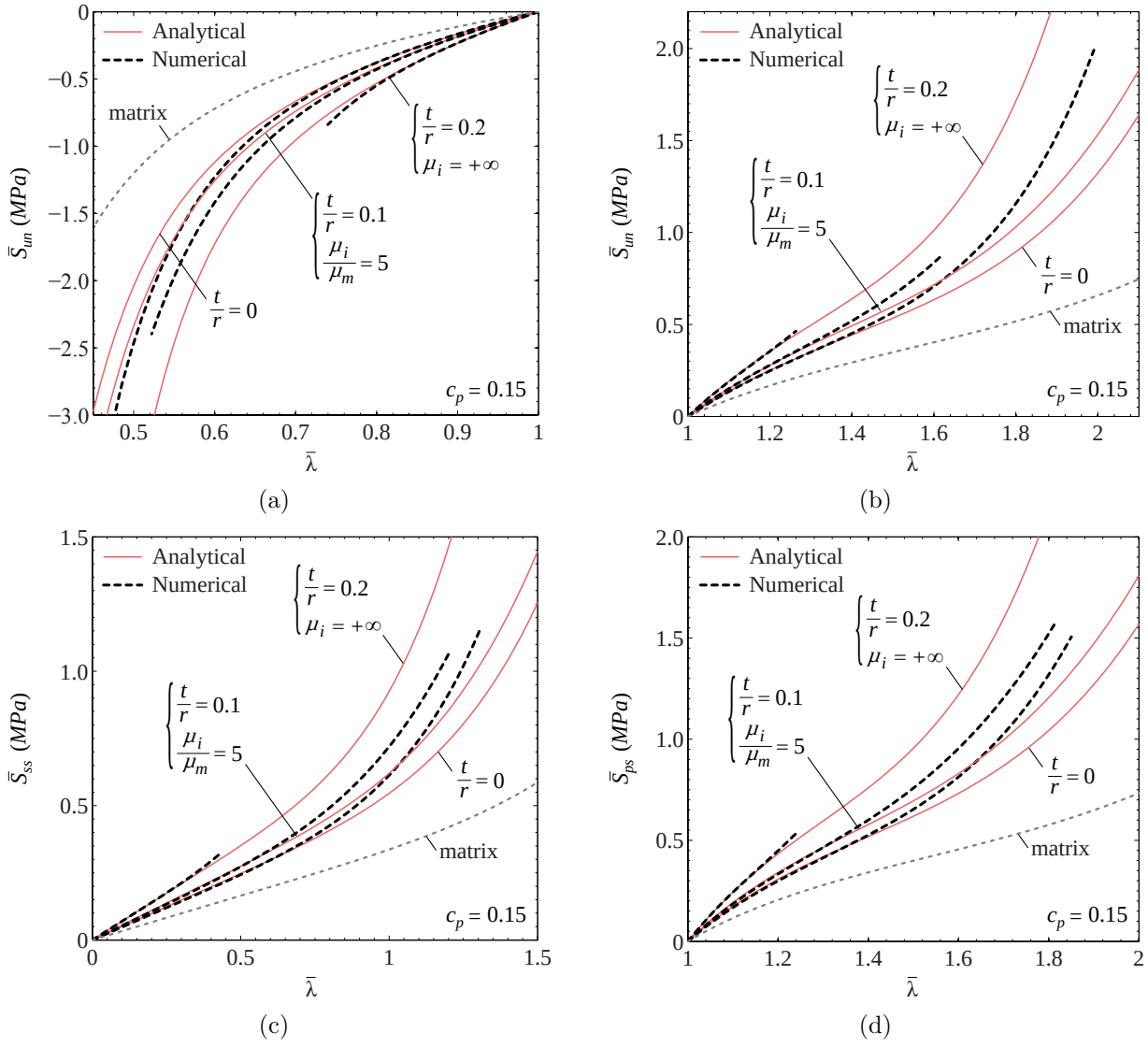

Figure 2.10: Macroscopic constitutive response of a particle reinforced non-Gaussian elastomer, considering the influence of interphases. Typical results are illustrated for loading under: (a) uniaxial compression, (b) uniaxial tension, (c) simple shear, and (d) pure shear. The particle concentration is fixed at $c_p = 0.15$, and the interphase thickness and stiffness is varied. The solid lines corresponds to the theoretical solution considering an infinitely polydisperse microstructure, and the dashed lines correspond to the numerical results considering a monodisperse microstructure.

2.6.3 Comparison with experiments

In this section, we verify that the proposed computational framework is capable of capturing representative experimental results from the literature. There are few experimental investigations which report all the necessary microscale and macroscale properties of the composite material, thus we make reasonable assumptions, and discuss them, where necessary. The experimental results selected for this comparison were reported in two separate investigations. The first investigation is that reported by Jha [120] into the influence of carbon black (N990) particles on the large deformation response of natural rubber. The carbon black particles are roughly spherical in shape and are well-dispersed in the specimen, with little agglomeration [120]. The average particle size is $0.285\mu m$, and the average agglomeration size is $0.483\mu m$. The filler concentration is set as $c_p = 0.052$ and the author reports the constitutive response of the unfilled rubber. Based on fitting the response of the rubber, we find an appropriate response of the rubber matrix, at least in uniaxial tension, follows the stored-energy function:

$$\Psi\left(I_1\right) = \frac{3^{1-\alpha_1}}{2\alpha_1}\mu_1\left[I_1^{\alpha_1} - 3^{\alpha_1}\right] + \frac{3^{1-\alpha_2}}{2\alpha_2}\mu_2\left[I_1^{\alpha_2} - 3^{\alpha_2}\right], \tag{2.43}$$

with material parameters $\mu_1 = 0.05MPa$, $\mu_2 = 0.335MPa$, $\alpha_1 = 2.0$, and $\alpha_2 = 0.35$. Given this partial information, we make assumptions on the presence and properties of interphases. We assume that the interphases are 10 times stiffer than the matrix, $\mu_i = 10 \times \mu_m = 10 \times (\mu_1 + \mu_2) = 3.85MPa$. Since the authors do not report the thickness of the interphases, we select them here by fitting the numerical results to the experimental results. As illustrated in Figure 2.11, an interphase-thickness-to-particle-radius ratio of $t/r = 0.4$ leads to good agreement with the experimental results.

The second investigation is that reported by Mullins and Tobin [118], wherein they consider filled elastomers with particle concentrations of $c_p = 0.138$ and $c_p = 0.2085$. Their results correspond to a well-dispersed distribution of roughly spherical aggregates of carbon black with an average particle radius of about $0.2\mu m$. The authors report, through the use of swelling experiments, that the elastic properties of the rubber matrix were essentially unmodified by the presence of the particles. However, they provide no comments on the amount or type of bound rubber present in the composite. Additionally, the authors report the response of the unfilled elastomer. By fitting the response of the unfilled elastomer in uniaxial tension, we determine that an appropriate response for the matrix can be captured using the stored-energy in Expression (2.43) with material parameters $\mu_1 = 0.04MPa$, $\mu_2 = 0.4MPa$, $\alpha_1 = 2.0$, and $\alpha_2 = 0.8$.

Since we have demonstrated that the monodisperse microstructures are suitable only up to

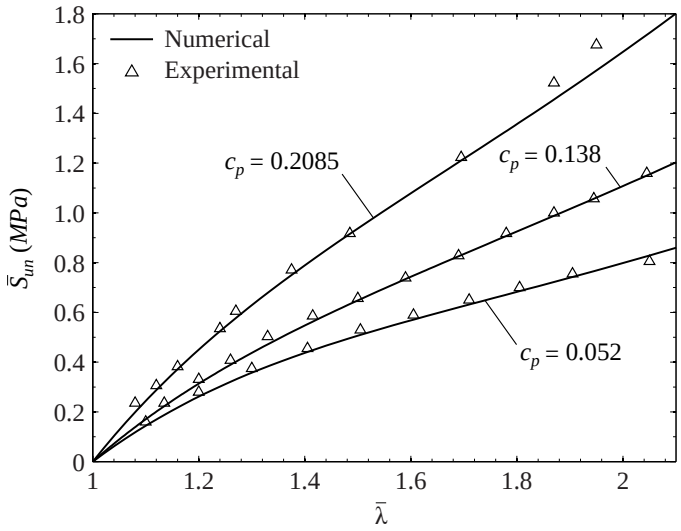

Figure 2.11: Comparison of the proposed computational framework with experimental data.

a particle concentration $c_p < 0.2$, for the case with a particle concentration of $c_p = 0.2085$, we assume a polydisperse distribution of particles. Through a series of numerical simulations, We assume that, for a particle concentration of $c_p = 0.138$, no interphases form around the particles, and for a particle concentration of $c_p = 0.2085$, the interphases are 2 times stiffer than the matrix, $\mu_i = 2 \times \mu_m = 2 \times (\mu_1 + \mu_2) = 0.88MPa$. Since the authors do not report the thickness of the interphases, we select them here by fitting the numerical results to the experimental results. As illustrated in Figure 2.11, an interphase-thickness-to-particle-radius ratio of $t/r = 0.2$ leads to good agreement with the experimental results.

In summary, the above comparisons with experiments demonstrate that the proposed computational framework is able to provide an explanation for the varied macroscopic response of filled elastomers at finite deformations. Additionally, it confirms the significant influence of not only particle inclusions, but also interphases on the constitutive response. Thus, it is not enough to consider only the influence of the particles in the design of such composites, but one must also consider the presence of interphases.

2.7 Concluding remarks

In this chapter, we explore the influence of perfectly bonded interphases on the macroscopic constitutive response of particle reinforced elastomers. We provide a brief summary of the historical background on the topic, including a discussion on the various theoretical approaches to this problem. Then, we outline a recently developed theoretical framework, developed by Goudarzi et al. [75], which is capable of capturing the response of these com-

posite materials in both the small deformation and large deformation regimes. The main contribution of this chapter, however, is the computational framework we propose to investigate these composites. We challenge the computational framework with the theoretically derived solution and demonstrate good agreement in all loading conditions we consider.

In the small deformation regime, we investigate the influence of interphases on the effective shear modulus of particle reinforced elastomers. Even though the theoretical solution assumes an infinitely polydisperse microstructure; the computational framework, using a finite number of particles, yields results in good agreement with those derived theoretically. The only outlying solutions correspond to those for monodisperse microstructures, with thick interphases, at high particle concentrations. Additionally, we compare our numerical results with experiments, and demonstrate that a wide range of experimentally obtained effective moduli can be captured by the inclusion of physically realistic interphases.

In the large deformation regime, we consider both Gaussian and non-Gaussian elastomeric matrices. For the case of a Gaussian elastomer, the difference between the numerical and analytical solutions is negligible. However, for the case of a non-Gaussian elastomer, good agreement is only demonstrated under moderate deformations. Under large deformations, the numerical results demonstrate a stiffer global response than that suggested by the theoretical solution.

We also note that, in addition to the hydrodynamic and interphasial reinforcement effects, occluded rubber may also provide additional reinforcement to the composite. Occluded rubber constitutes regions of elastomer which may be entrapped by the agglomeration of the particles. Because of its shielding from the rest of the elastomer, its constitutive behavior can be approximated as rigid. In this case, the presence of occluded rubber can be accounted for by the proposed computational framework by simply reinterpreting the concentration of particles as the combined concentration of particles and occluded rubber.

The computational framework proposed herein constitutes the first step in our objective of developing a more general computational framework capable of capturing the finite deformation interfacial debonding behavior of particle reinforced elastomers. In the next chapter we develop the tools necessary to account for interfacial debonding. Then, in Chapter 4, we combine the work in this chapter and the next, to investigate the combined influence of both interphases and interfacial debonding on the macroscopic constitutive response of particle reinforced elastomers.

Chapter 3

Fracture in Three-Dimensions Using the Intrinsic Cohesive Element Approach: Formulation and Implementation

This chapter provides an educational look at the implementation of cohesive elements into a finite element program, in accordance with their use in Abaqus (or a similar commercial finite element package with support for user-supplied subroutines). The intrinsic cohesive formulation is outlined, due to its compatibility with the implicit finite element framework present in Abaqus. The Park-Paulino-Roesler, potential-based traction-separation relation is chosen to describe the element's constitutive model. Specific components of the elements are highlighted; which potential future users may wish to modify, to meet specific research needs. Numerical examples are presented which verify the implementation and display the features of the elements. A sample element source code is provided in Appendix B, and electronic source files for the elements are supplied through the website of Professor Glaucio H. Paulino.

3.1 Introduction

The use of cohesive elements within the framework of the finite element method has proven to be a powerful technique for modeling material failure. The concept of the cohesive zone model was presented over half a century ago by Dugdale [2] and Barenblatt [1]. They proposed modeling the inelastic zone in front of a macrocrack with a traction-separation relation. In this method, as the crack separates, a softening traction is applied to the surrounding bulk material. There have been a variety of traction-separation relations proposed in the literature, including linear, bilinear, trilinear, trapezoidal, polynomial, and exponential softening models. A summary of many of the prevalent traction-separation relations may be found in the review paper by Park and Paulino [41].

A distinct feature of the cohesive element method is that the material model chosen for the bulk elements is independent of that chosen for the cohesive elements. For example, the bulk material may be linear elastic, viscoelastic, hyperelastic, etc. In this chapter, we focus on examples which use elastic material models under small deformations. In Chapter 4, we

will present an application where we use hyperelastic materials undergoing large deformations. Since the two constitutive models (bulk and cohesive) are independent, the modeling of functionally graded materials will require modifications to both the bulk and cohesive formulations. A means for modifying cohesive element formulations to permit the modeling of graded properties will be presented in Section 3.5.

Currently, there are only a few available (built-in) traction-separation relations for cohesive elements in the commercial software Abaqus. The available traction-separation relations typically consist of a linear hardening region, and either a linear or exponential softening region [103]. The traction-separation relation used in this work is the unified potential-based model presented by Park et al. [51]. This model has been implemented in the Warp3D software [121], and in the Finite Element All-Wheel Drive (FEAWD) software [122], but its use in Abaqus has been limited to two-dimensions [123]. The intrinsic model will be presented here, the extension of the model to an extrinsic formulation may be found in Chapter 5. This work is an extension of a previous publication; in which the authors present the two-dimensional user-defined element (UEL) for use in Abaqus [123]. The requests, from users of that UEL, for the corresponding extension to three-dimensions, has been the motivation behind the present work.

This chapter is organized as follows. Section 3.2 discusses related work and potential applications of the cohesive element method. Section 3.3 outlines the formulation of the three-dimensional UEL. The intrinsic formulation of the Park-Paulino-Roesler (PPR) cohesive model is presented in Section 3.4. It is understood that research, by its very nature, is diverse and ever-changing. To aid in the removal of the black-box nature of many codes, and to make this work more adaptable to potential future users, Section 3.5 describes areas of the code which may be of interest to the readers, to modify and incorporate into their own work. Section 3.6 presents some relevant examples which make use of the three-dimensional elements. Finally, some concluding remarks are provided in Section 3.7, and a representative implementation (interface cohesive elements between linear tetrahedral bulk elements) is included in Appendix B.

3.2 Related work using cohesive elements for fracture

Since their conception, cohesive zone elements have been used to describe fracture and fragmentation in a variety of complex problems. Cohesive elements have been extensively used to model fracture in concrete and asphalt. In 1976, Hillerborg et al. [42] used cohesive elements with a linear softening relation to study the fracture of plain concrete beams.

Following the work of Hillerborg, Petersson [43] used a bilinear softening relation to simulate the fracture of concrete and other quasi-brittle materials. More recently, Song et al. [124, 125, 126, 127] tailored both bilinear softening and exponential softening relations to capture crack propagation in viscoelastic asphalt beams. Spring [128] employed a graded bilinear softening relation to investigate the failure of functionally graded concrete slabs. Finally, Park et al. [44] developed a trilinear softening relation to model the fracture of functionally graded, fiber reinforced concrete beams. By accounting for the added fracture energy due to the inclusion of fibers, they were able to obtain an excellent correlation between numerical and experimental results.

There has also been a substantial amount of work employing cohesive elements to simulate impact damage and fragmentation. For example, Camacho and Ortiz [55] employed a linear softening relation to model pervasive fracture due to a high velocity impact event. They studied the problem of a steel pellet impacting a ceramic plate (an important problem in armor and turbine blade design), and captured results consistent with experiments. Espinosa et al. [129] combined cohesive elements with a continuum damage model to capture the fragmentation of ceramic rods under dynamic loading. Both Pandolfi et al. [130] and Zhou et al. [131] used cohesive elements to model the fragmentation of radially loaded, expanding rings. More recently, Mota et al. [132] studied the fragmentation of a human cranium due to a firearm injury. They used fully three-dimensional finite element simulations, to capture behavior consistent with that observed experimentally. Finally, Caballero and Molinari [133] used the same cohesive model as Camacho and Ortiz to study the fracture and fragmentation of kidney stones under direct impact. Their findings lead to the design of a new surgical tool which increases the efficiency of kidney stone dissipation.

In general, the numerical simulation of dynamic crack propagation has been a popular application for cohesive elements. Ortiz and Pandolfi [56] used effective-displacement, three-dimensional cohesive elements to model dynamic crack propagation. They considered quadratic cohesive elements, with an irreversible cohesive relation, and were able to capture an accurate crack trajectory in a drop-weight dynamic fracture test. Ruiz et al. [134] investigated the failure of a three-point-bend concrete beam under dynamic loading. They simulated fracture using three-dimensional cohesive elements with a linear softening relation. More recently, Zhang and Paulino [135, 136] were able to capture microbranching behavior during crack propagation in both homogeneous and functionally graded materials. In fracture simulations, particularly dynamic fracture simulations, it is important to take into consideration the effect of finite displacements. When cohesive elements are inserted into a model, they initially have zero thickness; however, once fracture progresses, they separate and rotate. By not taking into consideration the rotation of fracture surfaces, the mechanics

of the problem may not be accurately captured.

3.3 Cohesive element formulation

In this study, we implement three different cohesive elements. The three elements allow for compatibility with linear brick, linear tetrahedral, and quadratic tetrahedral bulk elements[1], as illustrated in Figure 3.1. As discussed previously, the constitutive relation for the bulk elements is selected independently of that for the cohesive elements.

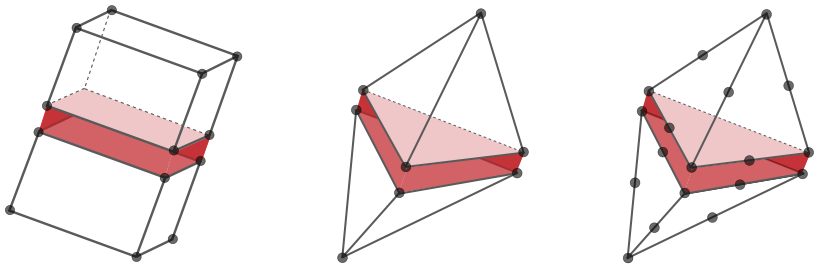

Figure 3.1: Cohesive elements compatible with (a) linear brick, (b) linear tetrahedral and (c) quadratic tetrahedral bulk elements. Cohesive elements, highlighted in red, are initially of zero thickness.

Intrinsic cohesive elements are inserted into a finite element mesh prior to the beginning of the simulation. Initially, intrinsic cohesive elements have zero thickness and, upon separation, impart a traction to the adjacent bulk elements. There are two common approaches to inserting intrinsic cohesive elements into a mesh. One may either insert cohesive elements along a pre-selected fracture path, restricting the crack to propagate where the user has specified; or one may insert cohesive elements between all bulk elements in a region of a mesh, allowing fracture to propagate freely within that region. When cohesive elements are inserted throughout a region of a mesh, the elements may introduce artificial softening into the model, effectively distorting the constitutive properties of the bulk elements [52, 54]. In addition, if cohesive elements are inserted between all bulk elements in a region of the mesh, the solution becomes highly non-convergent, and additional numerical measures need to be included in the solution scheme to account for these instabilities [73, 137]. An alternative method for allowing fracture to propagate freely would be to use adaptively inserted extrinsic cohesive elements [56, 57]. A discussion on the use of adaptively inserted extrinsic cohesive elements will be left to Chapters 5 and 6.

[1]At the time of this work, Abaqus does not have a built-in cohesive element that is compatible with quadratic elements.

Prior to the insertion of cohesive elements, the standard finite element formulation may be described analytically, using the principle of virtual work [5]:

$$W_{int} \equiv \int_{\Omega} \delta\mathbf{E} : \mathbf{S} d\Omega = \int_{\Gamma} \delta\mathbf{u} \cdot \mathbf{T}_{ext} d\Gamma \equiv W_{ext}, \tag{3.1}$$

where $\mathbf{E}$ is the Green strain tensor in the domain Ω, and $\delta\mathbf{u}$ is the virtual displacement on the boundary Γ. Moreover, $\mathbf{T}_{ext}$ is the external traction, and $\mathbf{S}$ is the 2nd Piola-Kirchhoff stress tensor. When cohesive elements are included in the formulation, they contribute an additional term to the internal work:

$$\int_{\Omega} \delta\mathbf{E} : \mathbf{S} d\Omega \; + \; \int_{\Gamma_c} \delta\boldsymbol{\Delta} \cdot \mathbf{T}_c d\Gamma_c = \int_{\Gamma} \delta\mathbf{u} \cdot \mathbf{T}_{ext} d\Gamma, \tag{3.2}$$

where $\mathbf{T}_c$ is the cohesive traction, acting on fracture surface Γ_c, corresponding to the virtual separation $\delta\boldsymbol{\Delta}$. Using the Galerkin method [5], we discretize the contribution from the cohesive elements:

$$[\mathbf{K}]_{el} = \int_0^1 \int_0^1 \mathbf{B}^{\mathrm{T}} \mathbf{R}^{\mathrm{T}} \mathbf{D}_{local} \mathbf{R} \mathbf{B} J d\xi d\eta, \tag{3.3}$$

$$[\mathbf{F}]_{el} = \int_0^1 \int_0^1 \mathbf{B}^{\mathrm{T}} \mathbf{R}^{\mathrm{T}} \mathbf{t}_{local} J d\xi d\eta, \tag{3.4}$$

where (ξ,η) denote intrinsic coordinates and J denotes the Jacobian. To incorporate a user-defined cohesive element into the existing Abaqus framework, we need to provide the element stiffness matrix ($[\mathbf{K}]_{el}$) and force vector ($[\mathbf{F}]_{el}$) within a user supplied subroutine (UEL). The global displacement-separation matrix, $\mathbf{B}$, is a $3 \times 3N$ matrix (where N is the number of shape functions) that computes the relative opening of the crack at any point in the cohesive element. The rotational matrix, $\mathbf{R}$, transforms from global to local coordinates. The local constitutive matrix, $\mathbf{D}_{local}$, and the local force vector, $\mathbf{t}_{local}$, are functions of the particular choice of cohesive model, and will be outlined for the Park-Paulino-Roesler cohesive model below.

The $\mathbf{B}$ matrix is computed from the shape functions N_i ($i = 1, 2, \ldots, N$), and the identity matrix $\mathbf{I}$:

$$\mathbf{B} = [\; N_1\mathbf{I}_{3\times3} \mid N_2\mathbf{I}_{3\times3} \mid \cdots \mid N_N\mathbf{I}_{3\times3} \;] \, [\; \mathbf{I}_{3N\times3N} \mid -\mathbf{I}_{3N\times3N} \;]. \tag{3.5}$$

The rotational matrix, $\mathbf{R}$, is a function of the normal vector ($\bar{\mathbf{n}}$) and two perpendicular tangential vectors ($\bar{\mathbf{t}}_2$, $\bar{\mathbf{t}}_3$); which form the basis of the midplane of the cohesive element, as illustrated in Figure 3.2:

$$\mathbf{R} = \begin{bmatrix} \bar{\mathbf{n}}^{\mathrm{T}} \\ \bar{\mathbf{t}}_2^{\mathrm{T}} \\ \bar{\mathbf{t}}_3^{\mathrm{T}} \end{bmatrix}. \tag{3.6}$$

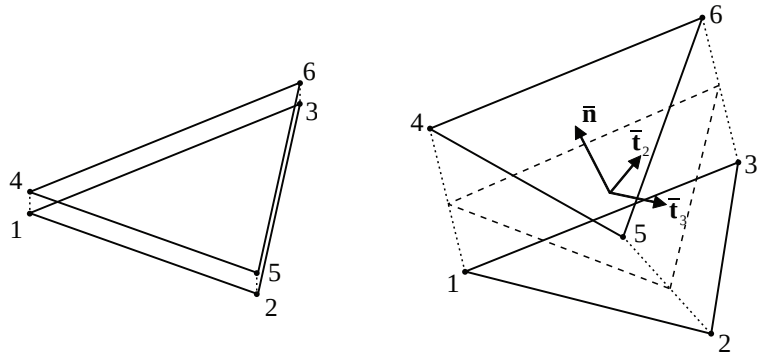

(a) (b)

Figure 3.2: A cohesive element in (a) its initial configuration with zero thickness and (b) its deformed configuration, depicting the normal and tangential vectors on the midplane of the cohesive element.

The local constitutive matrix, for any coupled cohesive model, is defined as:

$$\mathbf{D}_{local} = \begin{bmatrix} D_{nn} & D_{nt}\Delta_2/\Delta_t & D_{nt}\Delta_3/\Delta_t \\ D_{tn}\Delta_2/\Delta_t & D_{tt}\Delta_2^2/\Delta_t^2 + T_t\Delta_3^2\Delta_t^3 & D_{tt}\Delta_2\Delta_3/\Delta_t^2 - T_t\Delta_2\Delta_3/\Delta_t^3 \\ D_{tn}\Delta_3/\Delta_t & D_{tt}\Delta_2\Delta_3/\Delta_t^2 - T_t\Delta_2\Delta_3/\Delta_t^3 & D_{tt}\Delta_3^2/\Delta_t^2 + T_t\Delta_2^2/\Delta_t^3 \end{bmatrix}, \tag{3.7}$$

where D_{nn}, D_{nt}, D_{tn}, and D_{tt} are particular to the model. The variables Δ_2 and Δ_3 correspond to the crack opening widths in the plane perpendicular to the normal direction (Δ_1), as illustrated in Figure 3.3. The local force vector, $\mathbf{t}_{local}$, for any coupled cohesive model is:

$$\mathbf{t}_{local} = \begin{Bmatrix} T_n \\ T_t\Delta_2/\Delta_t \\ T_t\Delta_3/\Delta_t \end{Bmatrix}, \tag{3.8}$$

where we have considered the tangential opening directions to be coupled through the relation $\Delta_t = \sqrt{\Delta_2^2 + \Delta_3^2}$, on the fracture plane. The traction components (T_n and T_t) are also particular to the choice of cohesive model, and will be defined for the the PPR model in Section 3.4.

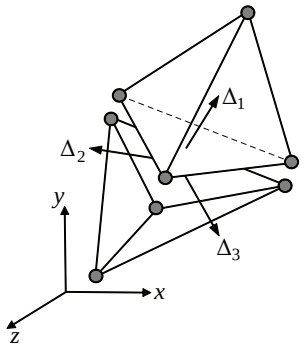

Figure 3.3: Definition of the crack opening directions in a typical element configuration.

3.4 Constitutive relations

The constitutive relation for the cohesive elements is chosen independently of that for the bulk elements. There have been many cohesive relations proposed in the literature (see [41] for a recent review of some of the prevalent relations); most of which suffer from deficiencies when trying to satisfy fracture boundary conditions, or which require non-physical input parameters. The PPR cohesive model is an adaptable cohesive model that was designed with the goal of overcoming the deficiencies suffered by previous models. The PPR model is capable of capturing both intrinsic and extrinsic fracture behavior [51], but the present implementation in Abaqus highlights the use of the intrinsic model. The extrinsic model will be discussed in Chapters 5 and 6. This section outlines the formulation of the intrinsic PPR cohesive model, as well as the choice of unloading/reloading and contact relations used in this work.

3.4.1 Intrinsic PPR potential-based cohesive model

The intrinsic PPR cohesive model is potential-based. Such models have an advantage over non-potential-based models, in that their traction-separation relations are determined by taking the derivative of the potential with respect to the normal and tangential crack opening widths. Similarly, since the second derivative of the potential yields the tangent matrix, it is guaranteed to be symmetric. The intrinsic PPR potential function is defined as:

$$\Psi(\Delta_n, \Delta_t) = \min(\phi_n, \phi_t) + \left[\Gamma_n \left(1 - \frac{\Delta_n}{\delta_n}\right)^{\alpha} \left(\frac{m}{\alpha} + \frac{\Delta_n}{\delta_n}\right)^{m} + \langle \phi_n - \phi_t \rangle\right] \times \left[\Gamma_t \left(1 - \frac{|\Delta_t|}{\delta_t}\right)^{\beta} \left(\frac{n}{\beta} + \frac{|\Delta_t|}{\delta_t}\right)^{n} + \langle \phi_t - \phi_n \rangle\right], \quad (3.9)$$

where Δ_n and Δ_t are the normal and tangential crack opening widths, respectively. There are eight user inputs to the PPR model, a feature that allows the model to capture a variety of cohesive relations. The eight inputs are the normal and tangential: fracture energies ($\phi_n,\ \phi_t$), cohesive strengths ($\sigma_{\max},\ \tau_{\max}$), shape parameters ($\alpha,\ \beta$), and initial slope indicators ($\lambda_n,\ \lambda_t$), respectively. All parameters have a physical interpretation. The shape parameters control the softening shape of the traction-separation relation. If α (β) is set equal to 2, the softening relation is almost linear, whereas if α (β) is less than or greater than 2, the relation is concave or convex, respectively. The initial slope indicators correspond to the ratio of the peak crack opening width to the final crack opening width. Thus, the smaller the initial slope indicator, the greater the initial slope in the traction-separation relation. The potential function is defined over a domain of dependence; which is bounded by the normal final crack opening width (δ_n) and the tangential final crack opening width (δ_t):

$$\delta_n = \frac{\phi_n}{\sigma_{\max}} \alpha \lambda_n \left(1-\lambda_n\right)^{\alpha-1} \left(\frac{\alpha}{m}+1\right) \left(\frac{\alpha}{m}\lambda_n + 1\right)^{m-1}, \tag{3.10}$$

$$\delta_t = \frac{\phi_t}{\tau_{\max}} \beta \lambda_t \left(1-\lambda_t\right)^{\beta-1} \left(\frac{\beta}{n}+1\right) \left(\frac{\beta}{n}\lambda_t + 1\right)^{n-1}. \tag{3.11}$$

The corresponding traction-separation relations, T_n and T_t, determined by taking the derivative of the above potential with respect to Δ_n and Δ_t, respectively, are defined as:

$$T_n(\Delta_n,\Delta_t) = \frac{\partial \Psi}{\partial \Delta_n} = \frac{\Gamma_n}{\delta_n} \left[m \left(1-\frac{\Delta_n}{\delta_n}\right)^{\alpha} \left(\frac{m}{\alpha}+\frac{\Delta_n}{\delta_n}\right)^{m-1} - \alpha \left(1-\frac{\Delta_n}{\delta_n}\right)^{\alpha-1} \left(\frac{m}{\alpha}+\frac{\Delta_n}{\delta_n}\right)^{m} \right] \left[\Gamma_t \left(1-\frac{|\Delta_t|}{\delta_t}\right)^{\beta} \left(\frac{n}{\beta}+\frac{|\Delta_t|}{\delta_t}\right)^{n} + \langle \phi_t - \phi_n \rangle \right], \tag{3.12}$$

$$T_t(\Delta_n,\Delta_t) = \frac{\partial \Psi}{\partial \Delta_t} = \frac{\Gamma_t}{\delta_t} \left[n \left(1-\frac{|\Delta_t|}{\delta_t}\right)^{\beta} \left(\frac{n}{\beta}+\frac{|\Delta_t|}{\delta_t}\right)^{n-1} - \beta \left(1-\frac{|\Delta_t|}{\delta_t}\right)^{\beta-1} \left(\frac{n}{\beta}+\frac{|\Delta_t|}{\delta_t}\right)^{n} \right] \left[\Gamma_n \left(1-\frac{\Delta_n}{\delta_n}\right)^{\alpha} \left(\frac{m}{\alpha}+\frac{\Delta_n}{\delta_n}\right)^{m} + \langle \phi_n - \phi_t \rangle \right] \frac{\Delta_t}{|\Delta_t|}. \tag{3.13}$$

These tractions are used to compute the local force vector, as per Equation 3.8. Representative traction-separation relations are plotted in Figure 3.4.

The energy constants, Γ_n and Γ_t, are related to the normal and tangential fracture energies. When the normal and tangential fracture energies are different ($\phi_n \neq \phi_t$), the energy constants become:

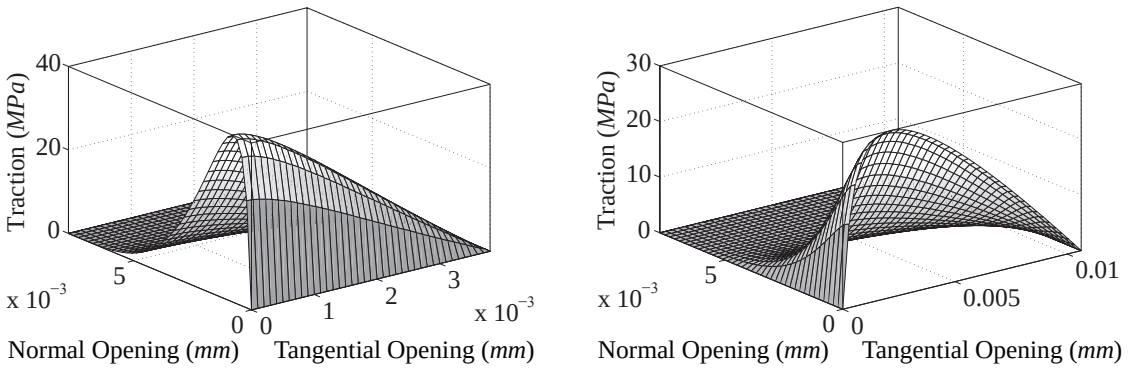

Figure 3.4: Traction-separation relations for (a) normal opening ($\phi_n = 100N/m$, $\sigma_{\max} = 40MPa$, $\alpha = 5.0$, and $\lambda_n = 0.1$), and (b) tangential opening ($\phi_t = 200N/m$, $\tau_{\max} = 30MPa$, $\beta = 2.0$, and $\lambda_t = 0.2$).

$$\Gamma_n = (-\phi_n)^{\langle \phi_n - \phi_t \rangle / (\phi_n - \phi_t)} \left(\frac{\alpha}{m}\right)^m \quad \text{and} \quad \Gamma_t = (-\phi_t)^{\langle \phi_t - \phi_n \rangle / (\phi_t - \phi_n)} \left(\frac{\beta}{n}\right)^n. \tag{3.14}$$

When the normal and tangential fracture energies are equal ($\phi_n = \phi_t$), the energy constants simplify to:

$$\Gamma_n = -\phi_n \left(\frac{\alpha}{m}\right)^m \quad \text{and} \quad \Gamma_t = \left(\frac{\beta}{n}\right)^n, \tag{3.15}$$

where the non-dimensional exponents, m and n, are evaluated from the shape parameters (α, β) and the initial slope indicators (λ_n, λ_t):

$$m = \frac{\alpha(\alpha - 1)\lambda_n^2}{(1 - \alpha\lambda_n^2)}, \quad n = \frac{\beta(\beta - 1)\lambda_t^2}{(1 - \beta\lambda_t^2)}. \tag{3.16}$$

The traction-separation relations are also valid in a domain of dependence. The domain for the normal traction is bounded by the final crack opening width in the normal direction (δ_n) and the conjugate final crack opening width in the tangential direction ($\pm\bar{\delta}_t$). Similarly, the domain for the tangential traction is bounded by the final crack opening width in the tangential direction ($\pm\delta_t$) and the conjugate final crack opening width in the normal direction ($\bar{\delta}_n$). The conjugate final crack opening width in the tangential direction ($\Delta_t = \bar{\delta}_t$) corresponds to the solution of the following nonlinear equation:

$$f_t(\Delta_t) = \Gamma_t \left(1 - \frac{\Delta_t}{\delta_t}\right)^\beta \left(\frac{n}{\beta} + \frac{\Delta_t}{\delta_t}\right)^n + \langle \phi_t - \phi_n \rangle = 0; \tag{3.17}$$

which is unique between 0 and δ_t. Likewise, the conjugate final crack opening width in the

normal direction ($\Delta_n = \bar{\delta}_n$) is the solution of the following nonlinear equation:

$$f_n\left(\Delta_n\right) = \Gamma_n \left(1 - \frac{\Delta_n}{\delta_n}\right)^{\alpha} \left(\frac{m}{\alpha} + \frac{\Delta_n}{\delta_n}\right)^{m} + \langle \phi_n - \phi_t \rangle = 0; \tag{3.18}$$

which is unique between 0 and δ_n. The resulting domains of dependence are illustrated in Figure 3.5.

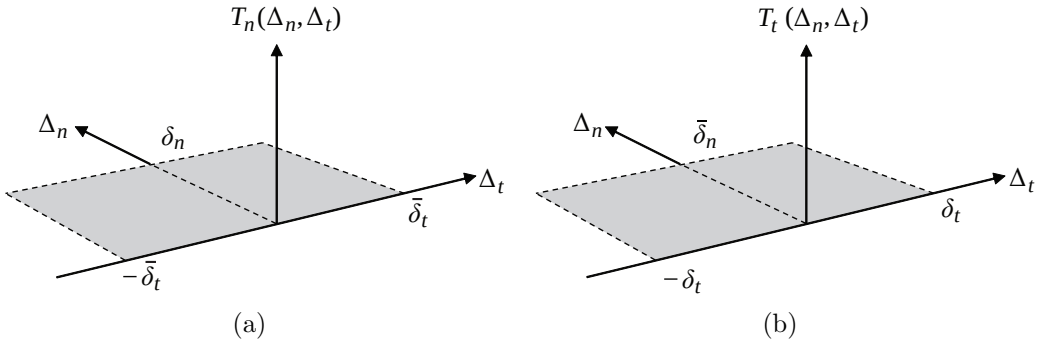

Figure 3.5: Domain of dependence for each traction-separation relation (T_n, T_t); bounded by the final crack opening widths (δ_n, δ_t) and the conjugate final crack opening widths ($\bar{\delta}_n$, $\bar{\delta}_t$).

To implement these elements into an Abaqus subroutine, we also need to provide the material tangent matrix, $\mathbf{D}_{local}$. This is calculated by taking either the second derivatives of the potential function (3.9), or the first derivatives of the traction relations (3.12) and (3.13), with respect to the normal and tangential crack opening widths (Δ_n and Δ_t):

$$D_{nn} = \frac{\partial^2 \Psi}{\partial \Delta_n^2} = \frac{\partial T_n}{\partial \Delta_n} \tag{3.19}$$

$$D_{tt} = \frac{\partial^2 \Psi}{\partial \Delta_t^2} = \frac{\partial T_t}{\partial \Delta_t} \tag{3.20}$$

$$D_{nt} = \frac{\partial^2 \Psi}{\partial \Delta_n \partial \Delta_t} = \frac{\partial T_n}{\partial \Delta_t} \tag{3.21}$$

Since the PPR model is potential-based, the tangent matrix is symmetric and $D_{tn} = D_{nt}$. The components of the material tangent matrix are combined to form the local constitutive matrix through Expression 3.7.

3.4.2 Choice of unloading/reloading relation

The unloading/reloading relation used in this model is uncoupled, in the sense that, unloading in the normal direction is viewed as independent of that in the tangential direction. The

unloading relation is activated when the normal or tangential separation is past the peak cohesive strength of the element, and effects both the tangent matrix (3.7) and the traction vector (3.8). The unloading/reloading relation in the model is selected to be linear to the origin, as illustrated in Figure 3.6. This is a very common approach to modeling unloading/reloading in cohesive elements [138, 139], and will likely satisfy the expectations of most users of this work. If an alternative unloading/reloading relation is desired, we outline a possible replacement in Section 3.5.2 and specify the portions of the UEL which will need to be updated.

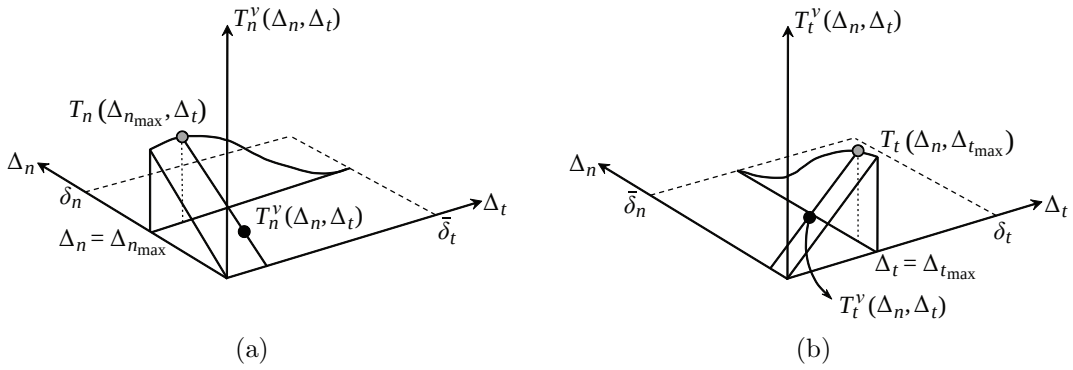

Figure 3.6: Depiction of the linear unloading/reloading relations for loading in the (a) normal direction, and (b) tangential direction.

3.4.3 Choice of contact relation

The selected contact relation is based on the penalty stiffness approach. As the normal separation becomes negative ($\Delta_n < 0$) contact forces resist interpenetration. The resisting force increases linearly in accordance with a corresponding stiffness; the modulus of which is chosen to correspond to the slope of the cohesive relation as it approaches zero opening displacement. Alternatively, other contact formulations could be used, such as the ones found in references [53, 140]. We will discuss the modifications necessary to alter the contact formulation in Section 3.5.4.

3.5 Implementation in commercial software and user modifications

To make this work as useful as possible, this section describes how to implement the cohesive elements into a finite element model, and outlines sections of the code that users may chose

to modify to suit their specific needs. This section provides the basis for other modifications not anticipated in this work.

3.5.1 Implementing cohesive elements into an Abaqus input file

To insert the cohesive zone elements (CZEs) into an Abaqus analysis, the Abaqus input file should refer to the CZEs using the following commands. In the case of the CZE with 8 nodes:

```
*USER ELEMENT, TYPE=U1, NODE=8, COORDINATES=3, PROPERTIES=8, VARIABLES=14
1, 2, 3
*ELEMENT, TYPE=U1, ELSET=ELSET_NAME
```

where the `VARIABLES` parameter indicates the number of solution-dependent state variables stored in each element [103]. For our purposes, these variables track the maximum opening at each Gauss point in the element, to determine if the element is opening or closing. The primary difference for the other elements is the number of nodes and variables. For the CZE with 6 nodes; `NODE=6` and `VARIABLES=8`, and for the CZE with 12 nodes; `NODE=12` and `VARIABLES=8`.

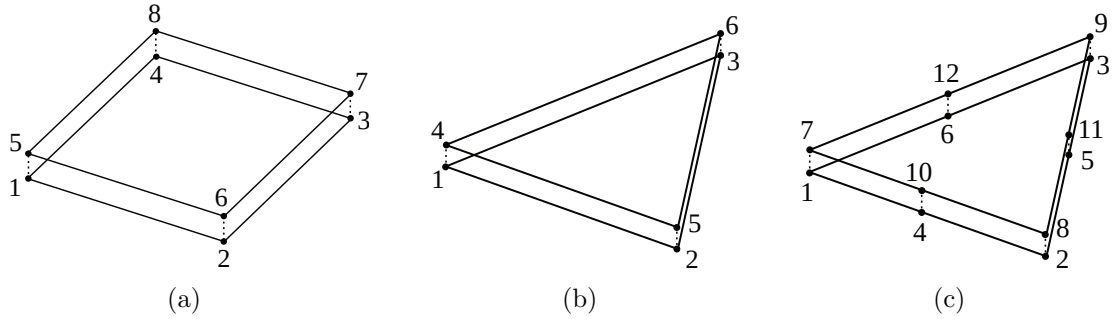

Figure 3.7: Node numbering for a cohesive zone element with (a) 8 nodes, (b) 6 nodes, and (c) 12 nodes.

Below these input lines, the user specifies the element number and the node numbers corresponding to the connectivity of the element. Nodes are numbered in the order shown in Figure 3.7. To assign properties to the elements, one needs to include the following lines to the input file:

```
*UEL PROPERTY, ELSET=ELSET_NAME
100, 200, 30e6, 40e6, 2, 5, 0.1, 0.2
```

where we have chosen, for example, $\phi_n = 100N/m$, $\phi_t = 200N/m$, $\sigma_{\max} = 30MPa$, $\tau_{\max} = 40MPa$, $\alpha = 2$, $\beta = 5$, $\lambda_n = 0.1$ and $\lambda_t = 0.2$, respectively. Note that the units are

important, and the values here assume that the dimensions of the mesh are given in meters, and any force boundary conditions are given in Newtons. Finally, when running this problem on a linux machine, the following command line prompt will run the problem:

```
abaqus job=job_name user=3DpprBrick.f
```

where '`job_name`' is the name of the input file.

3.5.2 Modifying the unloading/reloading relation

The current unloading/reloading relation in the model is linear to the origin, as illustrated in Figure 3.6. Some users may wish to modify this; which may be done by altering only a few lines in the UEL. Unloading effects the tangent matrix (3.7) and the traction vector (3.8), both of which will need updating. For purposes of illustration, we outline the steps necessary to implement a power-law unloading/reloading relation. Assuming a power-law relation, the corresponding tractions during the unloading phase are reformulated as:

$$T_n^v\left(\Delta_n, \Delta_t\right) = T_n\left(\Delta_{n_{\max}}, \Delta_t\right)\left(\frac{\Delta_n}{\Delta_{n_{\max}}}\right)^{\alpha_v}, \tag{3.22}$$

$$T_t^v\left(\Delta_n, \Delta_t\right) = T_t\left(\Delta_n, \Delta_{t_{\max}}\right)\left(\frac{|\Delta_t|}{\Delta_{t_{\max}}}\right)^{\beta_v}\frac{\Delta_t}{|\Delta_t|} \tag{3.23}$$

where α_v and β_v determine the shape of the unloading curve, as illustrated in Figure 3.8. Similarly, the tangent matrix components become:

$$D_{nn}^v = T_n\left(\Delta_{n_{\max}}, \Delta_t\right)\frac{\alpha_v}{\Delta_{n_{\max}}}\left(\frac{\Delta_n}{\Delta_{n_{\max}}}\right)^{\alpha_v - 1}, \quad D_{nt}^v = D_{nt}\left(\Delta_{n_{\max}}, \Delta_t\right)\left(\frac{\Delta_n}{\Delta_{n_{\max}}}\right)^{\alpha_v} \tag{3.24}$$

$$D_{tt}^v = T_t\left(\Delta_n, \Delta_{t_{\max}}\right)\frac{\beta_v}{\Delta_{t_{\max}}}\left(\frac{|\Delta_t|}{\Delta_{t_{\max}}}\right)^{\beta_v - 1}, \quad D_{tn}^v = D_{tn}\left(\Delta_n, \Delta_{t_{\max}}\right)\left(\frac{|\Delta_t|}{\Delta_{t_{\max}}}\right)^{\beta_v} \tag{3.25}$$

To implement these changes into the UEL, we first introduce additional input parameters, let them be called `alphaV` and `betaV`. This can be done in the input portion of the code (lines 36-43):

```
alphaV = PROPS(9)
betaV = PROPS(10)
```

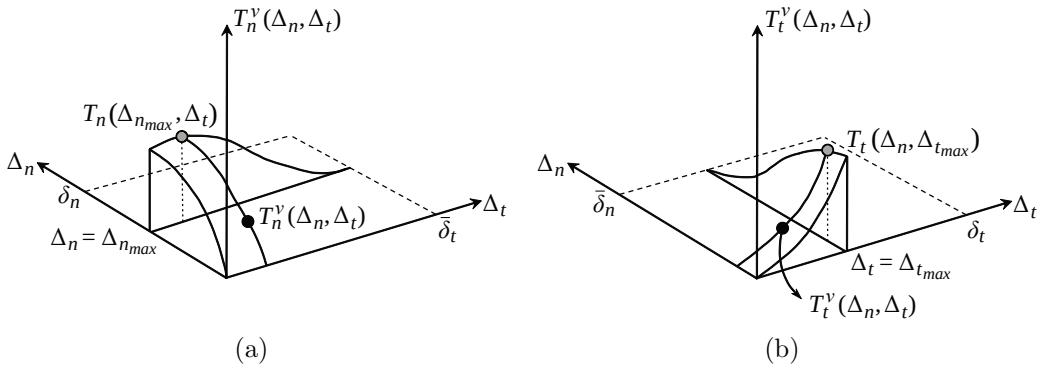

Figure 3.8: Depiction of the power-law unloading/reloading relations for loading in the (a) normal direction, and (b) tangential direction. If α^v or $\beta^v > 1$, the unloading/reloading relation is convex; whereas, if α^v or $\beta^v < 1$ the unloading/reloading relation is concave.

These variables are then passed into the subfunction `k_cohesive_law` on line 137. To update the normal unloading traction, we change line 256 to:

```
*(popn/pmax)**alphaV
```

Similarly, to modify the tangential unloading traction, we change line 273 to:

```
*(popt/tmax)**betaV
```

The process of updating the material tangent matrix follows in the same manner as the tractions. Updating is required to the variables D_{nn}, D_{nt}, D_{tt} and D_{tn} on lines 307, 314, 348 and 355, respectively. In the order that they appear, we change these lines to:

```
307: *(alphaV/pmax)*(popn/pmax)**(alphaV-1)
314: *(popn/pmax)**alphaV
348: *(betaV/tmax)*(popt/tmax)**(betaV-1)
355: *(popt/tmax)**betaV
```

respectively. It is important to note that, since the power-law unloading/reloading relation is not derived from a potential, the resulting tangent matrix is not guaranteed to be symmetric.

3.5.3 Modifications for material gradation

There are multiple methods by which one may chose to grade their material properties [141, 142]. This section will outline the modifications necessary to implement a graded normal fracture energy in the z-coordinate direction, based on the method proposed by Kim

and Paulino [142]. Based on this simple exercise, we hope that the users will be more familiar with the UEL, and more adept at making their own modifications. To allocate the range and region of gradation, we need additional user inputs; which may be included in the input section of the code (lines 36-43):

```
Gfn_min=PROPS(9)
Gfn_max=PROPS(10)
Zmin=PROPS(11)
Zmax=PROPS(12)
```

where `Gfn_min`, `Gfn_max`, `Zmin` and `Zmax` correspond to the minimum and maximum value of the fracture energy and to the minimum and maximum z-coordinates in the region of gradation, respectively. The remainder of the modifications need to occur prior to the first use of the fracture energy (on line 106). To compute the total change in the fracture energy, we include the line:

```
del_Gfn=Gfn_max-Gfn_min
```

Finally, assuming a linear variation of fracture energy, we include the lines:

```
Gfn1=Gfn_min+((Zmax-co_de_m(3,1))/(Zmax-Zmin))*del_Gfn
Gfn2=Gfn_min+((Zmax-co_de_m(3,2))/(Zmax-Zmin))*del_Gfn
Gfn3=Gfn_min+((Zmax-co_de_m(3,3))/(Zmax-Zmin))*del_Gfn
Gfn4=Gfn_min+((Zmax-co_de_m(3,4))/(Zmax-Zmin))*del_Gfn
Gfn = sf(1)*Gfn1+sf(2)*Gfn2+sf(3)*Gfn3+sf(4)*Gfn4
```

after we call the subfunction `k_shape_fun` on line 100, and before we determine the inputs to the cohesive model on line 104. The resulting cohesive model will have a varying final crack opening width, and corresponding softening curve, based on the variation of fracture energy. This method, although presented for a variation of fracture energy in the z-direction, can be extended to other parameters (including multiple parameters) in any direction, such as that illustrated in Figure 3.9 for the case of a graded shape parameter, α.

3.5.4 Modifying the contact relation

The current UELs are implemented with the common penalty stiffness approach to contact. The magnitude of the stiffness is in accordance with that of the hardening slope at the initiation of the intrinsic formulation. There is much debate about the appropriate method

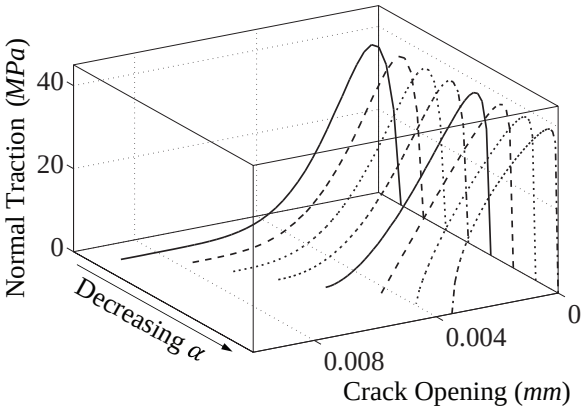

Figure 3.9: Influence of varying the shape parameter, α, on the normal traction-separation relation. Note the influence on both the shape of the softening curve and the final crack opening width.

of accounting for contact in a cohesive element formulation; thus, it may be a desired modification to the formulation [53, 140]. To change the contact formulation, the user needs to modify the corresponding part of the code in which contact is handled. In the subfunction `k_cohesive_law` the user needs to modify the section of the code in which the normal opening displacement is negative (line 279):

```
if (delu(3) .LT. 0.0) then
```

The users are able to modify any component of this section, and may include any additional variables external to this statement as they wish.

In addition to the contact condition considered within the element itself, one may choose to use the surface contact conditions built into Abaqus [103]. The surface contact conditions use the master-slave surface relation to prevent element interpenetration. This condition is suitable for situations in which the fracture surfaces are predefined, but would be very difficult to implement if the intrinsic cohesive elements were to be inserted throughout a region of the mesh. This method essentially requires one additional step in the analysis. One needs to define two surfaces, corresponding to the two fracture surfaces that make up the facets on which the cohesive elements are inserted. More information on how to implement this method may be found in the Abaqus users manual [103].

3.6 Three-dimensional example problems

Here, we verify the implementation and display some of the capabilities of the elements. The following problems are presented and discussed: (1) the patch test, (2) the mixed-mode

bending (MMB) test problem, and (3) the small deformation coated particle debonding of composite materials.

3.6.1 Patch test

To verify the implementation of the cohesive elements, a simple patch test is conducted for each of the elements, using the models illustrated in Figure 3.10. Two sets of material and cohesive parameters are considered. In the first study, the bulk material has an elastic modulus of $32MPa$ and a Poisson's ratio of 0.2; and the cohesive elements have a cohesive fracture energy of $100N/m$, a cohesive strength of $4MPa$, a softening shape parameter of 5, and an initial slope indicator of 0.2. Each cube is $1 \times 1 \times 1mm$ and is elongated at the top to a displacement of $0.025mm$, then compressed to a displacement of $-0.01mm$, and finally elongated to complete failure. The unloading/reloading relation is selected to be linear. A representative result from this study is illustrated in Figure 3.11(a). Upon loading, the stress increases to the cohesive strength, then softens due to the presence of the cohesive elements. The softening behavior is convex, as determined by the use of a shape parameter greater than 2 ($\alpha = 5$). As the model is unloaded, the stress linearly decreases to the origin, where contact is initiated. In the compressive region, the stress is linear with a slope equal to that of the initial hardening region.

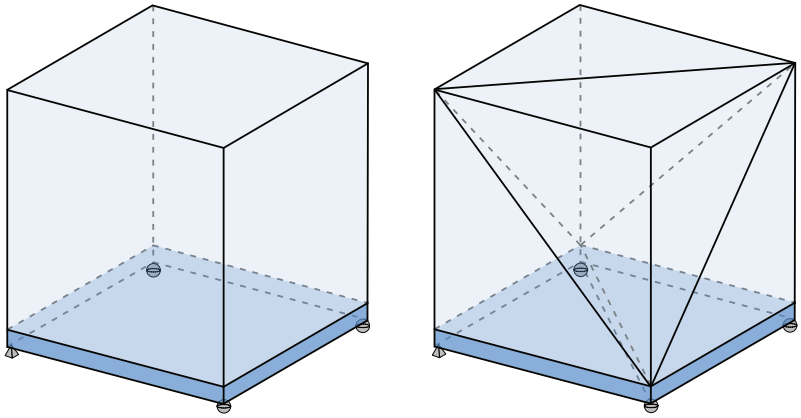

(a) (b)

Figure 3.10: Geometry and support conditions for the patch test using (a) brick elements, and (b) tetrahedral elements. The blue zones indicate the areas where cohesive elements are inserted, between the bulk elements and the boundary supports.

In the second study, the bulk constitutive relation is assumed to follow the incompressible neo-Hookean model; with corresponding stored-energy function [143]:

$$\Psi\left(I_1\right) = \frac{\mu}{2}\left[I_1 - 3\right], \tag{3.26}$$

where μ is the initial shear modulus, $I_1 = \mathbf{F} \cdot \mathbf{F}$ is the first principal invariant of the right Cauchy-Green tensor, and $\mathbf{F}$ is the deformation gradient. The shear modulus is selected as $\mu = 1.0MPa$; which is a representative value for a typical elastomer [74]. The cohesive elements have a cohesive fracture energy of $1N/m$, a cohesive strength of $0.5MPa$, a softening shape parameter of 3, and an initial slope indicator of 0.1. Each cube is $10 \times 10 \times 10\mu m$ and is elongated at the top to a displacement of $2.75\mu m$, then compressed to a displacement of $-1\mu m$ and finally elongated to complete failure. The unloading/reloading relation is selected to be linear. A representative result from this study is illustrated in Figure 3.11(b). The global response is similar to that observed in the first study, but displays a much softer initial slope, due to the softer bulk material, and a softening region with greater convexity.

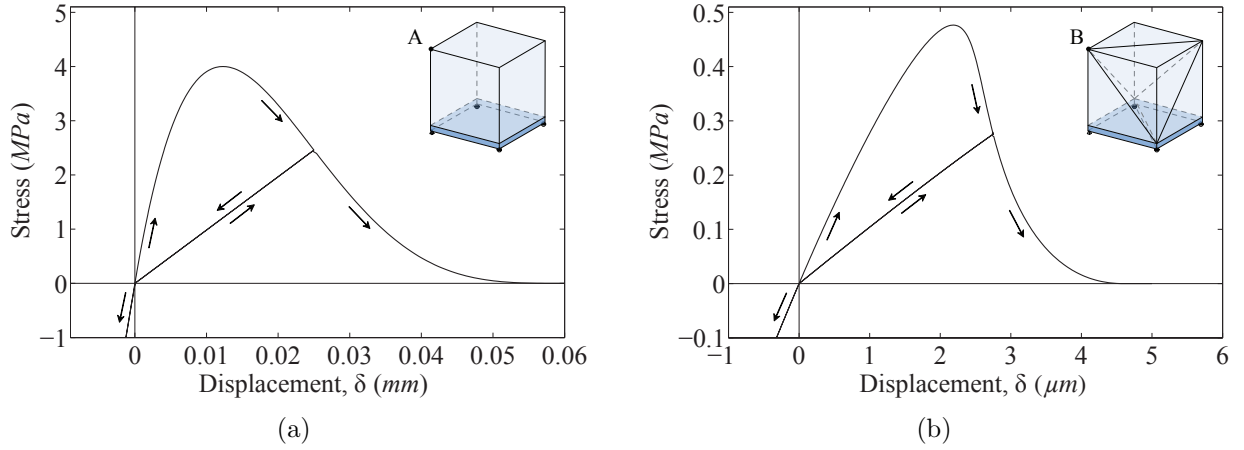

Figure 3.11: Representative results from the patch test study, with two different sets of material parameters: (a) a $1 \times 1 \times 1mm$ linear elastic cube, with displacements tracked at point A ($E = 32MPa$, $\nu = 0.2$, $\phi = 100N/m$, $\sigma = 4MPa$, $\alpha = 5$, and $\lambda = 0.2$); and (b) a $10 \times 10 \times 10\mu m$ nonlinear elastic cube, with displacements tracked at point B ($\mu = 1.0MPa$, $\phi = 1N/m$, $\sigma = 0.5MPa$, $\alpha = 3$, and $\lambda = 0.1$).

3.6.2 Mixed-mode bending specimen

The mixed-mode bending (MMB) specimen is a popular benchmark problem used to estimate fracture energies under mixed-mode loading conditions [144]. The geometry of the problem is illustrated in Figure 3.12. Its Cartesian geometry can be represented in a two-dimensional plane, and thus has received a lot of interest in fracture related publications [51, 145, 146, 147]. Adding to its popularity is the presence of an analytical solution. The analytical solution consists of three separate components [148, 149]. Initially, the response is linear,

and can be compared with results from linear beam theory. However, once fracture initiates, the response follows that derived from linear elastic fracture mechanics.

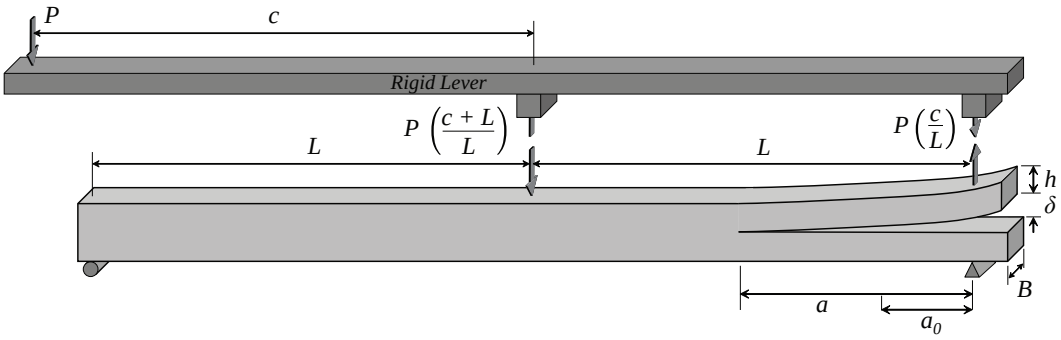

Figure 3.12: Geometry and boundary conditions of the MMB specimen. $L = 51mm$, $c = 60mm$, $B = 25.4mm$, $h = 1.56mm$, $a_0 = 33.7mm$, $P = 850N$.

The elastic beam has a modulus of $122GPa$, and a Poisson's ratio of 0.3. We consider two different scenarios for the cohesive properties. In both scenarios, the shape parameters $(\alpha,\ \beta)$ and initial slope indicators $(\lambda_n,\ \lambda_t)$ are set equal to 3 and 0.02, respectively. The first scenario considers a fracture energy of $500N/m$ in both the normal and tangential directions, and equivalent cohesive strengths in each direction. As the cohesive strengths increase, the numerical solution approaches the analytical solution, as illustrated in Figure 3.13(a). Similar behavior is observed for each element type (see Figure 3.1), thus only the results for linear tetrahedral bulk elements are illustrated. The second scenario considers different fracture energies in the normal ($\phi_n = 500N/m$) and tangential ($\phi_t = 1000N/m$) directions. The cohesive strength in the normal direction is set as $20MPa$ and the strength in the tangential direction is varied. As the tangential cohesive strength increases, the results approach the analytical solution, as illustrated in Figure 3.13(b). As expected, the present results for the three-dimensional problem are essentially the same as those obtained by Park and Paulino for an equivalent two-dimensional problem [123].

3.6.3 Extended example: Small deformation coated particle debonding

In this example, we take an extended look at the small deformation debonding behavior of coated particle reinforced composites. This example acts as a first look at the debonding behavior of particle reinforced composites in this thesis. Initially we will consider the simplified loading case of hydrostatic tension, where, based on experimental observations, debonding is expected to occur uniformly around the particle, as illustrated in Figure 3.14. Following this investigation, we will consider the case of uniaxial tension, where we expect

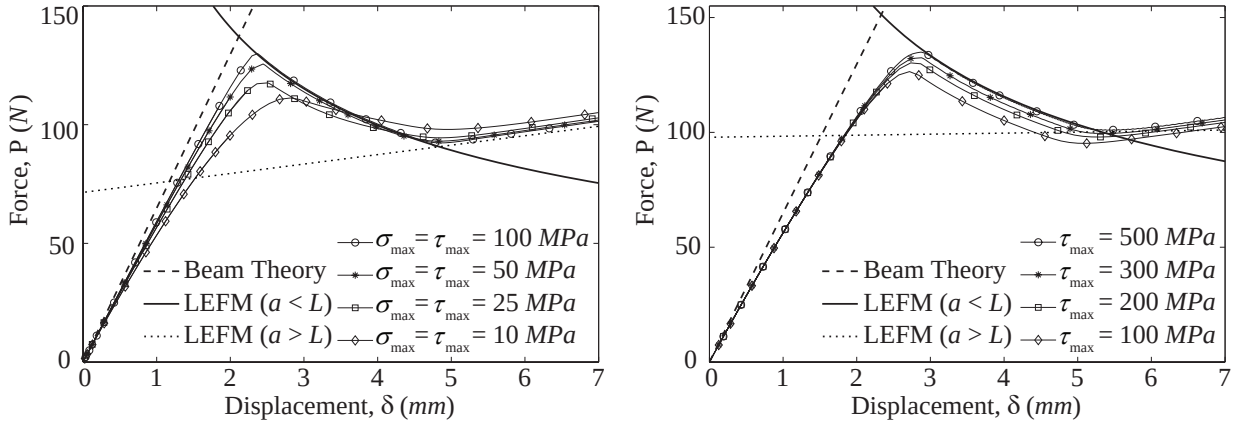

Figure 3.13: Representative results for the MMB specimen using linear tetrahedral elements. The results with linear brick and quadratic tetrahedral elements are similar and thus are not repeated here.

to see progressive debonding. In Chapter 4, we will investigate finite deformation debonding under multiple loading scenarios.

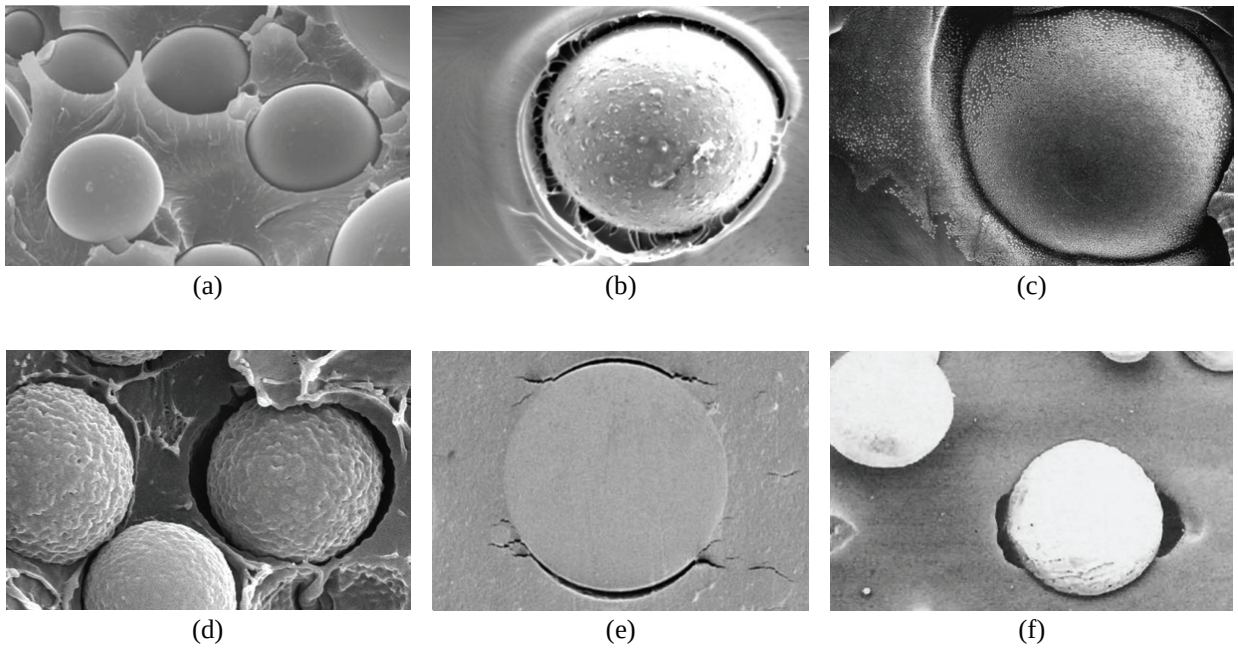

Figure 3.14: Experimental observations of interface debonding in particle reinforced composites undergoing (a)-(c) hydrostatic tension (images extracted from Tagliavia [150]; Kawaguchi and Pearson [151]; and Kraus et al. [152]); and (d)-(f) uniaxial tension (images extracted from Renner [67]; Tsui et al. [153]; and Kanetake et al. [154]).

To investigate particle reinforced composites under hydrostatic tension, we consider a single coated particle, embedded in a matrix, as illustrated in Figure 3.15. Linear brick elements are used to discretize the domain. Mesh refinement studies indicate that a mesh

with approximately 150,000 bulk elements produces sufficiently accurate results, and is the level of refinement used throughout this investigation, as illustrated in Figure 3.15(b). At both the particle-coating and coating-matrix interfaces, 3,230 cohesive elements are used to capture interfacial debonding behavior. Displacement boundary conditions are applied to the exterior surface of the model. In the following examples, unless stated otherwise, the bulk Poisson's ratio has been fixed at 0.25, and the cohesive parameters have been fixed at a cohesive fracture energy (ϕ) of $1.0N/m$, a cohesive strength (σ) of $15MPa$, a shape parameter (α) of 3, and an initial slope indicator (λ) of 0.005.

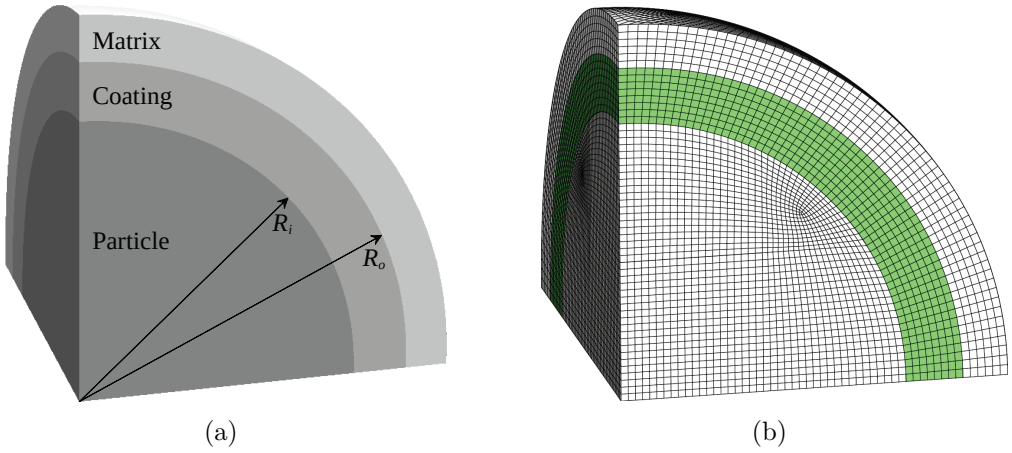

Figure 3.15: The single particle model used to investigate the hydrostatic tensile loading of a composite material with coated particle inclusions: (a) geometry, and (b) mesh.

In the following subsections, we will investigate the influence of many microstructural parameters; including particle size, particle volume fraction, coating thickness, bulk material properties, and cohesive properties, on the macroscopic constitutive response. In subsections 3.6.3.2 through 3.6.3.4 we consider hydrostatic tension, while in subsections 3.6.3.5 and 3.6.3.6 we consider uniaxial tension. For the cases which consider hydrostatic tension, we compare our numerical results to an analytical solution. The details of the analytical solution may be found in reference [155], here we briefly outline the solution for the case of particles with homogeneous coatings, and concurrent debonding occurring at both the particle-coating and coating-matrix interfaces. In this scenario, the macroscopic stress is computed as:

$$\bar{\sigma} = (1 - f)\,\bar{\sigma}_m + f_p\sigma_i + f_c\frac{(\sigma_i R_i^3 - \sigma_o R_o^3)}{(R_i^3 - R_o^3)}, \tag{3.27}$$

and the macroscopic strain is computed as:

$$\bar{\epsilon} = \frac{1-2\nu_m}{E_m}\bar{\sigma} + f_p\left(\frac{1-2\nu_p}{E_p} - \frac{1-2\nu_m}{E_m}\right)\sigma_i + f_c\left(\frac{1-2\nu_c}{E_c} - \frac{1-2\nu_m}{E_m}\right)\frac{(\sigma_i R_i^3 - \sigma_o R_o^3)}{(R_i^3 - R_o^3)} + f_c\frac{\Delta_o}{R_o}, \quad (3.28)$$

where f is the combined volume fraction of the particle (f_p) and coating (f_c); p denotes the particle; c denotes the coating; m denotes the matrix; i denotes the particle-coating interface; o denotes the coating-matrix interface; and Δ_o is the normal crack opening at the coating-matrix interface. The radial distances to the interfaces are denoted by R_i and R_o, as illustrated in Figure 3.15(a). In the above expressions, the stress at each interface is calculated as:

$$\sigma_i = \frac{\phi_n}{\delta_n}\left(\frac{\alpha}{m}\right)^m\left(1-\frac{\Delta_i}{\delta_n}\right)^{\alpha-1}\left(\frac{m}{\alpha}-\frac{\Delta_i}{\delta_n}\right)^{m-1}(m+\alpha)\frac{\Delta_i}{\delta_n}, \quad (3.29)$$

$$\sigma_o = \frac{\phi_n}{\delta_n}\left(\frac{\alpha}{m}\right)^m\left(1-\frac{\Delta_o}{\delta_n}\right)^{\alpha-1}\left(\frac{m}{\alpha}-\frac{\Delta_o}{\delta_n}\right)^{m-1}(m+\alpha)\frac{\Delta_o}{\delta_n}, \quad (3.30)$$

where, Δ_i is the normal crack opening at the particle-coating interface, and is computed as:

$$\Delta_i = \frac{1-2v_c}{E_c\left(R_i^3-R_o^3\right)}\left(R_i^3\sigma_i - R_o^3\sigma_o\right)R_i + \frac{1+v_c}{2E_c\left(R_i^3-R_o^3\right)}\left(\sigma_i-\sigma_o\right)R_o^3R_i - \frac{1-2v_p}{E_p}\sigma_i R_i. \quad (3.31)$$

Moreover, the stress in the matrix is computed as:

$$\bar{\sigma}_m = \frac{2E_m}{3\left(1-v_m\right)}\left\{\frac{\Delta_o}{R_o^3} + \left[\frac{1-2v_c}{E_c\left(R_i^3-R_o^3\right)}\left(R_i^3\sigma_i - R_o^3\sigma_o\right) + \frac{\left(1+v_c\right)R_i^3}{2E_c\left(R_i^3-R_o^3\right)}\left(\sigma_i-\sigma_o\right)\right]\right\} + \frac{\left(1+v_m\right)\sigma_o}{3\left(1-v_m\right)}. \quad (3.32)$$

Solving this system of equations in terms of Δ_o, we determine the macroscopic constitutive response of the corresponding composite material with concurrent separation at both interfaces.

3.6.3.1 Comparison between the single particle model and a full representative unit cell

To verify the simplified single particle model used in this investigation, we compare the response of the model to that of a representative unit cell. The unit cell contains 30 particles with a radius of $1mm$, placed in a random, but periodic, manner. Each particle has a $0.2mm$ thick coating, as illustrated in Figure 3.16. The size of the unit cell is such that the particles constitute a volume fraction of 10%. The geometry is discretized with approximately 330,000 linear tetrahedral elements and periodic boundary conditions are applied. The elastic modulus of the matrix is $80MPa$, and the elastic modulus of the particles is $400MPa$. Cohesive elements are inserted between each particle and its corresponding coating, and have a cohesive fracture energy of $1.0N/m$, a cohesive strength of $10MPa$, a softening shape parameter of 3, and an initial slope indicator of 0.005.

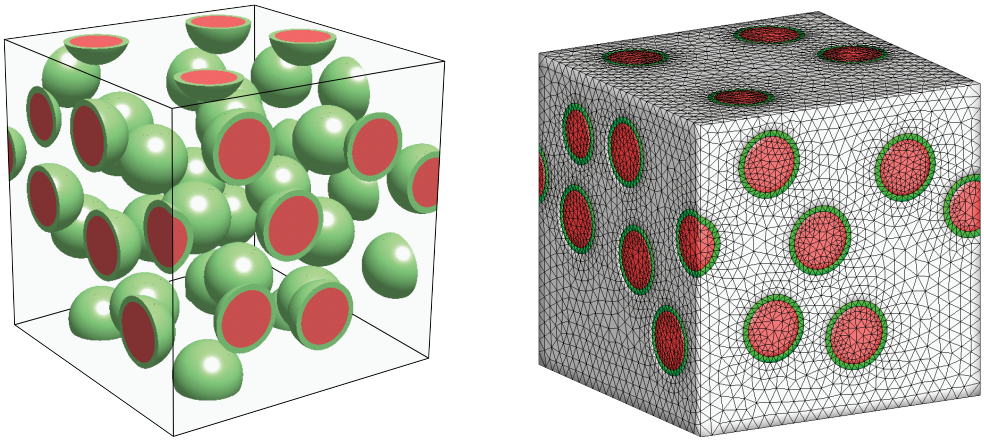

(a) (b)

Figure 3.16: The representative unit cell containing 30 particles placed in a random, but periodic, manner: (a) geometry, and (b) mesh.

The macroscopic constitutive response of the two different models is compared in Figure 3.17. As expected, the response of the single particle model and the representative unit cell model is in good agreement under hydrostatic tension. This study is useful to verify the effectiveness of the single particle model, and leads to increased confidence in using the simplified model. The single particle model has distinct advantages in this case, because it allows us to model higher volume fractions of the particle ensemble (particles and coatings). The volume fraction of the representative unit cell is limited by the requirement of having a well formed discretization between particles, and becomes cumbersome once the total volume fraction of the particle ensemble exceeds approximately 30%. Additionally, the single particle model allows for a direct visualization of the local debonding process, providing a greater understanding of the physical behavior at the microscale. Finally, the single particle model

allows for a greater resolution (finer mesh) to capture the debonding process at the interface. This becomes significant when the fracture properties are chosen such that they cause the fracture region to reduce in size. When the fracture region is small, the size of the mesh in the unit cell grows significantly, and, from a computational viewpoint, becomes prohibitive.

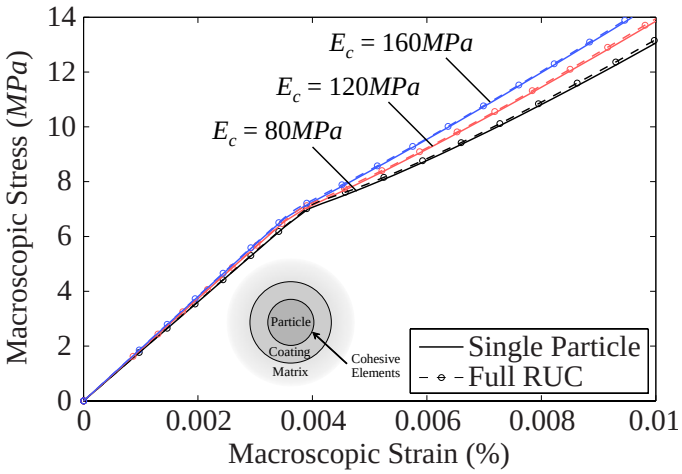

Figure 3.17: Comparison between the constitutive response of the single particle model and the representative unit cell model.

3.6.3.2 Homogeneous coatings: Single separation along the particle-coating interface

In this scenario, we assume that the coating is homogeneous, and that separation is only permitted at the particle-coating interface. The size of the particles is kept constant at $R = 1mm$, with a fixed volume fraction of $f_p = 0.3$. The elastic modulus of the particle is $100GPa$, and the elastic modulus of the matrix is $100MPa$. The volume fraction and elastic modulus of the coating is varied. When the coating is softer than the surrounding matrix ($40MPa$) the elastic stiffness of the material decreases as the volume fraction of the coating increases, as illustrated in Figure 3.18(a). In all cases, the softer coating leads to softening behavior past the elastic limit. When the coating is stiffer than the matrix ($400MPa$), the elastic stiffness of the composite increases as the volume fraction of the coating increases; however, the macroscopic stress at the elastic limit is only slightly altered, as illustrated in Figure 3.18(b). For a very small coating thickness ($f_c = 0.01$), the material displays softening behavior past the elastic limit; however, as the thickness of the coating increases, the material displays hardening behavior past the elastic limit.

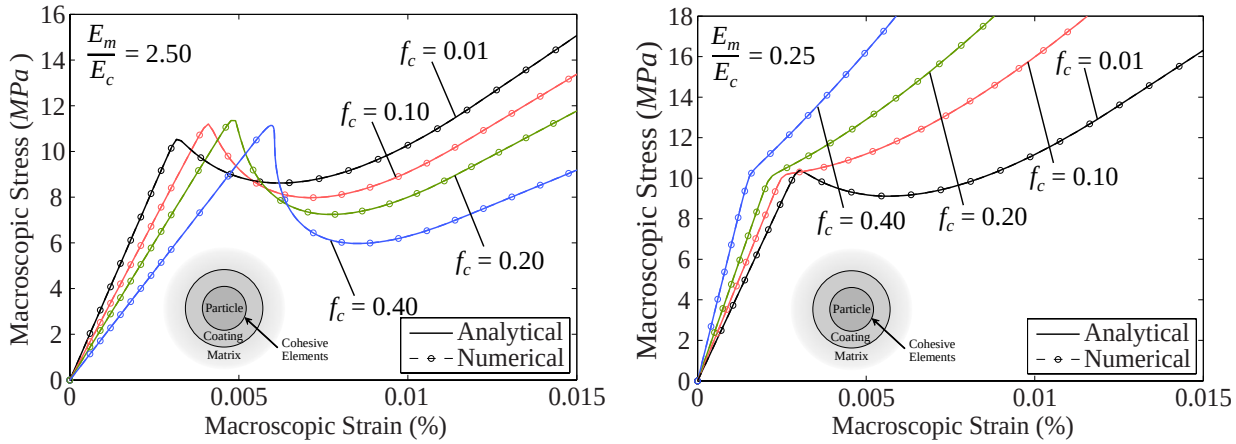

Figure 3.18: Effect of coating thickness on the constitutive response of a composite containing homogeneously coated particles with separation along the particle-coating interface ($R = 1mm$, $E_p = 100GPa$ and $f_p = 0.3$). Coating modulus of (a) $40MPa$, and (b) $400MPa$.

3.6.3.3 Graded coatings: Single separation along the particle-coating interface

The distribution of material in the coating influences the localization of stress at the particle-coating interface. In this study, we investigate the case of heterogeneous coatings with a graded elastic modulus in the radial direction. The modulus is linearly varied from that of the particle ($400MPa$) to that of the matrix ($80MPa$). The particle size is fixed at $R = 1mm$, and the influence of both the volume fraction of the particle and the thickness of the coating is investigated. For the case of a thin coating ($0.02mm$), as the volume fraction of the particle increases, the elastic stiffness and elastic limit of the material increases, as illustrated in Figure 3.19(a). In all cases, softening behavior is observed past the elastic limit. As the particle size decreases, complete debonding occurs earlier, and for a volume fraction of $f_p = 0.1$, snap-back behavior is observed in the post-peak response. For thicker coatings ($0.2mm$), the influence of the graded coating is increased. Similar to the case with thin coatings, as the volume fraction of the particle increases, the elastic stiffness and elastic limit of the material increases, as illustrated in Figure 3.19(b). The material generally displays softening behavior beyond the elastic limit, but transitions to hardening behavior after a small increase in macroscopic strain.

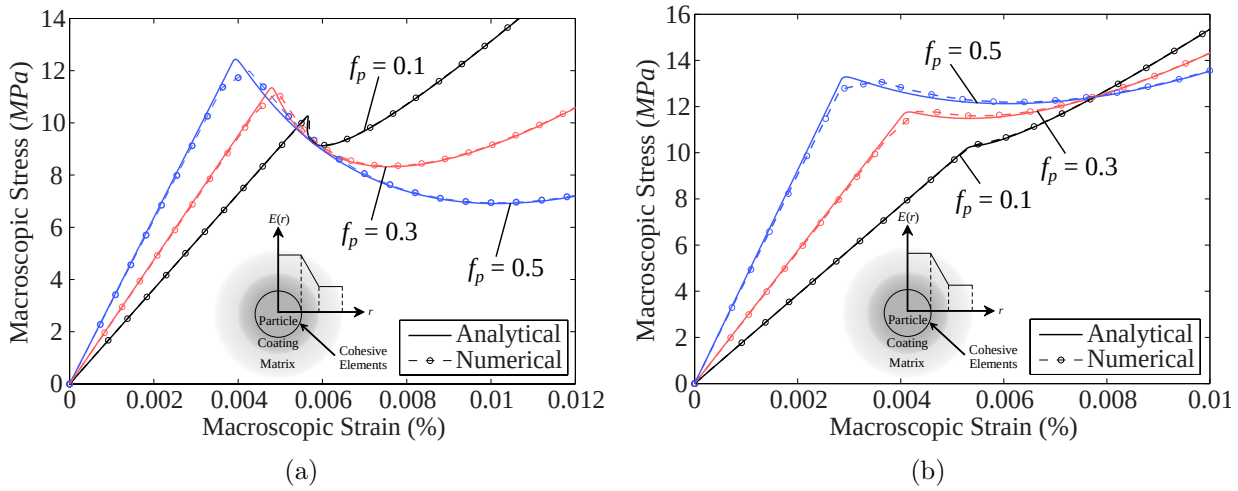

Figure 3.19: Effect of particle volume fraction on the constitutive response of a composite containing particles with functionally graded coatings, with separation along the particle-coating interface ($E_p = 400MPa$ and $E_m = 80MPa$.). Coating thickness of (a) $0.02mm$, and (b) $0.2mm$.

3.6.3.4 Homogeneous coatings: Concurrent separation at the particle-coating and coating-matrix interfaces

We now consider scenarios in which concurrent separation is permitted at both the particle-coating interface, and the coating-matrix interface. We assume that the coatings are homogeneous, and investigate the influence of both the particle size and the coating thickness. First, the effect of particle size is considered. The particle sizes are selected as $R = 0.5mm$, $1mm$, and $1.5mm$; with a fixed particle volume fraction of $f_p = 0.3$, and a fixed coating volume fraction of $f_c = 0.3$. The matrix has an elastic modulus of $100MPa$, the coatings an elastic modulus of $200MPa$, and the particles an elastic modulus of $100GPa$. For this investigation, the cohesive strength at both interfaces is $10MPa$. The initial elastic behavior of the composite is independent of the particle size, as illustrated in Figure 3.20(a). However, there are two distinct kinks in the stress-strain response of the material. Separation initiates at the particle-coating interface, at a macroscopic stress of approximately $6.8MPa$. Beyond this point, the stiffness of the material decreases with increasing particle size. The second distinct kink in the stress-strain response represents the initiation of separation at the coating-matrix interface. After the coating-matrix interface separates, the material hardens for fine particles ($R = 0.5mm$) and the material softens for coarse particles ($R > 0.5mm$).

To investigate the effect of coating thickness, we fix the particle size at $R = 1mm$. For a particle volume fraction of $f_p = 0.3$, the coating volume fraction is varied ($f_c = 0.15$, 0.3, 0.45). As the volume fraction of the stiff coating increases, the elastic stiffness of the composite increases; however, the macroscopic stress at the elastic limit remains the same, as

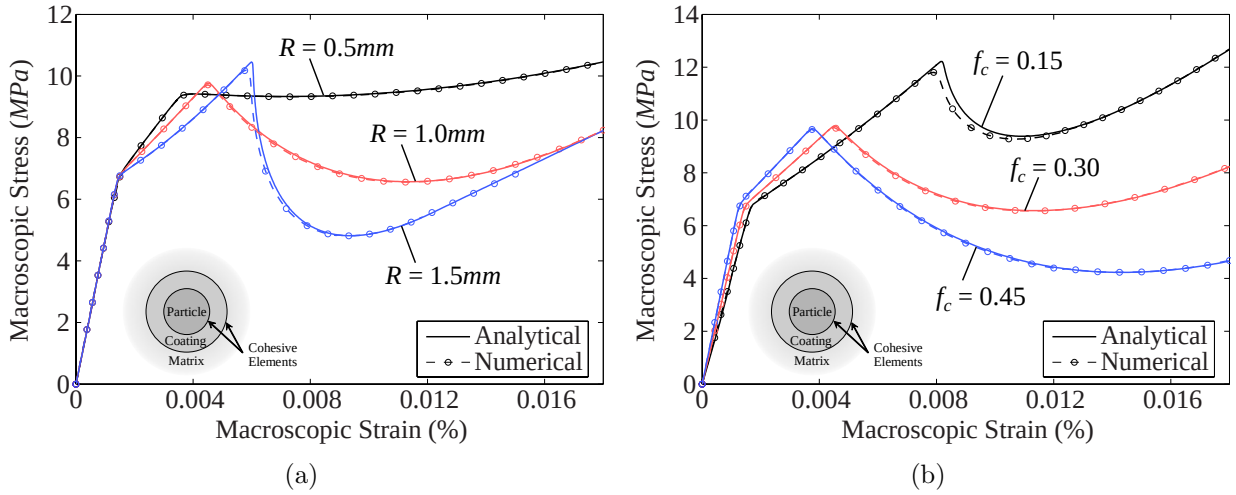

Figure 3.20: Effect of (a) particle radius, and (b) coating thickness on the constitutive response of a composite containing homogeneously coated particles with concurrent separation at the particle-coating and coating-matrix interfaces ($E_m = 100MPa$, $E_c = 200MPa$, $E_p = 100GPa$, $f_p = 0.3$, $f_c = 0.3$ and $\sigma_{\max} = 10MPa$).

illustrated in Figure 3.20(b). Separation initiates at the particle-coating interface, followed by that at the coating-matrix interface. For all cases considered, the material displays softening behavior after both interfaces have separated.

3.6.3.5 Homogeneous coatings: Uniaxial tension with single separation along the particle-coating interface

In the following two subsections, we consider the case of a composite material with coated particle inclusions loaded in uniaxial tension. Under uniaxial tension, the debonding of the matrix from the particle is not uniform, but instead, goes through gradual stages of partial debonding, as observed experimentally and illustrated in Figure 3.14.

The first scenario we consider investigates progressive debonding at the particle-coating interface. The geometry and mesh of the model we use is illustrated in Figure 3.21. The particle has a volume fraction of 20%, with a diameter of $1mm$, and a coating thickness of $0.1mm$. The elastic modulus of the matrix is $80MPa$ and the elastic modulus of the particle is $400MPa$. Cohesive elements are inserted between the particle and the coating, and have a cohesive fracture energy of $1.0N/m$, a cohesive strength of $15MPa$, a softening shape parameter of 3, and an initial slope indicator of 0.005. The geometry is discretized with approximately 100,000 linear tetrahedral elements, and 3,765 cohesive elements are used to capture interfacial debonding at the particle-coating interface. Rollers are placed on the faces corresponding to the planes of symmetry, and the lateral extension is displacement controlled, as illustrated in Figure 3.21(a).

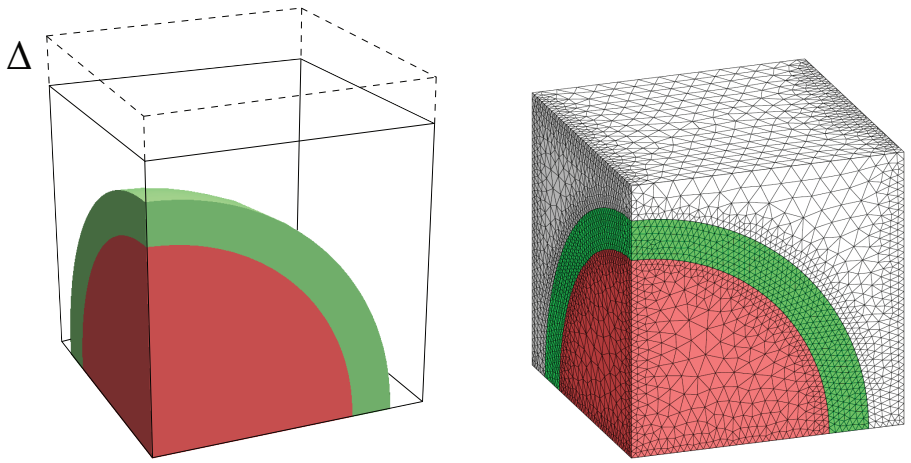

Figure 3.21: The single particle model used to investigate the uniaxial tensile loading of a composite material with coated particle inclusions: (a) geometry and (b) mesh.

The results of the analysis are illustrated in Figure 3.22(a). When the coating is introduced, the elastic stiffness and elastic limit increase slightly. However, the most significant influence of the coating is in the post-peak response of the composite. Without the coating, the composite displays a small region of softening prior to an extended region of hardening. When a coating is present, hardening behavior is observed past the elastic limit. In comparison to the hydrostatic loading cases considered throughout the rest of this example, the global strain at the elastic limit is 2 to 3 times greater. As well, the transition between the elastic range and the debonded range is more gradual in the case of uniaxial tension, because debonding occurs gradually; initiating at the pole of the particle and propagating down to the equator, as illustrated in Figure 3.23.

3.6.3.6 Homogeneous coatings: Uniaxial tension with concurrent separation at the particle-coating and coating-matrix interfaces

The last scenario we consider permits concurrent separation at both the particle-coating and coating-matrix interfaces. The same mesh as that used in the previous scenario is used, with an additional 5,812 cohesive elements inserted to capture debonding at the coating-matrix interface. Each cohesive element has a fracture energy of $1.0N/m$, a softening shape parameter of 3, and an initial slope indicator of 0.005. The cohesive strength is $8MPa$ and $12MPa$ at the particle-coating and coating-matrix interfaces, respectively. The results of the analysis are illustrated in Figure 3.22(b). As with the single separation case, when the coating is introduced, the elastic stiffness and elastic limit increase slightly, however,

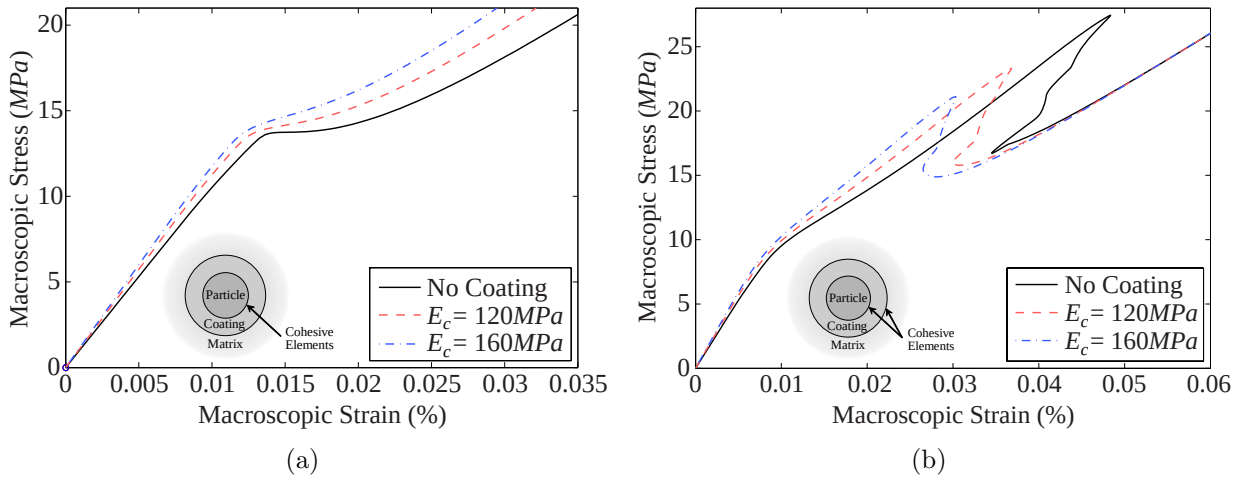

Figure 3.22: Constitutive response of a composite, loaded in uniaxial tension, containing homogeneously coated particles, with separation along (a) the particle-coating interface; and (b) both the particle-coating and coating-matrix interfaces. The following properties are considered: $E_m = 80MPa$, $E_p = 400MPa$, $f_p = 0.2$, $t_c = 0.1mm$, and $\phi_n = 1.0N/m$. For separation only at the particle-coating interface, $\sigma_i = 15MPa$, whereas, when concurrent separation is permitted at both interfaces $\sigma_i = 8MPa$ and $\sigma_o = 12MPa$.

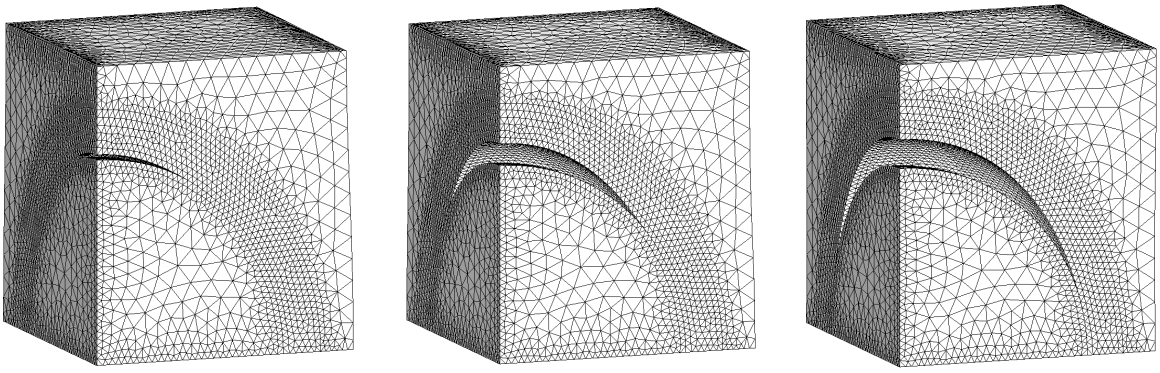

Figure 3.23: Progression of debonding of a coated particle under uniaxial tension. For illustrative purposes, the displacements are scaled by a factor of 10.

there are now two distinct kinks in the stress-strain response of the material. Separation initiates at the particle-coating interface, at a macroscopic stress of approximately 10MPa. Beyond this point, the stiffness of the material decreases with decreasing coating modulus. The second distinct kink in the stress strain response represents the initiation of separation at the coating-matrix interface. After the coating-matrix interface separates, the material displays snap-back behavior in all cases. At large macroscopic strains, complete separation occurs and the load is carried entirely by the matrix shell. The progression of debonding is illustrated in Figure 3.24.

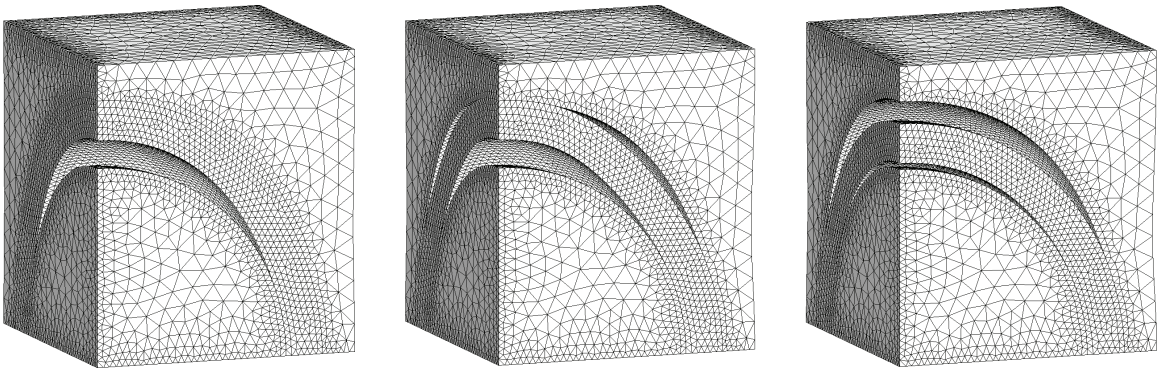

Figure 3.24: Progression of debonding of a coated particle under uniaxial tension when separation is permitted at both the particle-coating and coating-matrix interfaces. For illustrative purposes, the displacements are scaled by a factor of 10.

3.7 Concluding remarks

This chapter outlines the formulation and implementation of three-dimensional, intrinsic cohesive zone elements for use in Abaqus. In total, three different cohesive elements are implemented; which are compatible with linear brick, linear tetrahedral and quadratic tetrahedral bulk elements. The constitutive model for the cohesive elements is selected independently of that for the bulk elements. The selected constitutive model for the cohesive elements is the intrinsic PPR model. A linear unloading/reloading relation and a penalty stiffness approach to contact are chosen. The modulus of the penalty stiffness is set equal to the initial hardening slope at the initiation of the intrinsic formulation.

In addition to the base implementation, a series of suggested modifications is presented. These modifications highlight the sections of the code which require changing if the user chooses to implement alternate unloading/reloading and contact conditions. As well, the modifications necessary to implement functionally graded cohesive properties are presented. To verify the implementation and present the varied possible applications, three numerical examples are provided: the patch test, the mixed-mode bending test problem, and the small deformation debonding of composite materials containing coated particle inclusions.

For the small deformation coated particle debonding example, we take an extended look at the change in the macroscopic constitutive response of these composite materials due to changes in the microstructure. The effects due to a variation in the volume fraction of particles, coating thickness, constitutive properties, and location of separation are investigated. In general, the hydrostatic debonding behavior, captured numerically, agrees well with that predicted theoretically. Depending on the material properties, when multiple interfaces are permitted to separate, the particle-coating interface tends to separate first, followed by the coating-matrix interface, resulting in two distinct kinks in the constitutive response. Overall,

the results from the numerical investigation provide insight into the progressive debonding process of composite materials with coated particles. Throughout each of the examples, we demonstrate that this small library of cohesive elements is useful in a variety of applications, however, we hope that the library could be extended in the future, for compatibility with other types of bulk elements, such as shell and membrane elements.

This chapter constitutes the second step in our objective of developing a computational framework capable of capturing the finite deformation debonding behavior of particle reinforced composites. In Chapter 2 we developed a framework capable of capturing the influence of interphases, and now we have the tools capable of capturing the interfacial debonding behavior. In Chapter 4, we will combine these tools to reach our objective.

Chapter 4

Finite Deformation Response of Particle Reinforced Composites Considering both Interphasial and Interfacial Effects

There are four primary factors which influence the macroscopic constitutive response of particle reinforced composites: component properties, component concentrations, interphases, and interfacial debonding. Interphases are often a byproduct of surface treatments applied to the particles to control agglomeration. Alternatively, in polymer based materials such as carbon-black reinforced rubber, an interphase or "bound rubber" phase often occurs at the particle-matrix interface. This interphasial region has been known to exist for many decades, but is often omitted in computational investigations of such composites. In this chapter, we present an investigation into the influence of interphases on the large deformation response of particle reinforced composites. In addition, since particles tend to debond from the matrix at large deformations, we investigate the influence of interfacial debonding on the macroscopic constitutive response. The investigation considers two different microstructures; both a simplified single particle model, and a more complex polydisperse representative unit cell. Cohesive elements, which follow the Park-Paulino-Roesler traction-separation relation, are inserted between each particle and its corresponding interphase to account for debonding. To account for friction, we present a new, coupled cohesive-friction model and detail its formulation and implementation. For each microstructure, we discuss the influence of the interphase thickness and stiffness on the global constitutive response in both uniaxial tension and simple shear. To validate the computational framework, comparisons are made with experimental results available in the literature.

4.1 Introduction

The macroscopic response of particle reinforced composites is influenced by not only the component properties and component concentrations, but also the interfacial interaction between the particles and the matrix. In particular, the inclusion of stiff particles to a soft matrix can lead to an increase in composite stiffness, strength, impact resistance, and abrasion resistance [59, 156]. Additionally, at large deformations particles tend to debond

from the matrix, influencing both the ductility and fracture toughness of the composite [157, 158, 159]. To enhance or control these properties, the particles themselves can be tailored through surface treatments [62, 160, 61]. Often, surface treatments are applied to the particles of a composite material to meet various desired specifications. For instance, these treatments are often employed to reduce residual tensile stresses between the particles and the matrix or to reduce particle agglomeration [160, 161]. On the other hand, as a result of chemical interactions, an interphase may form between the particle and the matrix during manufacturing and processing [162]. Even though these interphases are typically microscopic, they can greatly influence the macroscopic behavior of composite materials. The extent and composition of this interphase depends on a number of factors, including the surface area and surface treatment of the particles, as well as the level of mixing and age of the composite [59, 60].

Recent experiments by Qu et al. [84, 163], used atomic force microscopy to conduct in-situ imaging of particle-elastomer interactions. They demonstrated that the macroscopic properties (in particular, the stiffness and scratch resistance) of the composite can be tailored, by selectively designing the surface chemistry of the particles. Ramier et al. [62, 61] investigated the influence of different surface treatments on the large deformation response of silica particle reinforced styrene butadiene rubber. They conducted a series of experiments on consistently prepared specimens, but applied a different surface treatment to the particles in each sample. Their investigation focused on the influence of the cross-linking that occurs in the matrix as a result of the different surface treatments, and concluded that the applied surface treatment on the particles is often the primary factor controlling the macroscopic constitutive response of the composite. Moreover, at large deformations, they observed the particles debonding from the matrix. Debonding is characterized by a localized region of failure (or interfacial debonding) that accumulates around the particle inclusions. There have been numerous experimental investigations demonstrating the interfacial debonding behavior of particles under large deformations; some examples of which are illustrated in Figure 4.1.

In contrast to the numerous experimental investigations, there have been few theoretical investigations which consider the effect of either interphases or interfacial debonding in the finite deformation regime. One of the few formulations for debonding under finite strains was presented by Brassart et al. [72]. They extend the Mori-Tanaka homogenization scheme [166] to account for the debonding of composite materials under finite strains; however, they only consider hydrostatic loading in three-dimensions and do not account for the presence of interphases. More Recently, Goudarzi et al. [75] presented a theoretical framework capable of describing the influence of interphases on the macroscopic constitutive response of particle

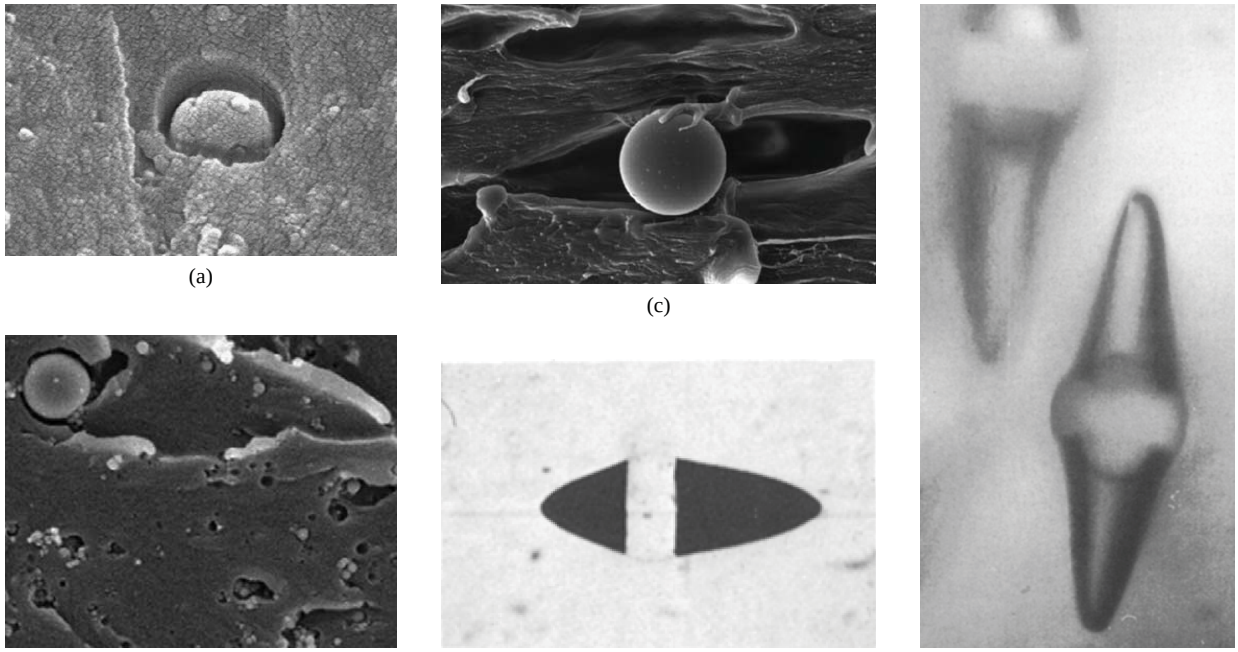

Figure 4.1: Experimentally observed debonding behavior of particle reinforced composites under large deformations. (a) Debonding of aluminum oxide particles from an epoxy resin (extracted from Wetzel et al. [164]). (b) Multiple locations of silane treated alumina particles debonding from an epoxy matrix (mse.rpi.edu). (c) A glass particle surrounded by the void created due to deformation of the polypropylene/glass composite (extracted from Thio et al. [66]). The glass particles in this investigation were treated using heptadecafluorodecyl trichlorosilane. (d) Glass beads, treated with ethylsilane, debonding from natural rubber (extracted from Gent and Park [165]). (e) Large void creation around glass particles in a high-density polyethylene matrix (extracted from Zhuk et al. [64]).

reinforced elastomers. They compare their formulation to both numerical and experimental results [62], and found excellent correlation with both. However, their investigation focuses on the influence of perfectly bonded interphases, excluding the consideration of interfacial debonding. To the best of the author's knowledge, there has been no theoretical formulation presented which accounts for both interphases and interfacial debonding under finite deformations.

There are four primary factors which influence the macroscopic constitutive response of particle reinforced composites: component properties, component concentrations, interphases, and interfacial debonding. This chapter presents a computational framework capable of capturing the influence of interphases and interfacial debonding on the finite deformation response of particle reinforced composites. The influence of the thickness and modulus of the interphase is considered, and debonding is accounted for through the use of cohesive elements. The remainder of the chapter is organized as follows. In Section 4.2, we discuss the computational framework for this investigation. Section 4.3 presents a new, coupled

cohesive-friction relation and details its formulation and implementation. Both single particle and multi-particle periodic microstructures are considered in this investigation. The results for the single particle microstructure are presented in Section 4.4.1, and those for the multi-particle microstructure are presented in Section 4.4.2. We validate the computational framework by challenging it with experimental data in Section 4.5. Finally, some conclusions, and potential extensions are discussed in Section 4.6.

4.2 Computational framework

In this investigation, we develop a fully three-dimensional computational framework capable of capturing the influence of interphases and interfacial debonding on the finite deformation response of particle reinforced composites. We consider both a single particle microstructure, and a multi-particle microstructure; and, for the most generality, in the multi-particle microstructure we consider a random distribution of polydisperse particles. The single particle microstructure is presented to illustrate the local behavior during progressive debonding. While this model is simplified, it can provide insight into the important characteristics, and provide guidance into tailoring the design of particle-reinforced composite materials. The multi-particle microstructure, however, is more representative of a real material.

4.2.1 Single particle microstructure

The single particle model replicates the case of a perfectly repeating, structured microstructure. The model considers a single particle placed at the centroid of a cube. The particle is assumed to be numerically rigid [89], and we assume that a compliant interphase forms around the surface of the particle. The particle is assumed to be spherical, and the interphase thickness is assumed to be uniform, as illustrated in Figure 4.2(a). The geometry is discretized with quadratic tetrahedral elements using the automatic mesh generator Netgen [114]. A sample mesh for the particle and interphase is illustrated in Figure 4.2(b).

4.2.2 Multi-particle microstructure

In the multi-particle model, we consider a random distribution of particles. These models, often referred to as representative unit cells (RUCs), are commonly used to represent realistic microstructures [104, 105]. For the most generality, we consider the particles to be polydisperse, represented through three families of particle sizes [89]. The particle locations

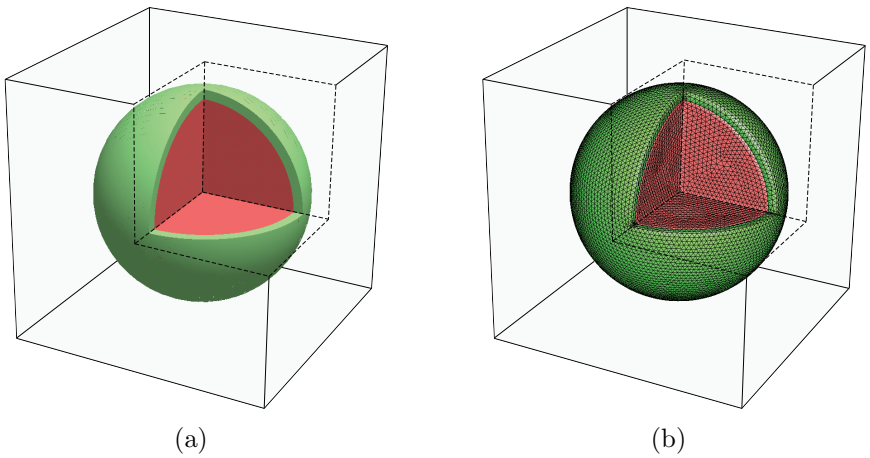

(a) (b)

Figure 4.2: The single particle model: (a) geometry and (b) sample mesh used for the particle and interphase. Note that the mesh for the bulk matrix is excluded from the figure for illustrative purposes only. Additionally, an octant of the geometry is removed to illustrate the particle and interphase.

are generated using a constrained adsorption algorithm [86, 89, 75]. The procedure we use to generate the polydisperse microstructures was described in detail in Chapter 2, and the interested reader is referred there for further details. In this investigation, we consider two different particle concentrations, $c = 0.1$ and $c = 0.2$, as illustrated in Figures 4.3 and 4.4, respectively.

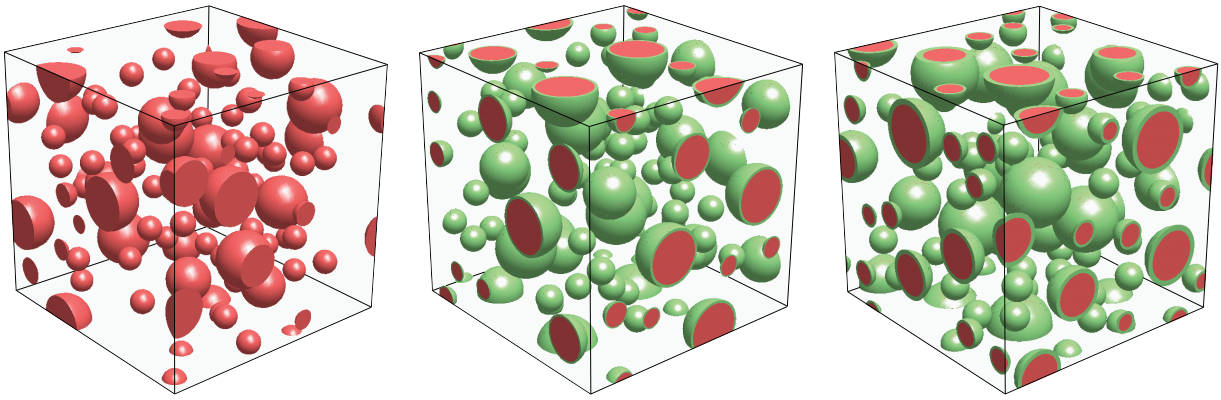

(a) (b) (c)

Figure 4.3: Representative polydisperse microstructures, containing a random distribution of 80 particles of three different radii. The particles constitute a concentration of $c = 0.1$ and are surrounded by (a) no interphase, (b) interphases with a thickness of $t = 0.1r_p^{(i)}$, and (c) interphases with a thickness of $t = 0.2r_p^{(i)}$.

A mesh refinement study was conducted using randomly generated meshes with approximately 100,000, 200,000 and 300,000 quadratic tetrahedral elements, as illustrated in Figure 4.5. Meshes with approximately 200,000 elements displayed a sufficient level of accuracy, and is the target mesh size for the results presented in the remainder of the investigation.

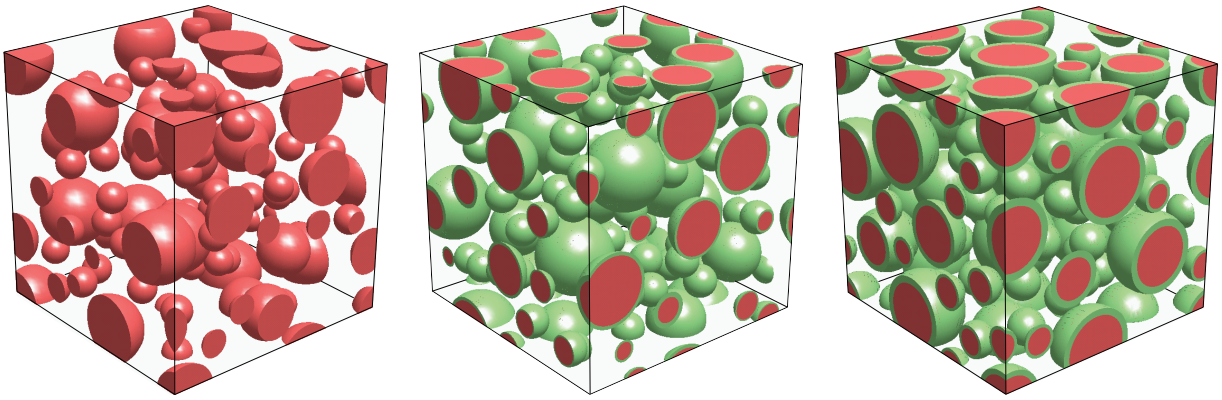

(a) (b) (c)

Figure 4.4: Representative polydisperse microstructures, containing a random distribution of 80 particles of three different radii. The particles constitute a concentration of $c = 0.2$ and are surrounded by (a) no interphase, (b) interphases with a thickness of $t = 0.1r_p^{(i)}$, and (c) interphases with a thickness of $t = 0.2r_p^{(i)}$.

Periodicity of the models is ensured through the use of both a periodic microstructure and periodic boundary conditions, as was detailed in Chapter 2.

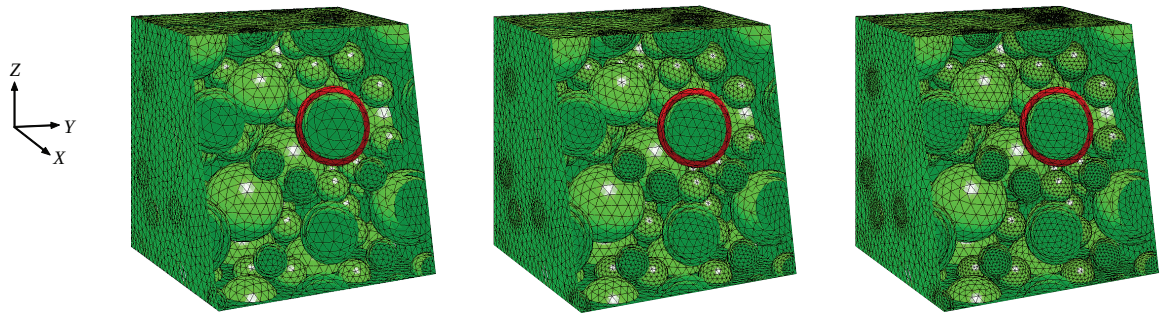

(a) (b) (c)

Figure 4.5: Three representative meshes in the undeformed configuration for a distribution of polydisperse particles with a concentration of $c = 0.2$, and an interphase thickness of $t = 0.2r_p^{(i)}$: (a) a coarse mesh with approximately 100,000 elements, (b) a fine mesh with approximately 200,000 elements, and (c) a very fine mesh with approximately 300,000 elements.

4.2.3 Assessment of isotropy

In all models containing a finite number of randomly placed particles, the isotropy of the microstructure is only approximate [89]. There are multiple approaches for determining whether the random placement of particles results in an approximately isotropic microstructure. Many authors take a geometric approach, computing the centroid or moment of inertia of the particles [86, 115, 111]. Alternatively, one could take a constitutive approach, by exam-

ining the co-axiality between the stress and strain tensors [89, 75]. In an isotropic material, the average Cauchy stress tensor, $\overline{\boldsymbol{\sigma}} = \overline{\mathbf{S}}\overline{\mathbf{F}}^{\mathrm{T}}$ and average left Green-Cauchy strain tensor $\overline{\mathbf{B}} = \overline{\mathbf{F}}\overline{\mathbf{F}}^{\mathrm{T}}$ are co-axial, and the angle between their principal axes (the angle of co-axiality) is zero. Since the constitutive approach is sufficient, it is the method we choose to assess the isotropy of our microstructures. Each microstructure is tested, and those which result in an angle of co-axiality greater than 0.05 radians are discarded [89, 75]. We use this approach for all loading conditions, particle concentrations and interphase thicknesses considered in this investigation.

4.3 Coupled cohesive-friction relation

To account for interfacial debonding, cohesive elements are inserted between each particle and its surrounding interphase, as illustrated in Figure 4.6. The cohesive elements initially have zero thickness, and, as the elements separate, they transfer normal and shear tractions to the surrounding bulk elements. There have been numerous traction-separation relations proposed in the literature, see for example the relations proposed by Xu and Needleman [50] and Ortiz and Pandolfi [56]. The traction-separation relation used in this investigation follows the Park-Paulino-Roesler (PPR) cohesive model [51]. The details of the PPR model were provided in the previous chapter. Here, we present a new three-dimensional frictional relation which is compatible with, and coupled to, the PPR formulation.

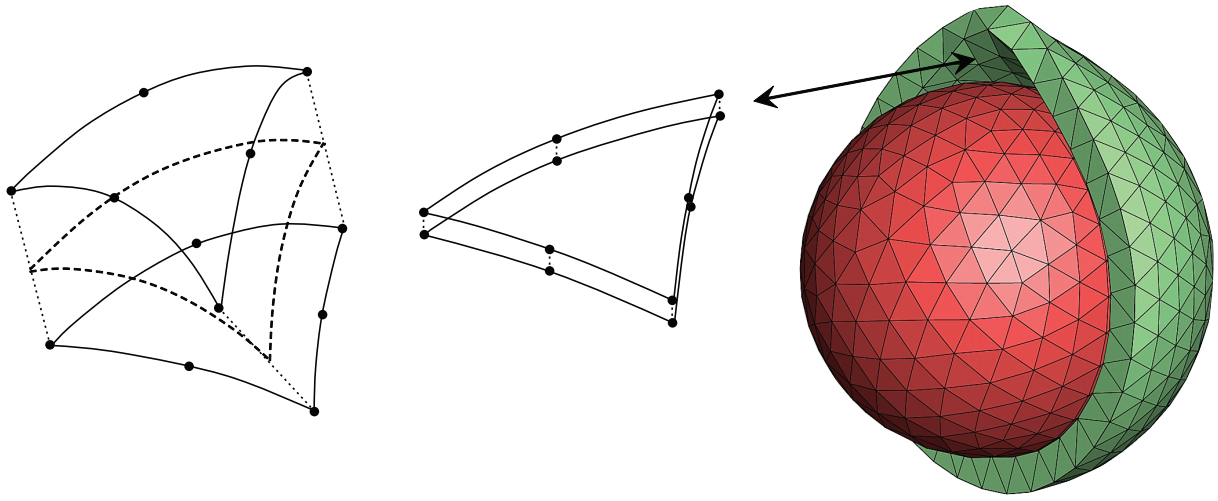

Figure 4.6: Cohesive elements with zero initial thickness are inserted between each particle and its corresponding interphase.

When a particle is in contact with its surrounding interphase, compressive and frictional forces (T_f) are generated. Since the potential-based cohesive formulation does not explicitly

account for a contact relation, we have chosen to use a simplified penalty approach to contact. As an element is distorted into an adjacent element the resisting force increases linearly in accordance with a corresponding stiffness. The modulus of this stiffness is chosen to correspond to a multiple of the slope of the cohesive hardening curve as it approaches zero opening displacement. Alternatively, other contact formulations could be used, such as the ones found in references [140, 167].

There have been multiple techniques proposed for coupling a friction relation to a cohesive model. One of the first approaches can be attributed to Tvergaard [168]. In this approach, the onset of friction is assumed to occur only after the cohesive model has completely softened. Later authors revised this assumption, setting the onset of friction to occur at the onset of irreversible damage [167, 169, 170, 171]. The main feature of this revised approach is that no frictional energy is dissipated prior to the onset of decohesion. Here, we outline a new mixed-mode frictional relation that, when coupled with the PPR cohesive model, presents a smooth transition from a cohesive zone to a pure frictional contact zone. In particular, the coupled frictional force is computed as:

$$T_f = \mu_f \kappa\left(\Delta_t\right) \left|T_n\right| \qquad \text{when} \;\; T_n < 0 \;\; \text{and} \;\; \Delta_t > \lambda_t \delta_t, \tag{4.1}$$

where μ_f is the coefficient of friction, and $\kappa\left(\Delta_t\right)$ may be thought of as a damage-type parameter, varying monotonically between 0 and 1 (when $\Delta_t > \lambda_t \delta_t$). The relation chosen for κ is expressed as:

$$\kappa\left(\Delta_t\right) = \left\{ \begin{array}{ll} 0 & \text{if } \Delta_t \leq \lambda_t \delta_t \\ \left(1 - \frac{T_t(0,\Delta_t)}{D_0 \Delta_t}\right)^s & \text{if } \Delta_t > \lambda_t \delta_t \end{array} \right\}, \tag{4.2}$$

where s is an input parameter which controls the rate of transition between cohesive and frictional forces. The influence of s on κ is illustrated in Figure 4.7(a). Moreover, $T_t\left(0, \Delta_t\right)$ is the tangential cohesive traction computed at zero normal opening displacement, and D_0 is the stiffness at the onset of decohesion (see Figure 4.7(b)) calculated as:

$$D_0 = \frac{\Gamma_t}{\delta_t} \left[n \left(1 - \lambda_t\right)^\beta \left(\frac{n}{\beta} + \lambda_t\right)^{n-1} - \beta \left(1 - \lambda_t\right)^{\beta - 1} \left(\frac{n}{\beta} + \lambda_t\right)^n \right] \times \left[\Gamma_n \left(\frac{m}{\alpha}\right)^m + \left\langle \phi_n - \phi_t \right\rangle \right] \frac{1}{\lambda_t \delta_t}, \tag{4.3}$$

where the input parameters Γ_t, Γ_n, δ_t, δ_n, n, m, α, β, and λ_t are the same as those in the PPR cohesive model.

The frictional force vector is coupled to the cohesive force vector through the following relation:

$$\mathbf{T} = \left\{ \begin{array}{c} T_n \\ T_t \frac{\Delta_2}{\Delta_t} + T_f \left(\frac{|\Delta_2|}{\Delta_t} \right) \frac{\dot{\Delta}_2}{|\dot{\Delta}_2|} \\ T_t \frac{\Delta_3}{\Delta_t} + T_f \left(\frac{|\Delta_3|}{\Delta_t} \right) \frac{\dot{\Delta}_3}{|\dot{\Delta}_3|} \end{array} \right\}, \tag{4.4}$$

where Δ_2 and Δ_3 correspond to crack opening widths in the tangential plane of fracture, and the $(\dot{})$ operator represents the change in the crack opening width. The tangential crack opening width, Δ_t, is coupled through the relation $\Delta_t = \sqrt{\Delta_2^2 + \Delta_3^2}$. A sample cohesive-friction relation is plotted versus the coupled tangential crack opening width in Figure 4.7(b). From the figure it is clear that frictional forces initiate at the onset of cohesive softening (irreversible damage), and that the transition from softening behavior to frictional behavior is monotonic and smooth. To illustrate the fully coupled, three-dimensional friction relation, the tangential components of the force vector (Equation 4.4) are decoupled then superimposed in Figure 4.8.

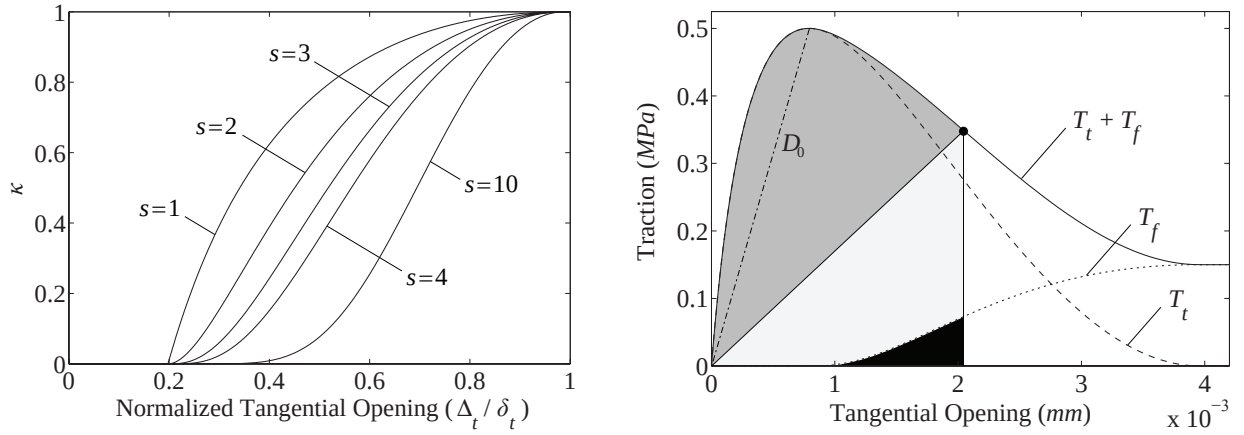

Figure 4.7: (a) Influence of the value of s on the damage variable, $\kappa(\Delta_t)$, as per Equation 4.2. (b) Tangential traction, including friction ($\Delta_n < 0$, $\lambda_t = 0.2$, and $s = 3$). The various energies at a given state are depicted: dark gray is the energy dissipated during the process of decohesion, light gray is the stored elastic energy, and black is the energy dissipated by friction.

The hysteretic response of the coupled cohesive-friction relation is illustrated in Figure 4.9. Initially, the loading follows the cohesive relation; however, beyond the peak stress, frictional forces are generated and energy dissipation due to friction accumulates. As unloading occurs, the direction dependent frictional force generates a jump in the traction. When the cohesive element has fully separated (i.e the cohesive force goes to zero), only frictional forces are generated.

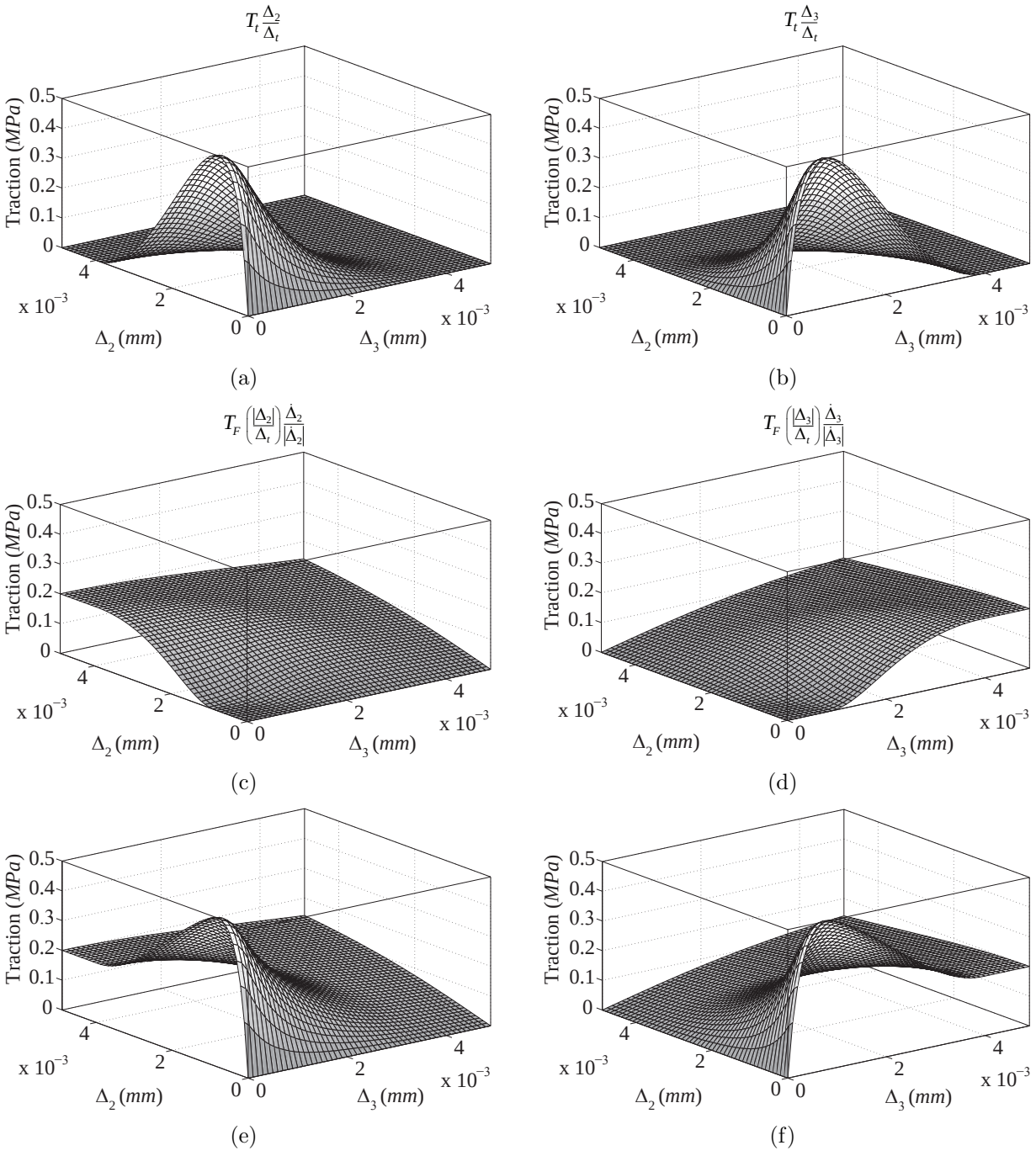

Figure 4.8: Visual decomposition of the three-dimensional, coupled cohesive-friction model: (a) cohesive traction in the Δ_2 direction; (b) cohesive traction in the Δ_3 direction; (c) friction traction in the Δ_2 direction; (d) friction traction in the Δ_3 direction; (e) coupled cohesive-friction traction in the Δ_2 direction; and (f) coupled cohesive-friction traction in the Δ_3 direction. The cohesive and friction parameters are: $\alpha = \beta = 3$, $\lambda_n = \lambda_t = 0.2$, $\phi_n = \phi_t = 1.0N/m$, $\sigma_{\max} = \tau_{\max} = 0.5MPa$, $s = 3$, $\mu = 0.5$, and $T_n = -0.4MPa$; and it is assumed that $\dot{\Delta}_2$ and $\dot{\Delta}_3 > 0$.

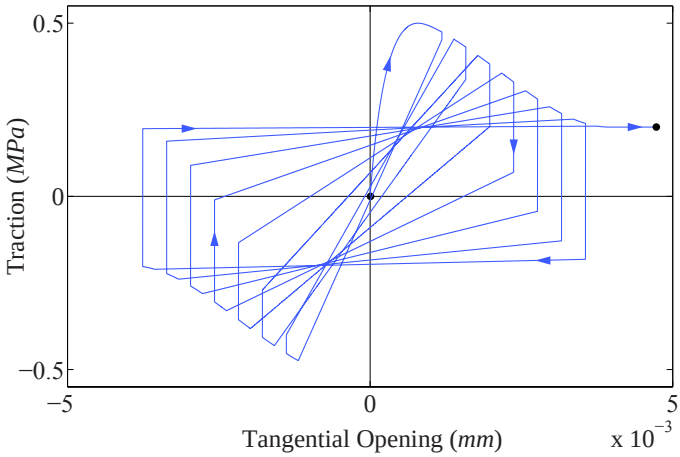

Figure 4.9: Tangential traction versus tangential opening during cyclic loading ($\Delta_n < 0$, $s = 3$ and $\mu = 0.5$).

Finally, to incorporate the coupled cohesive and friction relations, many finite element codes require the implementation of a material tangent stiffness matrix, $\mathbf{D}$:

$$\mathbf{D} = \begin{bmatrix} D_{11} & D_{12} & D_{13} \\ D_{21} & D_{22} & D_{23} \\ D_{31} & D_{32} & D_{33} \end{bmatrix}, \tag{4.5}$$

where the components of the stiffness matrix depend on the constitutive relation. Here, we list the components for any general coupled cohesive and any friction model:

$$D_{11} = \frac{\partial T_n}{\partial \Delta_n}, \qquad D_{12} = \frac{\partial T_n}{\partial \Delta_t}\frac{\Delta_2}{\Delta_t}, \qquad D_{13} = \frac{\partial T_n}{\partial \Delta_t}\frac{\Delta_3}{\Delta_t},$$

$$D_{21} = \frac{\partial T_t}{\partial \Delta_n}\frac{\Delta_2}{\Delta_t} + \frac{\partial T_f}{\partial \Delta_n}\frac{|\Delta_2|}{\Delta_t}\frac{\dot{\Delta}_2}{\left|\dot{\Delta}_2\right|},$$

$$D_{22} = \left(\frac{\partial T_t}{\partial \Delta_t}\Delta_2 + \frac{\partial T_f}{\partial \Delta_t}|\Delta_2|\frac{\dot{\Delta}_2}{\left|\dot{\Delta}_2\right|}\right)\frac{\Delta_2}{\Delta_t^2} + \left(T_t + T_f\frac{\Delta_2}{|\Delta_2|}\frac{\dot{\Delta}_2}{\left|\dot{\Delta}_2\right|}\right)\frac{\Delta_3^2}{\Delta_t^3},$$

$$D_{23} = \left(\frac{\partial T_t}{\partial \Delta_t}\Delta_2 + \frac{\partial T_f}{\partial \Delta_t}|\Delta_2|\frac{\dot{\Delta}_2}{\left|\dot{\Delta}_2\right|}\right)\frac{\Delta_3}{\Delta_t^2} - \left(T_t\Delta_2 + T_f|\Delta_2|\frac{\dot{\Delta}_2}{\left|\dot{\Delta}_2\right|}\right)\frac{\Delta_3}{\Delta_t^3},$$

$$D_{31} = \frac{\partial T_t}{\partial \Delta_n}\frac{\Delta_3}{\Delta_t} + \frac{\partial T_f}{\partial \Delta_n}\frac{|\Delta_3|}{\Delta_t}\frac{\dot{\Delta}_3}{\left|\dot{\Delta}_3\right|},$$

$$D_{32} = \left(\frac{\partial T_t}{\partial \Delta_t} \Delta_3 + \frac{\partial T_f}{\partial \Delta_t} |\Delta_3| \frac{\dot{\Delta}_3}{\left|\dot{\Delta}_3\right|} \right) \frac{\Delta_2}{\Delta_t^2} - \left(T_t \Delta_3 + T_f |\Delta_3| \frac{\dot{\Delta}_3}{\left|\dot{\Delta}_3\right|} \right) \frac{\Delta_2}{\Delta_t^3},$$

$$D_{33} = \left(\frac{\partial T_t}{\partial \Delta_t} \Delta_3 + \frac{\partial T_f}{\partial \Delta_t} |\Delta_3| \frac{\dot{\Delta}_3}{\left|\dot{\Delta}_3\right|} \right) \frac{\Delta_3}{\Delta_t^2} + \left(T_t + T_f \frac{\Delta_3}{|\Delta_3|} \frac{\dot{\Delta}_3}{\left|\dot{\Delta}_3\right|} \right) \frac{\Delta_2^2}{\Delta_t^3}.$$

For the specific friction model presented in this section:

$$\frac{\partial T_f}{\partial \Delta_n} = \left(1 - \frac{T_t\left(0, \Delta_t\right)}{D_0 \Delta_t} \right)^s \mu \frac{T_n}{|T_n|} \frac{\partial T_n}{\partial \Delta_n}, \quad \text{and}$$

$$\frac{\partial T_f}{\partial \Delta_t} = s \left(1 - \frac{T_t\left(0, \Delta_t\right)}{D_0 \Delta_t} \right)^{s-1} \mu |T_n| \left(\frac{T_t\left(0, \Delta_t\right)}{D_0 \Delta_t^2} - \frac{\partial T_t\left(0, \Delta_t\right)}{\partial \Delta_t} \frac{1}{D_0 \Delta_t} \right).$$

The partial derivatives ($\frac{\partial T_n}{\partial \Delta_n}$, $\frac{\partial T_n}{\partial \Delta_t}$, $\frac{\partial T_t}{\partial \Delta_n}$, and $\frac{\partial T_t}{\partial \Delta_t}$) for the PPR cohesive model were listed in Chapter 3.

4.4 Results and discussion

We now apply the above computational framework to several examples with various microstructural configurations. First, we investigate the single particle model, then present results for full field simulations on representative unit cells. In each configuration, we examine the influence of interphase thickness and stiffness on the macroscopic constitutive response in both uniaxial and shear loading. There are various stored-energy functions available for representing the behavior of hyperelastic materials [143], however the most commonly applied may be the neo-Hookean model. In this section, the matrix material is assumed to be an incompressible neo-Hookean rubber, with stored-energy function:

$$\Psi\left(I_1\right) = \frac{\mu}{2}\left[I_1 - 3\right], \tag{4.6}$$

where μ is the initial shear modulus, $I_1 = \mathbf{F} \cdot \mathbf{F}$ is the first principal invariant of the right Cauchy-Green tensor, and $\mathbf{F}$ is the deformation gradient. The matrix is assumed to have an initial shear modulus, μ_m, of $1.0MPa$, and the interphase surrounding each particle is assumed to have a modulus, μ_i, which is a multiple of that in the bulk. The particles are assumed to have a modulus that is four orders of magnitude greater than that in the matrix ($\mu_p = 10^4 \mu_m$), to numerically approximate the case of rigid particle inclusions [172, 111]. In each case, the cohesive parameters are set as $\sigma_{\max} = 0.5MPa$, $\phi = 1.0N/m$, $\alpha = 3$,

and $\lambda = 0.2$. For contact between the interphases and the rigid particles, the coefficient of friction is set at $\mu_f = 1.0$ and the rate of transition between cohesive and friction forces is set at $s = 3$, in Equation 4.2. The macroscopic strain is defined as $\epsilon = h/H - 1$, where h is the deformed length in the direction of loading, and H is the undeformed length of the edge of the cell. The macroscopic stress corresponds to the first Piola-Kirchoff stress, measured as the force calculated in the deformed configuration applied over the undeformed surface of the model.

4.4.1 Single particle results

First, we consider the single particle model, and investigate the influence of the interphase thickness and stiffness on the macroscopic constitutive response in both uniaxial tension and simple shear. We consider the case of microparticle inclusions, with an assumed particle diameter of $10\mu m$, and size the model based on the particle diameter and volume fraction. Thus, the cell dimensions for a particle concentration of $c = 0.1$ and $c = 0.2$ are $17.4 \times 17.4 \times 17.4\mu m$ and $13.8 \times 13.8 \times 13.8\mu m$, respectively. The objective of this investigation is to demonstrate the ability of the computational framework to capture the complex decohesion process along the particle-interphase interface.

4.4.1.1 Uniaxial tension

In uniaxial tension, progressive debonding occurs. Decohesion initiates at the poles of the particle, in the direction of loading, and propagates towards the equator. Upon decohesion, compressive regions are formed in the plane perpendicular to the axis of loading; due to the volume preserving nature of the matrix material. The void and compressive regions can be seen in the contour plots of principal stress, as illustrated in the deformed configuration in Figure 4.10. In the matrix, a band of stress is concentrated at the location of the particle. The stress distribution in the interphase is illustrated in Figure 4.10(b). The shape of the interphase coincides with the shape of the void. Contact between the interphase and the particle can be seen by the outward bulge in the deformed shape of the interphase. At the poles of the interphase, zero stress is observed, indicating a complete loss of load bearing capacity, or complete debonding of the particle. At the equator of the interphase, high contact stresses are distributed through a thick band in the interphase. The resulting stress distribution in the particle is illustrated in Figure 4.10(c). As expected, the stress in the particle is concentrated in the band that remains in contact with the interphase, and the particle carries zero stress in the fully debonded regions.

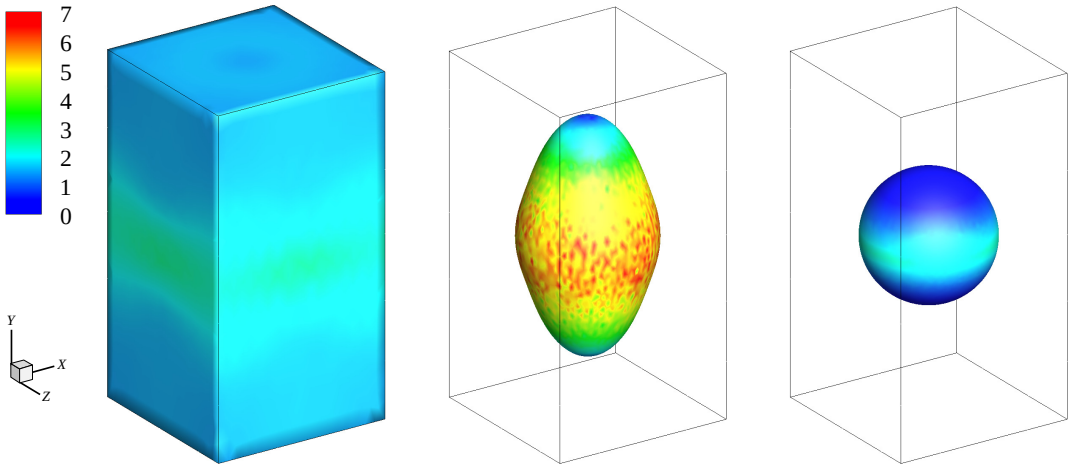

Figure 4.10: Contour plot of principal stress in uniaxial tension in the (a) matrix, (b) interphase, and (c) particle, for the single particle model.

The macroscopic constitutive response in uniaxial tension is plotted in Figure 4.11. We illustrate cases for particle concentrations of $c = 0.1$ and $c = 0.2$, and interphase thickness to particle radius ratios of $t/r_p = 0.1$ and $t/r_p = 0.2$. The thicker and stiffer the interphase, the greater the influence on the constitutive response. For the case with a small particle concentration ($c = 0.1$) and interphase thickness ($t/r_p = 0.1$), the influence is the smallest, but is still significant. For example, when we consider the case with an interphase stiffness of $\mu_i = 10\mu_m = 10MPa$ (a similar modulus to that observed experimentally [84]), at a strain of 0.4 the global response is approximately 25% greater than in the case when no interphase is considered, as illustrated in Figure 4.11(a). For the larger particle concentration, $c = 0.2$, the global response is approximately 115% greater than that without considering interphases, as illustrated in Figure 4.11(c).

4.4.1.2 Simple shear

The second loading condition we consider is simple shear. In this case, we observe a higher area of contact between the particle and the surrounding interphase in the deformed configuration. Thus, we expect the frictional forces in this scenario to be more significant; we will discuss and quantify this further in Section 4.4.2.1. The contour plots of principal stress for the matrix, interphase and particle are illustrated in Figure 4.12. In the direction perpendicular to the plane of shear, the stress in the interphase is lower than that in the plane of shear. Additionally, the void region is concentrated into a smaller zone than in the uniaxial tension case, as demonstrated by the deformed shape of the interphase in Figure 4.12(b).

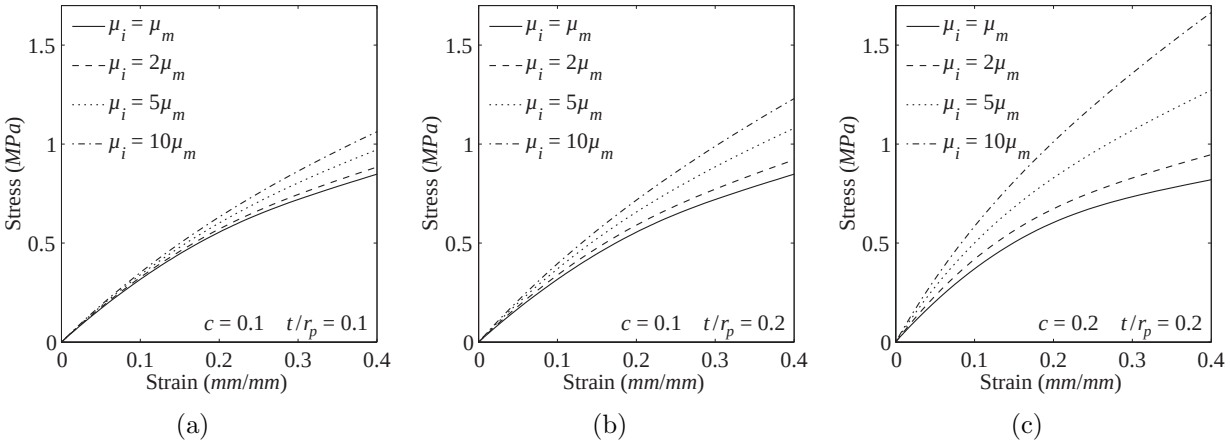

Figure 4.11: Macroscopic constitutive response in uniaxial tension for microstructures with: (a) $c = 0.1$ and $t/r_p = 0.1$; (b) $c = 0.1$ and $t/r_p = 0.2$; and (c) $c = 0.2$ and $t/r_p = 0.2$.

Because of the small void region, there remains a significant surface area of contact between the particle and the interphase, as demonstrated by the distribution of stress in the particle in Figure 4.12(c).

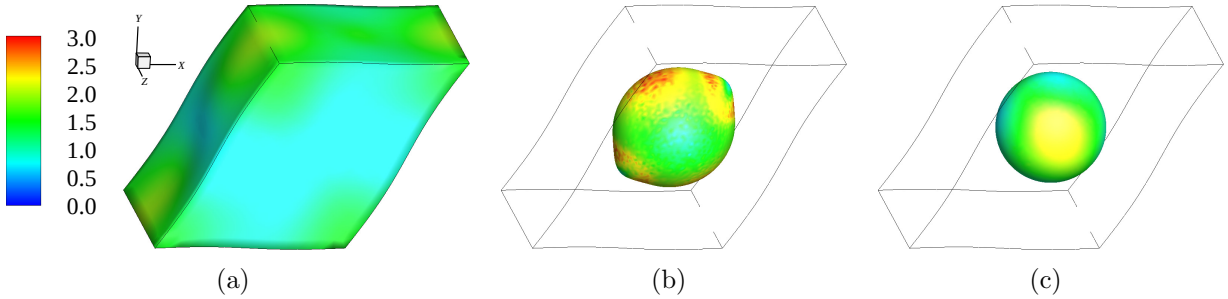

Figure 4.12: Contour plot of principal stress in simple shear in the (a) matrix, (b) interphase, and (c) particle, for the single particle model.

The macroscopic constitutive response in simple shear is illustrated in Figure 4.13. Similar to the case in uniaxial tension, we illustrate cases for particle concentrations of $c = 0.1$ and $c = 0.2$, and interphase thickness to particle radius ratios of $t/r_p = 0.1$ and $t/r_p = 0.2$. In simple shear, the influence of the interphase is noticeably less than in the case of uniaxial tension; however, the interphase continues to significantly alter the macroscopic constitutive response. For example, when we consider the case with a small particle concentration in Figure 4.13(a), and an interphase stiffness of $\mu_i = 10\mu_m$, at a strain of 0.4 the global response is approximately 18% greater than in the case when no interphase is considered. The influence of the interphase is magnified as the particle concentration, and thus the effective concentration of the interphase, increases, as illustrated in Figures 4.13(b) and 4.13(c).

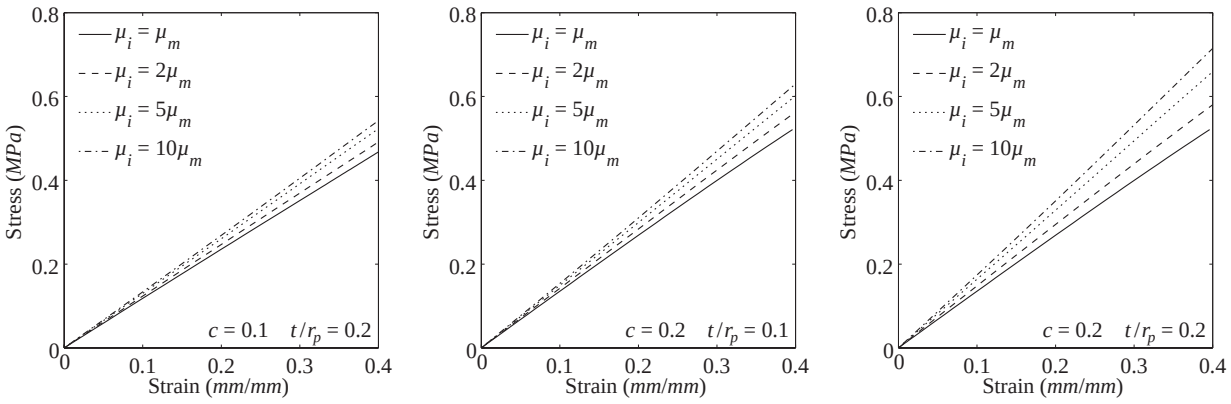

Figure 4.13: Macroscopic constitutive response in simple shear for microstructures with: (a) $c = 0.1$ and $t/r_p = 0.2$; (b) $c = 0.2$ and $t/r_p = 0.1$; and (c) $c = 0.2$ and $t/r_p = 0.2$.

4.4.2 Full representative unit cell results

Here we consider the case of more realistic microstructures, based on the full field simulations of polydisperse representative unit cells. The particle diameter is assumed to be $10\mu m$ for the largest family of particles, and the RUCs are sized based on the particle diameter and concentration. Thus, the cell dimensions for a particle concentration of $c = 0.1$ and $c = 0.2$ are $47.1 \times 47.1 \times 47.1\mu m$ and $37.4 \times 37.4 \times 37.4\mu m$, respectively. First, we investigate the influence of frictional forces on the constitutive response of various microstructures, then demonstrate the influence of the interphase thickness and modulus in both uniaxial tension and simple shear loading.

4.4.2.1 Influence of friction

To investigate the influence of frictional forces, we compare the full field results with and without friction, as illustrated in Figure 4.14. As in the case with a single particle, we consider both uniaxial tension and simple shear loading, with various particle concentrations, c, and interphase thickness to particle radius ratios, t/r_p. In the case of uniaxial tension, the frictional forces are shown to impart little effect on the macroscopic constitutive response of the composite, as illustrated in Figure 4.14(a). The inclusion of a frictional relation in the cohesive element formulation causes a slight increase in the effective stiffness of the composite, but, for the concentration and number of particles we have considered, it is negligible. It is valuable to note that the magnitude of frictional forces is dependent on the number of particles used to capture the respective concentration, thus, if a greater number of particles were used, the magnitude would increase. However, the underlying cause of

the low influence will not change, as will be discussed in the next section. In the case of simple shear, the frictional forces are shown to have a greater influence on the composite's constitutive response, as illustrated in Figure 4.14(b). This is expected behavior, since, in the previous investigation in the single particle model, we demonstrated that a large area of contact exists between the particle and the interphase in simple shear. This large area of contact generates large frictional forces.

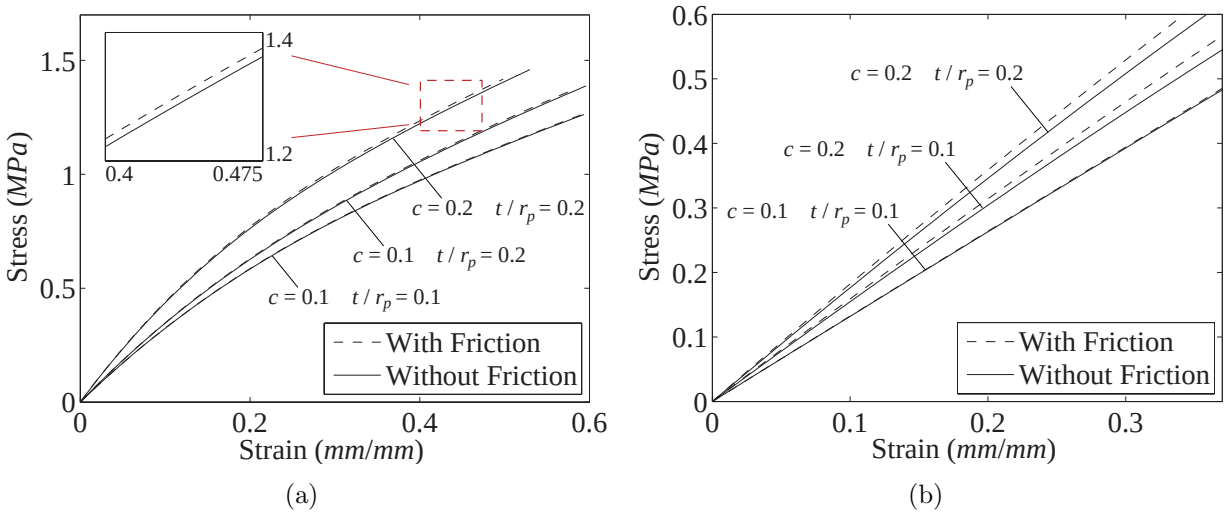

Figure 4.14: Influence of friction on the global constitutive response of RUCs in (a) uniaxial tension, and (b) simple shear.

We have demonstrated that the particle reinforced composite materials under investigation in this chapter demonstrate a small influence of friction, however, there are alternate applications wherein frictional forces are significant. In order to further verify and validate the newly proposed coupled cohesive-friction model presented in Section 4.3, we have included a supplementary example in C which demonstrates a significant dependence on friction.

4.4.2.2 Uniaxial tension

In uniaxial tension, a representative deformed microstructure is illustrated in Figure 4.15(a). Each particle debonds from the surrounding matrix, as seen both in the deformed shape and in the contour plots in Figures 4.15(b) and 4.15(c). Similar to the study on the single particle model, each particle is compressed by the surrounding matrix in a plane perpendicular to the direction of loading. The fully debonded regions alleviate the stress at the poles of the particles. The width of the small band of compression in the particles is indicative of the small area of contact wherein frictional forces can be generated, explaining the small influence of friction on the global response seen in Figure 4.14(a).

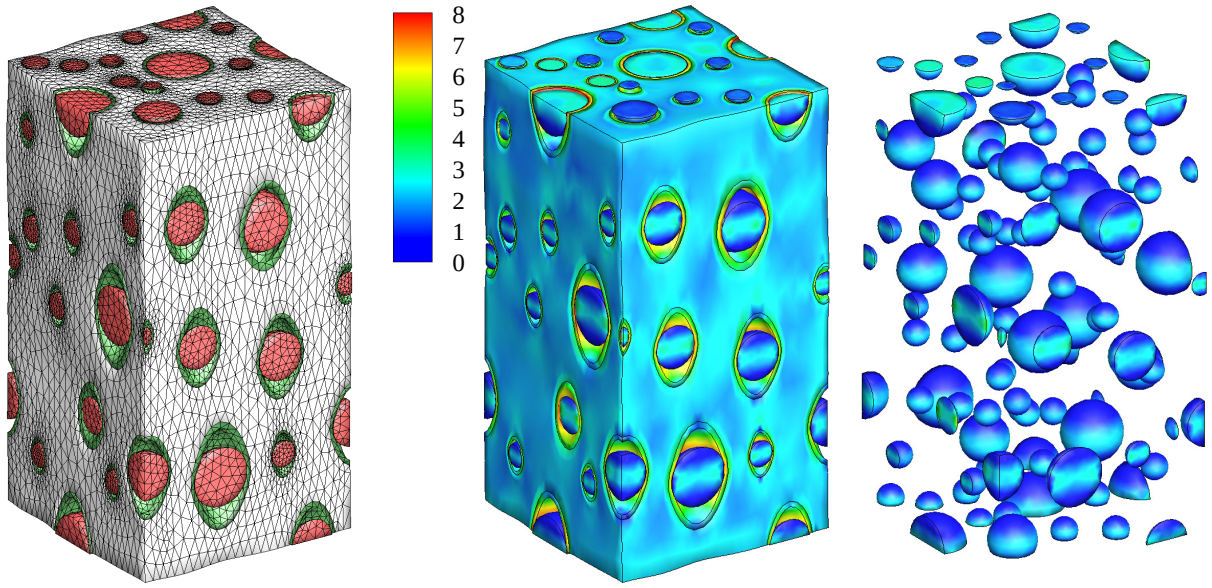

(a) (b) (c)

Figure 4.15: (a) Deformed geometry of a representative unit cell with a particle concentration of $c = 0.1$ and an interphase to particle radius ratio of $t/r_p = 0.2$, loaded in uniaxial tension. Contour plot of principal stress in uniaxial tension in the (b) entire model, and (c) particles.

The macroscopic constitutive response in uniaxial tension is plotted in Figure 4.16. We consider particle concentrations of $c = 0.1$ and $c = 0.2$, and interphase thickness to particle radius ratios of $t/r_p = 0.1$ and $t/r_p = 0.2$, and compare them to the response when no interphase is present. Because each microstructure is generated randomly, the response illustrated is an average of three simulations. As expected, the thicker and stiffer the interphase, the greater the influence on the constitutive response. Additionally, as is commonly noted in the literature [73], the large particles tend to debond from the matrix prior to the smaller particles fully debonding.

Even in the case with a small particle concentration ($c = 0.1$) and interphase thickness ($t/r_p = 0.1$), the interphase has a significant influence on the global response at relatively low strains. For example, at a strain of 0.4, microstructures with an interphase stiffness of $\mu_i = 10\mu_m$ produce a global response which is approximately 25% greater than in the case when no interphase is considered, as illustrated in Figure 4.16(a). For the larger particle concentration, $c = 0.2$, the global response is approximately 80% greater than that without considering interphases, as illustrated in Figure 4.16(c).

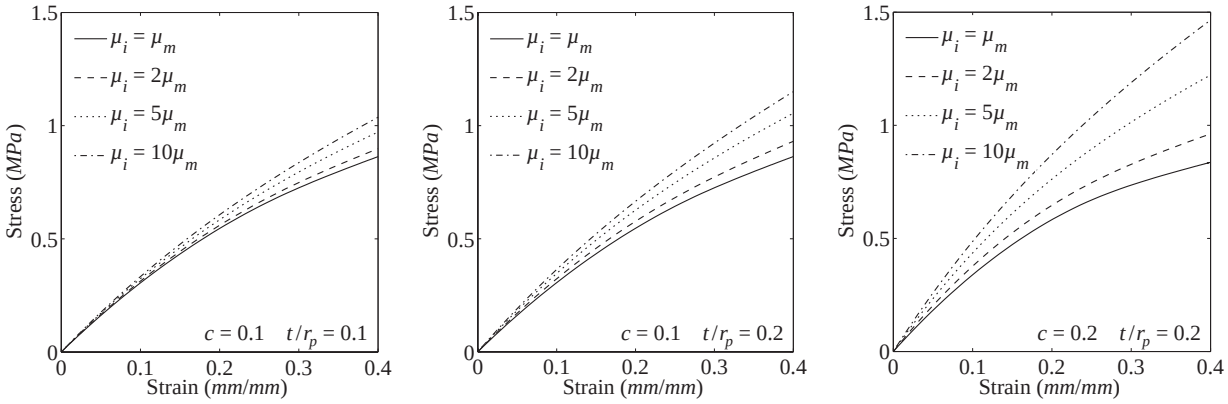

Figure 4.16: Macroscopic constitutive response in uniaxial tension for microstructures with: (a) $c = 0.1$ and $t/r_p = 0.1$; (b) $c = 0.1$ and $t/r_p = 0.2$; and (c) $c = 0.2$ and $t/r_p = 0.2$.

4.4.2.3 Simple shear

In simple shear, a representative deformed microstructure is illustrated in Figure 4.17(a). The zone of debonding around each particle is much smaller than that in uniaxial tension. Similar to the previous example, we also illustrate the stress contours in the particles in Figure 4.17(b). As with the single particle model, the stress in the particles remains high at large strains; which explains the higher contribution of friction to the global response, as discussed in Section 4.4.2.1.

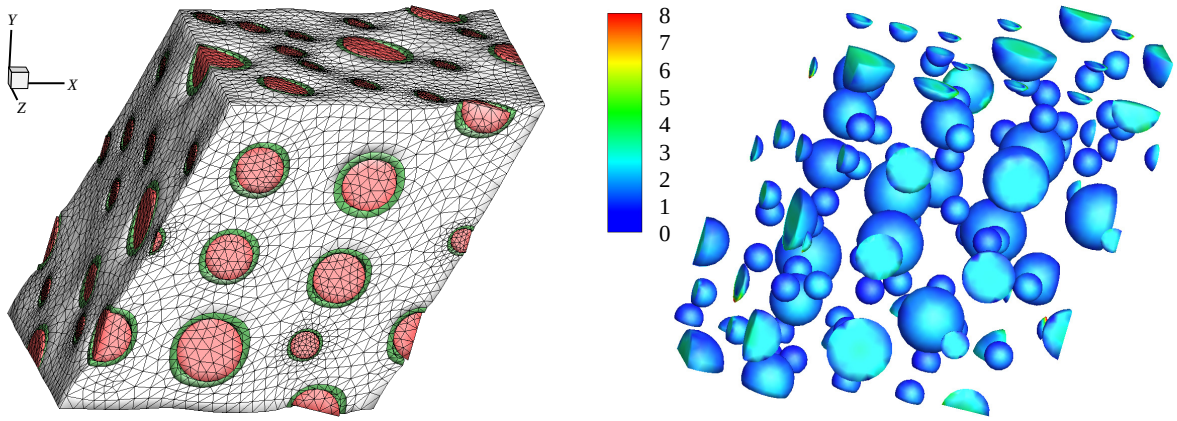

Figure 4.17: (a) Deformed geometry of a representative unit cell with a particle concentration of $c = 0.1$ and an interphase to particle radius ratio of $t/r_p = 0.2$, loaded in simple shear. (b) Contour plot of principal stress in the particles.

The macroscopic constitutive response in simple shear, for various microstructural configurations, is illustrated in Figure 4.18. Similar to the study on the single particle model, in

simple shear, the influence of the interphase is noticeably less than in the case of uniaxial tension; however, the interphase continues to significantly alter the macroscopic response. For the case with a small particle concentration in Figure 4.18(a), and an interphase stiffness of $\mu_i = 10\mu_m$, at a strain of 0.4 the global response is approximately 20% greater than in the case when no interphase is considered. For the case with a larger particle concentration and interphase thickness in Figure 4.18(c), at a strain of 0.4, the global response is approximately 45% greater than in the case when no interphase is considered.

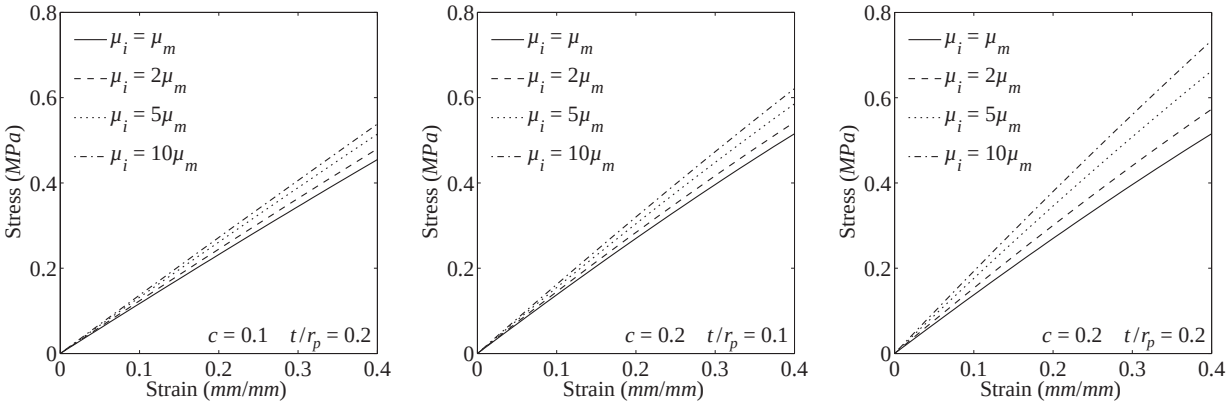

Figure 4.18: Macroscopic constitutive response in simple shear for microstructures with: (a) $c = 0.1$ and $t/r_p = 0.2$; (b) $c = 0.2$ and $t/r_p = 0.1$; and (c) $c = 0.2$ and $t/r_p = 0.2$.

In summary, this series of numerical investigations clearly demonstrates that the inclusion of physically significant, microscopic interphases can dramatically alter the macroscopic constitutive response of particle reinforced composites. We are also able to demonstrate that frictional effects are negligible in tension induced debonding. By demonstrating that the presence of interphases and interfacial debonding significantly alters the macroscopic constitutive response of these composite materials, we hope to motivate the inclusion of such interphases in future investigations which model such composites.

4.5 Experimental validation

In this section, we verify that the proposed computational framework is capable of capturing representative experimental results from the literature. There are few experimental investigations which report all the necessary microscale and macroscale properties of the composite material, thus we make reasonable assumptions, and discuss them, where necessary. The experimental results selected for this comparison were reported in a series of papers by Yat-

suyanagi et al. [161] and Suzuki et al. [160]. Their results correspond to a well-dispersed distribution of roughly spherical aggregates of silica particles in a styrene-butadiene rubber matrix. In their investigation, they study the influence of rubber/filler interaction, due to variations in coupling agents used in the surface modification process of the silica particles. Two different surface treatments are considered, labeled as A-50 and UM-2.

The authors used a tensile tester, at room temperature, to determine the stress-strain curves, and used transmission electron microscopy (TEM) observations to determine the global effect of the different surface treatments. The authors report, through the use of swelling experiments, that the elastic properties of the rubber matrix were essentially unmodified for the A-50 treatment, but the crosslink density in the rubber increased with surface treatment UM-2. However, they provide no comments on the amount or type of bound rubber present in the composite. They concluded that the constitutive relation of the composite is significantly influenced by the interactions between the filler particles and the matrix. In some cases, they demonstrate that the surface treatment caused strong interfacial bonding between the inclusions and the rubber, however, in other cases the surface treatment resulted in weak bonding; which lead to interfacial debonding (or dewetting) of the particles at large strains. In the following, we will only consider the reported cases which involved interfacial debonding.

Additionally, the authors report the response of the unfilled rubber. Based on fitting the response of the rubber, we find an appropriate response of the rubber matrix, at least in uniaxial tension, follows the stored-energy function [113]:

$$W = \frac{3^{1-\alpha}}{2\alpha}\mu\left[I_1^{\alpha} - 3^{\alpha}\right]. \tag{4.7}$$

with material parameters $\mu = 0.54$ and $\alpha = 0.2$, as illustrated in Figure 4.19. As mentioned, for the surface treatment labeled as UM-2, the authors report that the amount of sulfur used in this treatment increased the crosslink density in the rubber. To account for this, we assume that this increases the effective modulus of the rubber, resulting in an increase in the shear modulus in the stored-energy function ($\mu = 2.1$). The rubber is reinforced with a particle concentration of $c_p = 0.26$. Further, through a numerical investigation, we assume an interphase-thickness-to-particle-radius ratio of $t/r = 0.2$. Since the authors do not report the interphase stiffness, we select it here by fitting the numerical results to the experimental results. As illustrated in Figure 4.19, for the A-50 treatment, an interphase modulus 3 times stiffer than that for the matrix, $\mu_i = 3 \times \mu_m = 3 \times 0.54MPa = 1.62MPa$ leads to good agreement with the experimental results. Additionally, for the UM-2 treatment, an interphase modulus 2 times stiffer than that for the matrix, $\mu_i = 2 \times \mu_m = 2 \times 2.1MPa = 4.2MPa$

leads to good agreement with the experimental results. As seen in Figure 4.19, simulations of the same microstructures without the inclusion of interfacial debonding significantly overestimate the macroscopic constitutive response. The material properties used in the simulations are summarized in Table 4.1.

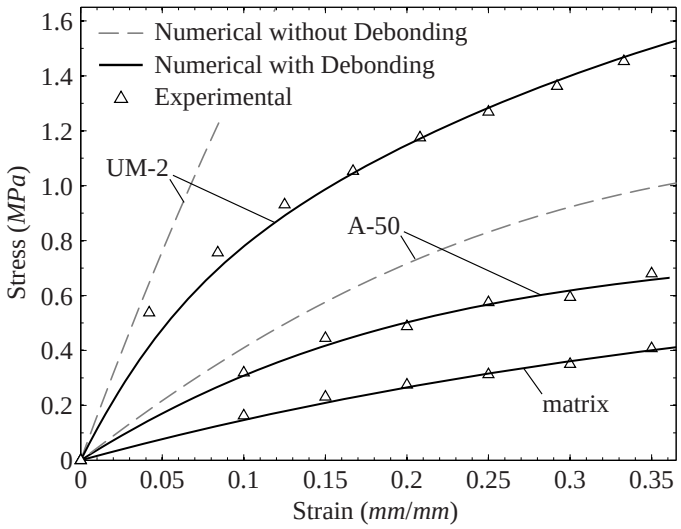

Figure 4.19: Comparison of the proposed computational framework with experimental data.

Table 4.1: Summary of material properties used in the numerical comparison with experiments. The rate of transition between cohesive and friction forces is set at $s = 3$, in Equation 4.2.

Treatment	Matrix Modulus	Interphase Modulus	Fracture Energy	Cohesive Strength	Coefficient of Friction
A-50	$0.54MPa$	$1.62MPa$	$1.0N/m$	$0.5MPa$	1.0
UM-2	$2.10MPa$	$4.20MPa$	$1.0N/m$	$0.5MPa$	1.0

In summary, the above comparisons with experiments demonstrate that the proposed computational framework is able to provide an explanation for the varied macroscopic response of particle reinforced composites at finite deformations. Additionally, it confirms the significant influence of not only particle reinforcements, but also interfacial interactions on the constitutive response. Thus, in order to design these composites from the bottom up, it is not enough to only consider the influence of the particles, but one must also consider the influence of the interactions between the particles and the matrix. Finally, we note that, due to the necessity to make assumptions on the specific constituent properties not provided in the experiments, there are other potential combinations of constituent properties which may also be suitable at capturing the above described behavior. For example, the properties of

the matrix may change in a different manner than we assumed, due to the use of the applied treatments, however, this doesn't negate the presence of interphases. And the influence of the interphases compounds the influence of the changes in the matrix.

4.6 Concluding remarks

In this chapter, we develop a computational framework to explore the influence of microscale features on the macroscale constitutive response of particle reinforced composites. While it has been shown experimentally that interphases significantly alter the macroscopic constitutive response of these composite materials, their inclusion in computational models of such composites is widely omitted. Through the use of representative unit cells, we demonstrate the influence of interphases and interfacial debonding on the global response of particle reinforced composites. We model interphases explicitly, and capture the interfacial debonding behavior of the particles, at large strains, using cohesive elements. To account for the frictional forces generated between each particle and its corresponding interphase, we developed a new, fully three-dimensional, coupled cohesive-friction constitutive relation. The use of this relation revealed that the consideration of friction in uniaxial tension can often be neglected, due to the small area of contact between the particles and the surrounding matrix. However, this is not the case when the microstructure experiences simple shear loading conditions; where we demonstrate that frictional forces can be significant, and should not be neglected. We validated the computational framework with experimental results from the literature which displayed both the presence of interphases and interfacial debonding. The comparison with experiments indicates that the proposed computational framework is able to provide an explanation for the varied macroscopic response of particle reinforced composites at finite deformations. Because of the challenges associated with experimentally obtaining the necessary measurements of material properties, a computational framework, such as the one presented in this chapter, could prove helpful in shedding some light on the key parameters influencing the global response of this important class of materials.

Finally, we note that entrapped or occluded rubber, may experience uneven curing, resulting in residual pressure/confinement stresses which may lead to premature damage or failure [173]. As discussed in Chapter 2, in our framework, we approximate the occluded rubber by reinterpreting the concentration of particles as the combined concentration of particles and occluded rubber, and assume that fracture does not occur within the particles. An extension of this work may incorporate the influence of cracks occurring within the particle (regions of occluded rubber), and would then be able to account for the presence and influence of

residual pressure/confinement on the fracture behavior.

In summary, this investigation has been able to clearly demonstrate the significance of interphases and interfacial debonding on the macroscopic constitutive response of particle reinforced composites under finite deformations. However, there are many areas of this topic which lend themselves to being explored further. For example, the use of 80 particles to represent the polydisperse nature of the composite fixes the particle surface area, and thus, the frictional area of contact. If fewer particles or more particles were to be used to generate the same particle concentration, the surface area of the particles in contact with the elastomer, and the resulting frictional forces, would change accordingly. Additionally, in this investigation we restrict our attention to spherical particles. The shape of the particles will likely influence the local stress field around the inclusion [174], and the strength of the adhesive binding between the particles and the matrix [175], thus a potential extension of this work would be to consider alternative particle shapes and investigate their influence on the modulus of the composite and their contribution to frictional effects. Ultimately, the goal would be to use experimental realizations of the microstructure to capture the precise locations and geometries of the particles and interphases. This could be done using the techniques of X-ray tomography or serial sectioning [176, 177]. Finally, one could consider the influence of hysteretic loading and rate effects on the global constitutive response. The stiffness of elastomers is known to be strain history dependent [178], wherein the global response of the elastomer irreversibly softens during cyclic loading. The stiffness of elastomers is also rate dependent. Some researchers use strain amplification factors to account for rate dependence in elastomers [85], and include experimentally determined fitting parameters to adjust the model to the specific material being investigated. A more rigorous approach might incorporate the rate dependence into the stored-energy function. The influence of hysteretic and rate effects was not pursued in our investigation, but could enable a new avenue for the analysis and design of elastomeric bearings and dampers.

Chapter 5

Geometrically, Topologically, and Constitutively Unstructured Methods for Reducing Mesh Dependency in Dynamic Cohesive Fracture Simulations

In this chapter, we present a series of methods for reducing mesh dependency in two-dimensional dynamic cohesive fracture simulations. In this setting, cracks are only permitted to propagate along element facets, thus a poorly designed discretization of the domain can potentially introduce artifacts the fracture behavior. To reduce the influence of the mesh, we consider unstructured polygonal finite elements. A randomly-seeded polygonal mesh leads to an isotropic discretization of the problem domain; which does not bias the crack direction. However, polygonal meshes tend to limit the possible directions a crack may travel at each node, making this discretization a poor candidate for dynamic cohesive fracture simulations. To alleviate this problem, we propose two new topological operators. The first operator we propose is adaptive element-splitting, and the second is adaptive mesh refinement. Both operators are designed to improve the ability of unstructured polygonal meshes to capture crack patterns in dynamic cohesive fracture simulations. However, we show that element-splitting is more suited to pervasive fracture problems, whereas, adaptive refinement is more suited to problems dominated by a single crack. In addition, the influence of bulk and cohesive material heterogeneity is investigated through the use of a statistical distribution of material properties. Cohesive elements are dynamically inserted, when and where necessary, and follow the constitutive response of the extrinsic Park-Paulino-Roesler cohesive model. The adaptive mesh modifications are handled through a compact topological data structure. Numerical examples highlight the features of the two operators in both capturing physical fracture patterns and reducing computational cost.

5.1 Introduction

To predict and understand the real world failure of structures under dynamic loads, investigators often turn to numerical simulations. Many numerical methods were discussed in Chapter 1, however, in this work, we employ the finite element method and inter-element cohesive zone modeling to simulate dynamic fracture. Cohesive elements are adaptively

inserted between bulk elements, and initially have zero thickness. As the bulk elements separate, signifying damage and fracture, the cohesive elements impart a softening traction (which corresponds to a specified cohesive model) on the adjacent facets of the bulk elements. As discussed in Chapters 3 and 4, elements with *intrinsic* cohesive models are inserted a priori into a mesh and have a traction-separation relation which consists of both an initial elastic range and a softening range. This initial elastic range may create an artificial compliance in the mesh and can lead to non-physical results [52, 54], thus they are primarily used in problems where the location of material failure is known beforehand. Alternatively, *extrinsic* cohesive elements are inserted adaptively into a mesh [55, 56, 57], and are useful in problems where the fracture path is not known a priori. The traction-separation relation, corresponding to an extrinsic cohesive model, only consists of a softening range and thus does not cause artificial compliance.

Since the cohesive element method restricts cracks to propagate along element facets, issues of crack branching, crack coalescence and fragmentation are naturally handled by the mesh topology. The primary drawback of this restriction is that the initial mesh, if designed poorly, can adversely influence the path(s) of crack propagation. Several meshing strategies have been proposed to circumvent this issue [179, 180, 181, 182, 183]. Unstructured meshes are preferred for fracture applications, because they possess no preferential paths for cracks to propagate along (i.e. they are isotropic), which can result in more realistic crack patterns than their structured counterparts [184, 185]. Motivated by this issue of mesh isotropy, we use unstructured polygonal meshes in this work.

Unstructured polygonal meshes demonstrate no directional preference for crack propagation, and have gained popularity of late. Li and Ghosh modeled multiple crack growth, in brittle materials, with the extended Voronoi cell finite element method (X-VCFEM) [186, 187, 188]. Ooi et al. [189, 190] developed a hybrid finite element-scaled boundary finite element technique to propagate cracks. Bishop and coworkers use a framework similar to that developed in this work, to model pervasive fracture behavior. They generate their finite element meshes with randomly close-packed Voronoi tessellations and cohesive elements are adaptively inserted at element boundaries [12, 191]. For a more detailed discussion of Voronoi tessellations applied to fracture problems, we direct the reader to [192]. Other than the dynamic insertion of cohesive elements, however, the meshes in the above investigations remain fixed throughout the simulation. Therefore, to obtain more realistic crack patterns, in the present study, we apply adaptive (on-the-fly) modifications to the mesh.

In this chapter, we propose two new topological operators for adaptive mesh modification, to improve fracture patterns in unstructured polygonal meshes. The first operator is more appropriately used in pervasive fracture simulations, while the second operator is more ap-

propriately used in problems dominated by a single crack. The remainder of the chapter is organized as follows. Section 5.2 outlines the numerical framework used in this study. In Section 5.3, we present the two new topological operators developed in this work, and detail their implementation. In Section 5.4, we briefly discuss the constitutive models used in this investigation, and the incorporation of constitutive unstructuredness in homogeneous materials. Examples which display pervasive fracture behavior are presented in Section 5.5; and examples dominated by a single crack are presented in Section 5.6. Finally, our concluding remarks and some potential extensions are presented in Section 5.7.

5.2 Numerical framework using polygonal finite elements

In this section, we present an overview of: the finite element formulation for dynamic fracture problems with cohesive elements; the method used for mesh generation; the polygonal element shape functions; the method of extrapolating computed values from Gauss points to nodes; and the topological data structure used to manage the on-the-fly mesh modifications.

5.2.1 Finite element formulation

For an arbitrary domain, Ω, the standard finite element formulation can be derived from the principle of virtual work. The principal of virtual work corresponding to the dynamic finite element formulation is [193]:

$$W_{int} \equiv \int_{\Omega} \left(\text{div}\boldsymbol{\sigma} - \rho\ddot{\mathbf{u}}\right) \delta\mathbf{u} d\Omega = \int_{\Gamma} \left(\mathbf{T} - \boldsymbol{\sigma}\mathbf{n}\right) \delta\mathbf{u} d\Gamma \equiv W_{ext}, \tag{5.1}$$

where ρ is the material density, $\boldsymbol{\sigma}$ is the Cauchy stress tensor, $\mathbf{u}$ is the displacement vector, $\ddot{\mathbf{u}}$ is the acceleration vector, and $\mathbf{T}$ is the surface traction along boundary Γ with normal $\mathbf{n}$. Rearranging Equation 5.1, and applying the divergence theorem and integration by parts, the following expression is obtained:

$$\int_{\Omega} \left(\boldsymbol{\sigma} : \delta\mathbf{E} + \rho\ddot{\mathbf{u}} \cdot \delta\mathbf{u}\right) d\Omega - \int_{\Gamma_{ext}} \mathbf{T}_{ext} \cdot \delta\mathbf{u} d\Gamma_{ext} = 0, \tag{5.2}$$

where $\mathbf{E}$ is the Green-Lagrange strain tensor, and $\mathbf{T}_{ext}$ is the traction applied on the external surface, Γ_{ext}. When cohesive elements are incorporated into the formulation, they contribute

an additional term to the expression:

$$\int_{\Omega} \left(\boldsymbol{\sigma} : \delta\mathbf{E} + \rho\ddot{\mathbf{u}} \cdot \delta\mathbf{u}\right) d\Omega - \int_{\Gamma_{coh}} \mathbf{T}_{coh} \cdot \delta\Delta\mathbf{u} d\Gamma_{coh} - \int_{\Gamma_{ext}} \mathbf{T}_{ext} \cdot \delta\mathbf{u} d\Gamma_{ext} = 0, \tag{5.3}$$

where the internal displacement jump, $\Delta\mathbf{u}$, produces a cohesive traction, $\mathbf{T}_{coh}$, on the internal cohesive surface, Γ_{coh}.

In fracture simulations, it is important to take into consideration the effect of finite displacements. When cohesive elements are first activated, they display zero thickness. But, as fracture progresses, the adjacent bulk elements separate and rotate. By not taking into consideration these finite rotations, the mechanics of the problem may not be accurately captured. In this work, finite displacements are taken into account by means of the total Lagrangian formulation. In this formulation, the deformation is described with respect to the undeformed configuration. Following a similar procedure to that described above, the final expression of the principal of virtual work, with respect to the undeformed configuration, becomes:

$$\int_{\Omega} \left(\mathbf{S} : \delta\mathbf{E} + \rho\ddot{\mathbf{u}} \cdot \delta\mathbf{u}\right) d\Omega - \int_{\Gamma_{coh}} \mathbf{T}_{coh} \cdot \delta\Delta\mathbf{u} d\Gamma_{coh} - \int_{\Gamma_{ext}} \mathbf{T}_{ext} \cdot \delta\mathbf{u} d\Gamma_{ext} = 0, \tag{5.4}$$

where $\mathbf{S} = J\mathbf{F}^{-1}\boldsymbol{\sigma}\mathbf{F}^{-\mathrm{T}}$ is the second Piola-Kirchoff stress tensor, $\mathbf{F}$ is the deformation gradient, and $J = \det\mathbf{F}$ is the Jacobian. For implementation, Equation 5.4 is expressed in matrix notation as:

$$\mathbf{K}\mathbf{u} + \mathbf{M}\ddot{\mathbf{u}} - \mathbf{R}_{coh} - \mathbf{R}_{ext} = 0. \tag{5.5}$$

Numerically, to progress the dynamic simulation, time is discretized using the explicit central difference method; which is a subset of the Newmark method [194]. The computation of nodal displacements, velocities, and accelerations at time $n+1$ are computed from those at time n through the following scheme:

$$\mathbf{u}_{\mathrm{n}+1} = \mathbf{u}_{\mathrm{n}} + \Delta t\dot{\mathbf{u}}_{\mathrm{n}} + \frac{1}{2}\left(\Delta t\right)^2 \ddot{\mathbf{u}}_{\mathrm{n}}, \tag{5.6}$$

$$\ddot{\mathbf{u}}_{\mathrm{n}+1} = \mathbf{M}^{-1}\left(\mathbf{R}_{ext} - \mathbf{R}_{int_{\mathrm{n}+1}} + \mathbf{R}_{coh_{\mathrm{n}+1}}\right), \tag{5.7}$$

$$\dot{\mathbf{u}}_{\mathrm{n}+1} = \dot{\mathbf{u}}_{\mathrm{n}} + \frac{\Delta t}{2}\left(\ddot{\mathbf{u}}_{\mathrm{n}} + \ddot{\mathbf{u}}_{\mathrm{n}+1}\right), \tag{5.8}$$

where Δt denotes the time step and $\mathbf{R}_{ext}$ is the external force vector. Moreover, $\mathbf{R}_{int}$ and $\mathbf{R}_{coh}$ are the internal and cohesive force vectors, obtained from the separate contribution of the bulk and cohesive elements, respectively. To compute the mass matrix, $\mathbf{M}$, we apply a standard mass lumping technique; in which the diagonal terms of the consistent mass matrix

are scaled, preserving the total mass, resulting in a diagonal mass matrix [5, 195].

5.2.2 Mesh generation

The unstructured polygonal meshes in this work are generated using the PolyMesher algorithm [196]; which discretizes a domain with a centroidal Voronoi tessellation (CVT). A CVT results in a higher quality discretization, which is more suitable for finite element analysis than one generated using randomly placed seeds [196, 20]. We refer to a mesh with more uniform edge lengths as better suited for finite element analysis than one with a large variation in edge length [196, 197] (see Section 5.3.4 for a statistical analysis of CVT quality). Detailed information on the generation of CVT tessellations can be found in the principal PolyMesher publication [196]; we just highlight a few critical details for completeness, and maintain the notation of [196] for consistency. Briefly, to initiate the tessellation, a random set of seeds are inserted into the problem domain. The number of seeds corresponds to the number of elements to be generated. Given a set of seeds, $\mathbf{P}$, the Voronoi tessellation, $\mathcal{T}$, of the domain, Ω, is defined as:

$$\mathcal{T}(\mathbf{P};\Omega) = \{V_{\mathbf{y}} \cap \Omega : \mathbf{y} \in \mathbf{P}\}, \tag{5.9}$$

where $V_{\mathbf{y}}$ is the Voronoi cell corresponding to point $\mathbf{y}$. The Voronoi cell consists of all points in the domain which are closer to $\mathbf{y}$ than to any other point in the set $\mathbf{P}$:

$$V_{\mathbf{y}} = \{\mathbf{x} \in \Omega : \|\mathbf{x}-\mathbf{y}\| < \|\mathbf{x}-\mathbf{z}\|, \forall \mathbf{z} \in \mathbf{P} \backslash \{\mathbf{y}\}\}. \tag{5.10}$$

The initial discretization, based off the initial set of seeds, results in a random polygonal tessellation, as illustrated in Figure 5.1(a). In dynamic fracture simulations, the time step required to produce a stable simulation is dependent on the element size [8]. Because the random placement of seeds may result in arbitrarily small elements and/or element edges, this initial discretization is not suitable for dynamic fracture simulations. To improve the quality of the mesh, Lloyd's iterative updating algorithm is employed [198]. It generates a new set of seeds at every iteration, based on the previous Voronoi tessellation. The new locations of the seeds correspond to the geometric centroids of the Voronoi cells in the previous tessellation. Figure 5.1(b) shows the resulting Voronoi tessellation after one update using Lloyd's algorithm on the random seeds in Figure 5.1(a). This updating process continues until the change in the energy of the tessellation, from one iteration to the next, falls below a selected tolerance [196]. The resulting tessellation after 50 iterations of Lloyd's algorithm is illustrated in Figure 5.1(c). The resulting mesh is more uniform, and is thus

more suited for use in dynamic fracture simulations. An investigation of the mesh quality can be found in the accompanying papers [199, 200], and will be briefly discussed in Sections 5.3.3 and 5.3.4.

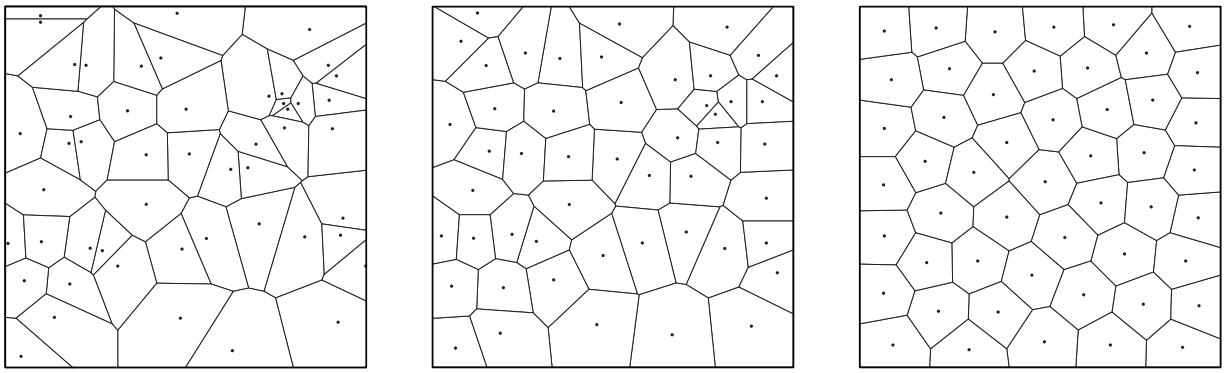

(a) (b) (c)

Figure 5.1: Depiction of the mesh generation procedure. (a) Initial placement of seeds and the corresponding Voronoi tessellation; (b) the Voronoi tessellation after the first iteration of Lloyd's algorithm; and (c) the final Voronoi tessellation [196].

5.2.3 Shape functions for polygonal elements

There are several polygonal interpolants available in the literature, see, for example, the review paper by Sukumar and Malsch [201]. Here, we adopt Wachspress shape functions [202], which satisfy the desirable properties of shape functions [203]. Isoparametric mapping is employed to map quantities from a regular n-gon in the reference coordinate system to an arbitrary convex n-gon in the physical coordinate system. The Wachspress shape functions [203] for a reference n-gon are expressed as:

$$N_i\left(\boldsymbol{\xi}\right) = \frac{\alpha_i\left(\boldsymbol{\xi}\right)}{\sum_{j=1}^{n} \alpha_j\left(\boldsymbol{\xi}\right)}, \tag{5.11}$$

where the interpolants α_i are of the form:

$$\alpha_i\left(\boldsymbol{\xi}\right) = \frac{A\left(\mathbf{p}_{i-1}, \mathbf{p}_i, \mathbf{p}_{i+1}\right)}{A\left(\mathbf{p}_{i-1}, \mathbf{p}_i, \boldsymbol{\xi}\right) A\left(\mathbf{p}_i, \mathbf{p}_{i+1}, \boldsymbol{\xi}\right)}, \tag{5.12}$$

and A denotes the area of the triangle made up of the points in its arguments. For example, Figure 5.2 shows a reference hexagon with shaded triangular regions indicating the areas used in the computation of α_i in the shape function of the node at $\boldsymbol{p}_i$ evaluated at point $\boldsymbol{\xi}$. For a detailed discussion of the construction and implementation of the Wachspress shape

functions for finite element applications, the reader is directed to [204]. The Wachspress shape functions are generated once, before the fracture simulation begins, and the necessary quantities (i.e. shape functions and their derivatives evaluated at the integration points) are stored and accessed on an as-needed basis.

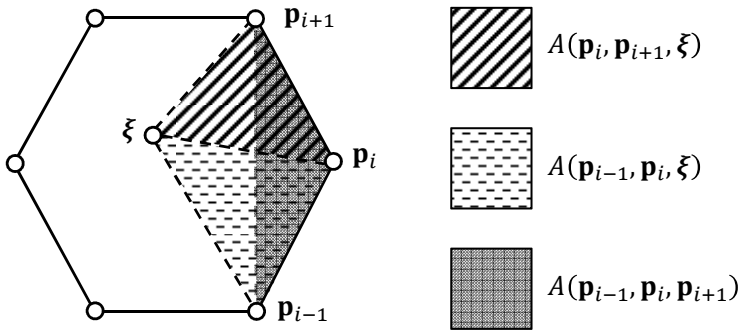

Figure 5.2: Triangular areas used to define the interpolants, α_i, in Equation 5.12.

5.2.4 Numerical integration and extrapolation from Gauss points to nodes

After discretization of Equation 5.1, integration is performed via numerical quadrature, for which there are many schemes available. One scheme is to use quadrature rules which have been designed specifically for polygonal domains [205, 206]. In this work we opt to subdivide the reference n-gon into triangles and use 3-point quadrature rules on each triangle, as illustrated in Figure 5.3. Then, the contribution from each triangle is summed, to get the integral over the entire element. Alternatively, the reference n-gon could be subdivided into quadrilaterals and a 2×2 quadrature rule used on each quadrilateral, as illustrated in Figure 5.3(c).

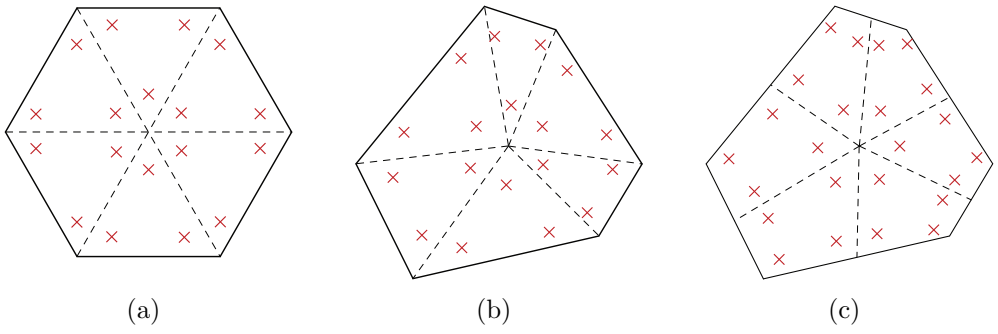

Figure 5.3: Quadrature schemes on polygonal elements. (a) Integration points using 3-point quadrature for each triangular subdivision of a reference 6-gon; (b) location of the integration points in the physical element; and (c) location of the integration points in the physical element for the quadrilateral subdivision scheme.

To achieve a continuous stress field across the domain (except across cracks), we first extrapolate stresses from the quadrature points to the nodes, then conduct a least squares minimization over each element [195]. This procedure is conducted throughout the domain - no differentiation is made between elements near or far from the crack-tip. To do this, we calculate the stresses at the integration points, $\sigma(\xi_i, \eta_i) = \sigma_i$, where σ is any stress measure of choice. We then define the smooth stress functions as:

$$\tilde{\sigma}(\xi_i, \eta_i) = \sum_{j=1}^{n} \tilde{\sigma}_j N_j(\xi_i, \eta_i), \tag{5.13}$$

where n is the number of nodes in the element, and $\tilde{\sigma}_j$ is the smoothed nodal stresses. The objective then is to find the smoothed nodal stresses, $\tilde{\sigma}_j$, which minimize:

$$\chi = \sum_{i=1}^{m} \left(\tilde{\sigma}(\xi_i, \eta_i) - \sigma(\xi_i, \eta_i)\right)^2, \tag{5.14}$$

which leads to the following system of equations:

$$\sum_{j=1}^{n} \sum_{i=1}^{m} N_j(\xi_i, \eta_i) N_k(\xi_i, \eta_i) \tilde{\sigma}_j = \sum_{i=1}^{m} N_k(\xi_i, \eta_i) \sigma_i. \tag{5.15}$$

By defining the following matrices:

$$\mathbf{S}_{kj} := \sum_{i=1}^{m} N_j(\xi_i, \eta_i) N_k(\xi_i, \eta_i) \quad \text{and} \quad \mathbf{F}_{ki} := N_k(\xi_i, \eta_i), \tag{5.16}$$

the transfer matrix, $\mathbf{T}$, is computed as:

$$\mathbf{S}\tilde{\boldsymbol{\sigma}} = \mathbf{F}\boldsymbol{\sigma} \quad \Rightarrow \quad \tilde{\boldsymbol{\sigma}} = \mathbf{S}^{-1}\mathbf{F}\boldsymbol{\sigma} := \mathbf{T}\boldsymbol{\sigma} \quad \Rightarrow \quad \mathbf{T} = \mathbf{S}^{-1}\mathbf{F}. \tag{5.17}$$

Finally, the nodal stress values are computed as the average of that node's stress contribution from each adjacent element. For efficient implementation, all searching and storing of shape functions, Gauss points, and transfer matrices is done in the preprocessing step. This information is then updated during crack propagation, as necessary, for elements which have been topologically modified. Alternatively, one could use a non-local smoothing approach; such as, the super-convergent patch recovery [207], which may provide more accurate results. However, this approach was not pursued in this work.

5.2.5 Consistent topological data structure

The insertion of extrinsic cohesive elements in front of the propagating crack-tip requires on-the-fly mesh modifications during the simulation. To handle the modifications to the adjacency relations, the present work uses the topological data structure TopS [208, 209]. TopS explicitly stores node and element information, and implicitly represents element facets, edges and vertices, as illustrated in Figure 5.4. Additionally, TopS is a complete topological data structure, meaning that, from any entity, all adjacent entities can be determined (e.g. from a given node, all adjacent nodes, elements, facets, edges and vertices can be accessed). Cohesive elements are also supported by TopS; in this work we use 2D linear cohesive elements to be compatible with the linear polygonal elements. With this data structure, the dynamic insertion of cohesive elements and the retrieval of adjacency information occurs in time proportional to the number of entities retrieved/inserted.

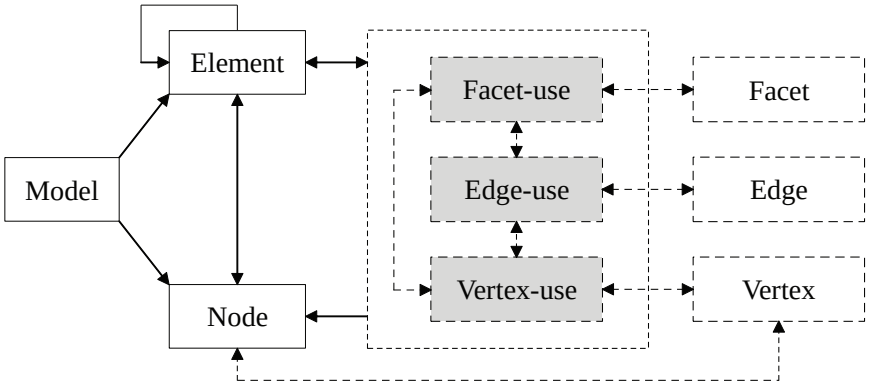

Figure 5.4: Schematic of the topological data structure TopS [208, 210]. The solid lines represent explicit entities while the dashed lines represent implicit entities. The solid arrows represent explicit references while the dashed arrows represent implicit references.

5.3 Adaptive topological operators

Crack patterns in geometrically structured meshes often suffer from mesh induced bias [181]. To reduce this bias, unstructured meshes, such as those employed in this work with polygonal elements, are desirable. However, polygonal element meshes are quite restrictive to crack propagation, because each node in the mesh typically only has three or four edges emanating from it. Thus, there are only two or three possible directions for a crack to continue propagating at each crack-tip node. To alleviate this problem, and increase the number of crack paths on polygonal element meshes, we propose two new topological operators. The

first operator we propose is adaptive element-splitting, and the second is adaptive mesh refinement.

5.3.1 Adaptive element-splitting

During dynamic fracture simulations, cracks are advanced by inserting extrinsic cohesive elements where and when needed. To determine the potential facets along which to insert cohesive elements, nodes with principal stress values greater than 90% of the cohesive strength are flagged. All the facets in the mesh are then iterated over, and if the facet contains two flagged nodes, the average normal and shear stress along the facet is computed. If either stress exceeds the corresponding strength along the facet, a cohesive element is inserted. Although a stress-based criterion has been adopted, the present methodology can be used in conjunction with other criteria [211, 212, 213, 214]. In addition to identifying potential sites for cohesive element insertion, the flagged nodes are also used to identify potential elements to be split.

Each element connected to a flagged node is checked for splitting. The element may be split along the line connecting the flagged node to the node which minimizes the difference in the areas of the two newly created elements. Since the element size is directly related to the critical time step for the explicit dynamic time integrator, limiting the nodes on which an element can be split minimizes the reduction of the already small time step. For this same reason, we also restrict the element to only be split once. To demonstrate the procedure of element-splitting, we illustrate a typical case in Figure 5.5. In Figure 5.5, node 1 is assumed to be flagged, and the element could be split with either node 3, 4 or 5. The areas of the resulting split elements are indicated as A_1 and A_2, in Figures 5.5(a) through 5.5(c). In this case, we see that the element is restricted to be split with node 4, as it produces two new elements whose difference in area is smaller than that if the element were to be split with either node 3 or node 5. To determine if the element should actually be split, we compute the average normal and shear stress, and compare them with the cohesive strength, as described previously. If the average normal or shear stress along the facet that would connect the splitting nodes is greater than the corresponding cohesive strength, the element is split. During a time step, element-splitting is performed before cohesive elements are inserted. Thus, since the criteria for inserting cohesive elements is the same as that to split an element, all split elements will have a cohesive element inserted along the new facet.

Since we restrict the elements to be split along the path which minimizes the difference between the areas of the resulting split elements, we introduce directionality into the

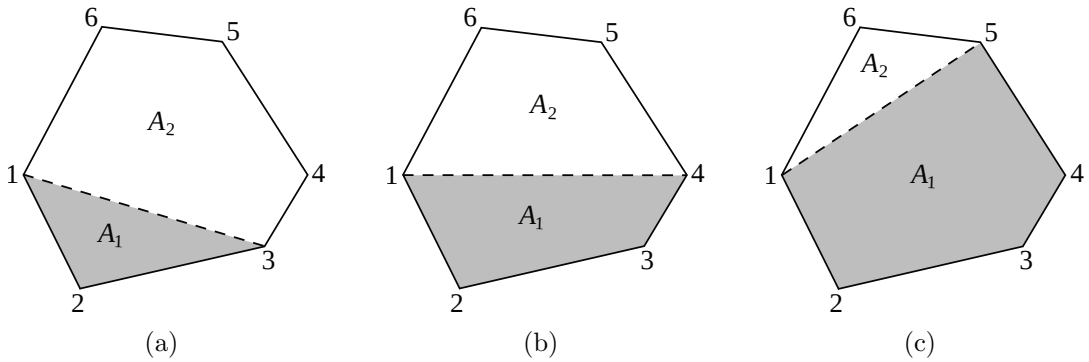

Figure 5.5: Schematic of potential new elements that would result from splitting the element between node 1 and (a) node 3, (b) node 4, and (c) node 5. The configuration shown in (b), where the element is split with node 4, minimizes the difference between the areas, A_1 and A_2, of the resulting new elements.

element-splitting operator. Take, for example, the scenario depicted in Figure 5.6. If a crack approaches the highlighted element from above (Figure 5.6(a)), the element would only be permitted to split along path 1. However, if a crack approaches the same element from below (Figure 5.6(b)), the element would only be permitted to split along path 2. Thus, if this element were to be split along path 1, during post-processing, we can deduce that the crack approached the element from above. This directionality will become significant when we assess the quality of the element-splitting operator in Section 5.3.3.

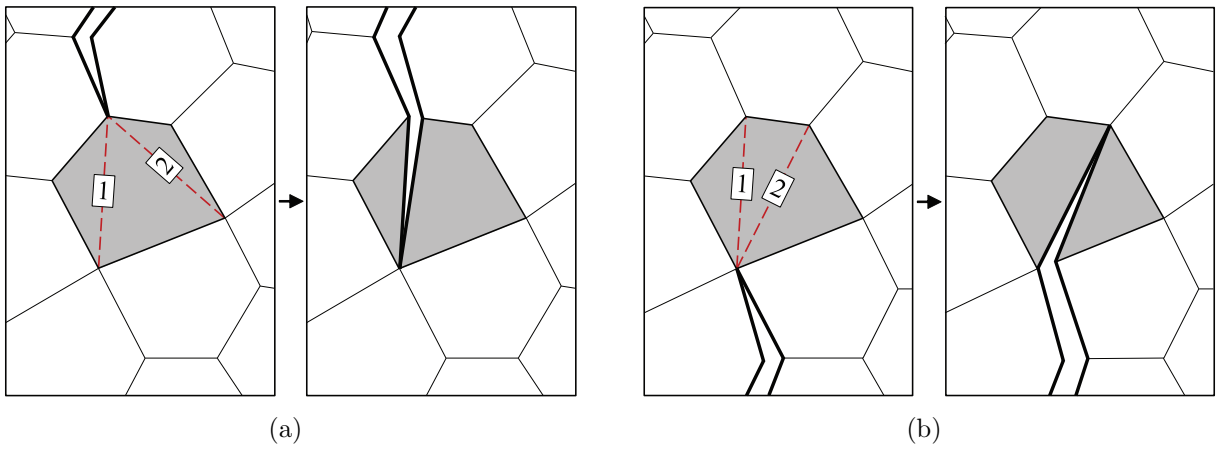

Figure 5.6: Schematic depicting the directionality of the element-splitting operator. The potential paths on which an element can be split (if no restrictions are placed) is dependent on the direction at which the crack approaches the element, as illustrated for the case of a crack approaching from (a) above, and (b) below.

Use of the TopS data structure, discussed in Section 5.2.5, ensures that the element-splitting operation is computationally efficient. The original polygonal element is removed, and two new polygonal elements replace it, using appropriate functions available in the TopS application programming interface (API). Linear polygons are used in this work, so no new

nodes are created when elements are split; therefore, it is not necessary to interpolate new nodal quantities. If higher order elements were to be used, mid-side nodal quantities would need to be interpolated from existing nodes. Moreover, since all of the polygons in the original mesh are convex, the polygons which result from element-splitting are also convex. Thus, we do not encounter issues of degenerate finite elements. The methodology presented here is effective because all of the elements (whether they have been split or not) are polygons, so the shape functions for the n-gons are always computed in the same fashion. This would not be the case, however, if element-splitting were employed on a mesh of alternative linear elements. For example, a split linear quad element would result in two linear triangles, which have fundamentally different shape functions.

Numerical integration of the split elements is accomplished by the same means as in the intact elements: the n-sided element is subdivided into n non-overlapping triangles that meet at the centroid of the polygon. Then, a 3-point quadrature rule is employed on each triangle and its contribution is added to the element. Thus, new integration points are created in the element-splitting procedure. In the current work, we use a bulk constitutive model in which the state of the material is completely characterized by the displacement field, and cohesive elements are never split. Thus, there is no need to map history-dependent internal state variables from the original set of integration points to the new set. However, if a more complex constitutive model were to be used, a technique to map internal state variables, such as that proposed in [215], would be necessary.

5.3.2 Adaptive refinement

The second topological operator we propose is adaptive refinement. Adaptive refinement schemes have been used to both minimize error in finite element analysis, and reduce computational cost [216, 217, 218]. In large scale simulations, to capture multiscale effects, fine meshes are used in regions containing high stress and strain gradients, and coarse meshes are used far from these regions [7]. In dynamic fracture simulations, the region in the vicinity of the propagating crack-tip has high stress and strain gradients and thus requires a fine mesh. Instead of prescribing a fine mesh in the region of expected crack propagation, an adaptive refinement scheme allows for the unrestricted dynamic propagation of the crack. This approach has been applied by many researchers: Molinari and Ortiz [219] developed an adaptive refinement technique based on Rivara's longest edge propagation path bisection algorithm; Park et al. [7] presented a multilevel refinement and coarsening strategy for 4k meshes; and Khoei et al. [220] proposed an adaptive mesh refinement scheme based on a

modified super-convergent path recovery technique.

Previously proposed adaptive refinement schemes, for two-dimensional dynamic fracture simulations, have used a 4k mesh structure [7]. Adaptive refinement using the 4k mesh structure has shown great promise. Since, in this case, the refined mesh also contains a 4k structure, a systematic procedure of refinement can be developed for one level of refinement which then translates directly to the next level. By keeping track of the levels of refinement, an analogous coarsening scheme can be generated. The drawback of using a 4k mesh is that it is an anisotropic discretization of the problem domain [183]. The 4k mesh is ideal for modeling cracks which propagate at angles which are a multiple of 45 degrees, but presents mesh-induced geometric errors when modeling crack paths which deviate greatly from these angles [183]. To minimize this effect, edge-swap and nodal perturbation operators were introduced to make the 4k mesh topologically and geometrically unstructured [221]. However, the unstructured 4k mesh has been shown to only moderately reduce, not remove, the effect of the anisotropies [183].

The refinement scheme we propose decomposes an n-sided polygon into n non-overlapping quadrilateral elements, as illustrated in Figure 5.7. To conduct the refinement within each element, we need to determine the location of the centroid of the n-gon. First, the signed area of the n-gon is calculated based on the physical coordinates of its vertices:

$$A = \frac{1}{2} \sum_{k=1}^{n} \left(v_x^k v_y^{k+1} - v_x^{k+1} v_y^k \right), \tag{5.18}$$

where (v_x^k, v_y^k) is the coordinates of the k^{th} vertex of the n-gon, $k = 1, ..., n$, and the $(n+1)^{th}$ vertex is assumed to be the 1^{st} vertex. From the area, the geometric location of the centroid (c_x, c_y) is calculated as:

$$c_x = \frac{1}{6A} \sum_{k=1}^{n} \left(v_x^k + v_x^{k+1} \right) \left(v_x^k v_y^{k+1} - v_x^{k+1} v_y^k \right), \tag{5.19}$$

$$c_y = \frac{1}{6A} \sum_{k=1}^{n} \left(v_y^k + v_y^{k+1} \right) \left(v_x^k v_y^{k+1} - v_x^{k+1} v_y^k \right). \tag{5.20}$$

We then insert nodes at the centroid and the midpoints of the edges of the original polygon. The original polygon is then removed and replaced with quadrilateral elements connected at the centroid, one vertex of the original polygon, and the midpoints of the two adjacent edges, as illustrated in Figure 5.7(b). The resulting nodal connectivities are illustrated in Figure 5.7(c).

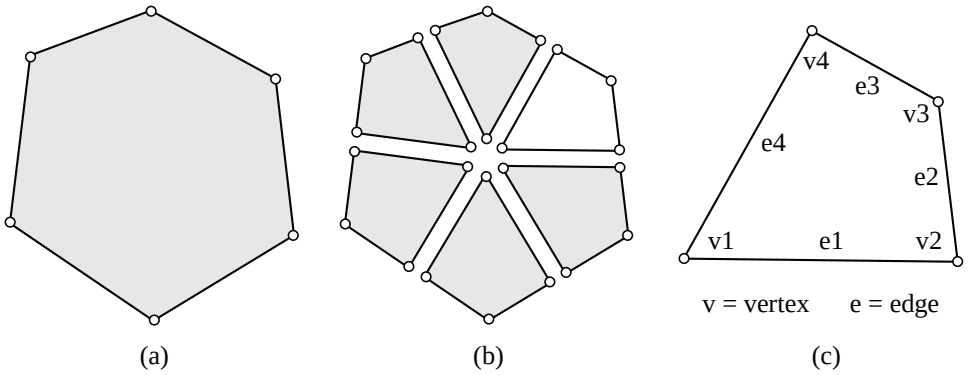

Figure 5.7: Local geometry in an arbitrary n-gon: (a) prior to refinement, and (b) after refinement with quadrilaterals. (c) Connectivity in a refined element.

While we only discuss the implementation for a single level of refinement, the extension to a multi-level refinement scheme can be considered as a simple extension of the above procedure. When nodes are added to the model, their attributes need to be initialized. Since we are using linear polygonal elements, the interpolation of nodal attributes is relatively straight forward.

5.3.2.1 Interpolation scheme

As discussed previously, in this work, we adopt Wachspress shape functions [202] to interpolate field quantities over each element. Thus, the centroidal nodal attributes, u_j^c, are interpolated from those of the original nodes of the n-gon using Wachspress shape functions. The interpolation takes the form:

$$u_j^c = \sum_{i=1}^{n} N_i\left(\boldsymbol{\xi}\right) u_i, \tag{5.21}$$

where n is the number of vertices in the original n-gon, N_i are the Wachspress shape functions defined on a parent domain, $\boldsymbol{\xi}$ is an interior point in the n-gon, and u_i are the attributes to be interpolated. The centroid of the n-gon, in the parent domain, is $\boldsymbol{\xi} = (0,0) = \mathbf{0}$. The Wachspress shape functions are then expressed as:

$$N_i\left(\mathbf{0}\right) = \frac{\alpha_i\left(\mathbf{0}\right)}{\sum_{j=1}^{n} \alpha_j\left(\mathbf{0}\right)}, \tag{5.22}$$

where α_i are interpolants of the form:

$$\alpha_i\left(\mathbf{0}\right) = \frac{A\left(\mathbf{p}_{i-1}, \mathbf{p}_i, \mathbf{p}_{i+1}\right)}{A\left(\mathbf{p}_{i-1}, \mathbf{p}_i, \mathbf{0}\right) A\left(\mathbf{p}_i, \mathbf{p}_{i+1}, \mathbf{0}\right)}, \tag{5.23}$$

where A denotes the area of the triangle made up of the points in its arguments (see Figure 5.2). For the nodes which are added to the midpoint of an edge, the nodal attributes, u_j^m, are interpolated from the two adjacent nodes on the edge. In this case, the interpolation simply takes the form:

$$u_j^m = \sum_{i=1}^{2} \frac{1}{2} u_i, \tag{5.24}$$

where u_i are the attributes to be interpolated. In this work, we use a bulk constitutive relation in which the material state is defined completely by the displacement vector, thus, only the displacement (a nodal quantity) needs to be mapped. As mentioned previously, if a constitutive relation which included rate or history effects were to be employed, it would be necessary to map internal state variables from the original integration points to the new ones [215]; however, this is outside the scope of the current work.

Because nodes are added to the midpoints of the edges, the nodes are initially left hanging, as illustrated in Figure 5.8. To account for this, all adjacent elements are modified to connect to the midpoint, resulting in three collinear nodes in each of these adjacent elements. The elements with collinear nodes remain convex, a condition which enables these elements to be handled naturally by the Wachspress shape functions. The refinement procedure does not increase the minimum number of paths a crack may travel along at the original nodes; however, the inserted midside nodes have 4 potential fracture paths (see Figure 5.9), and the centroid nodes have n potential fracture paths. To increase the number of fracture paths at each node, we allow elements to be split, using the element-splitting algorithm discussed previously.

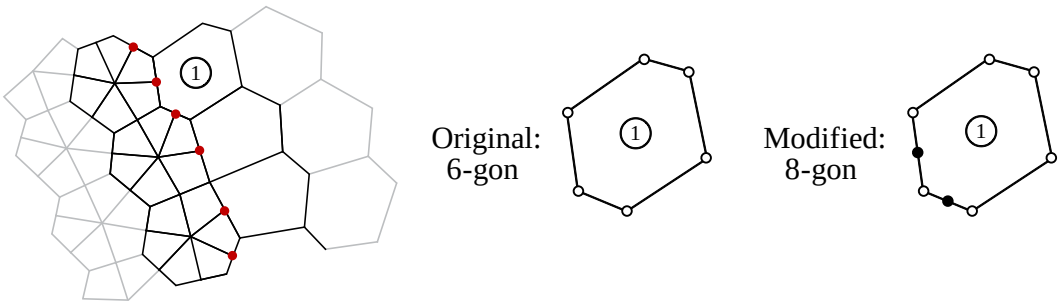

Figure 5.8: Hanging nodes adjacent to the region refined with quadrilateral elements and the subsequent modifications to the coincident edges of the adjacent elements.

Since, in the element-splitting algorithm, an element can only be split along any two, non-adjacent nodes, there is only one possible direction for quadrilateral elements to be split at each node. When combined with the adaptive refinement scheme, elements are always

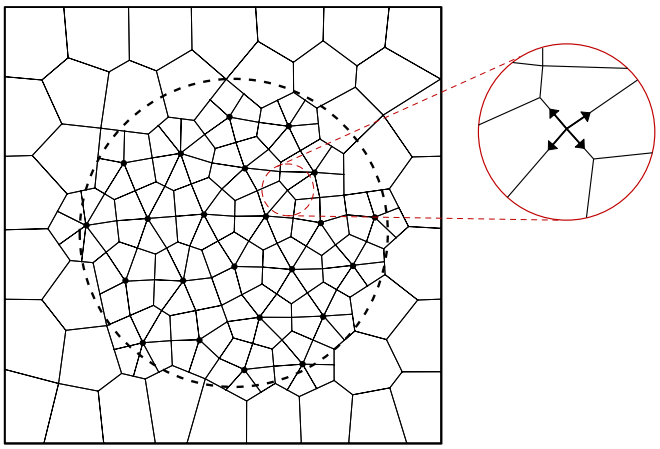

Figure 5.9: Circular zone of refinement and the corresponding refined mesh. The detail illustrates a typical midside node with the 4 potential paths along which a crack could propagate.

refined before splitting is performed. Thus, restricting the direction in which elements can be split is not necessary. With both refinement and element-splitting enabled, there are a total of $3n$ possible facets for cracks to propagate along, within an original element, as illustrated in Figure 5.10.

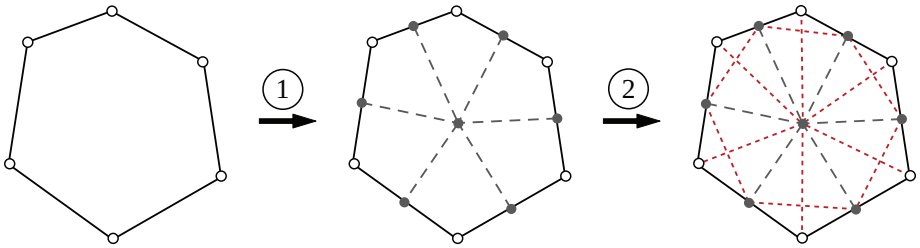

Figure 5.10: Possible facets for fracture, progression for an arbitrary n-gon (here 6-gon). Step 1: refinement (explicit facets) to introduce n possible facets for fracture within the element. Step 2: element-splitting (implicit facets) to introduce $3n$ possible facets for fracture within the element.

5.3.2.2 Refinement criteria

The simulation of dynamic fracture problems results in a propagating crack-tip, as illustrated in Figure 5.11. The mesh refinement procedure is conducted in an adaptive manner, in a circular region around the propagating crack-tip, as illustrated in Figure 5.9. If the centroid of a polygonal element falls within the circular region, the element is refined. The influence of the radius of the circular region of refinement is investigated further in Section 5.6.1. When refined with quadrilateral elements, the element-splitting procedure is used to implicitly allow fracture paths to split elements in this region, but does not increase the number of

"explicit facets" in the model. An explicit facet is a facet which is represented geometrically (as opposed to an implicit facet, which is only represented topologically).

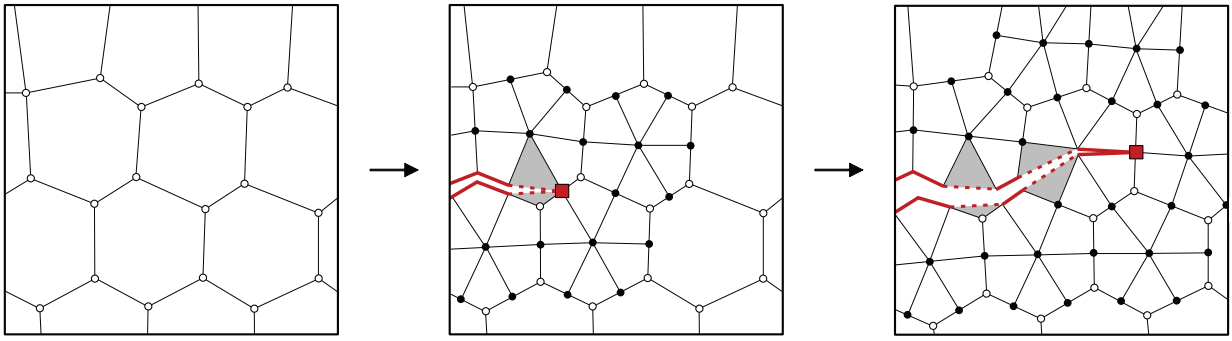

Figure 5.11: Schematic illustrating the adaptive refinement scheme and a possible crack path propagating along both refined and split element edges. The shaded elements depict those which have been split.

5.3.3 Geometric quantification of mesh isotropy and bias

In the cohesive element method, cracks are restricted to propagate along element facets, thus the mesh will undoubtedly influence the crack path. Consider the case of the arbitrary crack depicted in Figure 5.12. Due to the restriction of cracks only being permitted to propagate along element facets, the best representation of the crack, by the mesh, will be through a connection of points on the curve with straight line segments, as illustrated in Figure 5.12. The approximation of the crack length is then computed as the summation of the length of the segments. The length of the actual crack could then be approximated, in the limit, as the length of the line segments tend to zero.

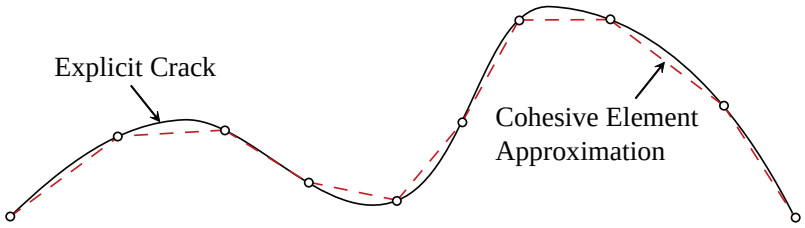

Figure 5.12: An arbitrary curve (solid), representing an explicit crack, and the straight line segments (dashed) representing the best representation of the curve by the mesh.

The topological operators we proposed in the previous two subsections are specifically designed to reduce mesh induced bias in polygonal meshes. Polygonal meshes, on average, present two potential directions for a crack to continue propagating along at each node. These limited paths can artificially increase the area of the fracture surface, and thus the

energy required to propagate a crack. In this section, we present a geometric study which quantifies the path deviation present in polygonal discretizations and illustrates the significant improvement provided by the new topological operators. Further investigation and quantification may be found in the accompanying publications [199, 200].

We define the path deviation, η, in two-dimensions as:

$$\eta = \frac{L_f}{L_c} - 1, \tag{5.25}$$

where L_f is the length of the fracture surface along the element facets, and L_c is the actual length of the crack which the fracture surface is attempting to represent. In this study, the actual crack length, L_c, is idealized as the straight line distance between a *start* and *end* point in the mesh. Following the reasoning in the above paragraphs, in order for a mesh to be able to represent an arbitrary crack, it is necessary that it be able to provide a good representation of a straight line segment. The length of the fracture surface is computed using Dijkstras greedy shortest path algorithm [222] between the same start and end points. Since the adaptive element-splitting operator is directional, restrictions are placed on the potential paths in the shortest path algorithm, such that the directionality is accounted for. The study is conducted on a circular domain of unit radius, centered on the origin. The start point is set as $(0, 0)$, and the end point is located at $(\sin\theta, \cos\theta)$, where $\theta = 1°, 2°, \ldots, 180°$. A schematic of the study for both a polygonal mesh and a refined mesh with element-splitting is illustrated in Figure 5.13.

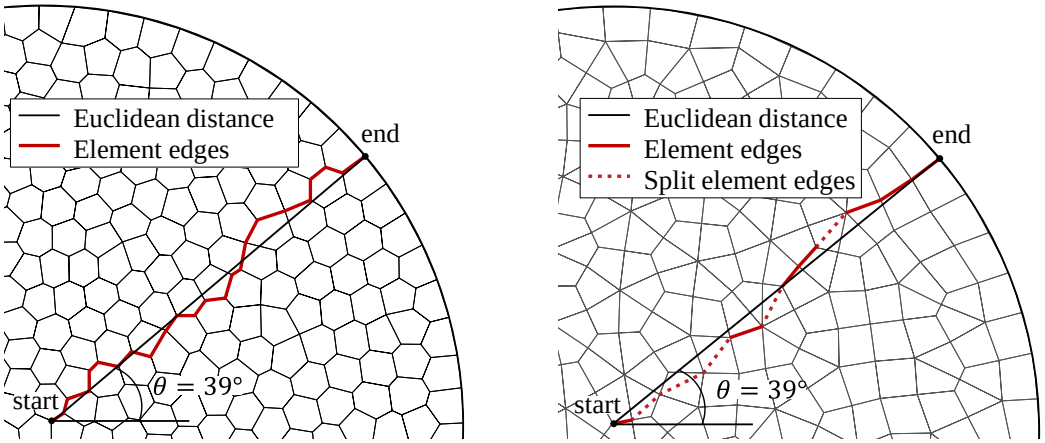

Figure 5.13: Schematic of the path deviation study, illustrating the shortest computed fracture surface (using Dijkstras shortest path algorithm) for (a) a polygonal mesh, and (b) a refined mesh. For visual clarity, the meshes illustrated here are much coarser than those used in the studies.

The results of the study are illustrated in Figure 5.14 and summarized in Table 5.1. From

the figure, it is clear that the polygonal mesh is isotropic, presenting no clearly preferred direction for crack propagation. In addition, both of the proposed topological operators maintain the isotropy of the base polygonal mesh. The base polygonal mesh produces an average path deviation of approximately 19.3%. When combined with element-splitting, the average path deviation reduces to approximately 4.45%, an improvement of over 75%. When the element-splitting operator is combined with adaptive refinement, the average path deviation reduces to approximately 1.71%, an improvement of over 90%. For comparison, the path deviation of the adaptively refined mesh with element-splitting is on par with that for the conjugate-directions mesh presented by Rimoli et al. [183]. However, because the refinement and element-splitting operators are performed adaptively, the computational storage costs are less than what they would be for the fixed conjugate-directions mesh.

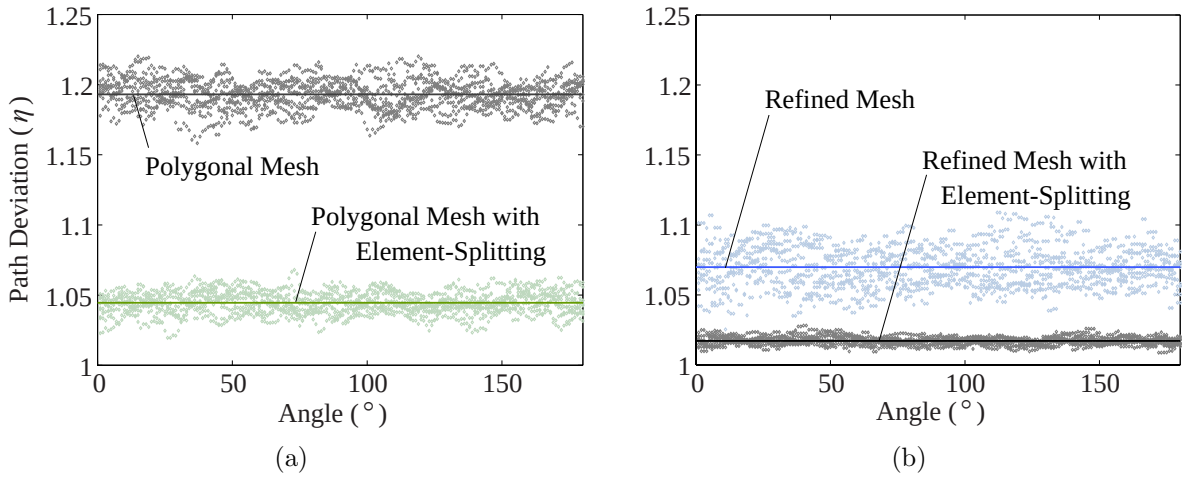

Figure 5.14: Results of the path deviation study. Results are displayed for ten, randomly generated: (a) polygonal meshes, with and without element-splitting; and (b) refined meshes with and without element-splitting. The horizontal lines represent the average deviation across all of the meshes.

Table 5.1: Summary of the results of the path deviation study for different meshing strategies.

Meshing Strategy	Average	Standard Deviation
Polygonal	0.1931	0.0013
Polygonal with Splitting	0.0445	0.0009
Polygonal with Refinement	0.0698	0.0021
Polygonal with Refinement and Splitting	0.0171	0.0004

5.3.4 Influence of topological operators on element quality

Here, we conduct a series of geometric studies on a mesh before and after the application of element-splitting and adaptive refinement. The studies are conducted on a circular domain, and the quality metrics used are the coefficient of variation in edge lengths, the element areas and the interior angles. First, we investigate the influence of collapsing small edges on element quality in the polygonal discretization. The element edge size is directly related to the critical time step for the explicit dynamic time integrator. Thus, when designing the discretization, we eliminate the presence of small edges. To eliminate small edges, the PolyMesher algorithm searches all the edges in the mesh by looping over all the elements. Given an edge of an element, the angle (β) between the vectors connecting the center of the element and the vertices forming the edge is computed [196]. The edge is collapsed into a single node when:

$$\beta < \epsilon \left(\frac{2\pi}{n} \right) \tag{5.26}$$

where n is the number of vertices of the element and ϵ is a user-defined tolerance. We investigate the influence of the user-defined tolerance on the coefficient of variation of the element edges when the mesh is adaptively refined with element splitting, as illustrated in Figure 5.15. In each case, we refine a mesh with 80 polygonal elements using the scheme outlined in Section 5.3.2. Further, we have randomly split each of the refined elements to demonstrate the worst case scenario for the adaptively-refined and split elements around the crack tip. From this preliminary investigation, we demonstrate that the higher the user-

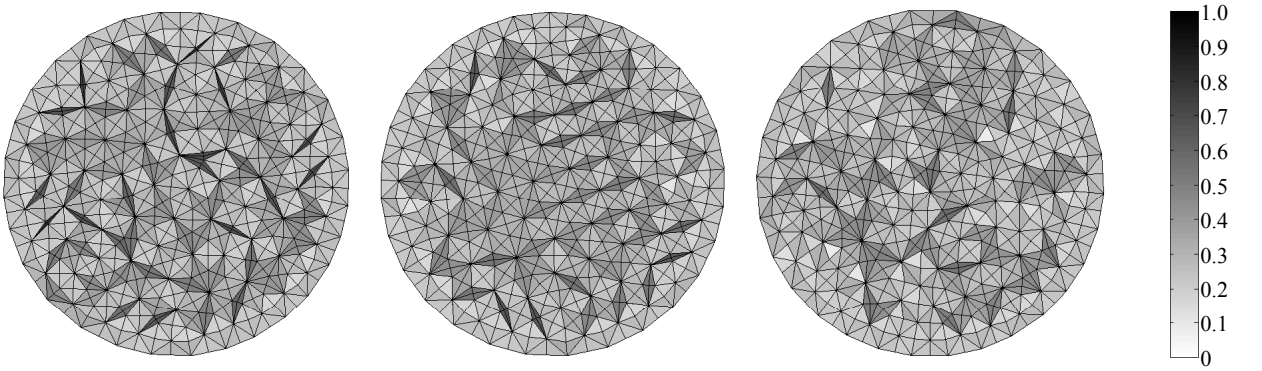

Figure 5.15: Influence of user-defined tolerance on the coefficient of variation of edge lengths. A user-defined tolerance of: (a) $\epsilon = 0.1$, (b) $\epsilon = 0.3$, and (c) $\epsilon = 0.5$.

defined tolerance, the higher the quality of the discretization after refinement and splitting. Based on this investigation, we recommend that the user-defined tolerance be selected as a

minimum of 0.4, for dynamic fracture simulations, which is the value used in the remainder of this chapter.

For each user-defined tolerance, we also investigate the change in the quality of the polygonal mesh with the application of the adaptive operators. We illustrate the results of our investigation, for $\epsilon = 0.4$ in Figures 5.16 to 5.18. The coefficient of variation in edge lengths is represented by a contour plot in Figure 5.16. Each mesh contains 946 elements. We observe that the uniform polygonal discretization is superior to the cases after the topological operators are applied, in terms of element quality. The polygonal mesh (Figure 5.16(a)) shows a very uniform distribution of low variation, while the split polygonal mesh demonstrates a uniform distribution of high variation. The refined polygonal mesh with splitting contains a wide range of variation.

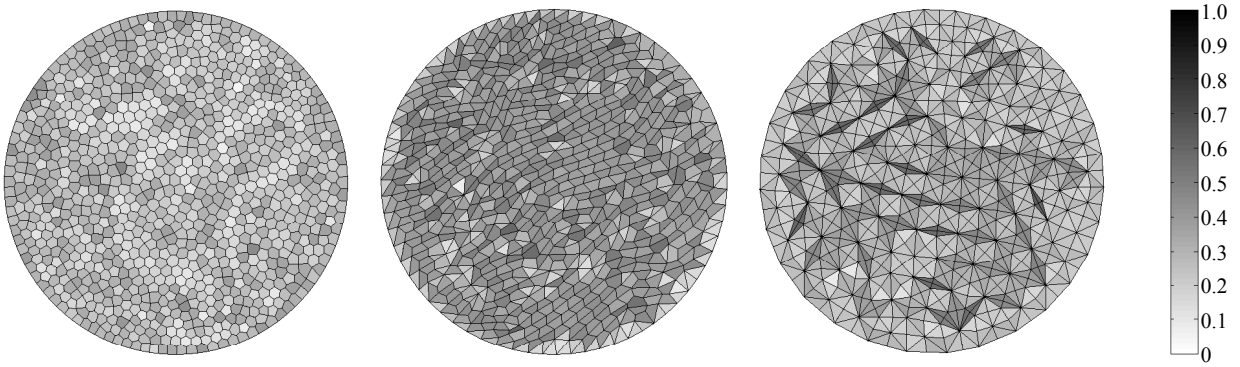

(a) (b) (c)

Figure 5.16: Influence of meshing strategy on the coefficient of variation of edge lengths. (a) polygonal mesh, (b) polygonal mesh with element-splitting, and (c) polygonal mesh with refinement and element-splitting.

To gain further insight into the influence of the topological operators on the mesh quality, we investigate the element areas and interior angles of the mesh. Each mesh contains $23,576$ elements. The histograms of element areas and interior angles are depicted in Figures 5.17 and 5.18. These plots indicate that topological operators reduce the quality of the polygonal mesh. However, we note that, since these operators are only applied in the immediate vicinity of the crack, its influence on the global response is limited, and the use of a high user-defined tolerance further limits the reduction in quality of the mesh.

5.4 Constitutive relations

While we have approached the problem of mesh induced bias with the geometrically and topologically unstructured methods outlined in this chapter, we also investigate the use of

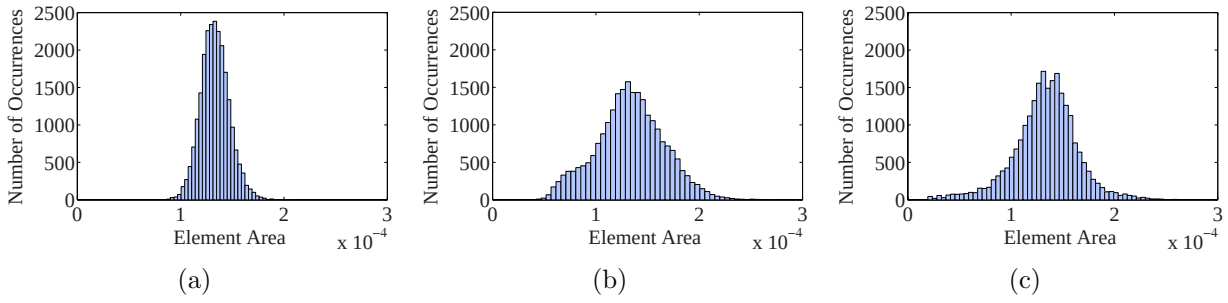

Figure 5.17: Histograms of element areas for a (a) polygonal mesh, (b) polygonal mesh with element-splitting, and (c) polygonal mesh with refinement and element-splitting.

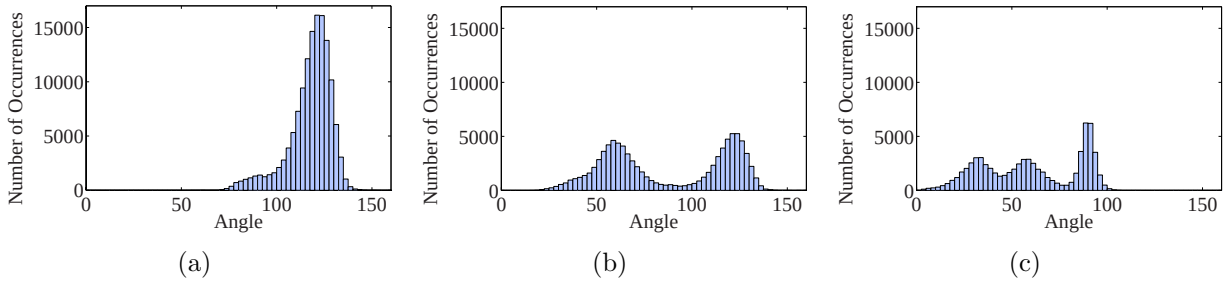

Figure 5.18: Histograms of interior angles for a (a) polygonal mesh, (b) polygonal mesh with element-splitting, and (c) polygonal mesh with refinement and element-splitting. Note, at the boundaries of the domain the polygonal elements tend to contain edges perpendicular to the outer edges - resulting in a small peak in frequency of angles around 90° for the polygonal mesh.

constitutively unstructured means to reducing mesh dependency [131]. A feature of the cohesive element method is the ability to separate the constitutive relation of the bulk elements from that of the cohesive elements. In this section, we discuss the bulk and cohesive constitutive relations used in this investigation, and the means by which we investigate microscale heterogeneities. A further discussion on this topic will be provided in Section 6.2.

5.4.1 Bulk material model

The focus of this work is on either homogeneous or homogenized materials; however, in reality, it is recognized that all materials contain inhomogeneities at the microscale. To account for these microscale inhomogeneities, the primary properties of the material are randomly assigned. The bulk material is elastic with an average elastic modulus, E_o, and Poisson's ratio, ν. While the elastic modulus is a global parameter, the modulus at the microscale is varied. To model this variation numerically, the elastic modulus is assigned to follow a statistically random Weibull [223] distribution:

$$E = E_o(-\ln(1-\rho)^{1/m}), \tag{5.27}$$

where E_o is the average elastic modulus, m is the Weibull modulus, and ρ is a randomly generated number between 0 and 1.

5.4.2 Extrinsic PPR potential-based cohesive zone model

In the dynamic simulations performed in this work, the creation of fractured surfaces, i.e. crack advancement, is achieved by means of cohesive zone elements, which are inserted at facets between finite elements. Once a cohesive element is inserted, its behavior is governed by the traction-separation relation of the extrinsic Park-Paulino-Roesler (PPR) cohesive model [51]. Next, we describe the extrinsic PPR softening model, and also comment on the unloading/reloading and contact formulations used in this work.

5.4.2.1 Cohesive softening relation

The extrinsic PPR cohesive model is chosen to represent the nonlinear softening behavior in the inelastic zone of damage in front of the crack-tip [51]. The extrinsic PPR cohesive model is potential-based, meaning that the traction-separation relation is derived from a potential function and the unloading and contact relations are independent of the model. The potential function for the extrinsic PPR model is given as:

$$\Psi\left(\Delta_n, \Delta_t\right) = \min\left(\phi_n, \phi_t\right) + \left[\Gamma_n \left(1 - \frac{\Delta_n}{\delta_n}\right)^{\alpha} + \langle \phi_n - \phi_t \rangle\right] \times \left[\Gamma_t \left(1 - \frac{|\Delta_t|}{\delta_t}\right)^{\beta} + \langle \phi_t - \phi_n \rangle\right], \tag{5.28}$$

where the Macaulay bracket $\langle \cdot \rangle$ is defined such that $\langle x \rangle = \left(|x| + x\right)/2$.

The normal, T_n, and tangential, T_t, tractions are calculated by taking the derivative of the potential with respect to the normal crack opening, Δ_n, and tangential crack opening, Δ_t, respectively:

$$T_n\left(\Delta_n, \Delta_t\right) = \frac{\partial \Psi}{\partial \Delta_n} = -\alpha \frac{\Gamma_n}{\delta_n} \left(1 - \frac{\Delta_n}{\delta_n}\right)^{\alpha-1} \left[\Gamma_t \left(1 - \frac{|\Delta_t|}{\delta_t}\right)^{\beta} + \langle \phi_t - \phi_n \rangle\right], \tag{5.29}$$

$$T_t\left(\Delta_n, \Delta_t\right) = \frac{\partial \Psi}{\partial \Delta_t} = -\beta \frac{\Gamma_t}{\delta_t}\left(1 - \frac{|\Delta_t|}{\delta_t}\right)^{\beta-1}\left[\Gamma_n\left(1 - \frac{\Delta_n}{\delta_n}\right)^{\alpha} + \langle \phi_n - \phi_t \rangle\right]\frac{\Delta_t}{|\Delta_t|}, \qquad (5.30)$$

where ϕ_n and ϕ_t are the mode I and mode II fracture energies, and α and β are the mode I and mode II shape parameters. The energy constants Γ_n, and Γ_t are defined as:

$$\Gamma_n = (-\phi_n)^{\langle \phi_n - \phi_t \rangle/(\phi_n - \phi_t)}, \qquad \Gamma_t = (-\phi_t)^{\langle \phi_t - \phi_n \rangle/(\phi_t - \phi_n)} \qquad (\phi_n \neq \phi_t) \qquad (5.31)$$

for different fracture energies, and simplify to:

$$\Gamma_n = -\phi_n, \qquad \Gamma_t = 1 \qquad (\phi_n = \phi_t) \qquad (5.32)$$

for equal fracture energies in both mode I and mode II separation.

Similar to the intrinsic traction-separation relations described in the previous chapters, the extrinsic traction-separation relations are defined within a domain of dependence, as illustrated in Figure 5.19. The normal and tangential final crack opening widths are:

$$\delta_n = \alpha \phi_n / \sigma_{\max} \quad \text{and} \quad \delta_t = \beta \phi_t / \tau_{\max}, \qquad (5.33)$$

respectively, and the normal and tangential conjugate final crack opening widths are:

$$\bar{\delta}_n = \delta_n - \delta_n \left(\frac{\langle \phi_n - \phi_t \rangle}{\phi_n}\right)^{1/\alpha} \quad \text{and} \quad \bar{\delta}_t = \delta_t - \delta_t \left(\frac{\langle \phi_t - \phi_n \rangle}{\phi_t}\right)^{1/\beta}, \qquad (5.34)$$

where $\sigma_{\max}$ and $\tau_{\max}$ are the mode I and mode II cohesive strengths, respectively. In total, there are six user inputs to the extrinsic PPR cohesive model: ϕ_n, ϕ_t, α, β, $\sigma_{\max}$, and $\tau_{\max}$. A set of sample traction-separation relations are illustrated in Fig. 5.20.

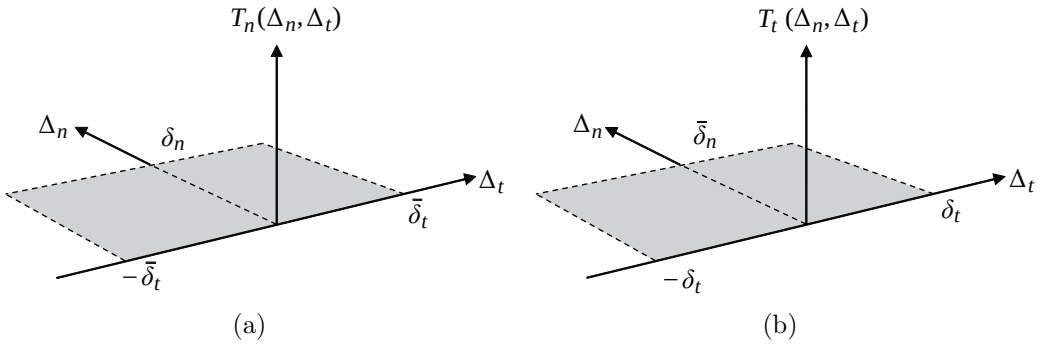

Figure 5.19: Domain of dependance for the (a) normal, and (b) tangential tractions; defined by the final crack opening widths (δ_n, δ_t), and the conjugate final crack opening widths ($\bar{\delta}_n$, $\bar{\delta}_t$).

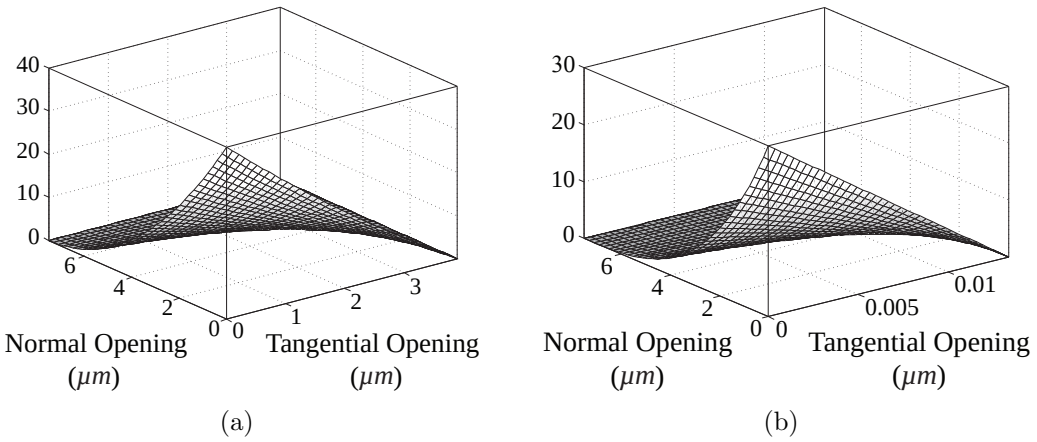

(a) (b)

Figure 5.20: Extrinsic traction-separation relations for (a) normal opening ($\phi_n = 100N/m$, $\sigma_{\max} = 40MPa$, $\alpha = 3.0$), and (b) tangential opening ($\phi_t = 200N/m$, $\tau_{\max} = 30MPa$, $\beta = 5.0$).

5.4.2.2 Unloading/Reloading relation

In this investigation, the unloading/reloading relation is coupled, meaning that unloading in the normal direction is coupled to that in the tangential direction. In addition, we assume that unloading occurs linearly back to the origin, as illustrated in Figure 5.21. Contact is assumed to occur when the normal separation within a cohesive element becomes negative. We use the penalty stiffness approach to contact, in which a high stiffness counteracts the interpenetration of elements. This approach is popularly implemented in conjunction with cohesive elements, however, others are available [53, 140, 224].

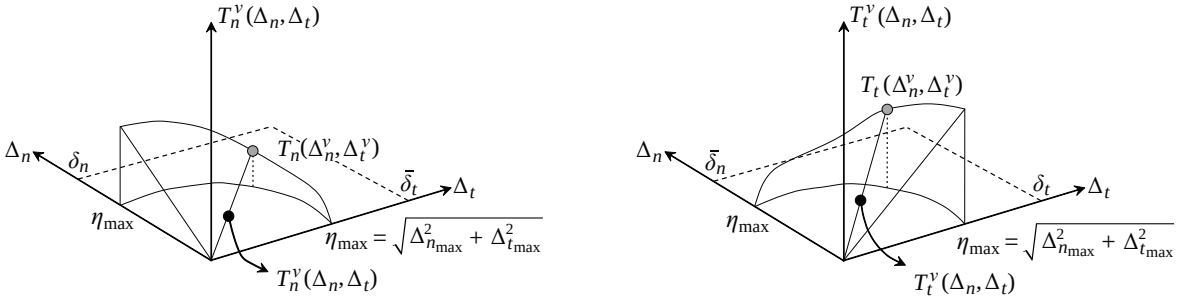

(a) (b)

Figure 5.21: Depiction of the coupled unloading schemes for (a) normal and (b) tangential tractions, with linear unloading/reloading to the origin [149].

5.4.2.3 Cohesive heterogeneity

To further investigate the influence of constitutively unstructured means on reducing mesh dependency, we also vary the primary cohesive parameters. Both the cohesive strength

and fracture energy, attributes of the cohesive elements, are individually selected to follow a modified weakest link Weibull distribution; where the probability of a cohesive element having a lower cohesive strength or fracture energy increases with increasing element size [131]:

$$\gamma = \frac{L_s^{1/m}}{L_f^{1/m}} \gamma_o (-\ln(1-\rho)^{1/m}), \tag{5.35}$$

where γ_o is the average cohesive property (in this work, γ_o is either the cohesive strength or the cohesive fracture energy), L_f is the length of the cohesive element, L_s is a scaling parameter, and m is the Weibull modulus. For a uniform mesh, the scaling parameter is selected to be the average facet length; whereas, for an adaptively refined mesh, the scaling parameter is selected to be the average facet length of an equivalent, uniformly refined mesh. Figure 5.22 illustrates the distribution of facet lengths for a typical mesh with approximately 16,000 facets before refinement, and approximately 67,000 facets after refinement. This approach was proposed by Zhou and Molinari [131], as a means to address mesh dependency from a constitutive perspective. While it has proven useful in many situations with triangular and tetrahedral elements, its use has not been investigated with polygonal elements.

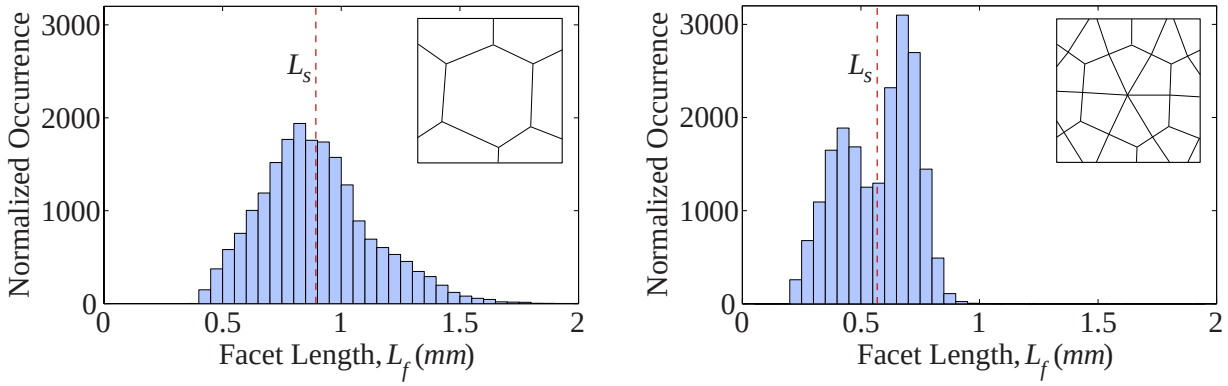

Figure 5.22: Facet length distribution for a typical random mesh consisting of 6,000 elements. There are approximately 16,000 facets before refinement and approximately 67,000 facets after uniform refinement. The domain for this example is $100 \times 100mm$. (a) Polygonal discretization, and (b) uniformly refined discretization. The dashed line corresponds to the average facet length in the mesh (L_s), and is equivalent for both the uniformly refined mesh and the adaptively refined mesh.

To illustrate the effect of the Weibull modulus on the material distribution, a sample mesh with 16,000 randomly numbered facets was generated, and the cohesive properties of each were randomly assigned. For example, when a mesh with an average cohesive strength $\sigma_o = 1.733GPa$ was modeled, the resulting variation of cohesive strength for a Weibull

modulus of $m = 50$, 30, and 10 is illustrated in Figure 5.23. Clearly, the smaller the value of m, the greater the range of assigned properties, and thus the greater the overall heterogeneity in the material. We recognize that there are other methods for randomly distributing material properties, and will discuss some alternatives in Chapter 6.

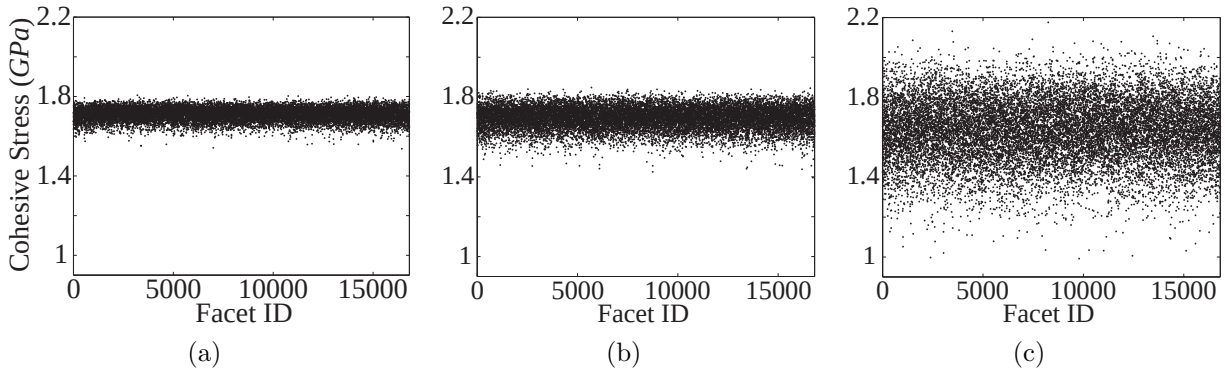

Figure 5.23: Example statistical distribution for a Weibull modulus of (a) $m = 50$, (b) $m = 30$ and (c) $m = 10$. The average cohesive strength is prescribed as $\sigma_o = 1.733GPa$.

5.5 Pervasive fracture and crack initiation example problems

In this section, we use two numerical examples to explore the effectiveness of the element-splitting operator in pervasive fracture and crack initiation problems. The first example considers the fragmentation of a thick cylinder due to an internal impact pressure. The second example investigates the crack initiation of an epoxy plate with randomly distributed holes. Comparisons to experiments are made where possible.

5.5.1 Pressure loaded cylinder

This example investigates the fragmentation of a cylinder with an internal impact pressure. This problem is particularly suitable for the use of unstructured meshes, as structured meshes can induce undesirable fracture patterns; see [131] for a discussion of unsatisfactory results obtained due to mesh dependency for the pressure loaded cylinder. The thick cylinder has an inner radius of $80mm$ and an outer radius of $150mm$, as illustrated in Figure 5.24(a). The internally applied pressure increases linearly from $0MPa$ to $400MPa$ over the course of $1\mu s$ then decreases exponentially according to $P(t) = 400e^{(-t/100)}$, as illustrated in Figure 5.24(b). The material has an elastic modulus of $210GPa$, a Poisson's ratio of 0.3 and a

density of $7850 kg/m^3$. The cohesive strength, fracture energy, and shape parameter in both modes are $850 MPa$, $2000 N/m$ and 2, respectively.

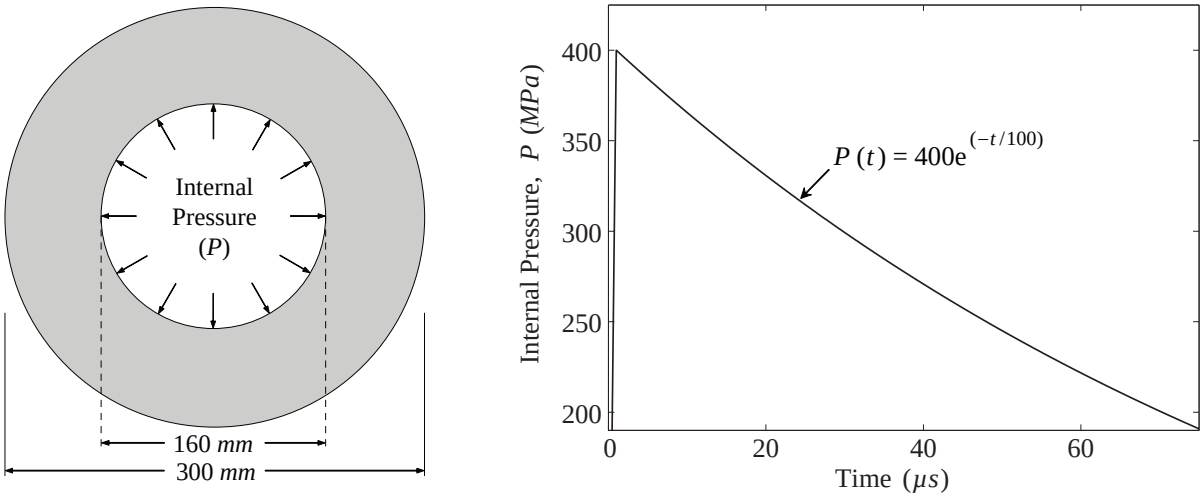

Figure 5.24: (a) Geometry of the thick cylinder example, and (b) evolution of internal impact pressure with time.

In a prior numerical investigation of this example, Rabczuk and Belytschko [32] used a mesh free cracking-nodes method, and observed that the number of large and small fragments are consistent, regardless of the number of particles used to model the geometry. Song and Belytschko [225] used a cracking nodes method within the finite element framework. To break the mesh induced symmetry in their model, they randomly perturbed the elastic modulus throughout the model by $\pm 5\%$. They also show that the number of fragments is consistent through mesh refinement, and are on the order of 20 fragments. Zhou and Molinari [131] implemented a similar problem in three-dimensions. They also distributed the cohesive strength based on a modified weakest link Weibull distribution to overcome mesh dependency in their model. Without distributing the cohesive strength, they found that cracks initiated in the interior of the cylinder wall. Paulino et al. [221], used an edge-swap operator to increase the number of fracture paths in their finite element mesh. To overcome symmetry in their model, they implemented nodal perturbation, but also imposed restrictions on the location of crack initiation, so that they do not initiate in the interior of the cylinder wall.

In the present study, the domain is discretized at two levels of refinement, 5,000 and 10,000 polygons, and we investigate cases with and without element-splitting. No external method (e.g. perturbation) is required to break mesh symmetry, because the mesh is inherently random, and no restrictions are placed on the initiation of fracture. The final crack patterns

for all cases are illustrated in Figure 5.25, and the evolution of the strain energy, as fracture progresses for the mesh containing 10,000 elements (with element-splitting enabled), is illustrated in Figure 5.26.

Regardless of the level of refinement, without element-splitting we observe that many cohesive elements are inserted near the internal boundary. The insertion of cohesive elements results in excessive material softening in this region, causing the cracks to arrest instead of propagating completely through the thickness of the cylinder. At a finer level of discretization, the standard polygonal meshes are still not able to capture the full fragmentation of the cylinder. Using the same initial polygonal meshes and boundary conditions, but allowing for element-splitting, the resulting behavior and fragmentation patterns agree with the expected results from the literature [32, 221, 225]. In comparison, the mesh with 5,000 polygonal elements contains 9,419 nodes, whereas that presented by Paulino et al. [221], for the 4k mesh, results in similar fracture behavior, but contains 12,800 quadratic elements and 25,920 nodes.

The stress and strain are initially concentrated around the inner boundary of the cylinder (Figure 5.26(a)), causing fracture to initiate almost uniformly around the inner surface (Figure 5.26(b)). The majority of these cracks arrest after a small amount of propagation, however, several cracks propagate through the entire thickness (Figures 5.26(c) to 5.26(e)). At the end of the simulation ($64\mu s$), we can quantify the number of fragments, where a fragment is defined as the volume of material between two cracks which are continuous and span the thickness of the cylinder. The final geometry consists of 18 fragments for the 5,000 element case and 23 fragments for the 10,000 element case, which is in good agreement with the results available in the literature.

5.5.1.1 Influence of material heterogeneity

Here, we investigate the influence of material heterogeneity on the number of fragments produced and the average crack-tip velocity. We consider variations in the bulk elastic modulus, the cohesive fracture energy and the cohesive strength. The investigation is conducted on a polygonal mesh containing 5,000 elements, with element-splitting enabled. For each material property we vary, we consider three different Weibull moduli, $m = 10$, 30, and 50; and for each modulus, three different random instances are simulated (a total of 27 simulations). A summary of the results is provided in Table 5.2. Based on the investigation, statistically distributing the material properties does not have a significant influence on the average crack-tip velocity. The only exception might be the case when the cohesive strength is randomly distributed, with a Weibull modulus of $m = 10$. In this case, cracking initiates

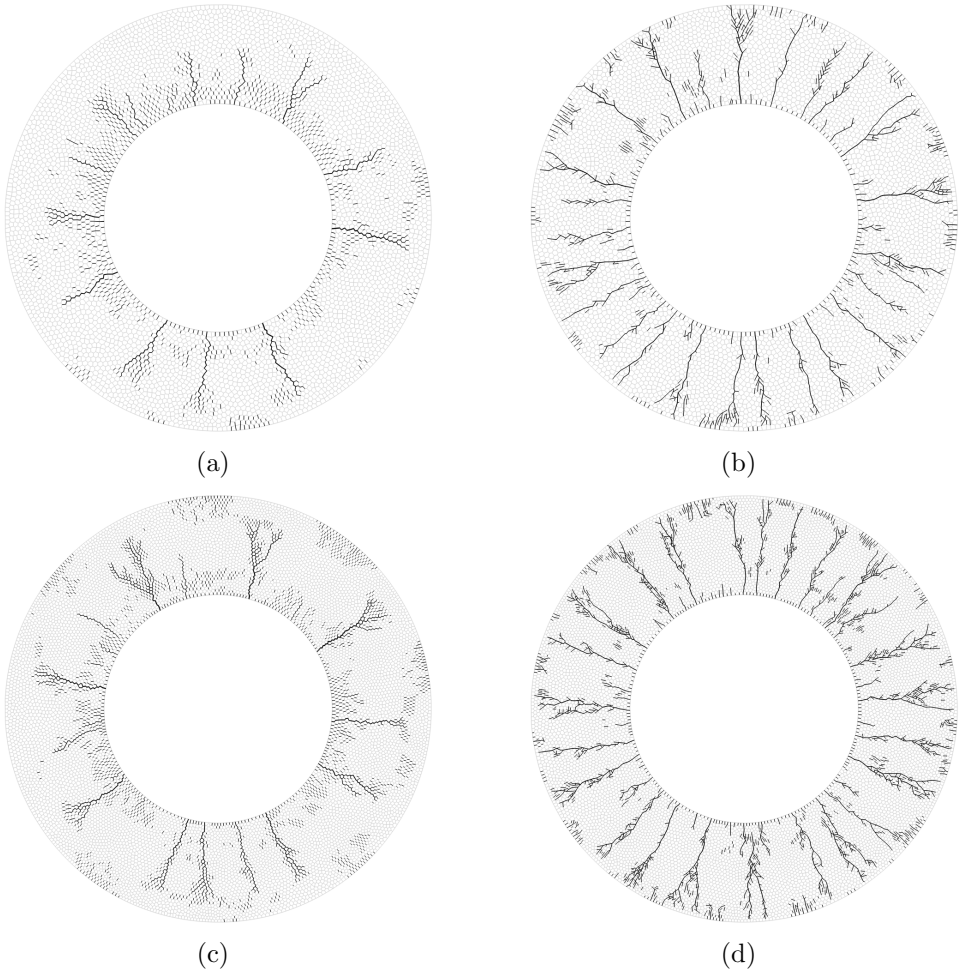

Figure 5.25: Comparison of the results of the pervasive fragmentation of a cylinder example. Results are displayed at a time of $64\mu s$. (a) 5,000 elements without element-splitting, (b) 5,000 elements with element-splitting, (c) 10,000 elements without element-splitting, and (d) 10,000 elements with element-splitting.

sooner, but the time taken to fail completely (29.7 μs) roughly corresponds to that of the other cases (an average of approximately 27.7 μs), resulting in an average crack-tip velocity close to that in all the other cases considered.

As well, there is little variation in the number of fragments produced. The only exception might be the case when the cohesive strength is randomly distributed, with a Weibull modulus of $m = 10$. A typical result for this case is illustrated in Figure 5.27. The black lines in Figure 5.27(b) represent all the cohesive elements which have been inserted in the model. The insertion of a cohesive element alone, does not signify the development of a crack, the crack is only fully developed once the cohesive element opens beyond the final crack opening width, as discussed in Section 5.4.2. However, the insertion of a cohesive element does signify some damage in the material has occurred, and the material in this region

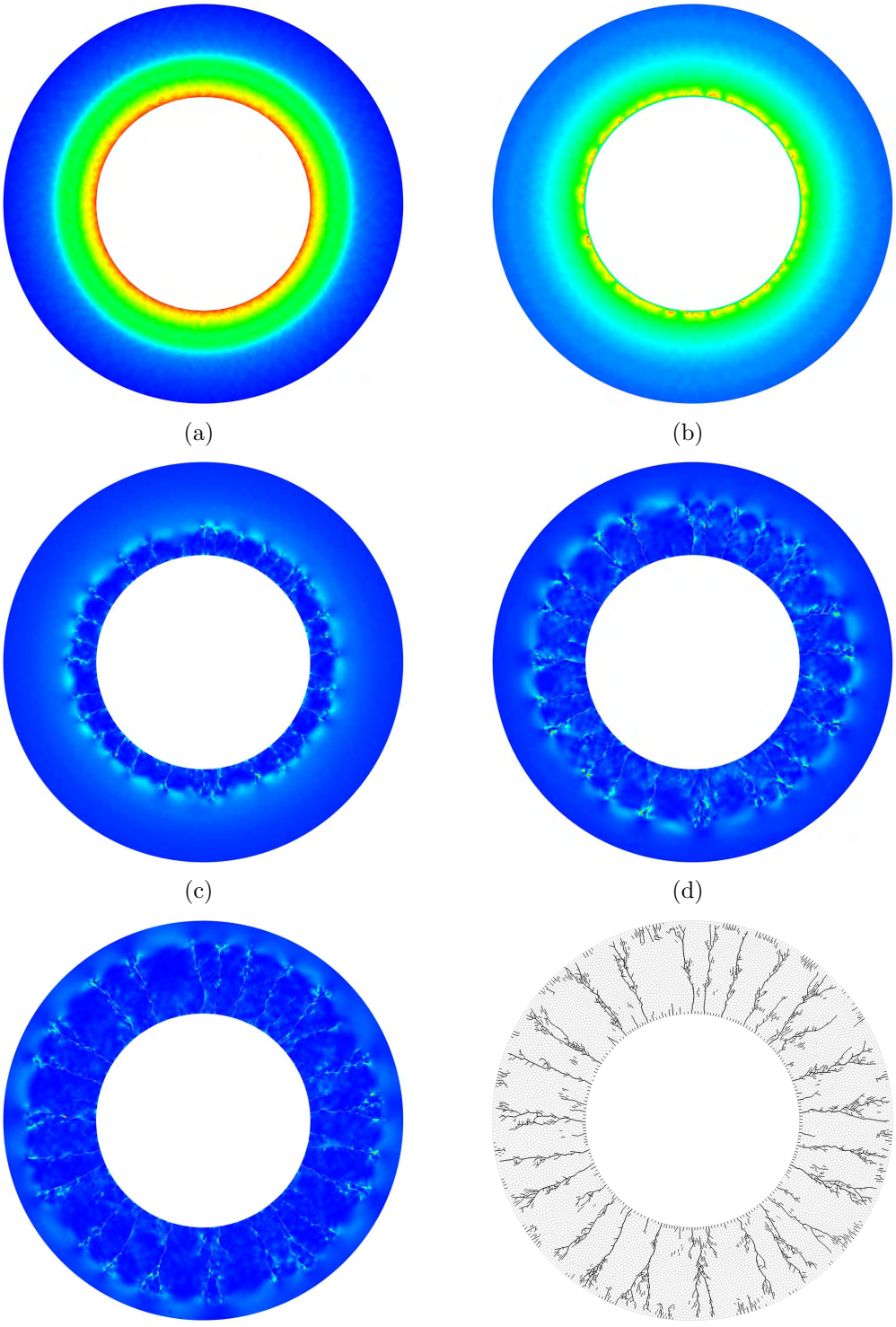

Figure 5.26: Evolution of strain energy through the fragmentation process, for a mesh containing 10,000 elements with element-splitting enabled. Results are displayed at a time of: (a) $30\mu s$, (b) $40\mu s$, (c) $47.5\mu s$, (d) $55\mu s$, and (e) $60\mu s$. (f) Final fragmented geometry at $64\mu s$.

Table 5.2: Summary of the investigation of material heterogeneity. A fragment is defined as the mass of material between two through-thickness cracks. For each case, the results are an average of three simulations.

		Number of Fragments	Crack-tip Velocity (m/s)
Elastic Modulus (E)	$m = 10$	17.67	2439
	$m = 30$	20.00	2517
	$m = 50$	19.00	2573
Cohesive Energy (ϕ)	$m = 10$	19.67	2592
	$m = 30$	19.67	2592
	$m = 50$	20.67	2592
Cohesive Stress (σ)	$m = 10$	15.33	2356
	$m = 30$	19.00	2473
	$m = 50$	20.33	2430

has softened. This damage in the material dissipates energy, and can prevent surrounding cracks from fully developing, thus, possibly providing a explanation as to why fewer cracks propagate through the full thickness of the cylinder.

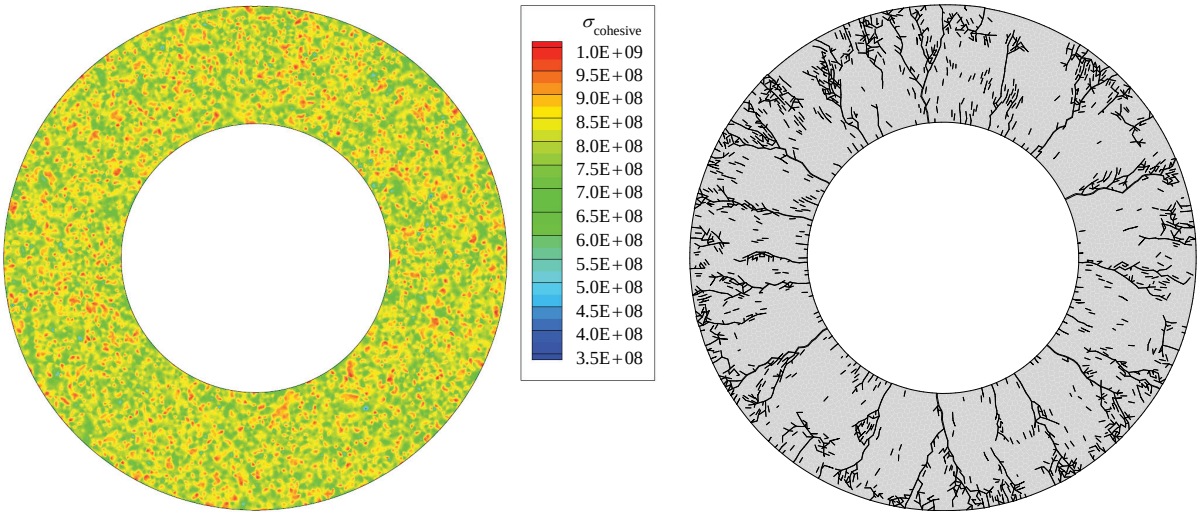

(a) (b)

Figure 5.27: (a) Contour plot of cohesive stress, illustrating the distribution of material heterogeneity, with a Weibull modulus of $m = 10$; and (b) the corresponding crack pattern after fragmentation.

5.5.2 Epoxy plate with holes

Adapted from a problem investigated experimentally by Al-Ostaz and Jasiuk [226], this example investigates the fracture of an epoxy plate with dimensions of $89 \times 98.4 \times 3.2mm$, containing 31 randomly distributed holes, as illustrated in Figure 5.28. In their experimental investigation, Al-Ostaz and Jasiuk observed different fracture patterns for several specimens containing the same arrangement of holes, as illustrated in Figure 5.29. They attributed the non-unique fracture patterns to microscopic inhomogeneities in the material, and to flaws or microcracks at the hole surfaces. Numerically, they simulated the experiments using both the finite element and the spring network methods. To model fracture, they removed elements, or bonds, based on a maximum elastic strain energy criterion. They investigated different fracture criteria and mesh discretizations, and captured different fracture paths for each scenario.

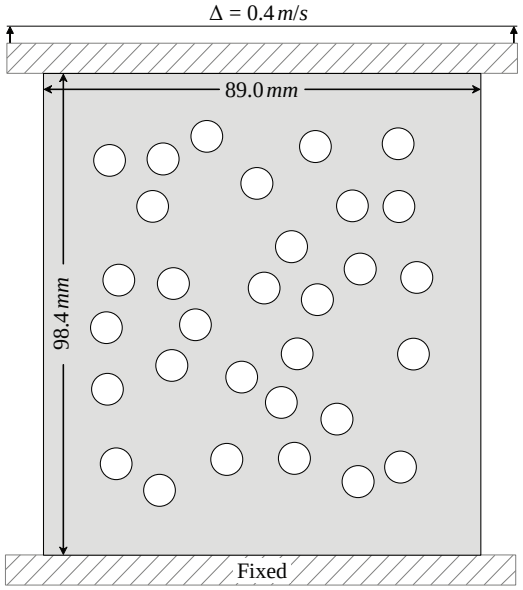

Coordinates of Hole Locations (mm)			
(14.86, 18.57)	(26.60, 55.30)	(72.46, 70.99)	(40.31, 36.25)
(23.70, 13.09)	(45.03, 54.38)	(63.01, 71.14)	(48.54, 31.07)
(13.03, 33.66)	(22.18, 70.99)	(50.67, 62.76)	(59.97, 27.56)
(37.26, 19.49)	(13.34, 80.59)	(64.69, 58.19)	(51.28, 19.64)
(26.14, 38.53)	(24.31, 80.74)	(76.27, 56.51)	(72.77, 17.96)
(12.73, 46.15)	(43.51, 75.71)	(55.85, 52.10)	(64.08, 14.91)
(31.01, 46.76)	(55.40, 83.18)	(75.51, 40.97)	(33.30, 85.31)
(15.32, 55.90)	(72.46, 83.94)	(51.59, 40.97)	

Figure 5.28: Geometry of the epoxy plate with holes example, and the corresponding hole locations (extracted from Figure 13 in [226]).

The problem of a plate with a random distribution of holes, has been investigated by many researchers, using multiple methods. The strain localization and fracture between holes in a plate was investigated by Becker and Smelser [227]. In their work, to simulate the loss of stiffness due to fracture, finite elements were deleted based on an out-of-plane strain criteria. When the local out-of-plane strain fell in the range of -0.25 to -0.30, the element was removed from the model. This method of fracture representation was noted to not be representative of any explicit fracture mechanism. Dynamic behavior was not considered, instead, mass scaling was used to represent the experiment's quasi-static loading

condition. Ostoja-Starzewski and Wang [228] employed particle modeling to simulate the dynamic fracture and fragmentation of epoxy plates with randomly distributed holes. The plates were assumed to be inhomogeneous, by applying a very small ($\pm 0.005\%$) random perturbation to the elastic modulus and the tensile strength. Their investigation of material heterogeneity illustrated that perturbations in the elastic modulus have a greater influence on the fracture patterns than perturbations in the tensile strength.

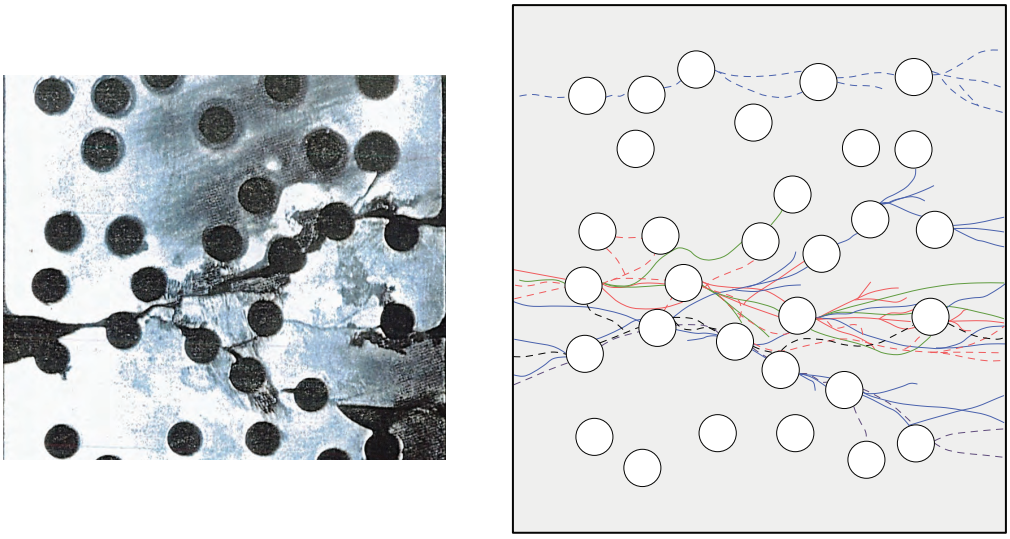

(a) (b)

Figure 5.29: (a) A sample experimental fracture path for one epoxy plate (image extracted from Al-Ostaz and Jasiuk [226]). (b) Compilation of seven experimental results, adapted from Figure 13 in [226], displaying the variation in fracture patterns for macroscopically similar plates.

To reproduce this problem, the hole locations are extracted from Figure 13 in reference [226], as they are not listed explicitly in the literature. Five unique meshes are generated, with 6,000 elements each. The element seeds are concentrated around the holes using the probability density function illustrated in Figure 5.30(a). A sample graded mesh is plotted in Figure 5.30(b). The epoxy has an elastic modulus of $3.26GPa$, a Poisson's ratio of 0.38, a density of $1100kg/m^3$, and plane stress conditions are assumed. The average mode I fracture energy (ϕ_n), cohesive strength ($\sigma_{\max}$), and shape parameter (α) are set as $100N/m$, $62.86MPa$ and 2, respectively. The mode II fracture properties are assumed to be the same as the mode I fracture properties. A small vertical velocity of $0.04m/s$ is applied to the upper surface of the plate, to mimic the quasi-static loading conditions in the experiments [228]. In this example, we investigate the influence of the holes on the distribution of stress in the plate, and the influence of material heterogeneity (both uniform and localized) on the global fracture patterns.

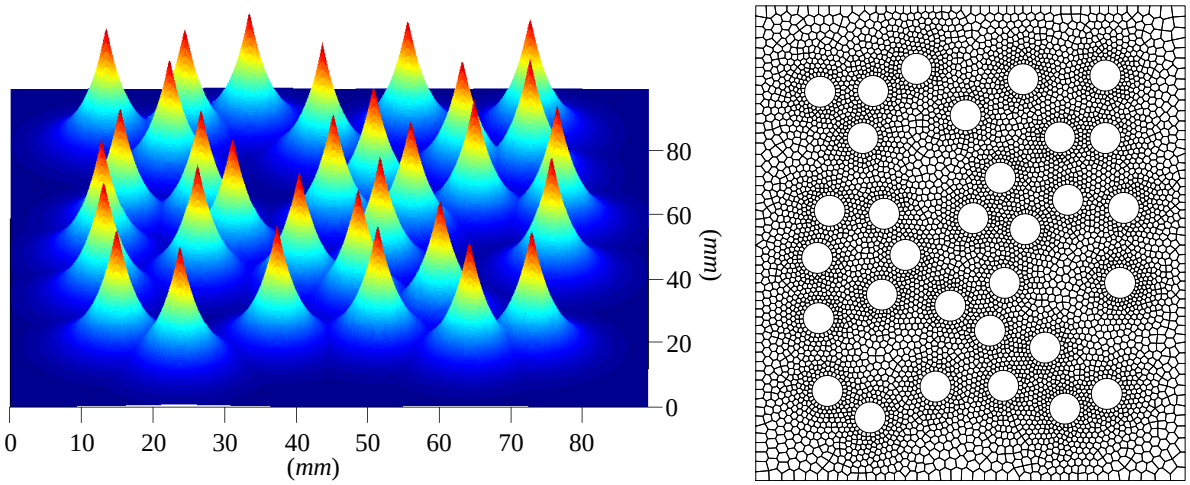

(a) (b)

Figure 5.30: (a) Three-dimensional contour plot of the probability density function, showing the concentrated probability of generating seeds around the holes. (b) Sample mesh for the epoxy plate with holes example, showing the gradation around each hole.

5.5.2.1 Influence of the holes on the stress field

First, we examine the elastic stress field in the uncracked specimen, immediately prior to fracture. Al-Ostaz and Jasiuk [226] experimentally observed the stress field in the specimen using photoelasticity. Their experimental results are illustrated in Figure 5.31(a). The numerically obtained principal stress field is illustrated in Figure 5.31(b), for the case of a homogenous material. The numerical results are shown to be in good agreement with the experimental results. Both approaches illustrate that the highest stresses occur at the surfaces of the holes along lines perpendicular to the line of loading, however, the magnitude of stress depends on the local geometry. For this particular arrangement of holes, the maximum stress is between the two holes placed in a most critical position. The maximum stress depends on the distance from, and direction to, neighboring holes; and the hole's location with respect to the applied load.

5.5.2.2 Influence of microscale heterogeneities on fracture patterns

In this section, we investigate the influence of constitutive heterogeneity in the specimen. We consider different cases for the distribution of material properties. The first case considers uniform heterogeneity in the material, as illustrated in Figure 5.32(a). However, in the experimental work of Al-Ostaz and Jasiuk [226], the authors mention that one source of the randomness in the fracture patterns may be due to a distribution of flaws at the surface of

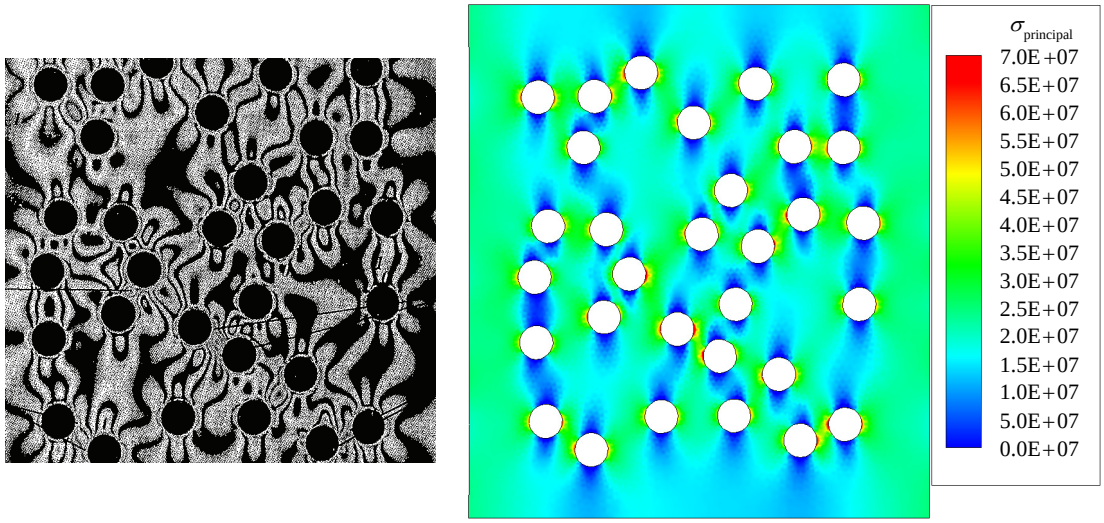

(a) (b)

Figure 5.31: (a) Stress field obtained by a photo-elasticity method for an epoxy plate (image extracted from Al-Ostaz and Jasiuk [226]), and (b) corresponding principal stress field obtained from the numerical simulation. The two results display similar stress contours and locations of concentration.

the holes (due to the manner in which the holes were drilled). Because of this, the second case we consider assumes that the material heterogeneity is concentrated around the holes, as illustrated in Figure 5.32(b). The results of our study demonstrated a negligible difference between the two different scenarios, so the conclusions we provide are general. For the sake of brevity, we only consider a variation in elastic modulus and cohesive strength, and only consider a Weibull modulus of $m = 5$ and 10. We continue to use 5 randomly generated meshes, and conduct 3 simulations for each random distribution (a total of 120 simulations).

When the elastic modulus of the epoxy plate is randomly assigned, we observe a wide variation in fracture patterns spanning the middle to lower portion of the plate. For the sake of brevity, we do not present all of the results, but provide typical results in Figure 5.33. The results shown are for a Weibull modulus of $m = 5$, but similar results were observed for the case of $m = 10$. Regardless of the material distribution, or mesh, cracks were not observed in the upper portion of the plate, contrary to the experimental results in Figure 5.29(b). Alternatively, when the cohesive strength of the plate is randomly assigned, we observe a range of fracture behavior, with cracks spanning the entire height of the plate. Similarly to before, we only illustrate typical results in Figure 5.34. As seen in Figure 5.34(b), with a variation in cohesive strength, cracks formed in the upper portion of the plate, capturing the outlying case observed in the experiments.

Through this numerical investigation, we were able to corroborate the conclusion of the authors who investigated this example experimentally; who noted that the different fracture

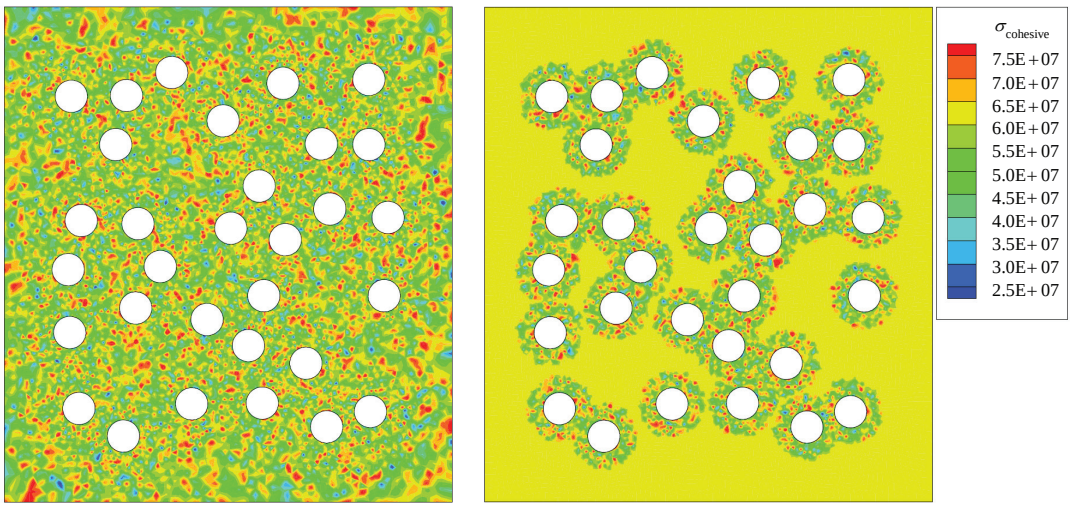

(a) (b)

Figure 5.32: Contour plot of cohesive stress showing the (a) uniform, and (b) local distribution of material heterogeneity.

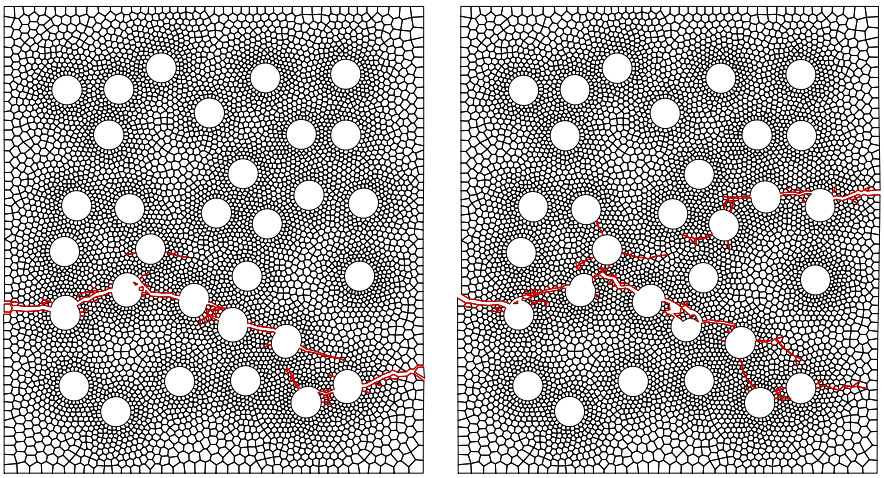

(a) (b)

Figure 5.33: Typical fracture patterns in the epoxy plate specimen, when the elastic modulus is statistically distributed. In the results shown, the modulus follows the Weibull distribution in Equation 5.27, with $m = 5$.

patterns for macroscopically similar plates may be due to microscale heterogeneities. While the above examples have shown that material heterogeneity has a significant influence on the fracture patterns of problems concerning pervasive fracture and crack initiation, the following three examples investigate its influence on problems dominated by a single crack.

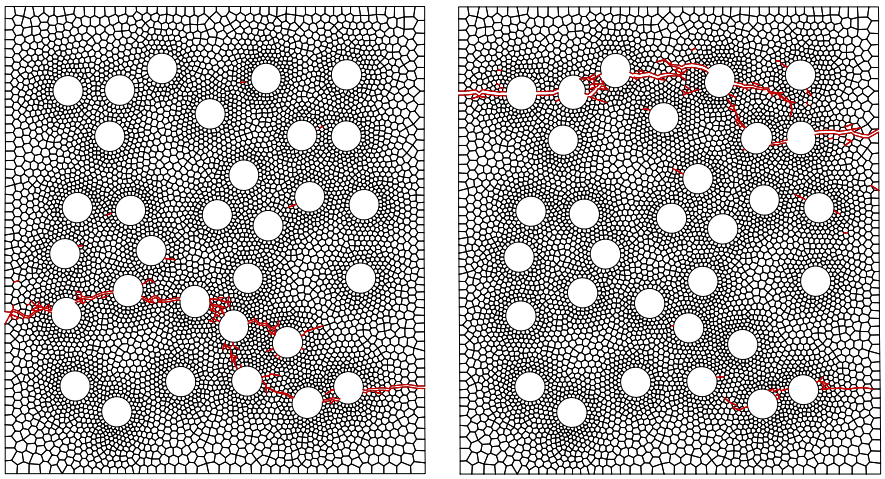

(a) (b)

Figure 5.34: Typical fracture patterns in the epoxy plate specimen, when the cohesive strength is statistically distributed. In the results shown, the strength follows the Weibull distribution in Equation 5.35, with $m = 5$.

5.6 Dominant crack example problems

In this section, we explore the effectiveness of the adaptive refinement and element-splitting operators in problems containing a dominant crack. The first example considers the impact of a double notched test specimen; which has well known fracture behavior. This will serve as the benchmark for our analysis, and we will use this opportunity to investigate the influence of the radius of the zone of refinement on fracture behavior. The second example focuses on the mixed-mode fracture behavior of a notched plate with a hole under impact load. In this example, we will consider the influence of both horizontal and angled notches. The third example considers microbranching behavior. All the examples have related experimental results in the literature, and comparisons will be made when possible. To compare the various meshing strategies highlighted in this work, five cases are analyzed: (1) a coarse polygonal mesh, (2) a coarse polygonal mesh with element-splitting, (3) an adaptively refined coarse polygonal mesh with element-splitting, (4) a fine polygonal mesh, and (5) a fine quadrilateral mesh with element-splitting. The five strategies are illustrated in Figure 5.35. The fine quadrilateral mesh is geometrically similar to the coarse polygonal mesh, where each polygon is refined with the scheme illustrated in Figure 5.9.

5.6.1 Double notched plate specimen

Kalthoff and Winkler [229] investigated the crack propagation of a double-notched plate specimen under impact load, as depicted in Figure 5.36(a). They demonstrate that, for

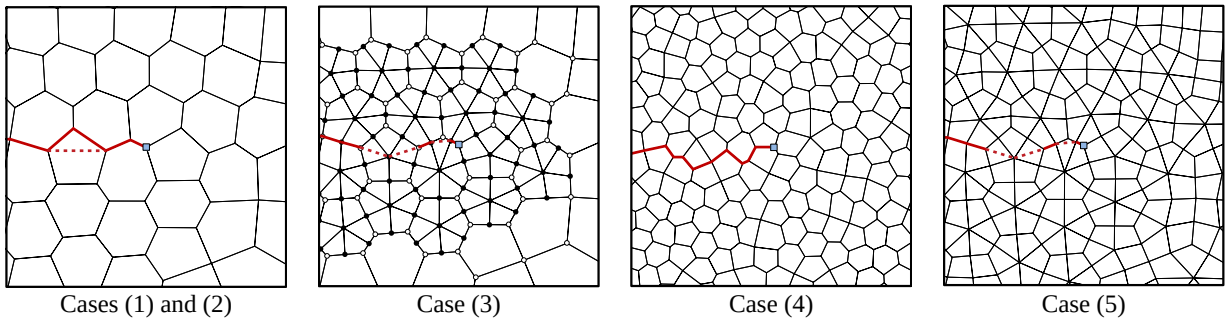

Figure 5.35: The five meshing strategies considered in this investigation: (a) a coarse polygonal mesh with and without element-splitting, (b) an adaptively refined coarse polygonal mesh with element-splitting (nodes are depicted to illustrate the ability of the polygonal elements to adaptively account for hanging nodes), (c) a fine polygonal mesh, and (d) a fine quadrilateral mesh with element-splitting. Note that the element-splitting is not explicitly represented in the mesh, as it occurs on-the-fly; which is why dashed lines are used to depict split elements.

this specimen, the failure mechanism changes from brittle to ductile failure as the impact velocity increases. In the case of brittle failure (low rates of loading), cracking initiates at an angle of approximately 70° from the initial plane of the notch. At higher rates of loading, the failure mechanism is dominated by plastic shear, and the crack initiates at an angle of approximately −10°. In this example we focus on the case of brittle fracture, and attempt to capture the initiation angle of 70°.

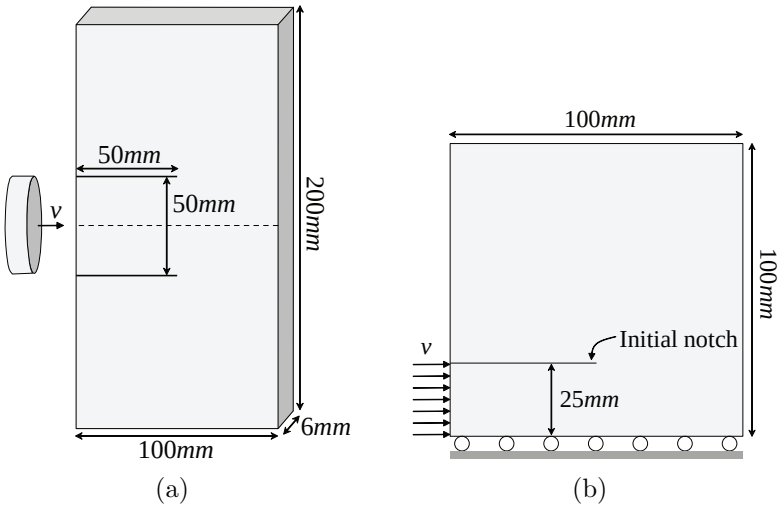

Figure 5.36: (a) The doubled notched plate test specimen used by Kalthoff and Winkler [229], and (b) the symmetric model used for computations.

Numerically, this problem has been investigated by many researchers. Belytschko et al. [213] used discontinuous enrichment functions, in the extended finite element method, and

captured a crack initiation angle of 58° with an average crack-tip velocity of 75% the Rayleigh wave speed. Zhang and Paulino [136] used intrinsic cohesive elements, inserted into the mesh a priori, and captured a crack initiation angle of between 72° and 74°, with an average crack-tip velocity of 65% the Rayleigh wave speed. More recently, Park et al. [7] used extrinsic cohesive elements with adaptive refinement and coarsening on a 4k mesh. They captured a crack initiation angle of approximately 62°, with an average crack-tip velocity of 71% the Rayleigh wave speed.

Due to the symmetry of the problem, the geometry can be reduced to that illustrated in Figure 5.36(b). The impact velocity is $16.54m/s$, and is linearly ramped up over $1\mu s$. Maraging steel, designated as 18Ni(300), as per the American National Standards Institute, is used as the representative material. The elastic modulus of the steel is $190GPa$, the Poisson's ratio is 0.3, and the density is $8000kg/m^3$. The mode I and mode II fracture parameters are assumed to be equivalent, with a fracture energy of $22.2kJ/m^2$, a cohesive strength of $1.733GPa$, and a shape parameter of 2.

To determine the influence of the chosen radius of refinement on fracture behavior, during adaptively refined simulations, we model this problem with a variety of selected radii. Cases with a radius of $r = 2mm$, $4mm$, and $6mm$ are considered, with a starting mesh of 6,000 polygonal elements. The smallest radius we consider ($r = 2mm$) is a result of the mesh size; with this radius, there are approximately 10 polygonal elements refined around each crack-tip. When a radius of $r = 1mm$ is selected, only 2 elements are refined; resulting in the possibility of unrefined elements at the crack-tip. The size of the starting mesh was determined through a mesh refinement study and was shown to display sufficiently accurate results. The velocity of the crack-tip, and the evolution of energy are the two parameters of interest in this investigation. For the purposes of computing the crack-tip velocity, the crack-tip is defined as the individual crack-tip which is the greatest distance from the end of the initial notch. The velocity of the crack-tip, illustrated in Figure 5.37(a), displays similar trends for each radius of refinement. For the case of $r = 2mm$, the crack initiates at a later time then in the other cases; however, the average velocity for each case is similar (approximately 60% of the Rayleigh wave speed), as illustrated in Figure 5.37(a).

When we consider the evolution of energy, the results again indicate that the radius of refinement has only a minor effect. The evolution of energy for each case, illustrated in Figure 5.37(b), is comprised of the strain (E_{int}), kinetic (E_{kin}) and fracture (E_{fra}) energies. The fracture energy is zero up to the point of crack initiation, then steadily increases over time. The strain energy increases due to the impact, but decreases over time as the crack propagates. The external energy is equal to the sum of the strain, kinetic, and fracture energies. The external energy is similar for all cases; however, a small discrepancy in the

strain energy is observed beyond approximately $60\mu s$. Based on these results, and due to the small variation in computational cost between the three refinement radii, we select a radius of $r = 4mm$ for all cases we consider.

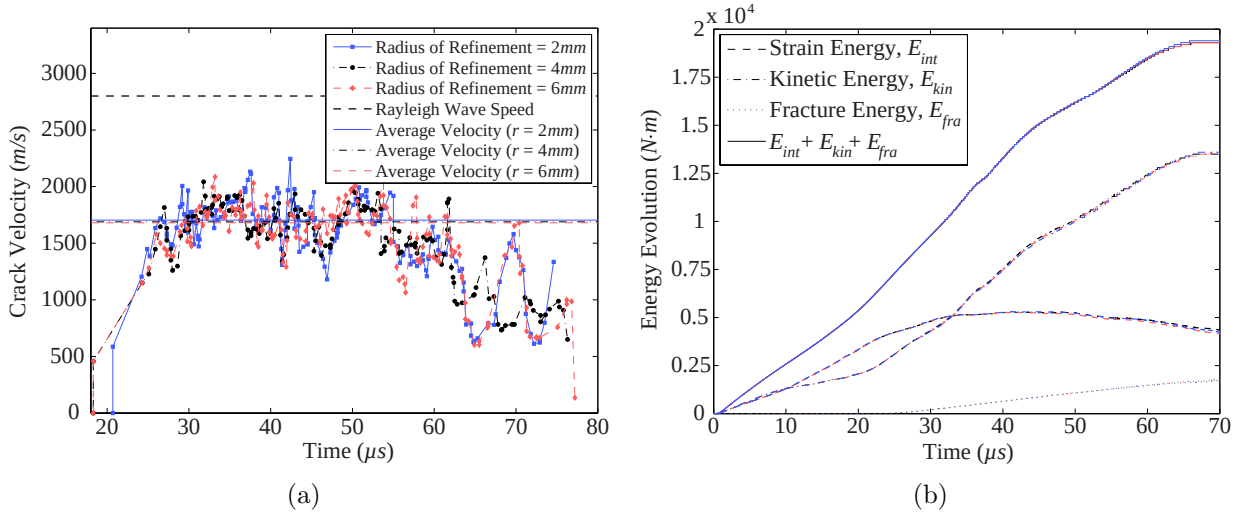

Figure 5.37: Results of the study on the radius of refinement: (a) velocity of the crack-tip, and (b) evolution of energy. The average velocity is calculated between a time of $25\mu s$ and $50\mu s$.

The base, coarse polygonal mesh, contains 6,000 elements. When uniformly refined with quadrilateral elements, the mesh contains 33,254 elements; which is the number of elements contained in the fine polygonal mesh. When adaptive refinement is used, a zone with a $4mm$ radius is initially refined at the notch tip, as illustrated in Figure 5.38(a). For this case, the refined finite element mesh discretizations at $47.5\mu s$ and $82.5\mu s$ are illustrated in Figures 5.38(c) and 5.38(e), respectively. Beside each mesh in Figure 5.38, we provide the composition of the mesh; which illustrates the evolution of the 4-gons throughout the simulation.

For all cases, the global fracture angles are similar (68° to 72°), and are in good agreement with the experimentally observed angle of 70°. However, the fracture surfaces for the coarse and fine polygonal meshes are noticeably biased by the polygonal element shapes, as illustrated by the fluctuating crack paths in Figure 5.39(a). Both coarse polygonal meshes (with and without element-splitting) display poor agreement with the expected fracture initiation angle, and produce the highest global fracture angles.

Even though the polygonal meshes produce fracture surfaces that are biased by the shape of the elements, the crack velocity for each case displays similar trends. The crack initiates approximately $20\mu s$ after impact, steeply ramps up, and fluctuates greatly thereafter, as illustrated in Figure 5.39(b). After roughly $50\mu s$ the velocity begins to gradually decrease. In all cases, the average velocity is approximately $1675m/s$ (or approximately 60% of the

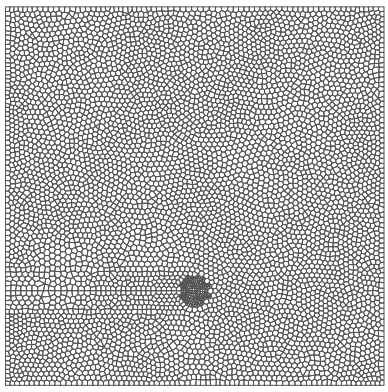

(a)

n	n-gon	number of n-gons
3		1
4		450
5		2361
6		3159
7		179
$(8 \leq n \leq 11)$		7
Total Elements		6157

(b)

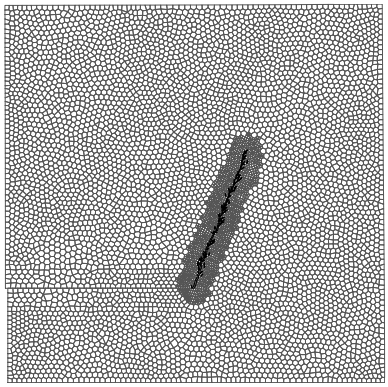

(c)

n	n-gon	number of n-gons
3		143
4		1602
5		2295
6		2968
7		190
$(8 \leq n \leq 11)$		43
Total Elements		7241

(d)

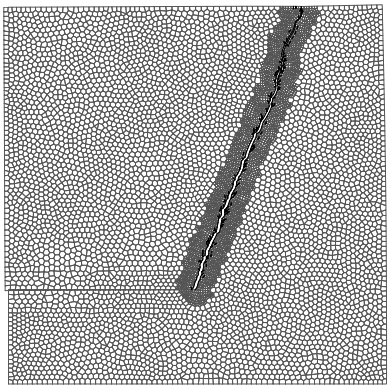

(e)

n	n-gon	number of n-gons
3		261
4		2688
5		2200
6		2834
7		192
$(8 \leq n \leq 11)$		72
Total Elements		8247

(f)

Figure 5.38: Results of the double notch plate specimen study, for the case of adaptive refinement with element-splitting. (a) Initial mesh discretization, with a zone of refinement at the notch tip, (b) composition of the initial mesh, (c) intermediate mesh at $47.5\mu s$, (d) composition of the intermediate mesh, (e) final mesh at $82.5\mu s$, and (f) composition of the final mesh.

Rayleigh wave speed). These results correspond well with those published in the literature [7, 136, 229].

Next, we investigate the progression of strain energy density throughout the crack propagation process in Figure 5.40. The strain energy density at times of $35\mu s$, $55\mu s$ and $75\mu s$, for

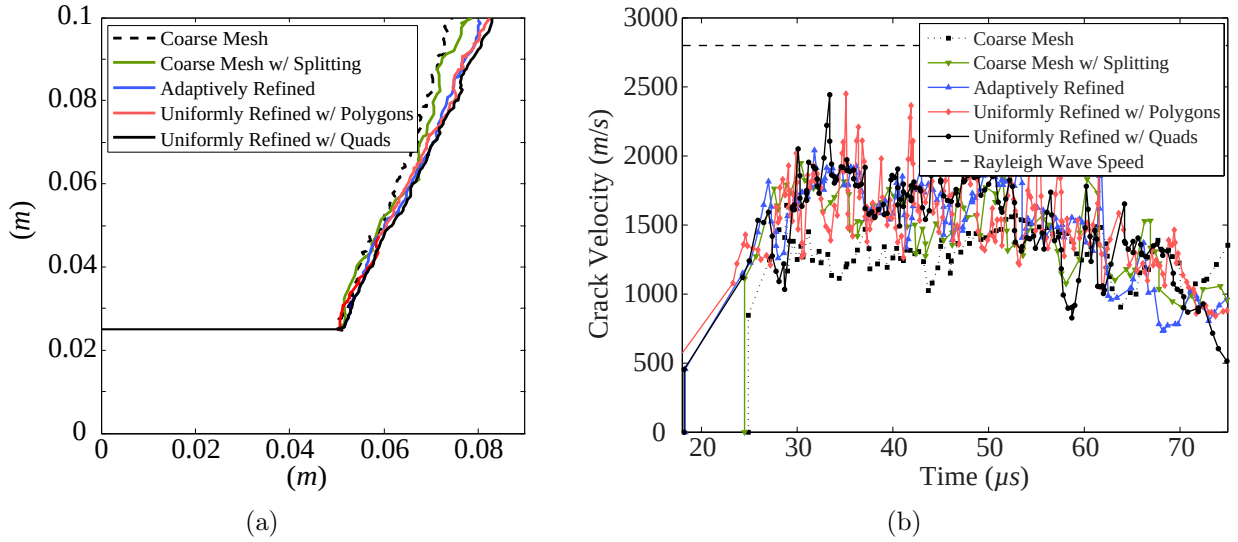

Figure 5.39: Comparison of (a) the crack paths, and (b) the crack-tip velocity for the five cases considered.

the first three cases in Figure 5.35, are illustrated in 5.40. In each case, it is apparent that the strain energy density concentrates at the crack tip and there is a clear influence of the propagating crack on the distribution of strain energy in the right portion of the specimen. In this portion of the specimen, the waves reflect between the rightmost boundary and the macroscopic crack [57].

The computational time is listed in Table 5.3. We compare the time it takes for the specimen to fracture completely, as the number of iterations for each mesh to fracture varies, due to the variations in path length and corresponding element type. The total cost is lowest for a coarse polygonal mesh with element-splitting, and highest for the fine polygonal mesh. Alternatively, one could make comparisons based on the cost per iteration. In this case, the coarse polygonal mesh becomes the lowest cost option, and has a smaller cost per iteration than the adaptively modified cases. This result is in line with expectations, as the adaptively modified cases; while they start with the same discretization, add elements (and nodes) to the problem as the simulation progresses. Also notable is that computations using the adaptive refinement scheme, when compared to those for the uniformly refined mesh of the same effective discretization, are approximately 3.4 times faster.

5.6.2 Horizontal notch in a plate with a hole

This example highlights the mixed-mode fracture of a notched PMMA plate with a hole. This problem was investigated experimentally by Grégoire et al. [230] using the geometry illustrated in Figure 5.41(a). The experiments demonstrate a fracture initiation angle of

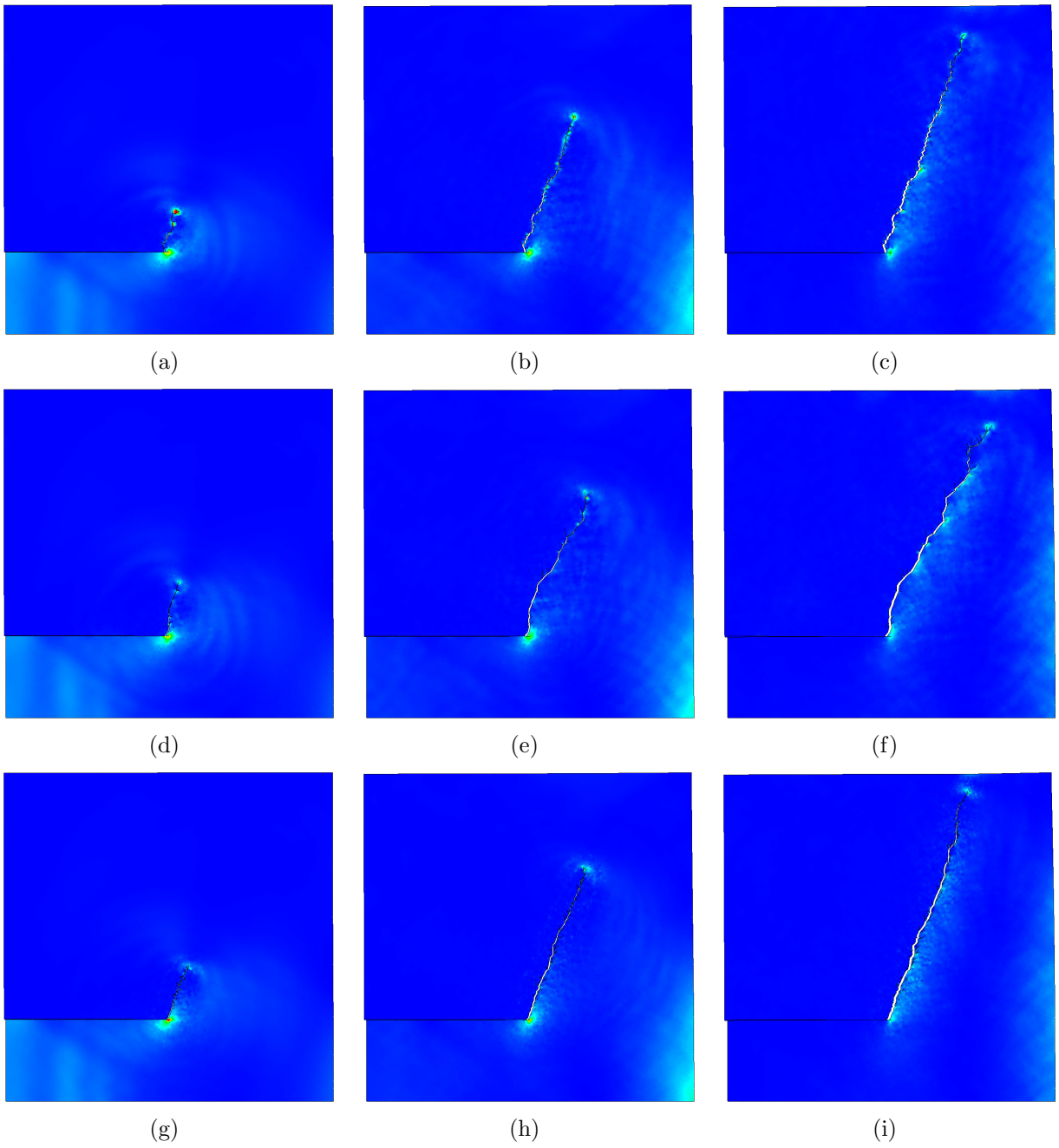

Figure 5.40: Strain energy density at times of $35\mu s$, $55\mu s$ and $75\mu s$ for (a)-(c) a coarse polygonal mesh, (d)-(f) a coarse polygonal mesh with element-splitting, and (g)-(i) a coarse polygonal mesh with adaptive refinement and element-splitting.

approximately 37.5°. The crack initially propagates in a mixed-mode manner then transitions into a mode I crack a short while after initiation. Numerically, this problem has been investigated using the XFEM method by Grégoire et al. [230] and Gravouil et al. [231]; and using the polygonal scaled boundary finite element method by Ooi et al. [189, 232]. To the

Table 5.3: Summary of computational cost to simulate the various cases considered for the double notched plate example. The five cases correspond to: (1) a coarse polygonal mesh, (2) a coarse polygonal mesh with element-splitting, (3) an adaptively refined coarse polygonal mesh with element-splitting (the final mesh contains 8,247 elements and 12,994 nodes), (4) a fine polygonal mesh, and (5) a fine quadrilateral mesh with element-splitting. The elements and nodes correspond to the initial discretization (the base mesh). The time step was held constant at $\Delta t = 5 \times 10^{-9} \mu s$.

Case	Elements	Nodes	Cost (min)	Iterations to Fracture	Cost/Iteration ($10^{-3}s$)
1	6,000	10,815	25.7	18,250	84.5
2	6,000	10,815	24.3	16,900	86.3
3	6,000	10,815	25.3	16,500	92.0
4	33,254	60,314	154.2	16,400	564.1
5	33,254	33,629	85.5	16,400	312.8

best of the author's knowledge, this problem has not been investigated using the cohesive element method.

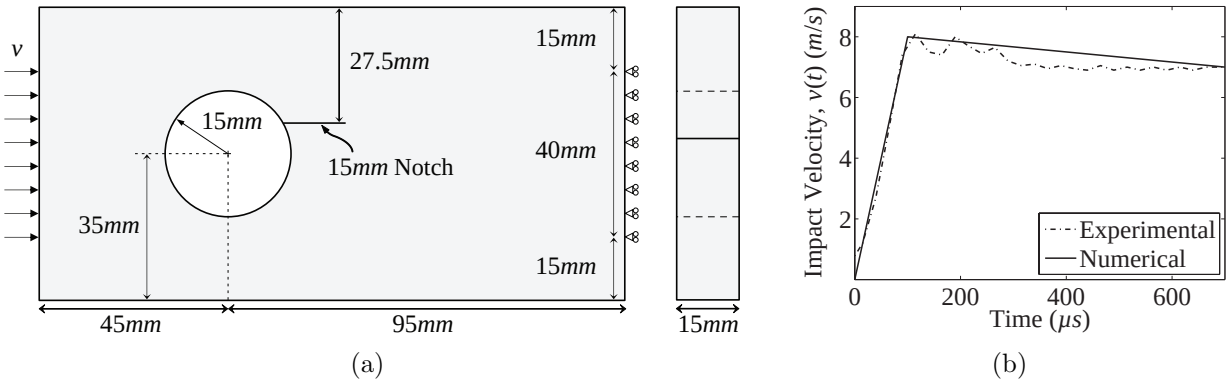

(a) (b)

Figure 5.41: (a) Geometry of the horizontal notch in a plate with a hole, and (b) impact velocity.

Experimentally, the specimen is impacted using a Hopkinson bar [233] with a diameter of $40mm$. Numerically, the impact is described by an applied velocity that ramps up to $8m/s$ over a period of $100\mu s$ then ramps down to $7m/s$ over a period of $600\mu s$, as illustrated in Figure 5.41(b). The mesh contains 6,000 elements and a radius of refinement of $4mm$ is used. The PMMA has an average elastic modulus of $3.3GPa$, a Poisson's ratio of 0.42, and a density of $1180kg/m^3$. The average mode I fracture energy (ϕ_n), cohesive strength ($\sigma_{\max}$), and shape parameter (α) are set as $352.4N/m$, $62.1MPa$ and 2, respectively. The mode II fracture properties are assumed to be the same as the mode I fracture properties, and the influence of the distribution of material properties on the global fracture patterns is investigated.

The experimentally obtained fracture pattern and crack initiation angle is shown in Figure 5.42(a). Sample results from our simulations are illustrated in Figures 5.42(b) through 5.42(f). In Figure 5.42(b) the coarse polygonal mesh displays a crack initiation angle of approximately 16°. This is not significantly improved when a fine polygonal mesh is used, as the crack in this case initiates at an angle of approximately 22° (Figure 5.42(e)). When element-splitting is enabled (Figure 5.42(c)), the crack initiation angle increases to approximately 31°, helping support our argument that element-splitting is a significant step towards obtaining accurate fracture patterns with polygonal elements. However, these results still do not approach the experimentally observed crack initiation angle of 37.5°, and do not quite transition to the mode I cracks we expect. Alternatively, when we use an adaptively refined mesh (Figure 5.42(d)) or an a equivalent, uniformly refined mesh (Figure 5.42(f)), we observe a much smoother fracture surface, with the crack initiating at an angle of approximately 35° and transitioning from a mixed-mode crack to a mode I crack a short while after initiation - results which approach those observed experimentally.

An investigation of the energy evolution is conducted for the case of adaptive refinement, as illustrated in Figure 5.43. The sum of the strain energy, kinetic energy and fracture energy shows good agreement with the external energy imparted on the specimen by the Hopkinson bar. The fracture energy remains equal to zero up until the point of crack initiation, and increases over time, however, it does not contribute significantly to the overall energy. The computational time is compared in Table 5.4 for the five cases considered (see Figure 5.35). The time step is set at $\Delta t = 2 \times 10^{-8} \mu s$, based on the Courant-Friedrichs-Lewy stability condition [234], and the number of iterations to fracture is 22,500 for all cases. The coarse polygonal mesh has the lowest cost per iteration, and, when adaptive operators are included (element-splitting and adaptive refinement), the cost increases slightly. Computations using the adaptive refinement scheme, when compared to those for the uniformly refined mesh of the same effective discretization, produce comparable results and are more than four times faster.

To investigate the influence of microstructural heterogeneities on the global fracture patterns, we vary the bulk elastic modulus, the cohesive fracture energy and the cohesive strength, as discussed in Section 5.4. The study is conducted on the first three cases considered; a coarse polygonal mesh, a coarse polygonal mesh with element-splitting, and an adaptively refined coarse polygonal mesh. For each material property considered, three different Weibull moduli are selected, $m = 10$, 30, and 50, and for each modulus three different random instances are simulated (a total of 81 simulations). Based on the study, statistically distributing the material properties has a negligible influence on the global fracture patterns. For the sake of brevity, not all of the results are shown here, but typical results are illustrated

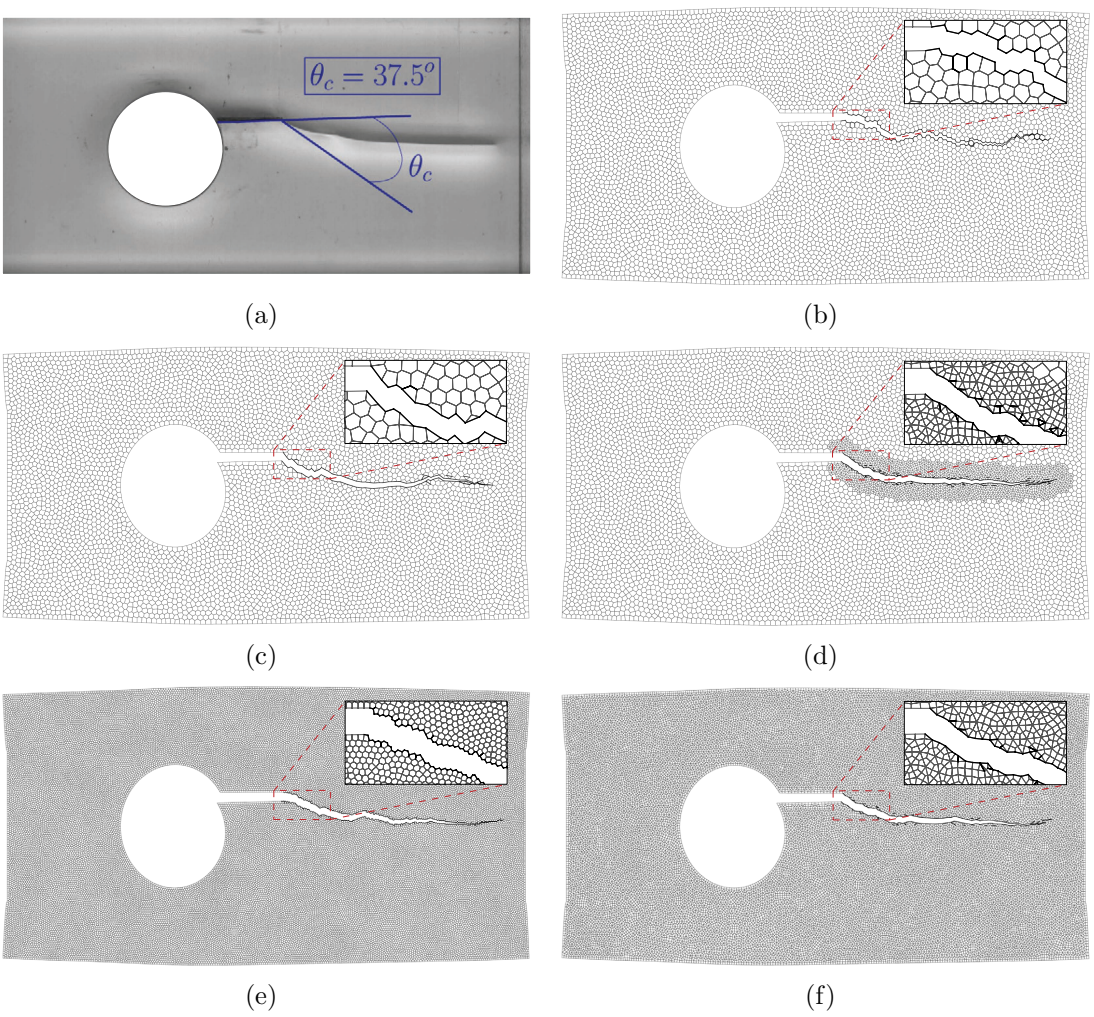

Figure 5.42: Results of the notched plate with a hole study. (a) Experimentally obtained fracture pattern and crack initiation angle of approximately 37.5° (image extracted from Grégoire et al. [230]). Simulated results for (b) a coarse polygonal mesh, (c) a coarse polygonal mesh with element-splitting, (d) an adaptively refined coarse polygonal mesh with element-splitting, (e) a fine polygonal mesh, and (f) a fine quadrilateral mesh with element-splitting.

in Figure 5.44. We illustrate the two meshing strategies in most need of improvement, coarse polygonal meshes with and without element-splitting, with the widest variation of material properties ($m = 10$) for each of the properties considered. From the results, it is clear that using a statistical distribution of material properties to overcome mesh dependency does not improve the global fracture patterns for the geometrically restrictive polygonal meshes.

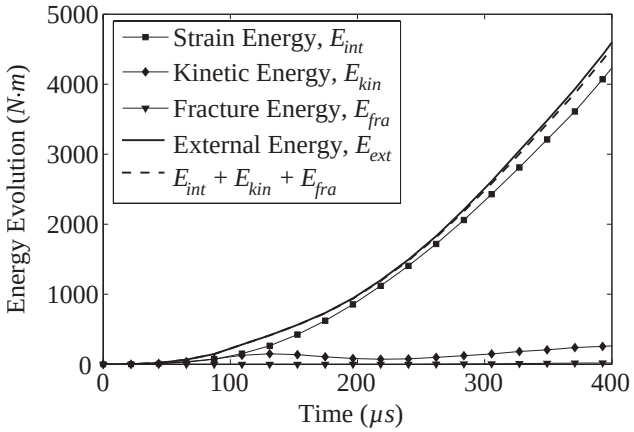

Figure 5.43: Evolution of energy for the horizontal notch in a plate with a hole example, using adaptive refinement with element-splitting.

Table 5.4: Summary of computational cost to simulate the various cases considered for the horizontal notch in a plate with a hole example. The five cases correspond to: (1) a coarse polygonal mesh, (2) a coarse polygonal mesh with element-splitting, (3) an adaptively refined coarse polygonal mesh with element-splitting (the final mesh contains 7,873 elements and 13,193 nodes), (4) a fine polygonal mesh, and (5) a fine quadrilateral mesh with element-splitting. The elements and nodes correspond to the initial discretization (the base mesh). The time step was held constant at $\Delta t = 2 \times 10^{-8} \mu s$.

Case	Elements	Nodes	Cost (min)	Cost/Iteration ($10^{-3}s$)	Crack Initiation Angle (°)
1	6,000	11,460	29.5	78.7	16
2	6,000	11,460	30.4	81.1	31
3	6,000	11,460	32.8	87.5	35
4	34,503	68,195	190.3	507.5	22
5	34,503	34,902	135.0	360.0	35

5.6.3 Angled notch in a plate with a hole

This example considers the same problem as in the previous example, but with an angled notch. This problem was also investigated experimentally by Grégoire et al. [230] using the geometry illustrated in Figure 5.45. The boundary conditions and material properties are the same as in the previous example, and the experimental results are shown in Figure 5.46(a).

Sample results from our investigation are presented in Figures 5.46(b) through 5.46(e). In this case, all of the crack initiation angles are in reasonable agreement with the experimentally observed angle. However, the fracture surfaces in the polygonal meshes are noticeably influenced by the element geometry, increasing the energy required to propagate the crack.

As before, we investigate the influence of microstructural heterogeneities on the global

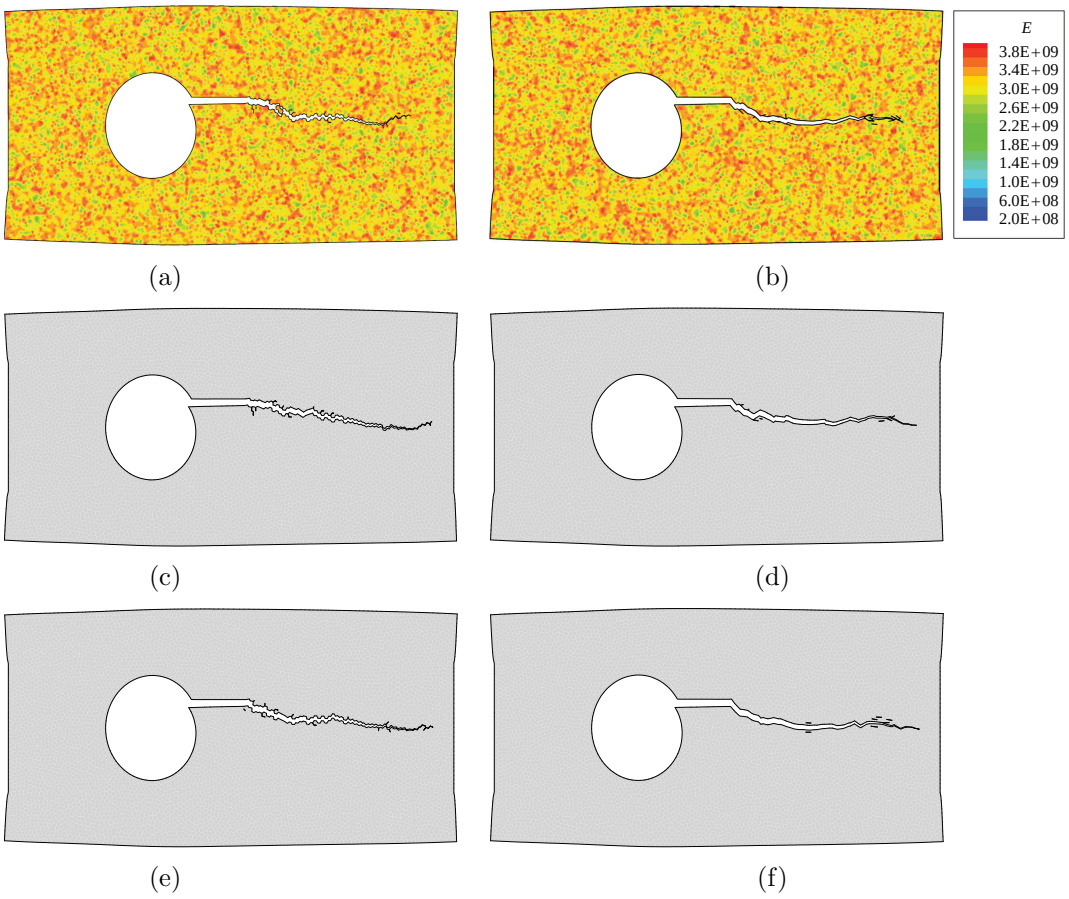

Figure 5.44: Global fracture patterns for the horizontal notch in a plate with a hole problem when the material is statistically distributed. Results are for: (a)-(b) a variation in elastic modulus for the case of a coarse polygonal mesh without element-splitting and with element-splitting, respectively; (c)-(d) a variation in cohesive energy ($140N/m \leq \phi_n \leq 440N/m$) for the same cases, respectively; and (e)-(f) a variation in cohesive strength ($25MPa \leq \sigma_{\max} \leq 78MPa$) for the same cases, respectively. Results are shown for a Weibull modulus of $m = 10$, but illustrate the minor effect that the constitutively unstructured method has on global fracture patterns when using unstructured polygonal elements.

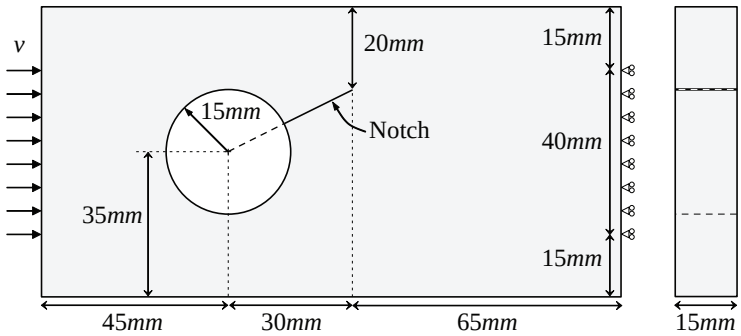

Figure 5.45: Geometry of the angled notch in a plate with a hole.

fracture patterns. We vary the bulk elastic modulus, the cohesive fracture energy and the cohesive strength. The study is conducted on the first three meshing strategies; a coarse

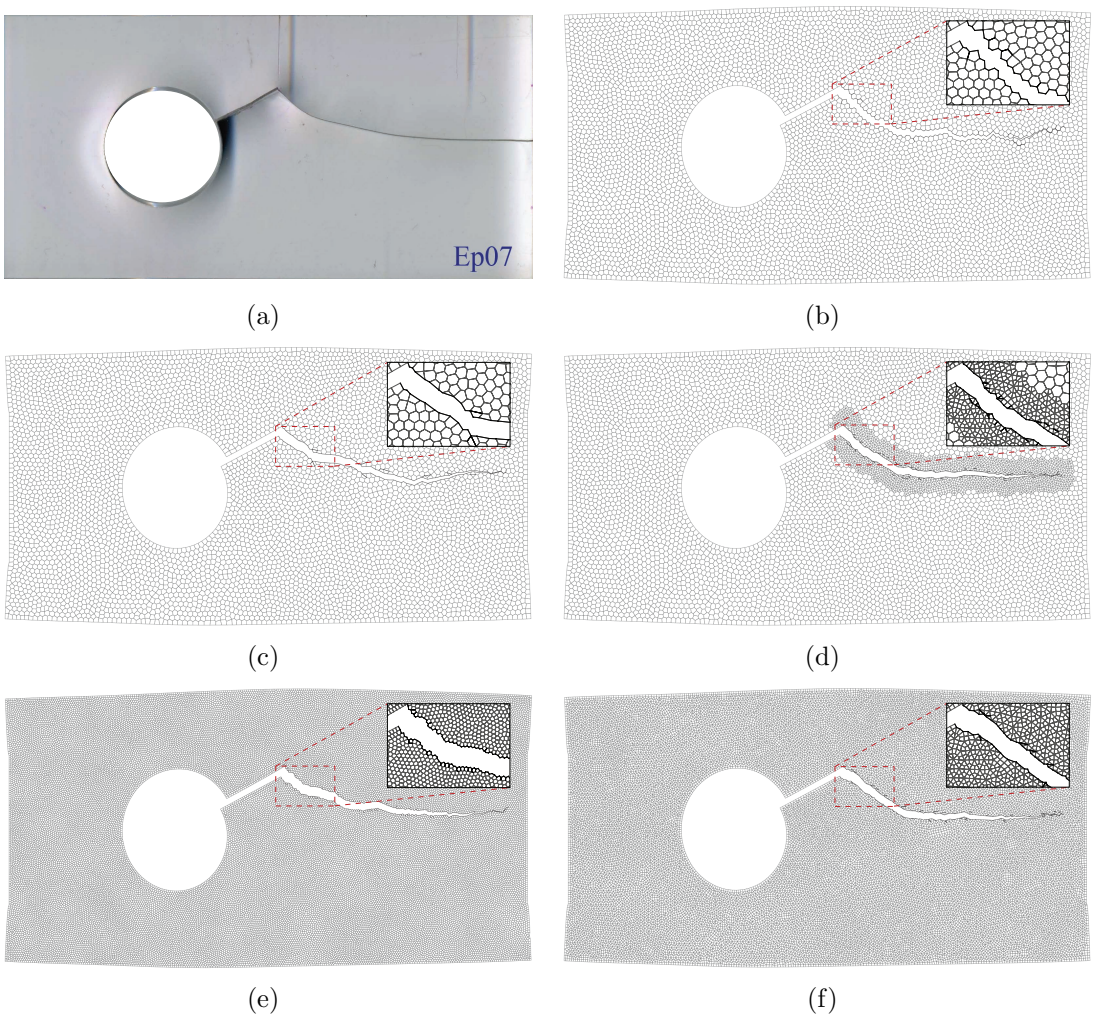

Figure 5.46: Results of the angled notch in a plate with a hole study. (a) Experimentally obtained fracture pattern (image extracted from Grégoire [235]). Simulated results for (b) a coarse polygonal mesh, (c) a coarse polygonal mesh with element-splitting, (d) an adaptively refined coarse polygonal mesh with element-splitting, (e) a fine polygonal mesh, and (f) a fine quadrilateral mesh with element-splitting.

polygonal mesh, a coarse polygonal mesh with element-splitting and an adaptively refined coarse polygonal mesh (see Figure 5.35). Typical results are illustrated in Figure 5.47. We illustrate the two meshing strategies in most need of improvement, coarse polygonal meshes with and without element-splitting, with the widest variation of material properties ($m = 10$) for each of the properties considered. From the results, it is clear that using a statistical distribution of material properties to overcome mesh dependency does not significantly influence the global fracture patterns.

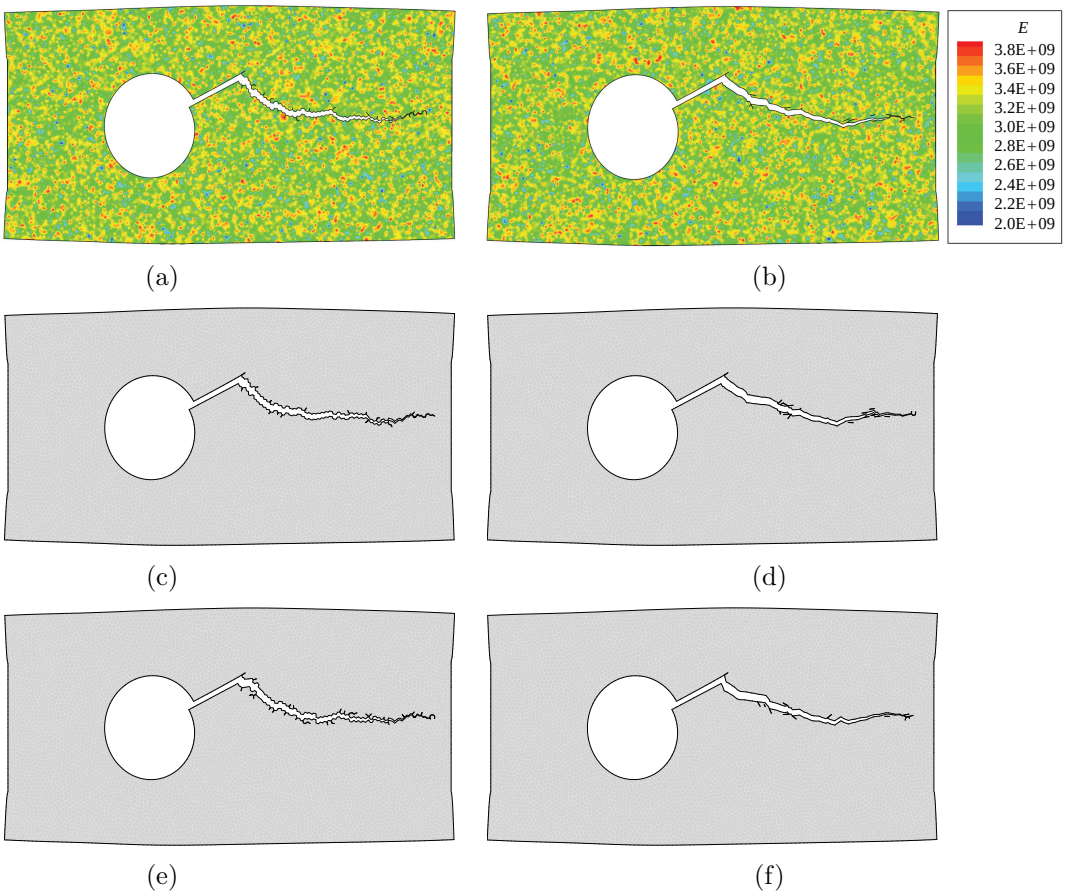

Figure 5.47: Global fracture patterns for the angled notch in a plate with hole problem when the material is statistically distributed. Results are for: (a)-(b) a variation in elastic modulus for the case of a coarse polygonal mesh without element-splitting and with element-splitting, respectively; (c)-(d) a variation in cohesive energy ($140N/m \leq \phi_n \leq 440N/m$) for the same cases, respectively; and (e)-(f) a variation in cohesive strength ($25MPa \leq \sigma_{\max} \leq 78MPa$) for the same cases, respectively. For each material property considered, three different Weibull moduli are selected, $m = 10$, 30, and 50, and for each modulus three different random instances are simulated (a total of 81 simulations). Results are shown for a Weibull modulus of $m = 10$, but illustrate the minor effect that the constitutively unstructured method has on global fracture patterns when using unstructured polygonal elements.

5.6.4 Microbranching

The microbranching instability in brittle materials undergoing dynamic fracture was experimentally investigated by Sharon and Fineberg [236, 237]. They conducted experiments on PMMA sheets with a width of $50mm$ to $200mm$ and a length of $200mm$ to $400mm$. Among others, Zhang et al. [57] illustrate that equivalent behavior can be achieved numerically, at a lower cost, with a reduced dimension model. Thus, the numerical study is conducted on a reduced dimension model having a width of $4mm$, and a length of $16mm$, as illustrated in Figure 5.48 [57]. The PMMA sheet has an average elastic modulus of $3.24GPa$, a Poisson's ratio of 0.35, and a density of $1190kg/m^3$. The average mode I fracture energy, cohesive

strength, and shape parameter are set as $352.4N/m$, $129.6MPa$ and 2, respectively. The mode II fracture properties are assumed to be the same as the mode I fracture properties, and the influence of the distribution of material properties on the global fracture patterns and crack-tip velocity is investigated.

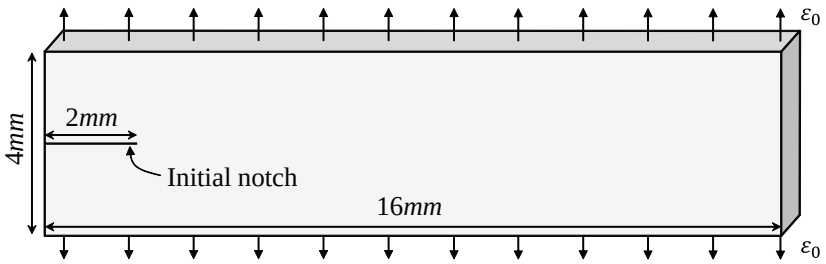

Figure 5.48: Geometry and boundary conditions used to investigate the microbranching instability in a PMMA sheet. A strain of $\epsilon_0 = 0.015$ is applied to the upper and lower surface of the specimen.

A number of researchers have investigated this problem numerically. For instance, Miller et al. [238] used intrinsic cohesive elements, distributed throughout the model, to investigate the energy dissipation due to microbranching. They show that crack branching leads to energy dissipation as the crack velocity increases; which is consistent with the same assertion made by Sharon and Fineberg [236, 237] based on their experimental investigation. Zhang et al. [57] used extrinsic cohesive elements, within a topological data structure, to capture the microbranching instability. Their simulations were conducted on structured 4k meshes; which lead to similar angles of initiation for the microbranches, but captured behavior in good agreement with experiments. More recently, Paulino et al. [221] used nodal perturbation and edge-swap operators to make a structured 4k mesh unstructured. Their results indicate that unstructured meshes capture varied microbranching angles; and lead to results which are more consistent with experiments.

For this investigation, we consider the same five cases as before: (1) a coarse polygonal mesh, (2) a coarse polygonal mesh with element-splitting, (3) an adaptively refined coarse polygonal mesh (4) a fine polygonal mesh, and (5) a fine quadrilateral mesh (see Figure 5.35). The base, coarse polygonal mesh, contains 4,000 elements. When uniformly refined with quadrilateral elements, the mesh contains 22,039 elements; which is the number of elements contained in the fine polygonal mesh. For the cases with adaptive refinement, a zone with a $0.4mm$ radius is refined at each crack-tip. The results of the investigation are illustrated in Figure 5.49. The case for the coarse polygonal mesh (Figure 5.49(a)) results in a fracture surface biased by the polygonal element shapes, and little crack branching occurs. When adaptively refined with quadrilateral elements (Figure 5.49(c)), the fracture surface is

more smooth, and the frequency of micro and macro branching increases. When uniformly refined with quadrilateral elements (Figure 5.49(e)), we get similar behavior to that for the case of adaptive refinement. For the adaptively refined case, and the two fine cases, the fracture patterns agree well with previous numerical investigations and experimental results [236, 237].

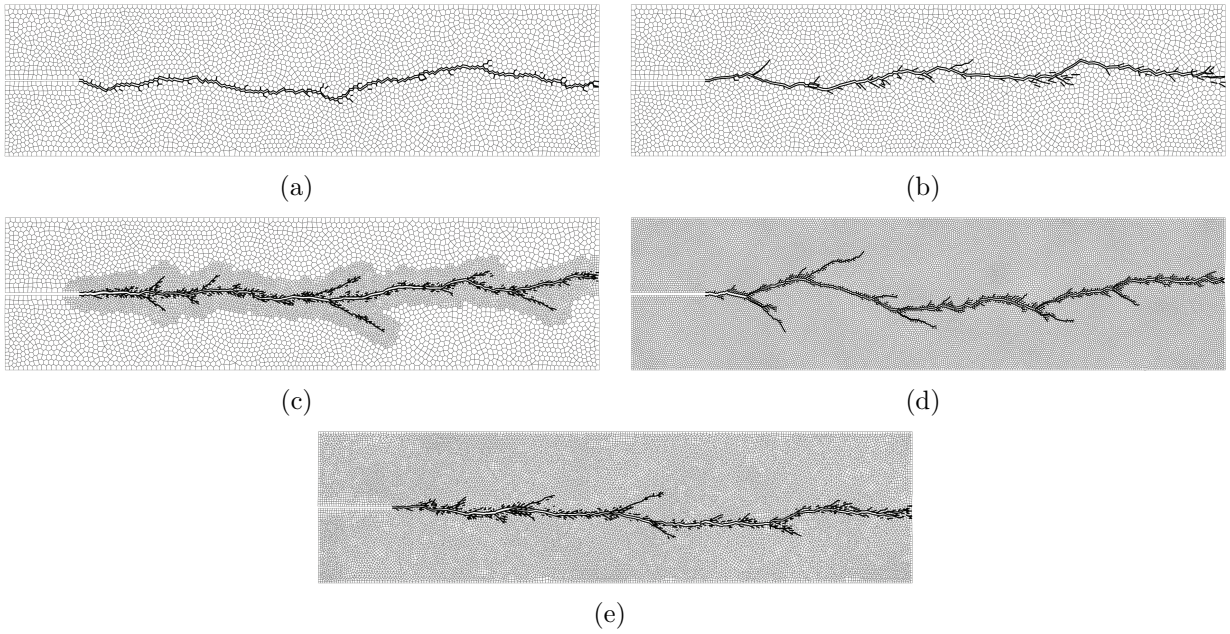

Figure 5.49: Simulated results of the microbranching problem, using (a) a coarse polygonal mesh (b) a coarse polygonal mesh with element-splitting, (c) an adaptively refined coarse polygonal mesh, (d) a fine polygonal mesh, and (e) a fine quadrilateral mesh with element-splitting.

The horizontal velocity of the crack-tip is tracked, for each case, and plotted in Figure 5.50(a). For the purposes of computing the crack-tip velocity, the crack-tip is defined as the individual crack-tip which is the greatest horizontal distance from the end of the initial notch. The average velocity of each case is also plotted, and is in close agreement with one another. Since the crack-tip velocity fluctuates significantly while the crack propagates, the average velocity is only representative of the overall trend and should not be taken as a precise value. The average velocity is lowest for the case of a coarse polygonal mesh (approximately $543m/s$), and is highest for the adaptively refined mesh (approximately $667m/s$). All cases have crack-tip velocities that fall within the range of those determined experimentally (as illustrated in Figure 4 in [237]).

Similarly to the previous examples, the evolution of energy is computed for the case of adaptive refinement and illustrated in Figure 5.50(b). Because there is no external work in this problem ($E_{ext} = 0$), the total energy (E_{tot}) is the sum of the strain energy (E_{int}), the kinetic energy (E_{kin}), and the fracture energy (E_{fra}). The total energy remains constant

throughout the problem; indicating that energy is conserved, and agrees well with results published in the literature [57, 221].

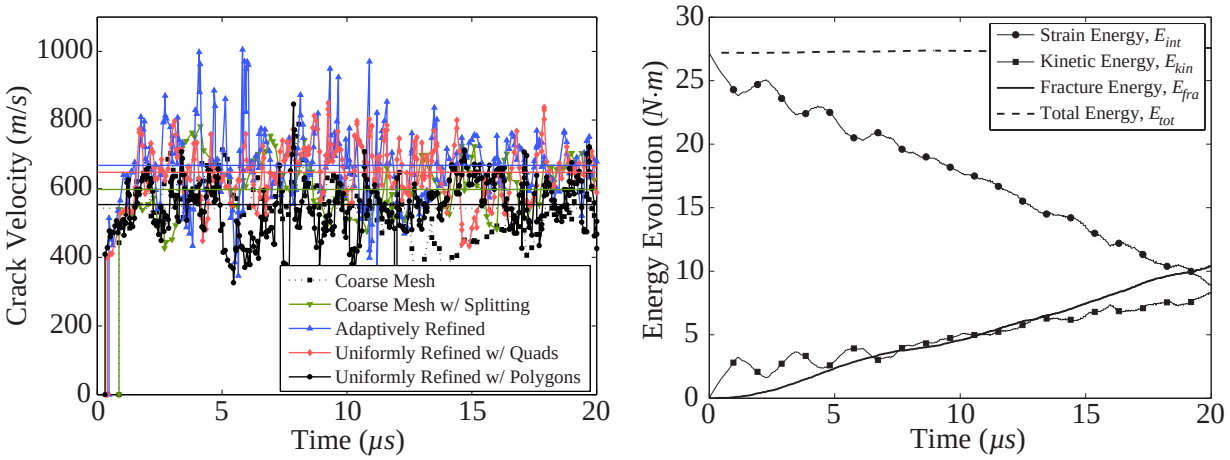

(a) (b)

Figure 5.50: (a) Horizontal velocity of the crack-tip for the five cases considered. The average velocities are included as horizontal lines. (b) Evolution of energy for the microbranching specimen using adaptive refinement with element-splitting.

We also investigate the influence of microstructural heterogeneities on the global fracture patterns, by varying the bulk elastic modulus, the cohesive fracture energy and the cohesive strength. The study was conducted on the coarse polygonal mesh, the coarse polygonal mesh with element-splitting and the adaptively refined coarse polygonal mesh. For each material property considered, three different Weibull moduli were selected, $m = 10$, 30, and 50, and for each Weibull modulus three different random instances were simulated (a total of 81 simulations). Typical results are illustrated in Figure 5.51. We illustrate the two meshing strategies in most need of improvement, coarse polygonal meshes with and without element-splitting, with the widest variation of material properties ($m = 10$) for each property we consider. For the most part, statistically distributing material properties to overcome mesh dependency does not significantly improve the global fracture patterns. The only noticeable exception is in the case of element-splitting, with a variation in cohesive strength (Figure 5.51(f)), where there is an observable increase in the frequency of microbranching.

In addition to the global fracture patterns, we investigate the influence of microstructural heterogeneities on the crack-tip velocity. The same scenarios as in the fracture pattern investigation are considered, and the average crack-tip velocities are summarized in Table 5.5. While the tabulated velocities all fall within the expected range observed experimentally [237], the coarse polygonal mesh consistently produces the lowest velocity, and the adaptively refined mesh consistently produces the highest velocity. There is no observable influence of

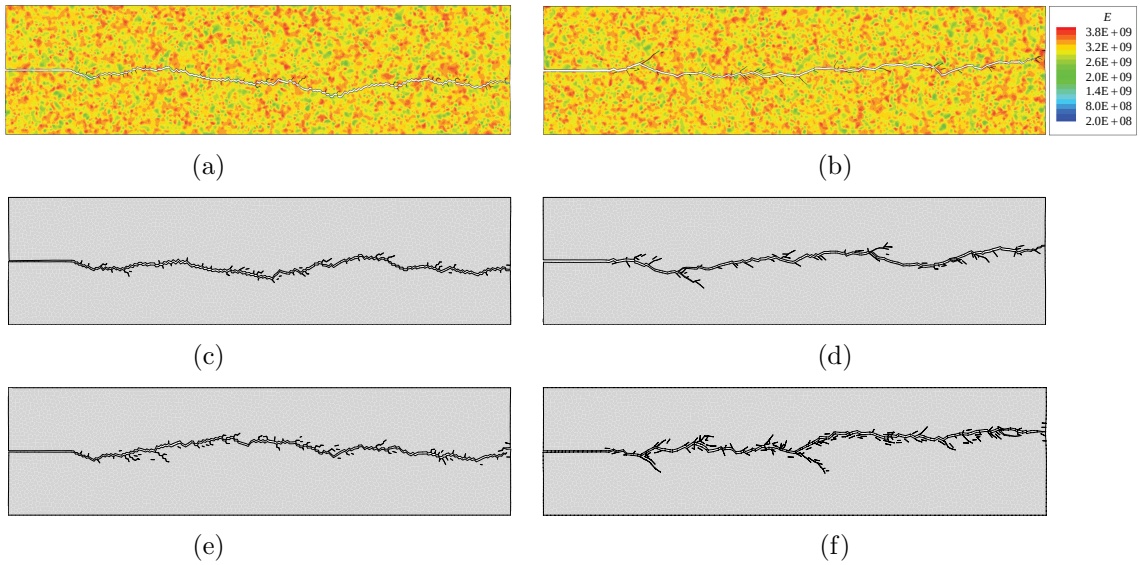

Figure 5.51: Global fracture patterns for the microbranching problem when the material is statistically distributed. Results are for: (a)-(b) a variation in elastic modulus for the case of a coarse polygonal mesh without element-splitting and with element-splitting, respectively; (c)-(d) a variation in cohesive energy ($140N/m \leq \phi_n \leq 440N/m$) for the same cases, respectively; and (e)-(f) a variation in cohesive strength ($55MPa \leq \sigma_{\max} \leq 162MPa$) for the same cases, respectively. Results are shown for a Weibull modulus of $m = 10$.

the statistical distribution of material properties.

Table 5.5: Summary of the average horizontal crack-tip velocity, when material properties are statistically distributed. Results are averaged over three different random instances and are listed in units of meters per second (m/s).

		Distribution of Material			
		Homogeneous	$m = 50$	$m = 30$	$m = 10$
Coarse Polygonal	Cohesive Stress (σ)	543	562	547	547
	Cohesive Energy (ϕ)		557	531	551
	Elastic Modulus (E)		533	521	504
Element-Splitting	Cohesive Stress (σ)	597	630	624	638
	Cohesive Energy (ϕ)		582	594	605
	Elastic Modulus (E)		607	589	605
Adaptive Refinement	Cohesive Stress (σ)	667	681	662	689
	Cohesive Energy (ϕ)		677	682	673
	Elastic Modulus (E)		654	669	650

The computational time is listed in Table 5.6. Similarly to the double notched plate

example, the number of iterations it takes for the specimen to fracture completely depends on the meshing strategy. The total cost is lowest for the adaptively refined coarse polygonal mesh, and highest for the fine polygonal mesh. Alternatively, when considering the cost per iteration, the coarse polygonal mesh becomes the lowest cost option. Once again, this is in line with expectations, as the adaptively modified meshes add elements (and nodes) to the problem as the simulation progresses. Computations using the adaptive refinement scheme, when compared to those for the uniformly refined mesh of the same effective discretization, produce comparable results and are almost three times faster.

Table 5.6: Summary of computational cost to simulate the various cases considered for the microbranching example. The five cases correspond to: (1) a coarse polygonal mesh, (2) a coarse polygonal mesh with element-splitting, (3) an adaptively refined coarse polygonal mesh with element-splitting (the final mesh contains 9,395 elements and 12,436 nodes), (4) a fine polygonal mesh, and (5) a fine quadrilateral mesh with element-splitting. The elements and nodes correspond to the initial discretization (the base mesh). The time step was held constant at $\Delta t = 1 \times 10^{-9} \mu s$.

Case	Elements	Nodes	Cost (min)	Iterations to Fracture	Cost/Iteration ($10^{-3}s$)
1	4,000	7,188	21.5	28,200	45.7
2	4,000	7,188	20.8	23,000	54.3
3	4,000	7,188	19.1	21,000	54.6
4	22,039	43,538	116.8	25,200	278.1
5	22,039	22,375	56.0	22,400	150.0

5.7 Concluding remarks

In this chapter, we perform two-dimensional dynamic cohesive fracture simulations using unstructured polygonal meshes. Unstructured polygonal meshes are isotropic, demonstrating no global directional preference for crack propagation, but limit the possible directions a crack may travel at each node. To alleviate these mesh induced restrictions, two new topological operators are presented: adaptive element-splitting and adaptive refinement. The influence of both operators on the crack path deviation is investigated through a probabilistic series of geometric studies. The studies quantify the ability of the various meshing strategies to represent arbitrary fracture patterns with minimal error. While the primary objective of this work is to promote the use of geometrically and topologically unstructured methods for addressing mesh dependency, we also investigate the use of a constitutively unstructured method. The constitutively unstructured method is investigated in the example

problems by statistically distributing the primary bulk and cohesive material properties, and investigating their effects on the global fracture behavior. Our investigation shows that the effects are minor and almost negligible, when compared to the improvements demonstrated by the topological operators.

The numerical methods developed in this chapter are verified with five example problems, most of which are supported with experimental results from the literature. The first two examples investigate pervasive fracture and crack initiation behavior, while the last three examples cover mode I, mixed-mode, and microbranching behavior. The examples demonstrate that adaptive element-splitting is more suited to pervasive fracture problems, and adaptive refinement is more suited to problems dominated by a single crack. Specifically, the problems dominated by a single crack illustrate the improvements that the adaptive refinement scheme presents in capturing crack initiation angles, crack-tip velocities, and global fracture patterns. Both the crack-tip velocity and the evolution of energy are computed in the examples, and compare well with experimental and numerical results published in the literature. The microbranching behavior, observed experimentally, is also captured when using the geometric and topological strategies proposed in this work. In addition to showing improved capabilities in capturing fracture behavior, the adaptive refinement scheme is shown to be computationally advantageous. The cost per iteration for the adaptive refinement scheme is shown to be only slightly higher than that for a coarse polygonal mesh. We also demonstrate that the standard polygonal element meshes do not provide the expected results in most of the examples we consider, when compared to numerical and experimental results available in the literature.

In this chapter, we focus on the unique geometric characteristics of polygonal elements for reducing mesh induced restrictions to crack propagation. However, we note that there is room for the extension of this work. For example, adaptive refinement of unstructured polygonal meshes, with the cohesive element framework, could allow one to bridge length scales in hierarchical materials. The fine scale features of a hierarchical material can be captured with the adaptive refinement technique detailed here, while the coarse regions of the mesh could be used to represent the homogenized response of the bulk material. Heterogeneity in the bulk material has been treated in this work with a simplified statistical distribution for nearly homogeneous materials, but the unstructured polygonal elements provide flexibility in representing distributions of heterogeneity in a material. For example, at small scales, the polygonal elements could represent grains in metals and alloys, while adaptive refinement and element-splitting could be used to represent either intergranular or intragranular fracture.

Alternatively, the philosophy of eliminating mesh induced bias in cohesive fracture sim-

ulations could be applied in the context of a recently proposed meshing strategy, known as "universal meshing" [239]. In this approach, a background mesh is fixed, and is locally deformed to conform to a given boundary (or crack). The fixed background mesh is termed as the "universal mesh". This approach has been used to successfully simulate the kink-free evolution of quasi-static cracks in brittle, isotropic, linearly elastic materials in two dimensions [239]. While this approach may be promising, it does have some inherent deficiencies. At its foundation, it is essentially a remeshing technique. In the simulation of a dynamic crack propagating through a domain, the crack boundary constantly changes, requiring a remeshing of the domain at frequent intervals. During remeshing, the transfer of variables from the former mesh to the new mesh would need to be performed. For arbitrary unstructured remeshing, the repeated application of mesh-to-mesh transfer operators may result in significant numerical diffusion [240]. Alternative, hybrid approaches to overcome this deficiency were proposed by Leon [20]. These include: (1) restricting the remeshing to the vicinity of the crack-tip to reduce the amount of numerical diffusion, and (2) increasing the intervals between remeshing, and using an element-splitting operator between each interval. While these approaches may reduce some of the issues related to the numerical diffusion induced by the mapping of variables from the old mesh to the new mesh, further investigation will need to be conducted to quantify their improvement.

Chapter 6

Regularizing Pervasive Cohesive Fracture and Fragmentation in Three-Dimensions

In this chapter, we present an investigation into the full spectrum of three-dimensional dynamic fracture behavior, using the extrinsic PPR cohesive model. While two-dimensional fracture simulations can capture the behavior of many important problems, the plane-stress or plane-strain assumptions are not always representative of the problem at hand. More importantly, two-dimensional fracture simulations can only model problems with homogeneous out-of-plane geometries. If the geometry in the out-of-plane direction varies, then fully three-dimensional simulations are necessary. In this chapter, we consider fully three-dimensional pervasive fracture simulations. Throughout pervasive fracture simulations, many cracks initiate, propagate, branch and coalesce simultaneously. Because of the cohesive element method's unique framework, this behavior can be captured in a regularized manner.

In three dimensions, it is common practice to use automatic mesh generators to discretize the domain. However, automatic mesh generators often conduct additional post-processing of the mesh; to remove elements with degenerate edges and sliver elements. In some cases, this additional post-processing leads these (initially random) meshes to contain an underlying structure. To remove this structure, we propose using the technique of nodal perturbation. The focus of this work is on the investigation of homogeneous or homogenized materials; however, we recognize that all materials contain heterogeneity (or defects) at the microscale. Defects naturally arise in materials due to grain boundaries, voids, or inclusions. As well, defects may be introduced through the act of processing or machining the material. These microscale defects constitute potential regions where stresses can concentrate and lead to damage or failure. To represent such heterogeneity, we propose using a statistical distribution of material properties. The behavior of quasi-brittle materials undergoing pervasive fracture and fragmentation is examined using three examples. The examples are selected to investigate some of the significant factors which influence pervasive fracture and fragmentation; including, geometric features, loading conditions, and material gradation.

6.1 Introduction

The pervasive fracture and fragmentation of structures occurs at various scales and in various contexts. When a structure is struck with either a high-velocity direct impact, or a blast load, the damage incurred typically pervades a region of the structure. Pervasive damage involves the entire spectrum of fracture behavior; from crack initiation, through crack propagation, branching and coalescence, all the way to complete fragmentation. At any one time, there may be hundreds or thousands of micro- to macro-cracks in the structure. Being able to capture and understand the factors which influence the fragmentation of structures can lead to better design practices in many fields of engineering. For example, understanding how a ceramic plate fragments when struck with a high velocity projectile can improve the design of armor for personnel carriers. Alternatively, understanding the process by which a kidney stone fragments may help in the design of surgical tools and procedures. However, due to the inherent complexity of modeling pervasive damage, there are few numerical methods capable of capturing the full spectrum of behavior in three-dimensions.

There are many methods which have been proposed for simulating fracture problems. Some of the popular methods consist of the extended (or generalized) finite element method (FEM); meshless or particle based methods; and the cohesive element method. A summary of the various methods was presented in Chapter 1; here, we briefly comment on the ability of the various methods to capture the full range of fracture behavior. The extended FEM uses discontinuous shape functions to represent the profile of a crack within a continuum. The discontinuity in the element's shape function effectively splits the element; which requires a lot of heuristic manipulations, and can present numerical integration and time-stepping issues in dynamic fracture simulations [7]. When faced with the full spectrum of fracture behavior, these limitations result in the extended FEM becoming prohibitively complicated [12]. Meshless methods have also shown promise in modeling problems dominated by a single crack, however, when faced with pervasive damage, many of them still suffer from volume deletion. As the continuum material fragments, it evolves into a collection of spheres; which have a theoretical maximum packing limit of 74% [12], leading to a nonphysical loss of volume in the model.

Alternatively, in this chapter, we demonstrate that the cohesive element method is particularly suited to capturing pervasive fracture and fragmentation behavior. The cohesive element method, motivated by the work of Dugdale [2] and Barenblatt [1], uses cohesive zone models to explicitly represent the inelastic zone of damage in front of the crack-tip. In dynamic fracture simulations, extrinsic cohesive elements are adaptively inserted ahead of a propagating crack-tip and resist the separation of the adjacent bulk elements through cohe-

sive forces [56, 241]. The insertion of cohesive elements is restricted to element facets. This restriction allows the cohesive element method some unique capabilities. The mesh topology regularizes the domain and naturally handles the branching and coalescence of fracture surfaces. The elements are not split, thus the minimum element size is fixed, and the time-stepping issue present in the extended FEM does not occur. Additionally, the restriction of fracture surfaces to element facets results in a continuous volume of bulk material as it fragments. However, restricting fracture to occur along element facets can result in mesh dependent behavior, and thus the meshing strategy in dynamic cohesive fracture simulations is important. If one were to choose a structured mesh, or to use mesh smoothing techniques on a randomly generated mesh, the resulting discretization could bias the fracture behavior. Thus, it is worth exploring means of introducing unstructuredness into the problem.

Unstructuredness can be introduced to a finite element problem through either topological, geometric, or constitutive means. The primary topologically unstructured methods consist of: remeshing, element-splitting and adaptive refinement. With remeshing or adaptive refinement, the internal state variables of the fine mesh need to be interpolated from those of the coarse mesh. For refinement around a propagating crack-tip, the repeated application of mesh-to-mesh transfer operators may result in significant numerical diffusion [240]. Additionally, these methods are not particularly suited to pervasive fracture problems, as the entire domain often needs to be refined, quickly losing the cost-saving advantages of adaptive refinement. Alternatively, some researchers apply element-splitting operators to increase the number of crack paths in three-dimensional tetrahedral meshes. The advantage of element-splitting is that it may be combined with an edge-collapse operator [219, 242], to coarsen regions far from the crack-tip. The downside of this technique is that element-splitting only provides a small amount of refinement, and the quality of the elements can deteriorate once split. Alternatively, in this chapter, we focus on geometric and constitutive methods for introducing unstructuredness into the problem.

Much of the numerical framework in three-dimensions is the same as that described in Chapter 5 in two-dimensions. In particular, the finite element formulation presented in Section 5.2.1 is unchanged when we move to three-dimensions, thus it will not be repeated. Additionally, the data structure we use to handle mesh modifications, and to store and retrieve data, is TopS; which was outlined in Section 5.2.5. The cohesive zone model selected to represent the dynamic failure behavior is the extrinsic Park-Paulino-Roesler (PPR) model. This work represents the first known instance of the use of the model in fully three-dimensional dynamic fracture simulations. The details of the model were presented in Chapter 5. The remainder of the chapter is organized as follows. In Section 6.2, we discuss constitutively unstructured methods for introducing randomness into a model. Section 6.3 outlines the

technique of nodal perturbation, to introduce geometric unstructuredness into a finite element mesh. Additionally, in this section, we conduct a series of geometric studies to investigate the influence of nodal perturbation on the quality of the mesh. In Section 6.4, we present three examples which highlight many of the significant factors influencing the pervasive fracture and fragmentation of structures. Section 6.5 presents an example where failure occurs due to a dominant, mixed-mode crack. In Section 6.6, we provide a global discussion on meshing strategies in two and three dimensions, and summarize the findings of our investigation on the topic. In Section 6.7, we propose a new meshing strategy called the 4k-patch mesh. Finally, we provide some concluding remarks in Section 6.8.

6.2 Unstructured constitutive relations by means of a statistical distribution

The focus of this work is on the investigation of homogeneous or homogenized materials, however, we recognize that all materials contain heterogeneity (or defects) at the microscale. Defects naturally arise in materials due to grain boundaries, voids, or inclusions [243, 244]. As well, defects may be introduced through the act of processing or machining the material [245]. These microscale defects constitute regions where stresses can concentrate and lead to damage or failure. In this work, we propose representing this heterogeneity by means of a statistical distribution of material properties, specifically a distribution of the strength of the material. Over the years, there have been many methods proposed for capturing the distribution of defects in a material.

One of the simplest methods for incorporating defects in the material is to distribute the material parameters based on a constant probability density function (PDF); which is equivalent to a random perturbation to the material's properties [225, 228, 246]. While this model is simple, it has no physically motivated basis. Alternatively, one could take a statistical approach, distributing the material strength based on a probabilistic model [247]. Peirce [248] developed a probabilistic failure model based on the weakest link theory and extreme value statistics. His model was later refined by Fréchet [249], among others [250, 251]. However, the most popular probabilistic model, for the study of material failure, is that of Weibull [223].

Weibull's probabilistic failure model was motivated by randomness he observed in the ultimate failure load of material specimens tested in an identical manner. He explained his motivation through a simple thought experiment. Consider a series of rods of length L, with cross-sectional area A, loaded to failure by an external load P. If one were to repeat this

experiment, the ultimate failure load would not be a constant, but would differ each time. The failure loads could then be grouped around a mean, and a statistical analysis could be completed. Based on a set of experiments, conducted on a variety of materials with multiple loading conditions, he proposed the well known Weibull distribution, with probability of failure, P_f, given by:

$$P_f = 1 - e^{-N(\sigma,V)}, \tag{6.1}$$

where V is the volume of the material, σ is the measure of stress, and $N(\sigma, V)$ is a material function, independent of the position. The specific form of $N(\sigma, V)$ is often the topic of debate; however, Weibull noted that it must be a monotonically increasing function of σ, and determined that an effective relation for most homogeneous materials is:

$$N(\sigma, V) = \frac{1}{V_0}\left(\frac{\sigma - \sigma_{\min}}{\lambda}\right)^m, \tag{6.2}$$

where m is the Weibull modulus, V_0 is a normalizing volume (often taken as $V_0 = 1$ [252]), λ is a scale parameter, and $\sigma_{\min}$ is the lower bound of material strength. To illustrate the influence of the Weibull modulus and scale parameter on the probability density function, some sample functions are illustrated in Figure 6.1.

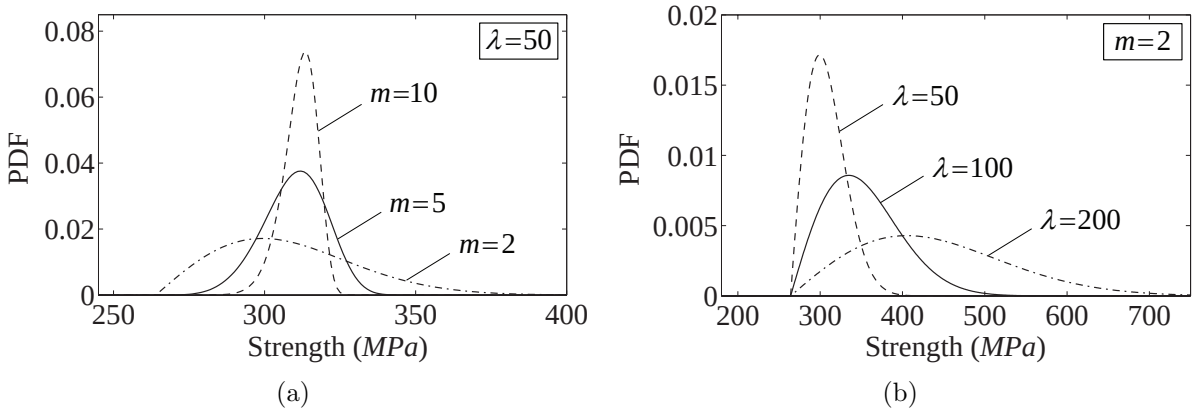

Figure 6.1: Effect of input parameters on the Weibull distribution: (a) λ, and (b) m. Here, we assume $\sigma_{\min} = 264MPa$ and $V_0 = 1$.

In the years since Weibull presented his distribution, many researchers have proposed alternate forms of $N(\sigma, V)$. Freudenthal [253] proposed a general distribution for homogeneous and brittle materials. He assumed that flaws do not interact, and that the probability of failure only depends on the number of critical flaws, $N_{c,S}$, present in a specimen of size S:

$$N(\sigma, V) = N_{c,S}(\sigma). \tag{6.3}$$

Later, Danzer [252] extended this distribution for inhomogeneous materials. Alternatively, Jayatilaka and Trustrum [254] proposed a model based on flaw size distribution and material strength:

$$N(\sigma, V) = N\frac{c^{n-1}}{n!}\left(\frac{\pi\sigma^2}{K_{IC}^2}\right)^{n-1}, \tag{6.4}$$

where N is the number of cracks, K_{IC} is the critical stress intensity factor of the material, and n and c are characteristic constants.

The abovementioned models assume that there is no interaction between defects. However, Afferrante et al. [255] demonstrated that the Weibull distribution of material strength (6.2) applies in a general sense, even if there is interaction between the defects. They also note that the Weibull modulus does not necessarily correspond to a material constant, and that it may be influenced by the interaction among cracks, or the interaction of cracks and the stress field. Thus, in the examples we investigate in Section 6.4, we will use the Weibull distribution and will vary the Weibull modulus to illustrate its influence on the global fracture behavior.

6.3 Unstructured geometry by means of nodal perturbation

There are many techniques for discretizing a volume into tetrahedral elements [256]; of which, the most popular may be the Delaunay triangulation [257, 258, 259]. Delaunay triangulation is the technique of choice for most automatic mesh generators [114, 260]. However, automatic mesh generators often conduct additional post-processing of the mesh; to remove elements with degenerate edges and sliver elements. In some cases this additional post-processing leads these (initially random) meshes to contain an underlying structure. To remove this structure, we propose using the technique of nodal perturbation (NP).

To implement the NP algorithm, we apply the following steps. First, all the nodes in the mesh are traversed, and restrictions are placed on boundary nodes. Corner nodes are fixed, edge nodes are restricted to the original line of the edge, and face nodes are restricted to the boundary face. At each node, the minimum distance between the node and the opposite faces of the adjacent tetrahedrons is computed. The node is then perturbed in a random direction; where the magnitude of the perturbation corresponds to the computed distance multiplied by a perturbation factor (perturbation factor < 1). After perturbing the nodes, a Laplacian smoothing technique is used to improve the mesh quality [221, 261]. In this step, each element in the mesh is visited, and the quality of the element is assessed. The element

quality is quantified by Lo's parameter [256], γ:

$$\gamma = \frac{72\ \sqrt{3}\ V_{\text{tetrahedron}}}{\left(\sum \text{square of edges}\right)^{3/2}}, \tag{6.5}$$

where $V_{\text{tetrahedron}}$ is the volume of the tetrahedron. Equivalently:

$$\gamma\left(A,B,C,D\right) = \frac{12\ \sqrt{3}\ \left(AB \times AC\right) \cdot AD}{\left(\|AB\|^2 + \|BC\|^2 + \|CA\|^2 + \|AD\|^2 + \|CD\|^2 + \|BD\|^2\right)^{3/2}}, \tag{6.6}$$

where A, B, C, and D correspond to the nodal positions of the tetrahedron. The higher the Lo's parameter, the higher the quality of the element. For example, equilateral tetrahedra have a Lo's parameter of 1.0. If an element fails to meet a minimum specified Lo's parameter, the position of each node in the element is displaced by the average of the distance vectors to the neighboring nodes on the edges incident to the node [221]. This procedure is iterated until all elements in the mesh meet minimum specified quality requirements.

Here, we conduct a series of geometric studies on a mesh before and after NP. The studies are conducted on a cubic domain, randomly discretized with $47,924$ tetrahedral elements, as illustrated in Figure 6.2. An illustration of the effect of NP on a typical Delaunay mesh is shown in Figures 6.2(b) to 6.2(d). The NP factors used in this study range from $0.0 - 0.6$, in increments of 0.1. Three unique meshes are generated for each random NP factor, and the results of the studies are averaged. To quantify the effect of NP, we track three metrics: element quality (Lo's parameter), minimum interior angle, and maximum interior angle.

The results of the study on Lo's parameter are illustrated in Figure 6.3. The desired average mesh quality parameter is selected as 0.7; which is generally acceptable for finite element simulations [221]. The minimum Lo's parameter for an unperturbed mesh is 0.434, and decreases with increasing NP factor. For the unperturbed mesh, and the same mesh with a NP factor of 0.4, we plot the spatial distribution of Lo's parameter for each element in Figures 6.3(a) and 6.3(b), respectively. A histogram of the mesh quality for increasing NP factors is illustrated in Figure 6.3(c). As the NP factor increases, the range of Lo's parameters broadens and skews to lower values. Regardless of the NP factor, the maximum Lo's parameter in the mesh remains approximately equal to 1.0.

To gain additional insight into the influence of NP on the mesh, we investigate the minimum and maximum interior angles of the elements in the mesh. The interior angles can give insight into the initial distortion of the elements. For example, the commercial software Abaqus qualifies elements with interior angles less than 10° or greater than 160° as distorted [103]. A histogram of the minimum interior angle is presented in Figure 6.4(a), while one

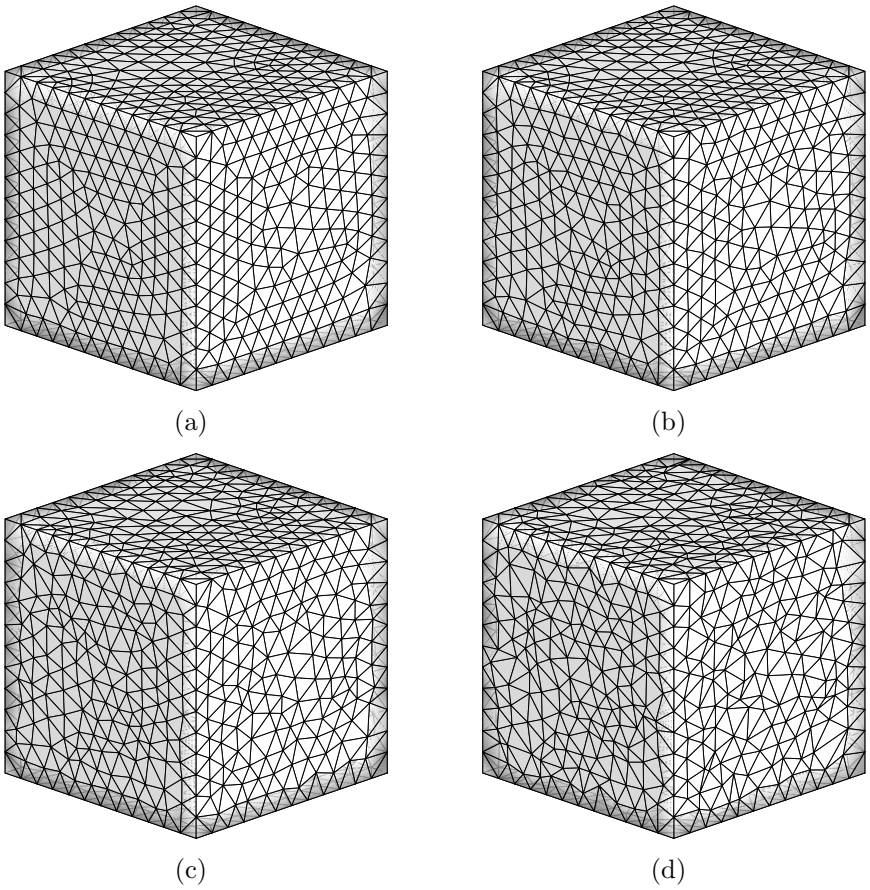

Figure 6.2: Influence of nodal perturbation on meshes generated using a Delaunay triangulation [114]. (a) Unperturbed, (b) a nodal perturbation factor of 0.2, (c) a nodal perturbation factor of 0.4, and (d) a nodal perturbation factor of 0.6.

for the maximum interior angle is presented in Figure 6.4(b). For the unperturbed case, the smallest minimum interior angle is approximately 25.3°, and decreases with increasing NP factor. Similarly, the largest maximum interior angle for the unperturbed case is approximately 120.7° and increases with increasing NP factor. These results are in line with expectations, as perturbing the nodes distorts the elements, and the higher the perturbation factor, the higher the level of distortion.

The results of the geometric study are summarized in Table 6.1. Based on the results, a NP factor of 0.4 is the largest factor which still maintains a high quality mesh and conforms to the recommended interior angles [103]. Thus, this is the NP factor we use in the remainder of the chapter.

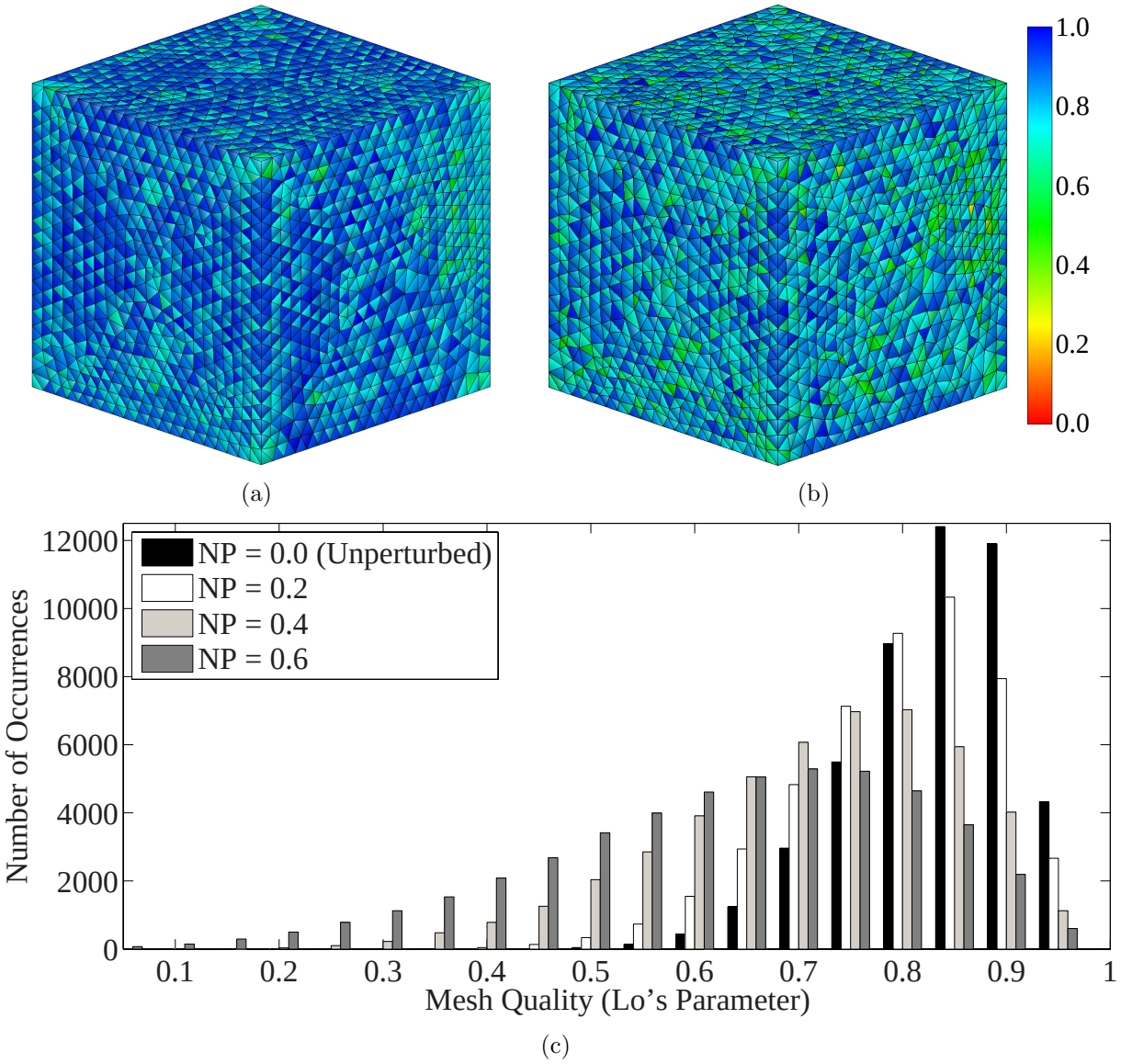

Figure 6.3: Contour plot of Lo's parameter for each element, considering (a) NP= 0.0 (Unperturbed), and (b) NP= 0.4; and (c) a histograph of mesh quality for various nodal perturbation factors.

6.4 Pervasive fracture example problems

In this section, three example problems are investigated which display pervasive fracture behavior. The first example considers the centrifugal loading of a spinning disk. The second example investigates the impulse loading of a hollow sphere, where focus is placed on the influence of geometric features on the fragmentation behavior of the sphere. The third example considers the fragmentation of a kidney stone under direct impact. Since kidney stones often display a radial gradation of material properties, we consider both homogeneous and functionally graded stones. Unless noted otherwise, we consider a fragment to be a

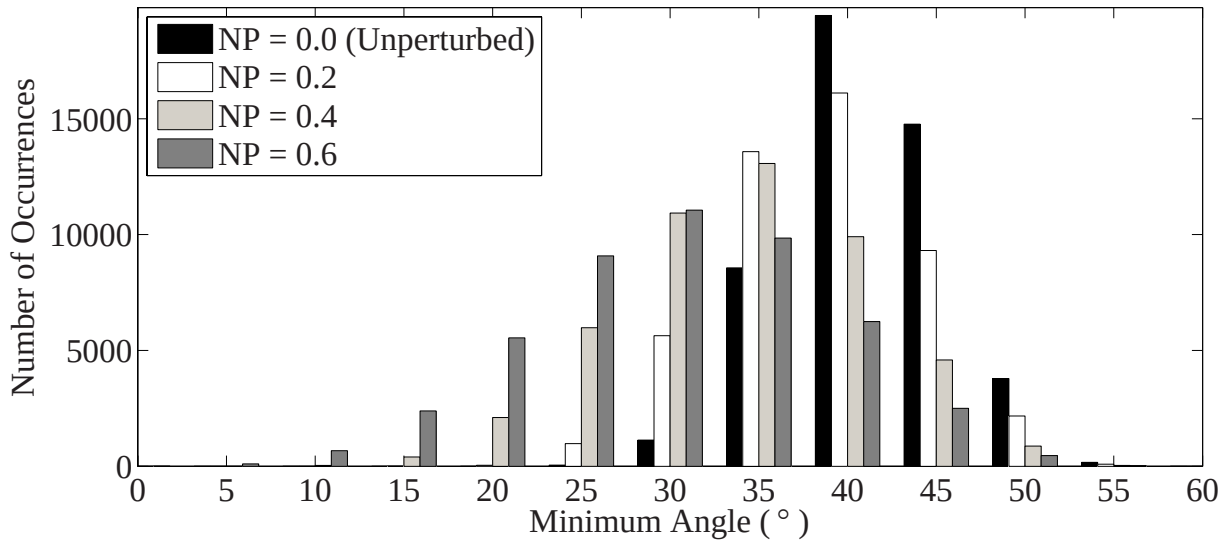

(a)

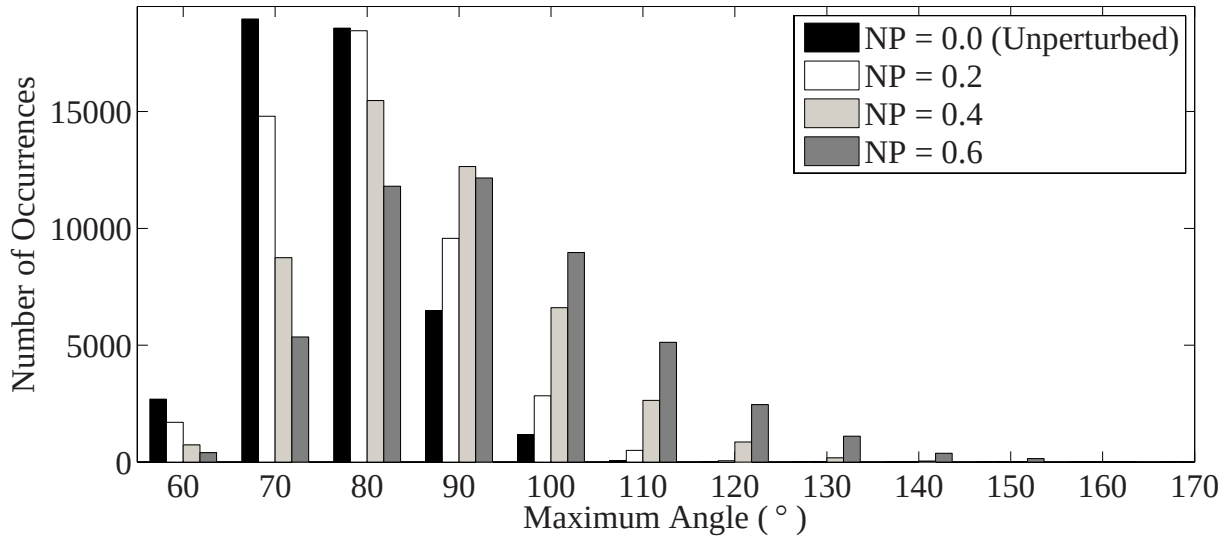

(b)

Figure 6.4: Results of the study on the interior angles in the mesh: (a) histograph of minimum interior angles, and (b) histograph of maximum interior angles.

mass of bulk elements (and cohesive elements which have not fully separated) completely surrounded by boundary facets and/or fully separated cohesive elements. A pseudo code of the procedure we use to determine the fragments is provided in Algorithm 1. The objective of the algorithm is to create a list of fragments, and all bulk elements belonging to that fragment. Comparisons to experiments are made where possible. In all of the examples, we consider the influence of randomness in the material strength on the fragmentation behavior. The Weibull function (6.2) is selected to describe the distribution of material strength.

Algorithm 1 Procedure for determining the distribution of the fragments.

```
input: nBulkElems          //number of bulk elements in the model
  nVisited = 0             //number of bulk elements visited
  while (nVisited < nBulkElems)
    Iterate over all the elements in the model
      if (element is cohesive) continue; end if
      if (element has been visited) continue; end if
      Create a new fragment structure
      Add the bulk element to the fragment, and flag it as visited
      Increment nVisited
      for (i = 0; i < number of bulk elements in the fragment; i++)
        Get current element in the fragment
        for (j = 0; j < number of adjacent elements; j++)
          if adjacent element is cohesive and not flagged as visited
            Flag cohesive element as visited
            if (cohesive element has failed completely) continue; end if
            for (k = 0; k < number of adjacent bulk elements; k++)
              if (element has been visited) continue; end if
              Add the bulk element to the fragment, and flag it as visited
            end for
          else
            if (element has been visited) continue; end if
            Add the bulk element to the fragment, and flag it as visited
            Increment nVisited
          end if
        end for
      end for
  end while
output: Fragments
```

Table 6.1: Summary of the results for the mesh quality study. The quantities for each metric are averaged over three randomly generated meshes.

	Lo's Parameter (γ)			Minimum Angle ($^\circ$)			Maximum Angle ($^\circ$)		
NP Factor	min	mean	max	min	mean	max	min	mean	max
0.0	0.434	0.858	0.999	25.3	43.7	58.1	61.5	81.8	120.7
0.1	0.419	0.848	0.998	24.3	43.0	58.4	61.9	82.6	123.1
0.2	0.292	0.820	0.998	19.9	41.1	58.1	62.0	84.8	132.5
0.3	0.225	0.782	0.997	15.2	38.8	57.9	62.5	87.8	142.0
0.4	0.132	0.738	0.996	11.5	36.5	57.3	62.5	90.9	152.4
0.5	0.064	0.695	0.996	7.2	34.4	57.6	63.3	94.2	162.7
0.6	0.027	0.656	0.998	3.7	32.6	58.0	61.6	97.1	171.0

6.4.1 Centrifugal loading of a spinning disk

This example considers the fragmentation of a spinning disk; which is motivated by the use of structural ceramics in the high stress environment of a spinning turbine. We consider two different geometries for the disk, as illustrated in Figure 6.5. The two disks, from this point forward, will be referred to as the small disk and the large disk, respectively. Each disk is ceramic, constituted of silicon nitride (Si_3N_4); the elastic modulus of which is $300GPa$, the Poisson's ratio is 0.3, and the density is $3250kg/m^3$. The mode I fracture energy (ϕ_n) and shape parameter (α) are set as $180N/m$ and 2, respectively. The minimum cohesive strength, $\sigma_{\min}$, is set as $425MPa$. Two Weibull moduli, $m = 2$, 5, and two scale parameters $\lambda = 40MPa$, $80MPa$ are considered. The mode II fracture properties are assumed to be the same as the mode I fracture properties.

Experimentally, the small disk specimen was investigated by Swank and Williams [262]; however, to the best of the author's knowledge, there have been no numerical investigations using this geometry and loading condition. To simulate this problem, we use a randomly generated mesh containing $124,882$ linear tetrahedral elements ($30,421$ nodes), and a NP factor of 0.4. The spinning of the disk is represented as a centrifugal force, with an angular velocity (ω) of $4\pi \times 10^3 rad/sec$. To model the centrifugal force, a body force ($\mathbf{b}$) is applied to the model:

$$\mathbf{b} = \rho\omega^2\mathbf{r}, \tag{6.7}$$

where ρ is the density of the material and $\mathbf{r}$ is the radial vector of the point of loading. The angular velocity is ramped up linearly over $100\mu s$ and held constant thereafter, as illustrated in Figure 6.6. For each Weibull modulus (m) and scale parameter (λ) we run three simulations (a total of 12 simulations). For this example, we illustrate each of the

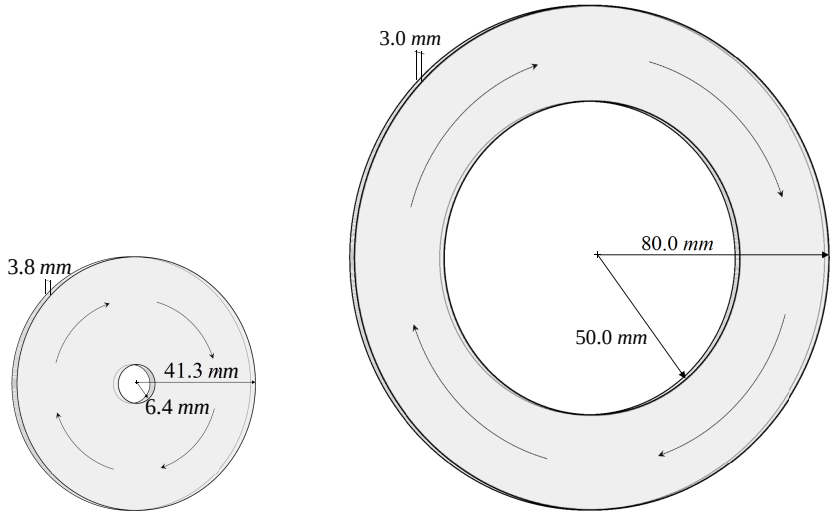

Figure 6.5: Geometries investigated in the spinning disk example: (a) small disk, and (b) large disk.

results in Figure 6.7. Each result displays the final fragmented form of the specimen.

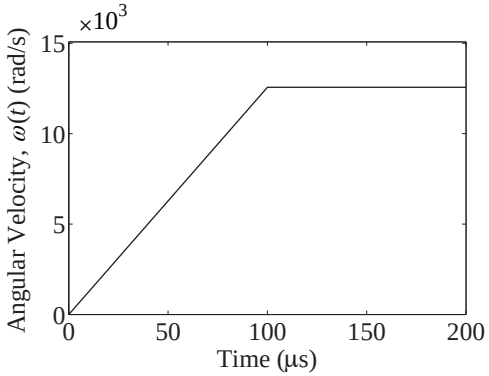

Figure 6.6: Applied angular velocity, over time, in the small disk specimen.

Based on the results, it is clear that the random distribution of material strength, and the random perturbation of nodes, produces a random result in each simulation. However, qualitatively there are many similarities among the fracture patterns. For the most part, the small disk specimen fractures into approximately four large fragments and $1-3$ medium fragments. The large fragments are defined as the bulk of material between two cracks which span the entire width of the cylinder. A medium fragment is defined as the bulk of material that results after the branch of a through-width crack reaches the outer boundary of the specimen. For example, the result illustrated in Figure 6.7(f) displays four large fragments and two medium fragments. In addition to the qualitative fracture patterns, we also calculate the average crack-tip velocity through the specimen. The crack-tip velocity is determined

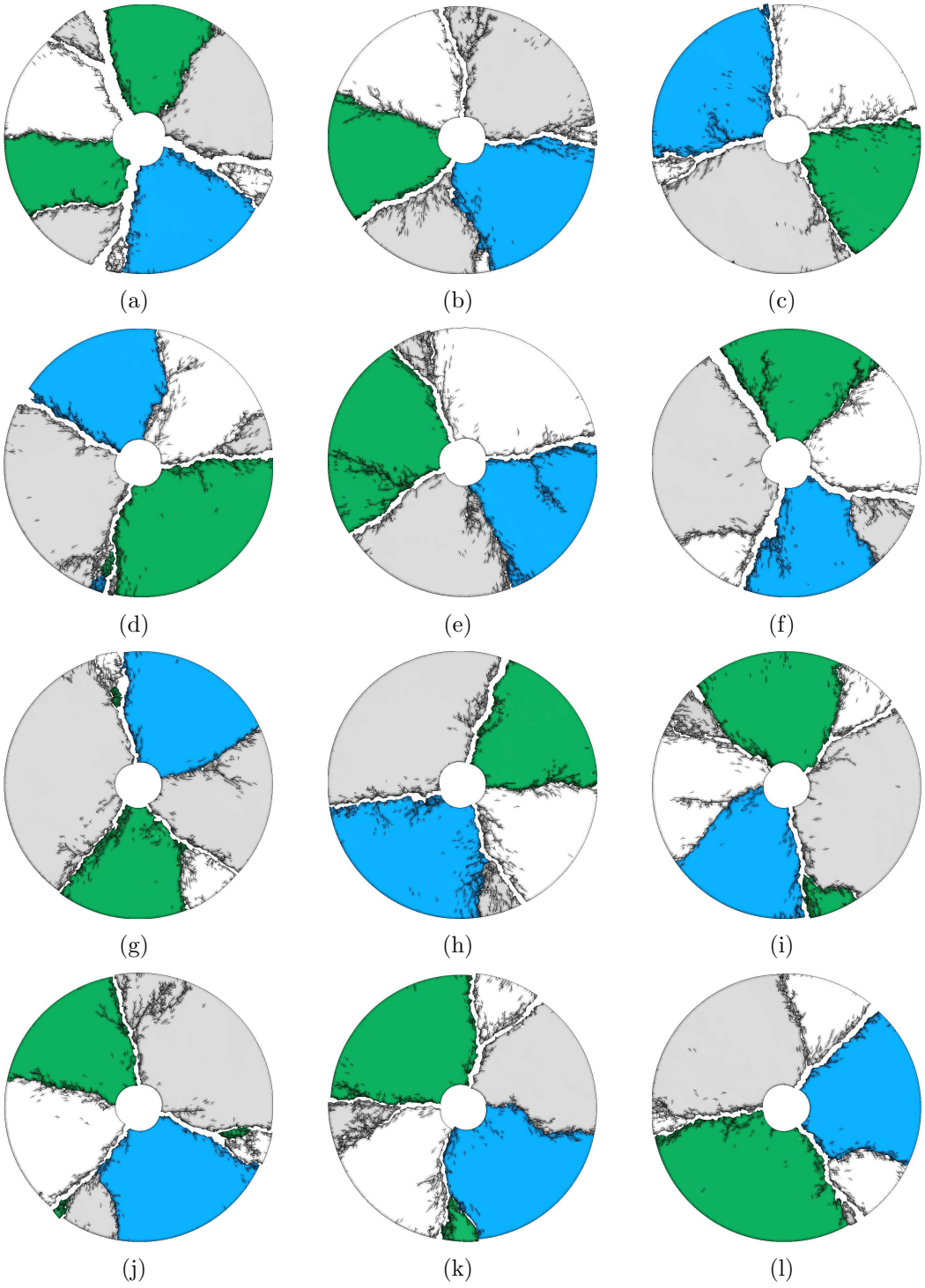

Figure 6.7: Results for the small disk geometry with Weibull parameters: (a) $\lambda = 40MPa$, and $m = 2$; (b) $\lambda = 40MPa$, and $m = 5$; (c) $\lambda = 80MPa$, and $m = 2$; and (d) $\lambda = 80MPa$, and $m = 5$. All the results are illustrated in their final fragmented form, which occurred in the range of $118\mu s$ to $127\mu s$. For visual clarity, the small fragments (those comprised of fewer than 10 bulk elements) have been removed from the displayed results.

by simply documenting the time it takes for a crack to propagate through the entire width of the disk. A summary of the results is presented in Table 6.2.

The average crack-tip velocity varies between $2769m/s$ and $3181m/s$, depending on the distribution of material strength. For the wider distribution of strength, $m = 5$, the crack-tip velocity is higher than that observed for a more homogeneous, or narrow, distribution of strength, $m = 2$. The Rayleigh wave speed, C_R, for Si_3N_4 is $5600m/s$, thus the computed values fall in the range of $0.49C_R$ to $0.57C_R$; which is consistent with the experimentally expected crack velocity [237].

Scale Parameter (λ)	Weibull Modulus (m)	Large Fragments	Medium Fragments	Crack-tip Velocity
40 MPa	2	4.33	2.67	2888 m/s
40 MPa	5	4.00	2.67	3181 m/s
80 MPa	2	4.00	2.33	2769 m/s
80 MPa	5	3.67	3.33	3179 m/s

Table 6.2: Summary of the small disk results. Each result is the average of three simulations. A large fragment is defined as the bulk of material between two cracks which span the entire width of the cylinder. A medium fragment is defined as the bulk of material that results after the branch of a through-width crack reaches the outer boundary of the specimen.

The large disk specimen was investigated experimentally by Hashimoto et al. [263]. Numerically, this problem has been simulated by Zhou and Molinari [131]. They simulate fracture using a linear cohesive traction-separation relation, and also consider the influence of material heterogeneity. Their investigation determined that the greater the heterogeneity in the material (i.e. the wider the range of cohesive strength), the fewer fragments were produced. In addition, they compute an average crack-tip velocity of $5500m/s$, or 98% of the Rayleigh wave speed; a result which they note is inconsistent with experiments [131].

To simulate this problem, we use a model containing $140,339$ elements ($40,768$ nodes). Similarly to the small disk, we represent the spinning of the large disk as a centrifugal force, with an angular velocity of $2.8\pi \times 10^3 rad/sec$. The angular velocity is ramped up linearly over $100\mu s$ and held constant thereafter. For each Weibull modulus (m) and scale parameter (λ) we run three simulations (a total of 12 simulations). For this example, we only illustrate a typical result for each combination of Weibull modulus and scale parameter in Figure 6.8. Each result displays the final fragmented form of the specimen. The resulting number of large and medium fragments is summarized in Table 6.3. For the smaller scale parameter, $\lambda = 40MPa$, a greater number of large and medium fragments is produced than in the case with a larger scale parameter, $\lambda = 80MPa$. Overall, the fracture patterns correspond well

to those observed experimentally (see Figure 4 in [263]), and the distribution of fragments corresponds well to those in alternate numerical investigations [131].

The velocity of the through-width cracks is also tracked, and the results are included in Table 6.3. The average crack-tip velocity varies between $3165m/s$ and $3390m/s$, depending on the distribution of material strength. Similar to the small disk geometry, for a wider distribution of strength, $m = 5$, the crack-tip velocity is higher than that observed for a more homogeneous distribution of strength, $m = 2$. For comparison, the computed values fall in the range of $0.56C_R$ to $0.61C_R$.

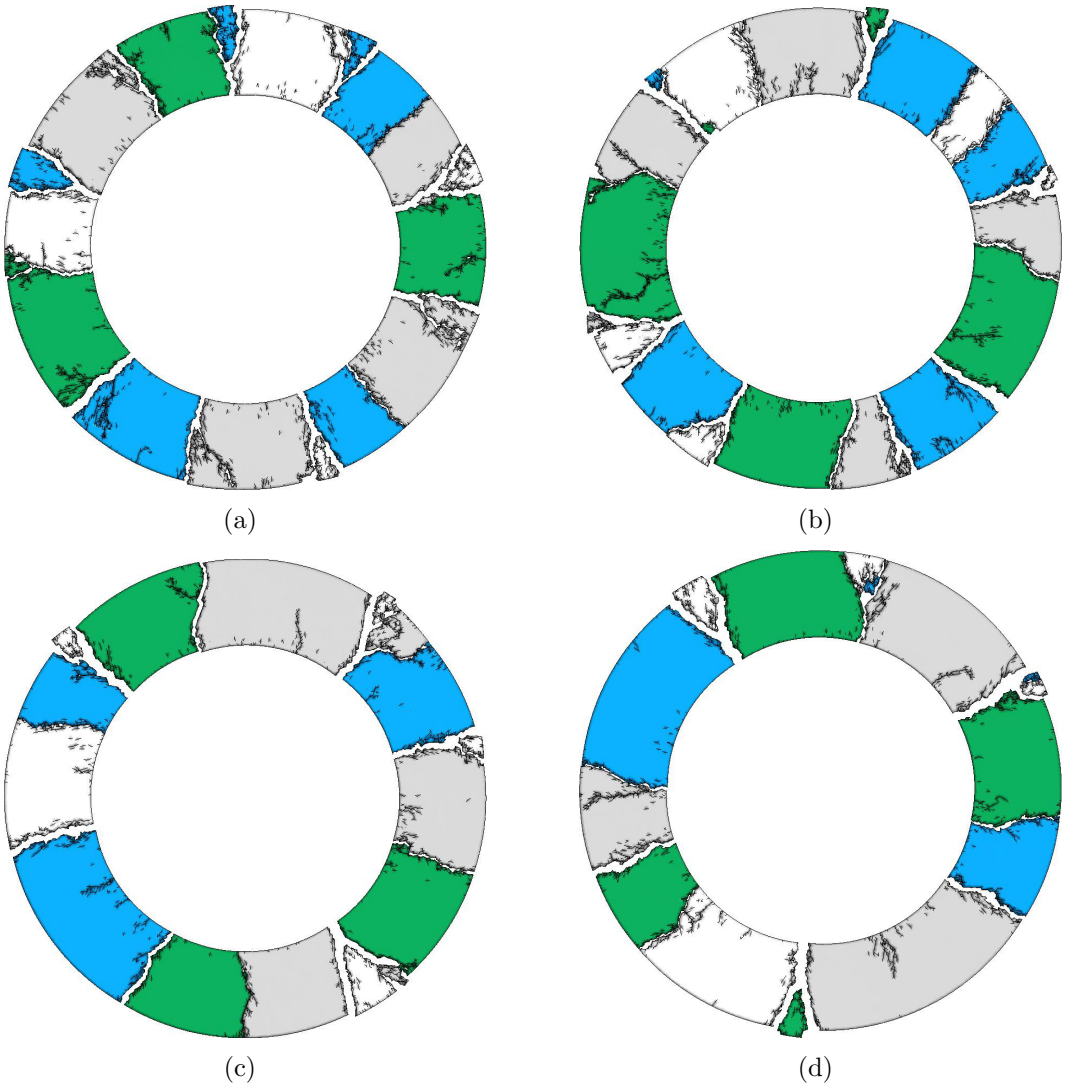

Figure 6.8: Typical results for the large disk geometry with Weibull parameters: (a) $\lambda = 40MPa$, and $m = 2$; (b) $\lambda = 40MPa$, and $m = 5$; (c) $\lambda = 80MPa$, and $m = 2$; and (d) $\lambda = 80MPa$, and $m = 5$. All the results are illustrated in their final fragmented form, which occurred at approximately $87\mu s$. For visual clarity, the small fragments (those comprised of fewer than 10 bulk elements) have been removed from the displayed results.

Scale Parameter (λ)	Weibull Modulus (m)	Large Fragments	Medium Fragments	Crack-tip Velocity
40 MPa	2	12.33	6.67	3165 m/s
40 MPa	5	13.67	7.00	3390 m/s
80 MPa	2	11.33	4.33	3203 m/s
80 MPa	5	10.67	5.67	3346 m/s

Table 6.3: Summary of the large disk results. Each result is the average of three simulations. A large fragment is defined as the bulk of material between two cracks which span the entire width of the cylinder. A medium fragment is defined as the bulk of material that results after the branch of a through-width crack reaches the outer boundary of the specimen.

6.4.2 Impulse loading of a hollow sphere

This example investigates the fragmentation of a hollow sphere impacted with a radial impulse load. We consider both a smooth sphere (Figure 6.9) and a sphere containing surface features (Figure 6.10). The influence of surface features in this investigation is included to illustrate the use of simple geometric design features to regularize fragmentation patterns. Alternatively, surface features may be viewed as geometric defects, and investigating their impact on the global fragmentation response is equally significant. Numerically, the smooth sphere geometry was investigated by Levy [245]. She investigated the effect of the thickness of the sphere on the shape and distribution of fragments. In this study, we set the inner radius of the sphere to be $9.25mm$,and the outer radius to be $10mm$, as illustrated in Figure 6.9(a). The geometry is discretized with approximately 100,000 linear tetrahedral elements (approximately 25,000 nodes), as illustrated in Figure 6.9(b). The sphere is constituted of aluminum oxide (Al_2O_3); the elastic modulus of which is $370GPa$, the Poisson's ratio is 0.22, and the density is $3900kg/m^3$. The mode I fracture energy and shape parameter are set as $50N/m$ and 2, respectively. The minimum cohesive strength, $\sigma_{\min}$, is set as $264MPa$. Two Weibull moduli, $m = 2$, 5, and two scale parameters $\lambda = 50MPa$, $100MPa$ are considered.

The sphere is loaded with a radial impulse. Since we assume the sphere to be centered on the origin, the initial nodal velocities are prescribed as:

$$v_x(x,y,z) = \dot{\varepsilon}x, \qquad v_y(x,y,z) = \dot{\varepsilon}y, \quad \text{and} \quad v_z(x,y,z) = \dot{\varepsilon}z, \tag{6.8}$$

where x, y, and z, are the nodal coordinates, and $\dot{\varepsilon}$ is the applied rate of strain. In this study we will consider two different strain rates, $\dot{\varepsilon} = 2500s^{-1}$ and $\dot{\varepsilon} = 5000s^{-1}$. Once again, for each geometry, loading rate, Weibull modulus and scale parameter, we run three simulations (a total of 72 simulations). For visual clarity, the fragments will be individually colored in

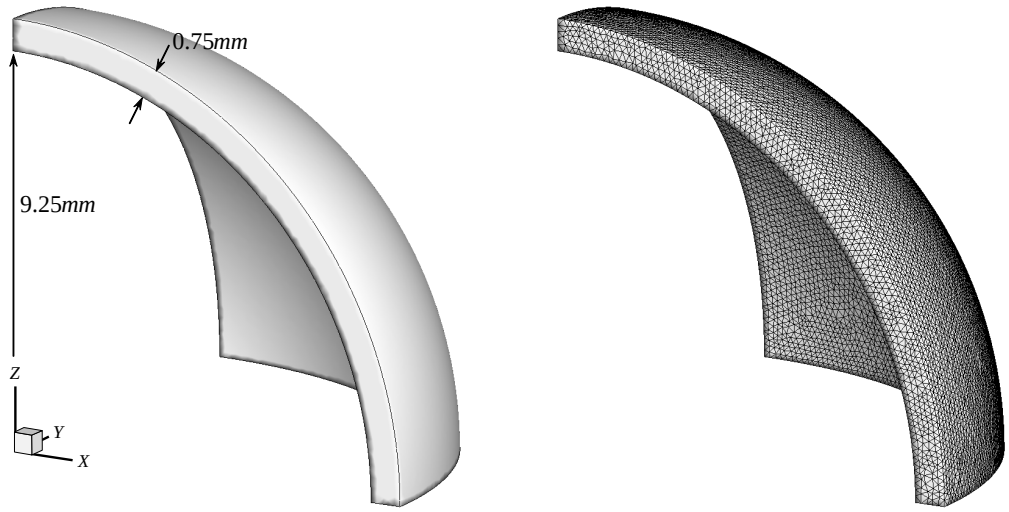

(a) (b)

Figure 6.9: Model of a smooth, hollow sphere: (a) geometry, and (b) mesh.

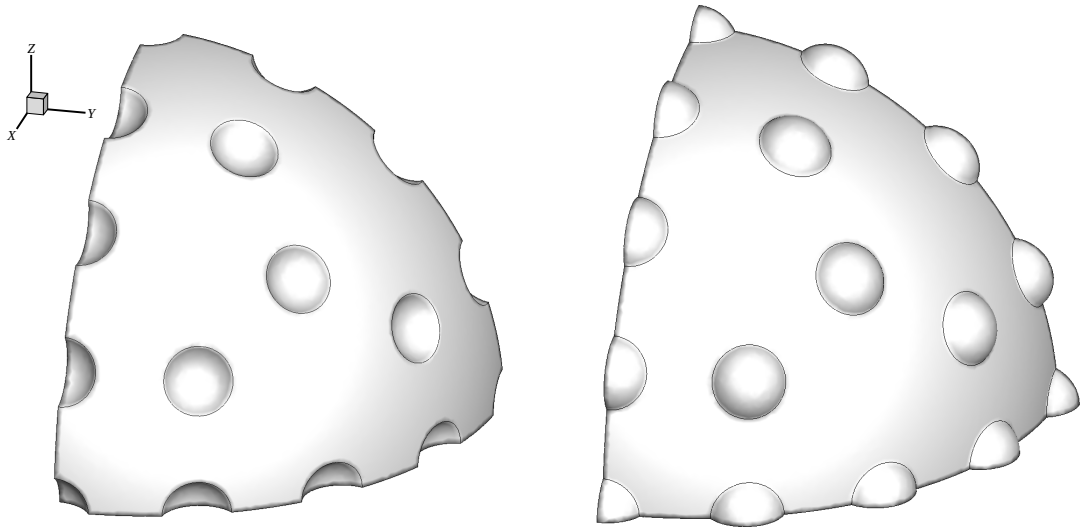

(a) (b)

Figure 6.10: Geometry of a hollow sphere with different surface features, (a) dimples, and (b) bumps. The dimples are generated by removing material that intersects with spheres of radius, $r = 1.1mm$, placed at a radial distance of $10.5mm$ from the origin. The bumps are generated through the union of the smooth sphere and spheres of radius, $r = 1.1mm$, placed at a radial distance of $9.5mm$ from the origin.

each of the results we illustrate.

For a strain rate of $\dot{\varepsilon} = 2500s^{-1}$, we illustrate some typical results in Figure 6.11 for a Weibull modulus of $m = 2$ and scale parameter $\lambda = 50MPa$. As illustrated in Figure 6.11(a), the smooth sphere fragments into large pieces with no discernible pattern. Alternatively, each case with surface features displays a distinct pattern by which it fragments. For the case with surface dimples, fracture was observed to initiate at the centroid of the dimples and to

radiate outwards. This is not surprising, as the geometry is thinnest at this location, causing stresses to concentrate here, as illustrated in Figure 6.12. Additionally, the placement of the dimples appears to control the geometry of the fragments. In Figure 6.11(b), one can see that the edges of the fragments align with the centroids of nearest neighbor dimples. Alternatively, when we consider the case with bumps (Figure 6.11(c)), there is clear evidence that the edges of the fragments are deflected away from the bumps. Thus, the bumps remain intact during fragmentation. While we only display selected results here, this behavior was shown across all the Weibull modulus and scale parameter values we considered.

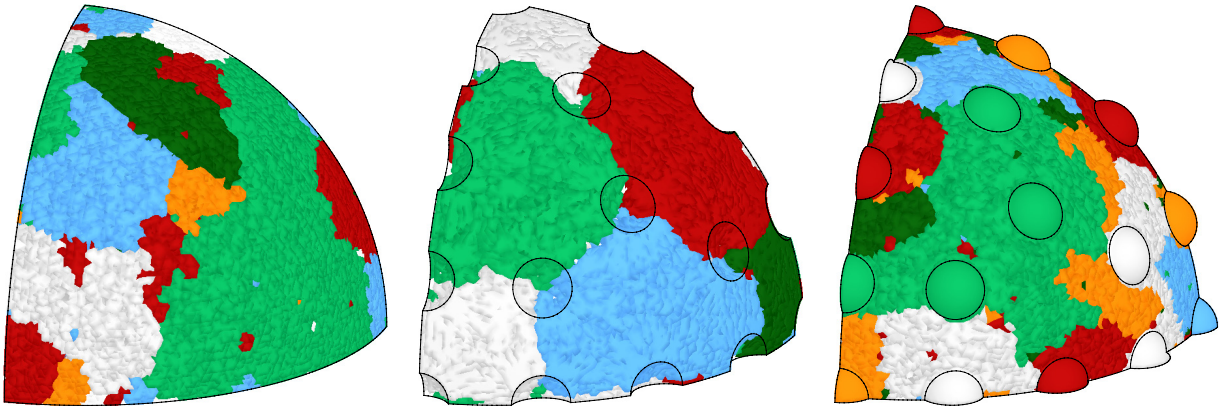

(a) (b) (c)

Figure 6.11: Final fragmented geometries, after impacted with an impulse load at a rate of $\dot{\varepsilon} = 2500s^{-1}$, for: (a) a smooth sphere, (b) a sphere with dimples, and (c) a sphere with bumps. The results show typical fracture patterns, but are for the case with $\lambda = 50MPa$ and $m = 2$. The fragments are colored for visual clarity, and the small fragments (those comprised of fewer than 10 bulk elements) have been removed from the displayed results.

If we increase the applied rate of strain to $\dot{\varepsilon} = 5000s^{-1}$, fragmentation becomes more pervasive, as illustrated in Figure 6.13. Similar to the previous case, the fragmentation of the smooth sphere does not display any discernible pattern. However, fracture continues to initiate at, and to radiate outwards from, the dimples; and each bump is wholly contained in a single fragment. Once again, this behavior was shown across all the Weibull modulus and scale parameter values we considered.

To further examine the fragmentation behavior, we plot the evolution of fragmentation through time in Figure 6.14. Results are illustrated for a variation in scale parameter, λ, with a constant Weibull modulus of $m = 2$. In each scenario, fragmentation initiates quickly (after approximately $0.5\mu s$ to $2\mu s$), and takes approximately $20\mu s$ to complete. In all the cases with a higher applied rate of strain, $\dot{\varepsilon} = 5000s^{-1}$, the majority of the fragmentation occurs in the first $10\mu s$, and fragmentation evolves slower in cases with $\lambda = 100MPa$ than they do in cases with $\lambda = 50MPa$. When we examine cases with a lower rate of strain,

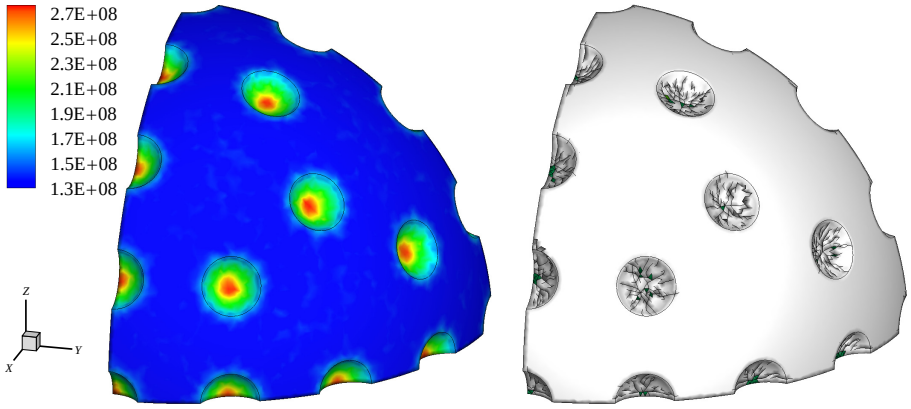

(a) (b)

Figure 6.12: Initial stages of fracture in a sphere with dimples. (a) Contour of principal stress, illustrating the concentration of stress at the centroids of the dimples, immediately prior to fracture; and (b) fracture initiating at the dimples.

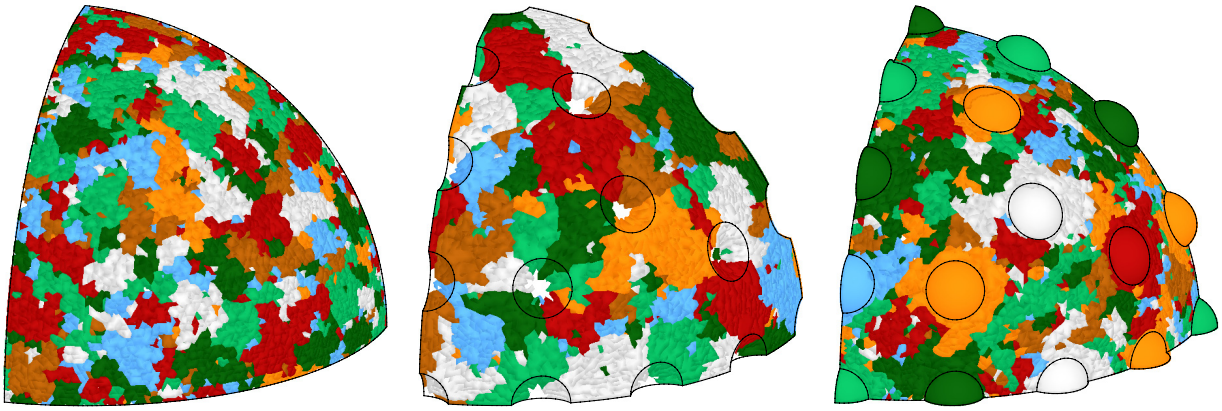

(a) (b) (c)

Figure 6.13: Final fragmented geometries, after impacted with an impulse load at a rate of $\dot{\varepsilon} = 5000s^{-1}$, for: (a) a smooth sphere, (b) a sphere with dimples, and (c) a sphere with bumps. The results show typical fracture patterns, but are for the case with $\lambda = 50MPa$ and $m = 2$. The fragments are colored for visual clarity, and the small fragments (those comprised of fewer than 10 bulk elements) have been removed from the displayed results.

$\dot{\varepsilon} = 2500s^{-1}$, little difference is observed in the cases with $\lambda = 50MPa$ and $\lambda = 100MPa$. However, for the case with dimples (Figure 6.13(b)) fragmentation evolves at a faster rate than when we consider a smooth sphere, or a sphere with bumps. From this investigation, we see that the distribution of material parameters does have an impact on the manner in which fragmentation occurs; however, the fragmentation patterns are also significantly influenced by geometric features. This investigation provides support to the idea of being able to regularize fragmentation behavior through simple geometric design features.

An investigation of energy evolution is conducted for the case of the smooth sphere, as

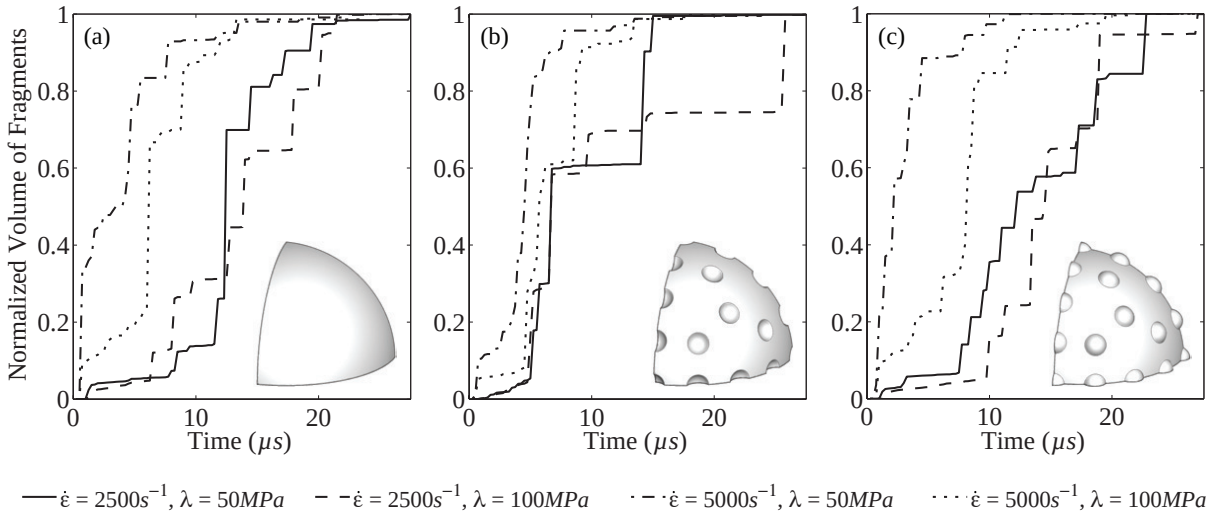

Figure 6.14: Evolution of fragmentation for: (a) a smooth sphere, (b) a sphere with dimples, and (c) a sphere with bumps. The results shown consider a Weibull modulus of $m = 2$.

illustrated in Figure 6.15. The energy is comprised of the strain (E_{int}), kinetic (E_{kin}) and fracture (E_{fra}) energies. The impulse load on the structure results in a large initial kinetic energy, which is converted into strain energy in the system. The fracture energy remains equal to zero up until the point of crack initiation, and monotonically increases over time. The summation of energy in the system remains constant over time, indicating a conservation of energy. For a higher rate of strain, the initial kinetic energy in the system is larger, as illustrated in Figure 6.15(b). This higher rate of strain also leads to an earlier onset of fracture, however, the relative magnitudes of strain and fracture energy in each system is similar.

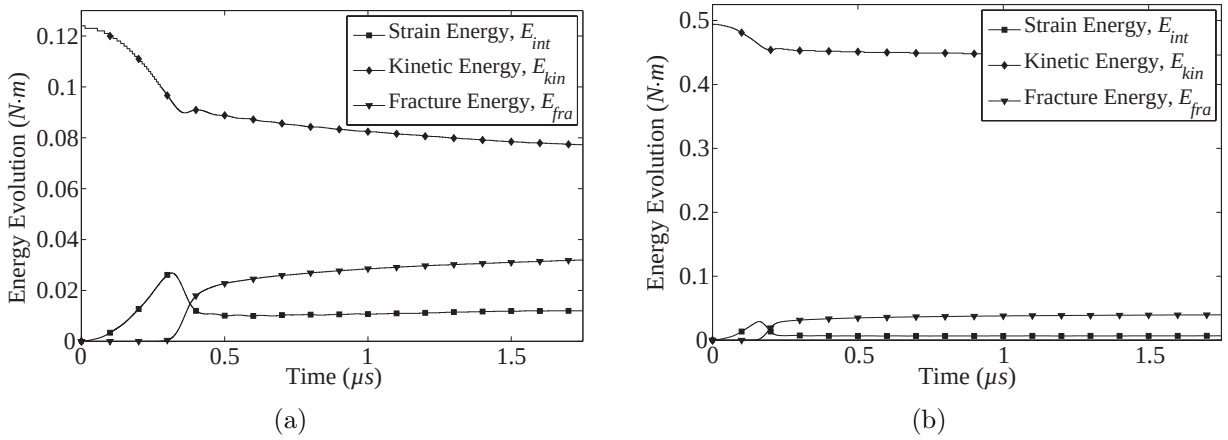

Figure 6.15: Evolution of energy for a hollow sphere under an impulse load with an applied rate of strain of: (a) $2500s^{-1}$, and (b) $5000s^{-1}$.

6.4.3 Direct impact of a kidney stone

This example considers the direct impact of a kidney stone through the use of a Lithoclast. A Lithoclast is a surgical tool which propels a metallic probe against the stone. The kinetic energy of the probe is dissipated throughout the stone, forming cracks and fragments, allowing for easier removal or passage. The structure of the kidney stone has long been known to be nonhomogeneous [264, 265, 266], however, most attempts at simulating such problems have assumed homogeneous material properties [133, 267, 268]. Mota et al. [267] studied the fragmentation of manufactured, cylindrical stones made from gypsum. They loaded the stone using the technique of Lithotripsy, wherein a pulse of pressure is applied to the exterior of the stone. They also conducted experiments and demonstrated the cohesive element method's ability to capture fragmentation patterns which agreed with those observed experimentally. Caballero and Molinari [133, 268] simulated the direct impact of a kidney stone with the Lithoclast, but only considered the simplified case of a homogeneous stone structure. In this example, we investigate the influence of a radially heterogeneous microstructure within the stone, and include the influence of randomly distributed material strength.

The geometry of the problem is illustrated in Figure 6.16. The kidney stone model is assumed to be spherical, with a radius of $10mm$. The site of impact with the Lithoclast is assumed to be circular, with a radius of $0.325mm$. The stone is discretized with 51,746 elements (10,424 nodes), as illustrated in Figure 6.16. The elements at the site of impact have a maximum size of $0.1mm$, and those in the bulk of the stone have a maximum size of $0.65mm$. In this investigation, we will consider the three distinct sets of material properties listed in Table 6.4. We will first investigate the fragmentation behavior for a homogeneous stone; then consider the behavior when the core of the stone is comprised of a different material than the outer layer of the stone. The numerical framework described in Section 5.2.1 applies to both homogeneous and functionally graded materials. To numerically capture the gradation of the material between distinct zones, we use graded finite elements; which incorporate the material gradation at the size-scale of the element. There have been multiple methods designed to allow for graded material properties at the element scale [141, 142], however, in this work, we use the generalized isoparametric method proposed by Kim and Paulino [142]. In the generalized isoparametric method, the element shape functions are used to interpolate the material parameters from the Gauss points to the nodes. Between distinct zones we grade all bulk and cohesive material properties, as well, we continue to assume a random distribution of material strength.

The impact of the probe is modeled by displacing the nodes in the impact site by a

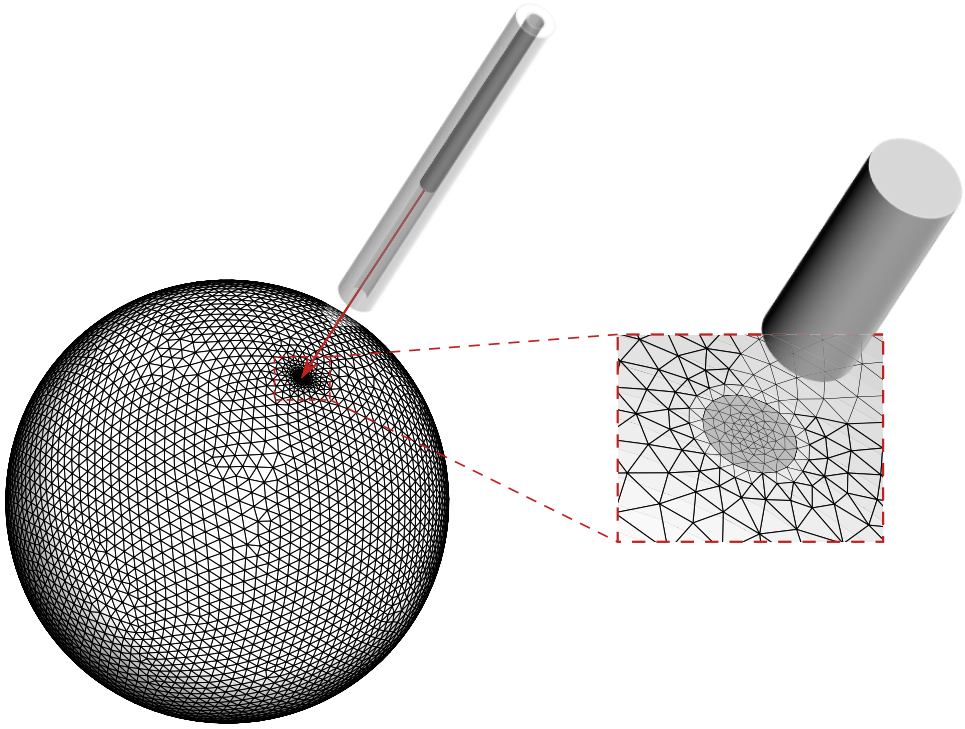

Figure 6.16: Geometry and mesh of the kidney stone model.

Stone Composition (%)	$\phi\ (N/m)$	$\sigma\ (MPa)$	$\rho\ (kg/m^3)$	$E\ (MPa)$
COM	0.735	1.500	2038	25.162
CA	0.382	0.500	1732	8.504
CA(50)/COM(50)	0.553	1.000	1885	16.833

Table 6.4: Summary of material properties in common kidney stones. COM: calcium oxalate monohydrate; and CA: carbonate apatite [265].

prescribed velocity. The velocity of the probe is not known precisely, but we assume that it decreases monotonically. Caballero and Molinari [133, 268] suggest that the impact velocity follows the relation:

$$\dot{u}\left(t\right) = \dot{u}_0 \left[1 - \frac{e^{-\alpha \frac{t}{t_{\max}}}}{1 + \left(e^{-\alpha} - 1\right) \frac{t}{t_{\max}}}\right], \tag{6.9}$$

where $\alpha \in (-\infty, +\infty)$, $\dot{u}_0$ is the initial velocity of the probe, and $t_{\max}$ is the total time of contact. The total time of contact is determined through the relation:

$$t_{\max} = \frac{u_{t_{\max}}}{\dot{u}_0} \frac{\left(e^{-\alpha} - 1\right)^2}{1 - e^{-\alpha}\left(1 + \alpha\right)}, \tag{6.10}$$

where $u_{t_{\max}}$ is the maximum displacement achieved by the probe after impact. The particular velocity relation used in this investigation is illustrated in Figure 6.17.

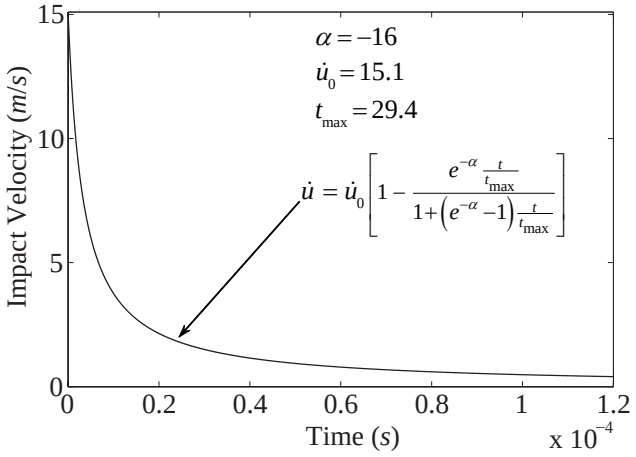

Figure 6.17: Impact velocity of the metal probe on the kidney stone.

First, we examine the fragmentation behavior of the homogeneous kidney stone. We consider all three materials listed in Table 6.4 and plot the evolution of fragmentation through time in Figure 6.18. Results are illustrated for a variation in both scale parameter, λ, and Weibull modulus, m, for each material. In general, the fragmentation evolves slower for the most compliant material (CA), than it does for the least compliant material (COM). When considering the random distribution of material strength, the scale parameter is shown to have a much greater influence on the evolution of fragmentation that the Weibull modulus. For a smaller scale parameter, $\lambda = 0.2MPa$, fragmentation occurs sooner and is more pervasive than in the case of a large scale parameter, $\lambda = 0.4MPa$. Additionally, the final volume of fragments indicates that the stone does not fully fragment when the range of material strength increases. The results shown are for a single instance of the simulated problem, however, each scenario was simulated three times, and the present results and conclusions are typical across each simulation.

When we assume that the stone contains a different constitutive make-up in the inner core than it does in the outer layer, the fragmentation behavior changes significantly. In this investigation, we consider scenarios with both a more compliant and less compliant material in the inner core. Based on experimental observations of the microstructure of kidney stones [264, 265, 266], the outer core is assumed to be 15% the thickness of the radius, and the zone transitioning between the inner core and outer layer is assumed to be 20% the thickness of the radius. Multiple values were investigated for the thickness of both the outer layer and zone of transition, but these values did not significantly influence the global response. Typical results are illustrated in Figure 6.19. When we have a more compliant inner core,

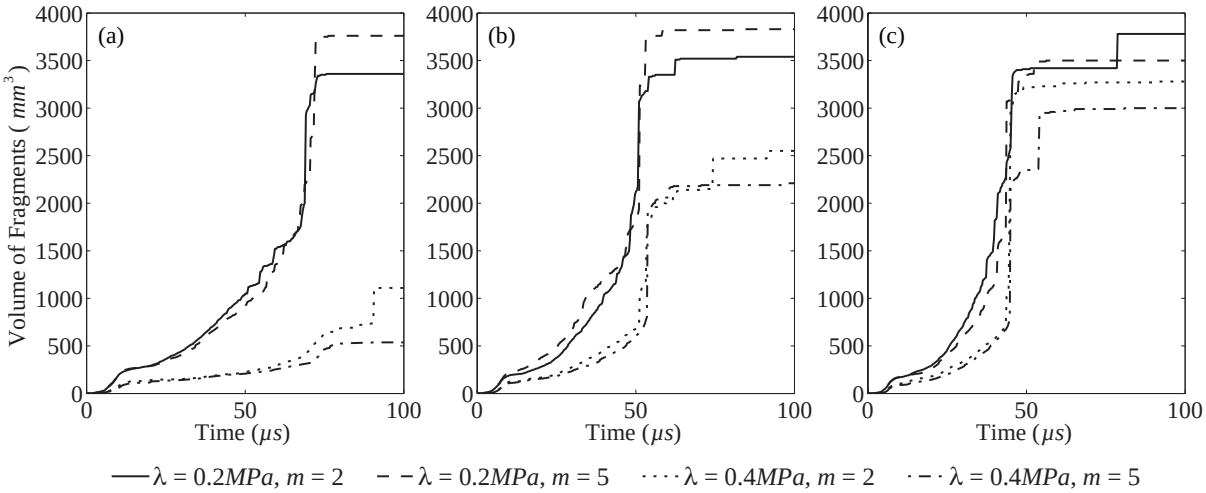

Figure 6.18: Evolution of fragmentation for a homogeneous kidney stone constituted of: (a) CA, (b) CA(50)/COM(50), and (c) COM.

as in Figures 6.19(a) and 6.19(b), complete fragmentation evolves rapidly (in approximately $40 - 45\mu s$), regardless of the material in the core. Additionally, the distribution of material strength has a much smaller influence than in the homogeneous stones. Alternatively, when a less compliant material is present in the inner core, as in Figure 6.19(c), fragmentation is significantly restricted. The maximum volume of fragments produced was approximately $125mm^3$, significantly less than the volume of the stone ($4189mm^3$). This small volume of fragments demonstrates the limited ability of the softer outer layer to transmit enough energy to the inner core, from the impacting probe, to cause fragmentation to occur. Similar behavior was observed across all scenarios we considered, including scenarios with different material combinations and thicker and thinner outer layers. This investigation provides support to the idea of being able to regularize fragmentation behavior through constitutive design.

Similarly to the the previous example, we investigate the evolution of energy throughout the simulation. In this case, we examine the evolution of energy for two homogeneous stones, as illustrated in Figure 6.20. The external energy from the impacting probe is converted into strain, kinetic and fracture energy. In the initial stages of impact, the external energy is primarily converted into strain energy. The strain energy increases rapidly, but decreases as the damaged region in the stone expands. As the stone begins to fracture, the kinetic energy and fracture energy increase. Over time, the problem reaches equilibrium, and the fracture of the stone stops. At equilibrium, the external energy is converted into kinetic and fracture energy, each of which remain constant with time.

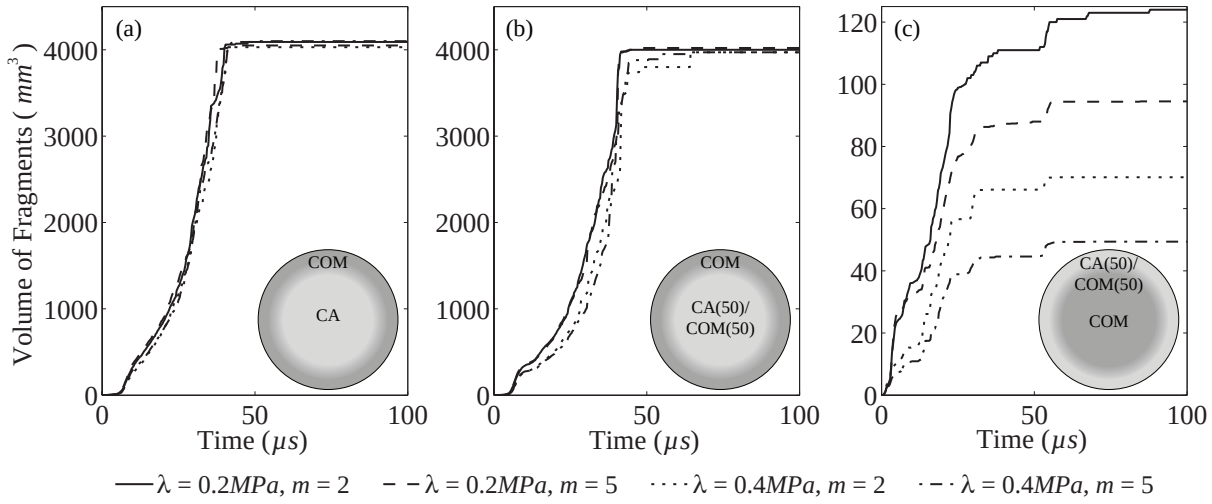

Figure 6.19: Evolution of fragmentation for a heterogeneous kidney stone constituted of: (a) an inner core of CA, and an outer layer of COM; (b) an inner core of CA(50)/COM(50), and an outer layer of COM; and (c) an inner core of COM, and an outer layer of CA(50)/COM(50).

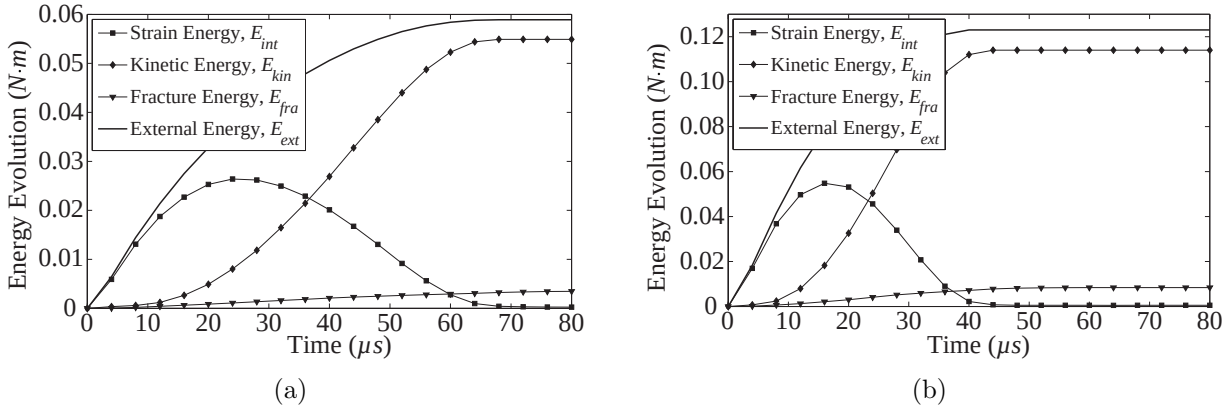

Figure 6.20: Evolution of energy for a homogeneous kidney stone constituted of: (a) CA, and (b) COM.

6.5 Dominant crack example problem

The truly unique characteristics of the cohesive element framework in three-dimensions is most prevalent in pervasive fracture problems, wherein the full spectrum of fracture behavior is captured in a regularized manner. However, in this section we present an example which illustrates the ability of the cohesive element method to also capture the behavior of problems dominated by a single crack. In particular, we investigate the mixed-mode fracture of a PMMA plate with a hole. This problem was investigated experimentally by Grégoire [235] using the geometry illustrated in Figure 6.21(a). The plate has an inclined notch through the thickness (at an angle of 22°), making this a fully three-dimensional problem. The crack initially propagates in a mixed-mode (I + III) manner, then transitions into a mode I crack

a short while after initiation. To the best of the author's knowledge, there have been no numerical investigations using this geometry and loading condition.

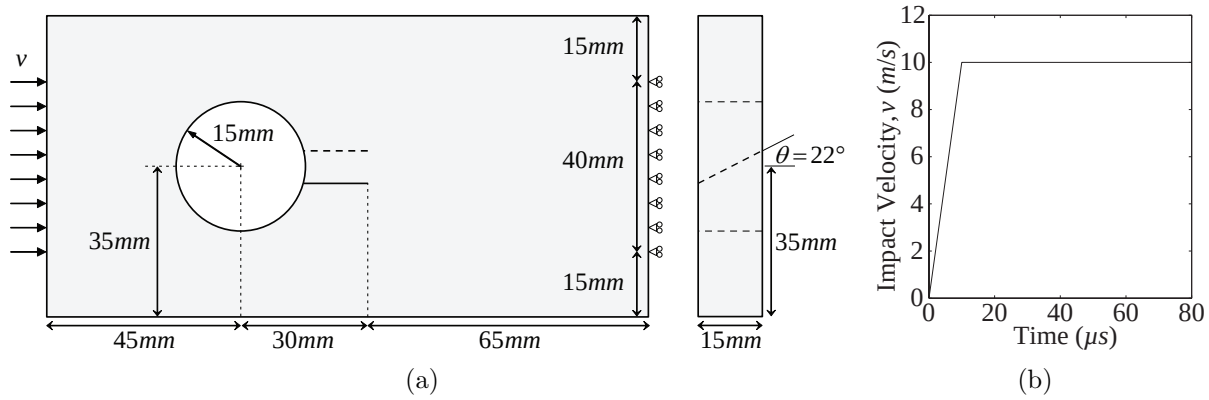

Figure 6.21: Model of the out-of-plane angled notch in a PMMA plate with hole: (a) geometry, and (b) impact velocity.

Experimentally, the specimen is impacted using a Hopkinson bar [233] with a diameter of $40mm$. Numerically, the impact is described by an applied velocity of $10m/s$, which is linearly ramped up over $10\mu s$, as illustrated in Figure 6.21(b). The mesh contains 286,545 elements (52,758 nodes) with a refined zone in the region in which fracture is expected to occur, as illustrated in Figure 6.22. The PMMA has an elastic modulus of $3.24GPa$, a Poisson's ratio of 0.35, and a density of $1190kg/m^3$ [235]. The mode I fracture energy (ϕ_n), cohesive strength (σ_n), and shape parameter (α) are set as $352.3N/m$, $62.1MPa$ and 2, respectively. The mixed-mode fracture properties are assumed to be the same as the mode I fracture properties.

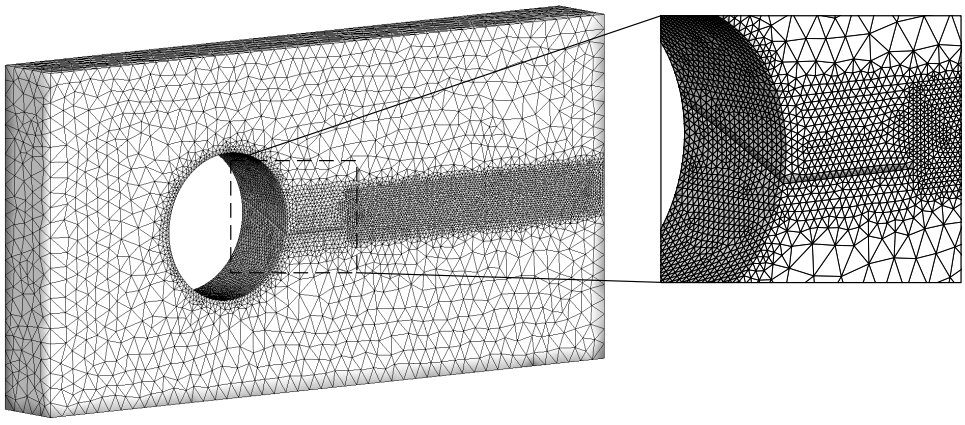

Figure 6.22: Finite element mesh showing the explicit representation of the angled notch through the specimen thickness. The mesh is a priori refined, in the region in which fracture is expected to occur.

The experimentally obtained fracture pattern is illustrated in Figures 6.23(a) and 6.23(b).

In Chapter 5 we demonstrated that constitutive heterogeneity (by a statistical distribution of material properties) does not significantly influence the fracture behavior in problems dominated by a single crack. Since this example exhibits a dominant crack, we will not investigate the influence of material heterogeneity in this example. Sample results from our simulations are presented in Figures 6.23(c) and 6.23(d). The numerical results demonstrate good agreement with those observed experimentally. The crack emanates from the notch in a mixed-mode (I + III) manner, then transitions to a mode I crack a short while after initiation.

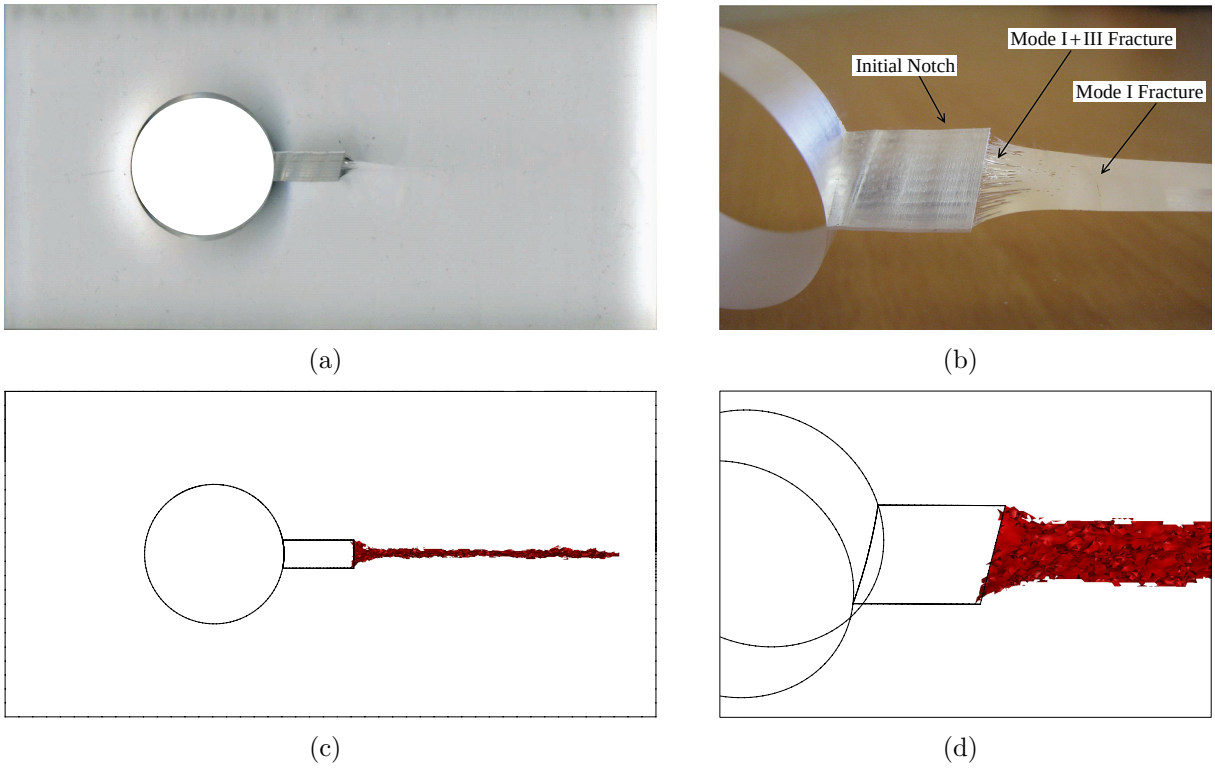

Figure 6.23: Experimental result of the out-of-plane angled notch in a PMMA plate with a hole: (a) global fracture pattern, and (b) close up of the notch-tip region, showing the transition to a mode I crack (images extracted from Grégoire [235]). Numerical result of the out-of-plane angled notch in a PMMA plate with a hole: (c) global fracture pattern, and (d) close up of the notch-tip region, showing the transition to a mode I crack.

6.6 Some comments on mesh dependency in three-dimensions

The issue of mesh dependency in two dimensions has been thoroughly discussed in Chapter 5 and the accompanying publications [199, 200]. In this section, we aim to take the knowledge

we gained in our two-dimensional investigation, and apply it to three-dimensional meshes. But, first, we look at the current state of meshing techniques in three-dimensions.

In this chapter, we proposed a nodal perturbation technique to increase the geometric randomness in three-dimensional Delaunay triangulations. While Delaunay triangulations might be prevalent in three-dimensional applications, they are not without their disadvantages. Without adaptive operators, a fixed three-dimensional mesh may be computationally prohibitive. For example, for the three-dimensional dynamic fracture simulations presented in this chapter, simplifications had to be made to model the problems in a reasonable amount of time (such as a priori defining a finely meshed region where fracture is expected to occur), and even then, the computational cost can be immense.

Besides the Delaunay triangulation, there are a variety of alternative meshing strategies which have been developed and applied to three-dimensional dynamic fracture problems. The 4k mesh has been extended to three-dimensions [57, 20]. The qualities of the two-dimensional 4k mesh make it an attractive option in three-dimensions; in particular, the multi-level refinement and coarsening capability of the mesh significantly reduces computational cost. However, the mesh presents an isotropic discretization of the problem domain, showing preference to cracks which propagate at angles which are a multiple of 45°. The polygonal mesh has been extended to three-dimensions as well, and has seen limited application to fracture problems [191, 269]. The isotropic nature of the two-dimensional polygonal meshes carries over to three-dimensional polyhedral meshes.

To illustrate the isotropy of polyhedral meshes in three-dimensions, we conduct a geometric study where we compute the average path deviation for a set of randomly generated meshes. The path deviation study attempts to quantify the ability of the mesh to capture arbitrary crack patterns. Additionally, since the fracture energy necessary to propagate a crack is proportional to the area of the fracture surface, we prefer mesh discretizations which limit the amount by which they artificially increase this area. The path deviation in three-dimensions, η, is computed as:

$$\eta = \frac{A_f}{A_p} - 1, \tag{6.11}$$

where A_f is the area of the fracture surface along the facets of the elements, and A_p is the area of the plane which the fracture surface is attempting to reproduce.

In Chapter 5, to compute the path deviation in a two-dimensional mesh, we were able to take advantage of Dijkstra's shortest path algorithm [222] to compute the fracture surface, A_f. Since there is no three-dimensional counterpart to this algorithm, a slightly modified approach is taken. The study is conducted on a unit cube, and a plane is used to represent

the target fracture surface, as illustrated in Figure 6.24(a). For each planar slice through the mesh, all elements whose centroid falls on the side of the plane containing the positive normal are removed. The resulting mesh contains approximately half of the original elements, and the remaining elements produce a rough representation of the plane (see Figure 6.24(b)). The rough planar surface, composed of polygonal facets, is extracted, as illustrated in Figure 6.24(c); and the area of this surface is set as the area of the fracture surface, A_f. This rough polygonal surface is then projected onto the original plane, as illustrated in Figure 6.24(d); and the area of the projected surface is set as the area of the plane which the fracture surface is attempting to reproduce, A_p. An alternative approach would be to determine the area of the fracture surface based on a surface-based criterion, as opposed to the centroid-criterion based criterion. For example, for each element intersected by the target fracture surface, evaluate the area of the boundary of the element above and below the plane and discard elements which have a larger area above than below. We also implemented this surface-based criterion and found that the change in the computed path deviation is negligible, thus each of the conclusions we present below is unaltered by the selected criterion.

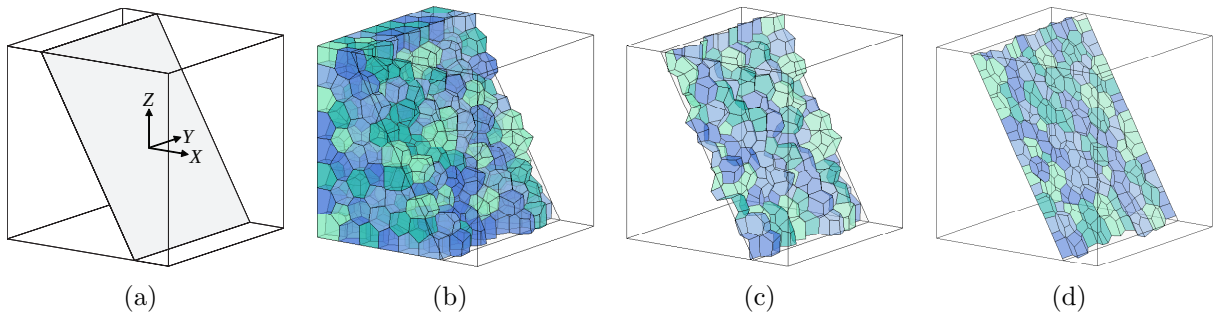

Figure 6.24: Steps of the isotropy study of polyhedral meshes in three-dimensions: (a) planar slice (b) polyhedral elements isolated below the plane, (c) polygonal surface representing plane, and (d) projected face on the plane.

The study is conducted on three different levels of mesh refinement (2400, 4800, and 7200 elements) and, for each level of refinement, three random meshes are generated. Typical discretizations are illustrated in Figure 6.26. The planar slice is rotated 360°, in increments of 1°, around the X, Y, and Z axes. We also evaluated the path deviation when the plane is rotated about arbitrarily oriented axes and found that, due to the random nature of the discretization, the results were consistent. The results for each level of refinement are averaged over the nine different sets of studies. The path deviation is plotted on a polar graph in Figure 6.25. It is clear from this study that three-dimensional polyhedral meshes are isotropic. However, it is also clear that these meshes impart a significant influence on the fracture surface, increasing the area the crack has to propagate along by approximately

49%. Also evident from these plots is that the bias is independent of the level of refinement.

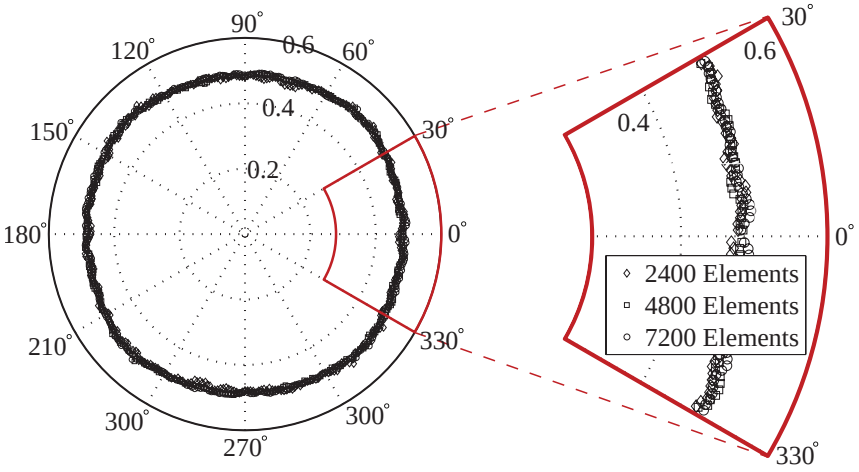

Figure 6.25: Comparison of mesh deviation, η, in the three-dimensional polyhedral meshes; for various levels of refinement.

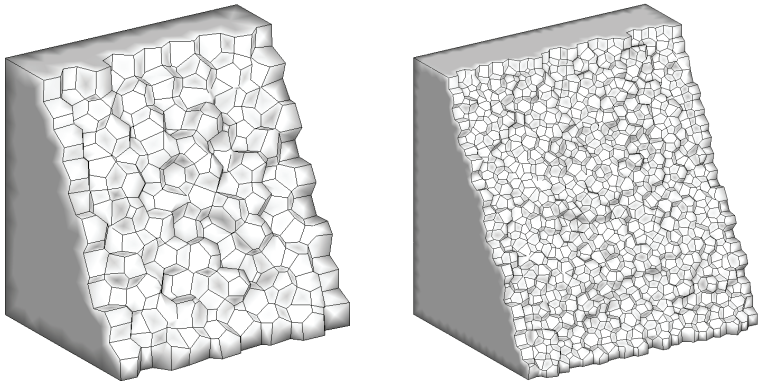

Figure 6.26: Representative fracture surfaces for: (a) a coarse polyhedral mesh, and (b) a fine polyhedral mesh. The surfaces are illustrated for a planar slice of 30°.

The above geometric study illustrates that; while polyhedral elements are able to discretize arbitrary problem domains, they display similarly poor representations of fracture surfaces as polygonal meshes do in two-dimensions (see Section 5.3.3). The element-splitting operator presented in Chapter 5 could potentially be extended to three-dimensions, however, the splitting of polyhedral elements would entail the addition of new nodes and new faces (as a planar cut between opposing vertices of a polyhedral element is not guaranteed to be conforming). While not impossible, these heuristic manipulations could become very complicated very quickly.

Clearly, there is a no meshing strategy which is suitable for all scenarios. Each strategy has its own advantages and disadvantages. Through our investigation of meshing strategies

in both two- and three-dimensions, we have compiled a list of qualities to look for in an ideal mesh for dynamic cohesive fracture simulations:

- **The mesh should be able to discretize any arbitrary domain**. The domain of the problem should not be limited by the meshing strategy.
- **The mesh should be unstructured and isotropic**. A structured mesh introduces paths upon which cracks will prefer to propagate along. Any bias induced by the mesh should be uniform in all global directions of crack propagation.
- **The mesh should produce a minimal bias to fracture patterns**. The restriction of cracks to element facets should not significantly increase the resulting fracture surface.
- **The beneficial qualities of the mesh should not be dependent on the use of additional topological operators**. Not all research centers have access to data structures capable of handling complicated adaptive topological operators. And, for broad use, commercial codes often lack the ability to change the topology of a mesh on-the-fly.
- **The mesh should have a three-dimensional counterpart**. For the most generality, the mesh should not be limited to two-dimensional applications.
- **The mesh should ideally allow for a hierarchical multi-level adaptive refinement and coarsening scheme**. In two dimensions, computational cost is not a significant limiting factor for most problems. In three dimensions, the size of a comparable two-dimensional problem increases immensely. Thus, in three dimensions, adaptive refinement and coarsening strategies could be applied to significantly reduce computational cost.

In the following section, we propose a new meshing strategy which satisfies each of the desired qualities listed above.

6.7 The 4k-patch mesh

In Chapter 5, we presented a technique for discretizing an n-sided polygonal element into n quadrilaterals. By combining this refinement scheme with the element-splitting operator, as illustrated in Figure 6.27(a), we were able to greatly reduce the mesh dependency in dynamic

cohesive fracture simulations. This approach was motivated as a means for overcoming the mesh anisotropy we noticed in some of our previous work which used a 4k mesh discretization [7, 199, 221]. As mentioned previously, the primary advantage of the 4k mesh over the polygonal mesh is the 4k mesh's intrinsic hierarchical refinement and coarsening capability. If this capability could be combined with the isotropic geometry of an unstructured polygonal discretization, a robust meshing strategy could be developed. This lead us to the idea of using a patch of 4k discretizations inside each polygon, as illustrated in Figure 6.27(b).

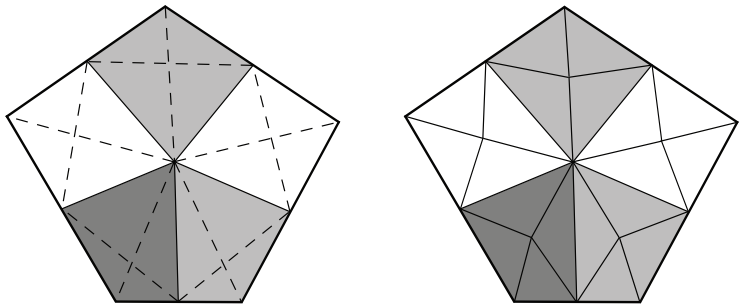

Figure 6.27: Depiction of the similarities in potential fracture paths for a polygonal element with refinement and element-splitting, and a polygonal element with a 4k-patch. (a) Refined polygonal element where the dashed lines represent the implicit facets on which elements could be split, and (b) a 4k-patch discretization of a polygonal element. Notice the similarity of the structure in each of the shaded regions.

The 4k-patch mesh combines the positive features of both the 4k and polygonal discretizations: it can discretize arbitrary domains; it is isotropic; it presents minimal bias to fracture patterns; it contains a hierarchical multi-level adaptive refinement and coarsening scheme; its qualities can be combined with, but are not dependent on topological operators; and it has a three-dimensional counterpart. The following subsections further investigate some of these claims.

6.7.1 Investigation of isotropy and bias in the 4k-patch mesh

To generate a 4k-patch mesh, the domain is initially discretized with polygons (n-gons). Then, each n-gon is discretized by n quadrilateral elements in the same manner as was described in Section 5.3.2. Each quadrilateral is further discretized with four triangles, connected at the centroid of the quadrilateral, as depicted in Figure 6.27(b). In Section 5.3.3 we conducted a geometric study which demonstrated the isotropy of a polygonal mesh. To demonstrate that the 4k-patch mesh retains this isotropy, we conduct a similar geometric study.

The study computes the path deviation, η, as per Equation 5.25; where L_f is computed using Dijkstra's shortest path algorithm [222] between any two nodes, and L_c is the Euclidean distance between the same two nodes. The study is conducted on a circular domain discretized with 1000 n-gons. Each n-gon is then discretized with n 4k-patches, leading to an average of approximately $22,800$ triangular elements in the discretization. Ten random meshes are generated, and paths over $0°$ to $180°$, in $1°$ increments, are analyzed. The results of the study are illustrated in Figure 6.28. From the figure, it is clear that the 4k-patch mesh retains the isotropy of the polygonal mesh. Additionally, it only introduces a path deviation of approximately 2.1%; almost on par with that using the refinement with element-splitting scheme in Chapter 5 (see Table 5.1). For comparison, the path deviation of the 4k-patch mesh is also on par with that for the conjugate-directions mesh presented by Rimoli et al. [183]. The downside of the conjugate-directions mesh is that it does not contain a multi-level refinement and coarsening scheme.

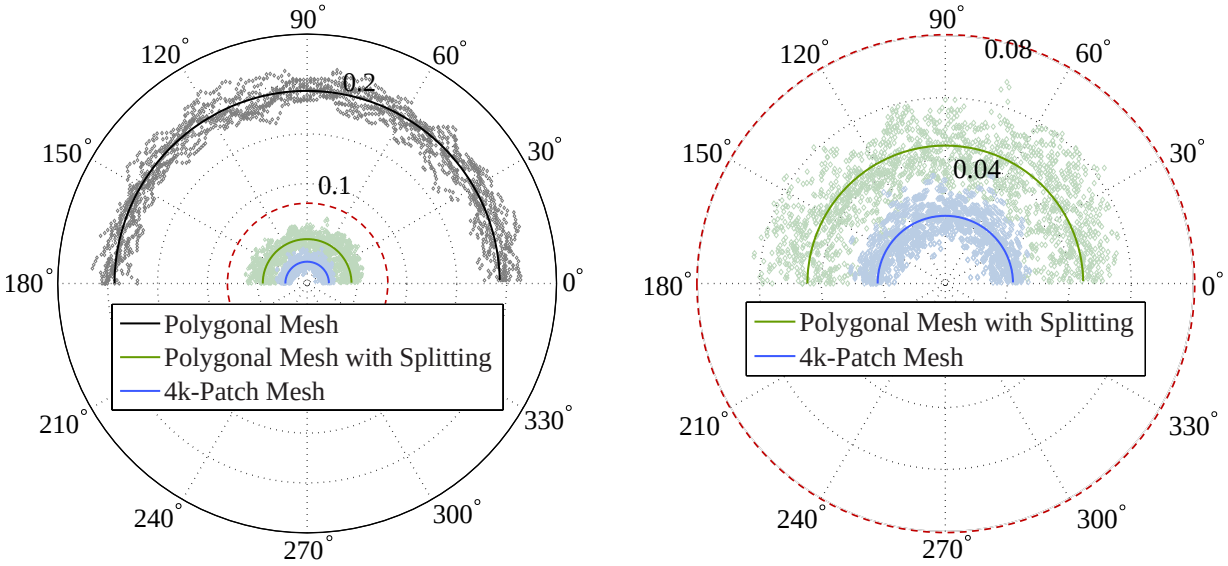

Figure 6.28: Comparison of mesh deviation. (a) Deviation of polygonal meshes (with and without element-splitting) and the 4k-patch mesh; and (b) close up view of the deviation for the polygonal mesh with element-splitting and the 4k-patch mesh.

6.7.2 Element quality in the 4k-patch mesh

Here, we conduct a series of geometric studies which quantify the quality of the 4k-patch mesh. The studies are conducted on a circular domain, and the quality metrics used are the coefficient of variation in edge lengths, the Lo's parameter, the element areas and the

interior angles. We summarize the result of our study in Figure 6.29. In Figure 6.29(a), we illustrate the coefficient of variation of the element edges. This mesh is coarser than those used in the remainder of the study, for illustrative purposes. As illustrated, the 4k-patch mesh results in a small variation in the coefficient of edges lengths, however, because the initial polygonal discretization is of high quality (see Section 5.3.4), the variation is low and the element quality is acceptable.

Additionally, we illustrate the distribution of Lo's parameter, element area and interior angles in Figures 6.29(b) to 6.29(d), respectively. Each mesh contains $22,896$ elements. These plots indicate that the 4k-patch mesh has a lower quality than the polygonal mesh (see Section 5.3.4). However, the 4k-patch mesh may be adaptively applied in the immediate vicinity of the crack, limiting its influence on the average element quality.

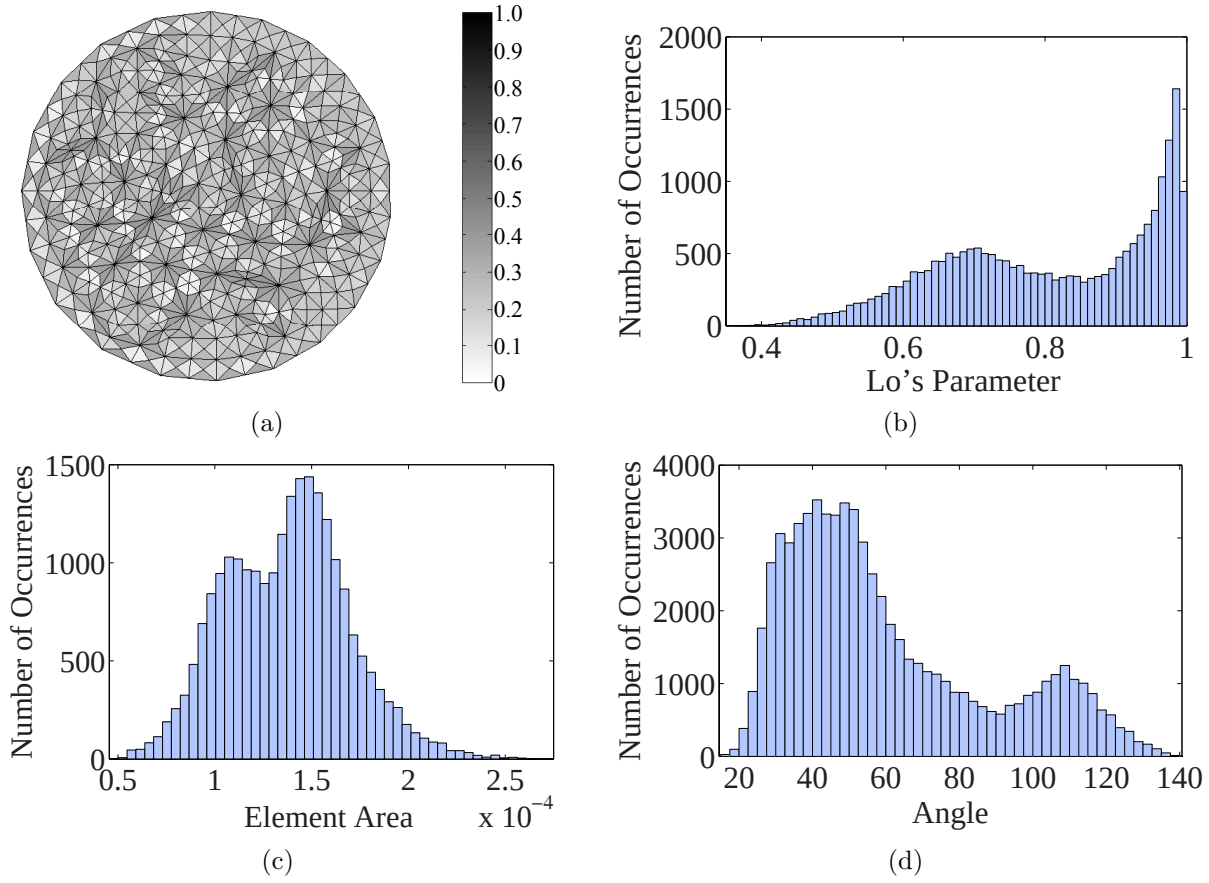

Figure 6.29: Summary of results of study on the element quality in a 4k-patch mesh, considering: (a) coefficient of variation of edge lengths, (b) Lo's parameter, (c) element area, and (d) interior angles.

6.7.3 Multi-level refinement and coarsening scheme in the 4k-patch mesh

The 4k-patch mesh retains the adaptive refinement and coarsening qualities of the 4k mesh presented by Park et al. [7]. Here, we briefly summarize the procedure. Mesh refinement proceeds through the use of an edge-splitting operator. The operator splits an edge into two-edges in such a way that the 4k structure is retained. The procedure works by recursively splitting edges of neighboring triangles until an allowable pattern is achieved, as illustrated in Figure 6.30. If we select the dashed edge in Figure 6.30(a) to be split, we can not directly split that edge without losing the structure of the mesh. To maintain the necessary 4k structure, we split adjacent edges (as illustrated in Figures 6.30(b) and 6.30(c)). This is similar in nature to the longest edge-bisection procedure used for unstructured triangles, such as those in Delaunay triangulations, but presents a greater number of paths on which a crack may propagate [7].

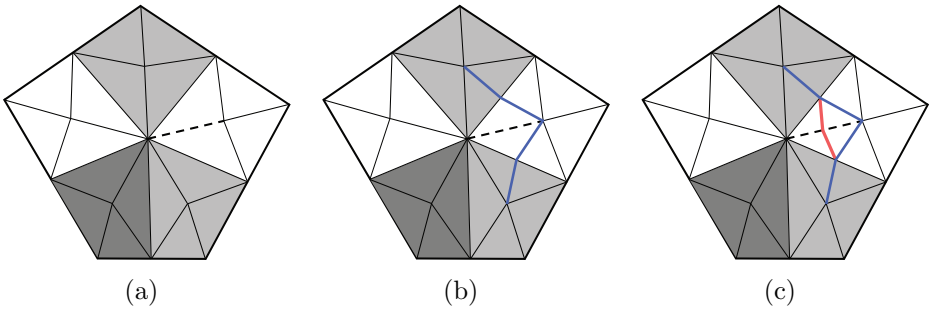

Figure 6.30: Recursive edge split procedure: (a) request for an edge-split along the edge with a dashed line; (b) split edges to create an allowable pattern; and (c) split edge along the dashed edge.

During the refinement procedure, the depth of the refinement (edge depths) are tracked. In the initial mesh, all edges are considered to have an edge depth of zero. When a new edge is created, the edge is assigned a depth that is one greater than the maximum depth of all edges in the adjacent triangles, as illustrated in Figure 6.31(a). An illustration of the refinement procedure over a region spanning multiple patches is presented in Figure 6.32.

Mesh coarsening is conducted through a sequence of vertex-removal operators, as illustrated in Figure 6.31(b). For each vertex which is removed, the edges, incident to the vertex, with the greatest depth are deleted and the adjacent elements are merged. For example, we apply the vertex-removal operator to the highlighted node in the first part of Figure 6.31(b). The maximum edge depth of edges incident to this node is 3. Thus, the two edges with this depth are deleted and the two other edges incident to this node are merged.

It is also valuable to note that the 4k-patch mesh is equally suitable to both linear and quadratic elements. In addition, the 4k-patch meshing strategy can incorporate adaptive edge-swap operators, as noted by Paulino et al. [221].

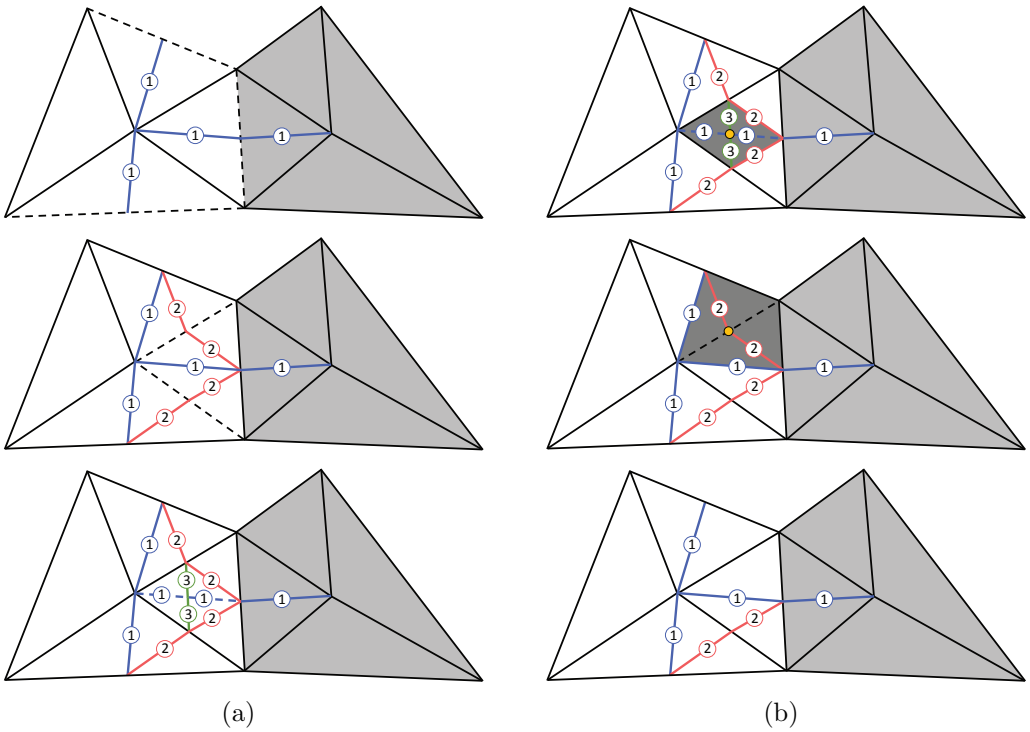

Figure 6.31: (a) Sequence of edge-split operations along the dashed edges, and (b) sequence of vertex-removal operations in shaded unstructured 4k-patches.

6.7.4 Extending the 4k-patch mesh to three dimensions

Similar to the generation of the two-dimensional 4k-patch mesh, the three-dimensional 4k-patch mesh is generated by first discretizing the domain with polyhedral elements. Then, each polyhedral element is discretized by 8-node (6-sided) brick elements, as illustrated in Figure 6.33(b). Each 8-node brick is formed using the element center, three edge mid-points, three face centroids and the corner node [270, 271]. Each brick element is further discretized with 24 tetrahedral elements, connected at the centroid of the brick, as described in [57] and illustrated in Figure 6.33(c).

While the 4k-patch mesh can be extended to three dimensions, mesh generators which are able to generate the necessary, high quality base polyhedral discretization are still in a growth stage. There are very few mesh generators which can handle polyhedral elements, and even fewer which are robust and available to the research community. Thus, there is a need for an open-source mesh generator, for complicated domains; which uses polyhedral elements. A new approach to polyhedral mesh generation, presented by Thedin et al. [197], may provide a potential avenue. In their approach, they use an energy minimization formulation; which, they demonstrate, produces higher quality polyhedral elements suitable for use as finite elements in numerical analysis.

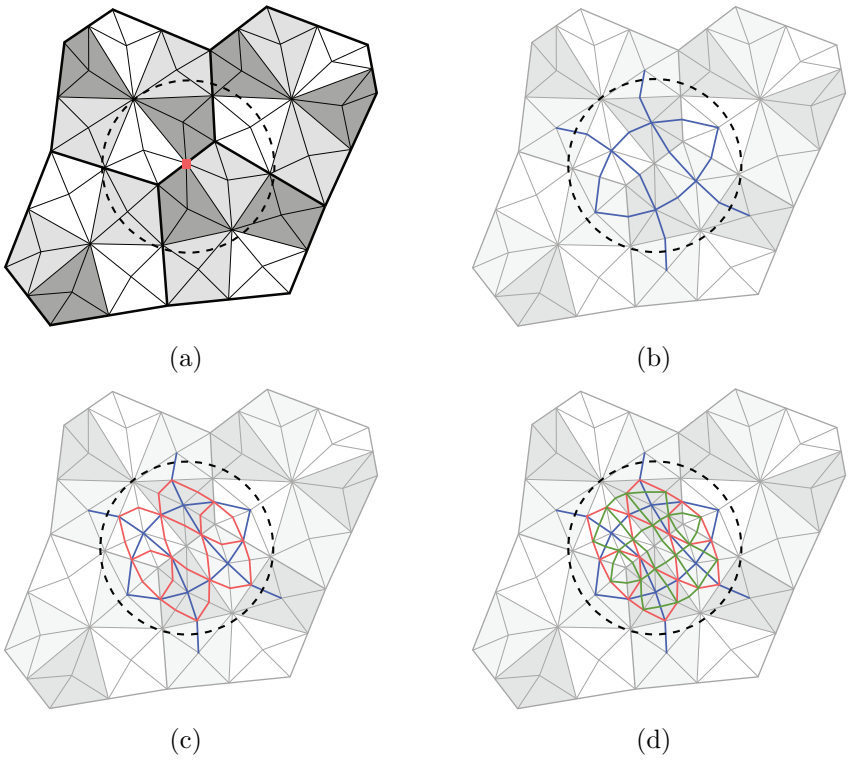

Figure 6.32: Adaptive refinement over multiple patches in a 4k-patch mesh. (a) Circular zone with: (b) level 1, (c) level 2, and (d) level 3 refinement.

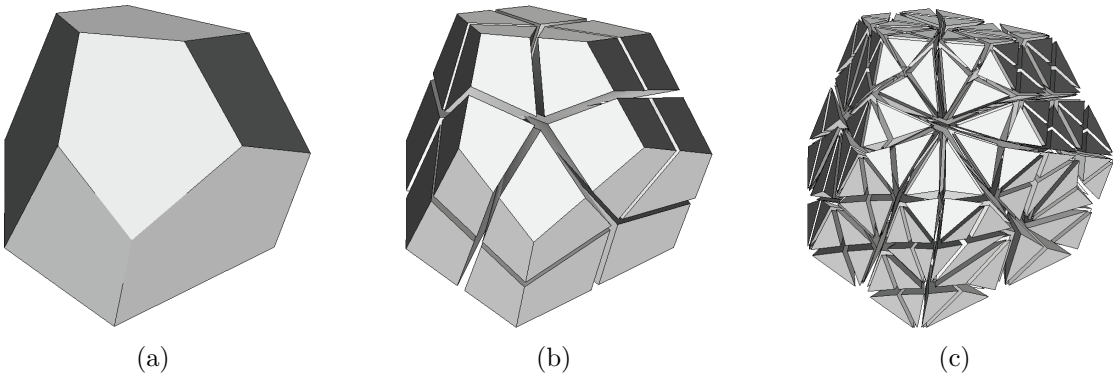

Figure 6.33: Extension of the 4k-patch mesh to three-dimensions. (a) Polyhedral element (b) Polyhedral element refined with brick elements, and (c) Polyhedral element refined first with brick elements then with tetrahedral elements. Note: each 8-node brick is formed using the element center, three edge mid-points, three face centroids and the corner node.

6.8 Concluding remarks

The cohesive element method's unique ability to capture the full range of fracture behavior: from crack initiation, through crack propagation, branching and coalescence, all the way to complete fragmentation, has allowed us to study the pervasive fracture problems herein. To

reduce mesh induced artifacts on fracture behavior, often caused by the use of smoothing operators in automatic mesh generators, we propose the nodal perturbation operator to introduce geometric unstructuredness. We perform a geometric study on Lo's mesh quality parameter and the minimum and maximum interior angles in the mesh, before and after nodal perturbation. Through the investigation, we demonstrate that the use of a nodal perturbation factor of 0.4 is able to produce a highly randomized mesh while still maintaining high quality elements which satisfy requirements on Lo's parameter and interior angles.

To further alleviate the influence of the mesh on the fracture patterns, we discuss the use of constitutively unstructured methods. Constitutively unstructured methods are motivated by the idea that no material is truly homogeneous, but contains heterogeneities (or defects) at the microscale. We provide a summary of many of the prominent methods, for representing these microscale heterogeneities, including the well-known Weibull distribution. We use these statistical methods to distribute the strength of the material in the problems we investigate. To capture the failure response of the material, we implement the extrinsic PPR cohesive model, and adaptively insert cohesive elements in front of each crack-tip to capture the nonlinear fracture behavior.

Three pervasive fracture examples are presented, which are specifically selected to investigate many of the prominent features influencing the fragmentation of structures. The first example considers the high-speed spinning of a ceramic disk. The combination of geometric and constitutive randomness results in random fracture behavior; which corresponds well to experimentally observed fragmentation patterns and crack speeds. The second example demonstrates the ability of using geometric features, on structures undergoing blast or impact loads, to regularize fragmentation patterns. The third example demonstrates the significance of accounting for material gradation in the investigation of structures under direct impact. By using the case of a graded kidney stone, we demonstrate that the gradation of the material can significantly influence the fragmentation behavior, and in some cases can even inhibit fragmentation from occurring altogether. Additionally, an example dominated by a single crack was presented. The example considers the impact of a plate with an inclined notch. The inclination of the notch results in the formation of a mixed-mode (I + III) crack at the notch tip; which transitions to a mode I crack a short while after initiation. The results from the numerical analysis agree well with those obtained experimentally.

Throughout our investigation of dynamic fracture using the cohesive element method, we noticed some common, desirable qualities to look for in a meshing strategy. In this chapter, we discuss these qualities, and propose a new type of mesh which incorporates all of the qualities we highlight. We refer to the new mesh as a 4k-patch mesh. We investigate the 4k-patch mesh and show that it is isotropic, and imparts little influence on the fracture

patterns. We also demonstrate that the 4k-patch mesh can be procedurally generated, has a hierarchical refinement and coarsening scheme, and can be extended to three-dimensions.

Chapter 7

Conclusions and Future Work

In this thesis, the mechanisms behind material failure are investigated in soft and quasi-brittle materials with nonhomogeneous microstructures. To numerically capture the behavior of failure, we use cohesive zone models in the finite element framework. First, a new computational framework is developed to investigate the complex problem of finite deformation interfacial debonding in particle reinforced composites, considering the influence of interphases. In the process of this investigation, we developed a small library of cohesive elements for use with a commercially available finite element analysis software package. Second, we develop a research code that uses unstructured polygonal discretizations for the simulation of dynamic cohesive fracture in two-dimensions. To overcome one of the primary critiques of the cohesive element method - mesh dependency - we designed two new topological operators which minimize mesh induced bias on fracture behavior. Finally, we take advantage of the cohesive element method's unique framework and develop a three-dimensional fracture code to investigate the pervasive fracture and fragmentation of quasi-brittle materials under impact or blast loading. In all of our investigations into dynamic failure, we take into account the influence of material heterogeneity (or defects) using a statistical distribution of material properties. In this chapter, a brief summary of the content of this thesis is presented, and suggestions for future work are provided.

7.1 Concluding remarks

The main topics covered in the thesis are outlined in Chapter 1. The current state-of-the-art in simulating material failure is discussed and a summary of the prevalent frameworks for modeling material failure is presented. In this thesis, we investigate failure processes using the finite element method with cohesive zone elements to represent the inelastic zone of damage in the region of failure. The primary classification subsets of the cohesive models present in the literature are summarized and nomenclature is introduced. Additionally, one of the main topics investigated in this thesis is the influence of microscale features on the

macroscopic constitutive response of particle reinforced composites. Since this is a significant problem covered in this thesis, the topic is outlined and motivated.

In the next three chapters, we develop a computational framework which is capable of quantifying the macroscale effect of microscale features in particle reinforced composites. Both the influence of interphases and interfacial debonding is considered. When a particle is embedded into an elastomer, the polymer chains in the elastomer tend to anchor onto the surface of the particle; creating a region in the vicinity of each particle with distinct properties from those in the bulk elastomer. In Chapter 2, we discuss how the bulk properties of the elastomer, in the region around the particles, are effected, and the significance of this on the macroscopic response of such composites. In most computational investigations of such composites, the interphasial region is often omitted. We are able to show that this omission can significantly limit the validity of these models for most composites of this nature. Perfectly bonded interphases were shown to dramatically alter the constitutive response of the composite, and provide an explanation for the variation in results, observed experimentally, of macroscopically similar test specimens.

In Chapter 3, we develop a small library of three-dimensional cohesive elements for use in commercial software. The elements are implemented as user defined element subroutines of Abaqus, and follow the intrinsic Park-Paulino-Roesler traction-separation relation. We discuss the formulation and implementation of the elements from an educational perspective. Additionally, we emphasize the adaptability of the elements, by including a detailed discussion on the modifications one may wish to make to adapt the elements to suit their own needs. We also take an extended look at the small deformation debonding behavior of coated particle inclusions. Our investigation highlights the influence of many microstructural parameters; including particle size, particle volume fraction, coating thickness, and material properties. We consider cases involving both a single location of separation and multiple locations of separation; and observe different microscopic debonding processes with respect to different macroscopic constitutive relations (e.g. hardening, softening and snap-back).

Chapter 4 combines the work in Chapters 2 and 3, to develop a computational framework capable of capturing the behavior of both interphases and interfacial debonding in particle reinforced composites as they undergo large strains. In the framework, interphases are explicitly modeled, and interfacial debonding is accounted for through the use of intrinsic cohesive elements. To account for frictional forces generated between each particle its surrounding interphase, we develop a new, fully three-dimensional, coupled cohesive-friction relation compatible with the intrinsic PPR cohesive model. In most prior investigations of particle reinforced composites, the influence of friction is often neglected. In our investigation, we demonstrate that this assumption is reasonable when the composite is loaded in

uniaxial tension, but also show that frictional forces can be significant in simple shear loading cases. We conduct a small parametric study demonstrating the significance of interphases and debonding on the macroscopic constitutive response, and validate our framework with experimental data from the literature.

The issue of mesh dependency in cohesive fracture simulations was motivated in the Introduction. Since the cohesive element method is only able to propagate cracks along element facets, a poorly designed discretization of the problem domain may introduce artifacts into the simulated results. In Chapter 5, we present two new topological operators, designed for unstructured polygonal discretizations, to address this issue of mesh dependency in dynamic fracture simulations. The first operator we developed is adaptive element-splitting, and the second is adaptive mesh refinement. We quantify the mesh induced bias, and the improvement made by the new operators, through a series of probabilistic geometric studies. The new operators demonstrate a reduction in mesh induced bias by over 90% from that of traditional approaches. This places the proposed meshing strategy on par with the best, fixed meshing strategy that has been proposed in the literature - the conjugate directions mesh. However, because the refinement and element-splitting operators are performed adaptively, the computational storage costs are less than what they would be for the conjugate directions mesh. Both operators are designed to improve the ability of unstructured polygonal meshes to capture crack patterns in dynamic cohesive fracture simulations. However, through a series of experimentally supported examples, we show that the element-splitting operator is more suited to pervasive fracture problems, whereas, the adaptive refinement operator is more suited to problems dominated by a single crack.

In Chapter 6, we investigate the full spectrum of pervasive fracture and fragmentation behavior in three-dimensions. Throughout pervasive fracture simulations, many cracks initiate, propagate, branch and coalesce simultaneously. Because of the cohesive element method's unique framework, we show that this behavior can be captured in a regularized manner. Additionally, we investigate and quantify the ability of three-dimensional nodal perturbation techniques to introduce geometric unstructuredness into a finite element mesh. We then use three numerical examples to investigate the behavior of quasi-brittle materials undergoing pervasive fragmentation. The examples are selected to investigate some of the significant factors which influence pervasive fracture and fragmentation; including, geometric features, loading conditions, and material gradation. Through the examples, we demonstrate that fragmentation behavior can be regularized with the use of simple geometric features or the use of functionally graded materials. The work in this chapter serves as the first known instance of the use of the extrinsic PPR cohesive model in three-dimensional fracture simulations.

The problem of mesh dependency in three-dimensions is still an unresolved problem. While nodal perturbation allows for the generation of unstructured meshes, the mesh upon which the nodal perturbation is applied typically contains some underlying structure. Through our investigation of meshing strategies, in both two- and three-dimensions, we compiled a list of qualities to look for in an ideal mesh for dynamic cohesive fracture simulations. In Chapter 6, we summarize these qualities, and present a new meshing strategies, called the 4k-patch mesh; which incorporates all the qualities we highlight.

While the focus of this thesis is on the investigation of homogeneous or homogenized materials, we recognize that all materials contain heterogeneity (or defects) at the microscale. Defects naturally arise in materials due to grain boundaries, voids, or inclusions. As well, defects may be introduced through the act of processing or machining the material. These microscale defects constitute regions where stresses can concentrate and lead to damage or failure. In our investigation of dynamic fracture in quasi-brittle materials, the representation of this heterogeneity is achieved by means of a statistical distribution of material properties.

7.2 Suggestions for future work

Due to the eclectic nature of this work, there are many avenues along which it could be extended. In the concluding remarks section of each of the previous chapters, some suggestions for extensions were provided, specific to the material in that chapter. This section discusses some global ideas which may or may not be considered as direct or indirect extensions of this work.

7.2.1 Three-dimensional fracture of soft materials with polyhedral finite elements

In Chapter 2, we developed a computational framework to demonstrate the significance of interphases in particle reinforced elastomers. However, due to numerical difficulties associated with large element distortions, the maximum global stretch attained by the model was relatively small. Recently, interest has grown in the use of polygonal elements for soft materials undergoing large deformations. The applications have, thus far, been restricted to two dimensions [272], but have clearly demonstrated that polygonal elements are able to undergo much greater distortions than any of their traditional counterparts.

The development of a polyhedral element framework in three-dimensions has been hindered due to difficulties in developing a robust meshing strategy, and to the development of

appropriate shape functions for three-dimensional polyhedrons. Recently, the Wachspress shape functions were extended to three-dimensions [273]. These shape functions could provide an avenue for the use of polyhedrons in the finite element framework. Alternatively, the virtual element framework has recently been extended to three-dimensions, and has shown to be stable and to produce accurate results for linear elasticity problems [270]. The virtual element method is also capable of capturing the behavior of arbitrary non-convex elements in a computationally efficient manner, allowing for a much wider range of meshing capabilities. If this framework could be extended to account for finite displacements and deformations, it may be a viable option for the study of soft materials [274].

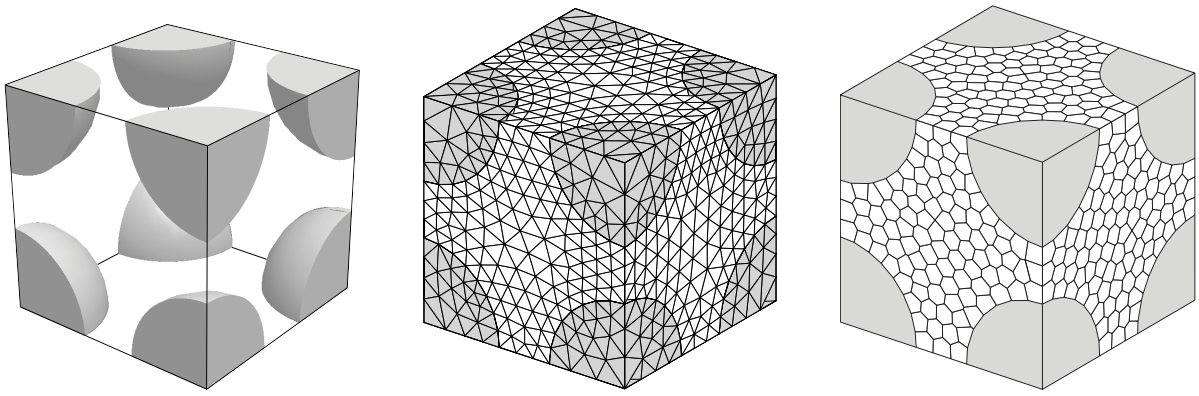

Figure 7.1: Representative unit cell of a particle reinforced composite material. (a) Geometry of the microstructure, (b) discretization using tetrahedral elements and (c) discretization using polyhedral elements, where each particle is represented with a single polyhedral element.

In the context of the particle reinforced composites investigated in Chapters 2 and 4, the geometric qualities of the polyhedral elements provide multiple advantages. First, because there is no restriction on the number of sides in a polyhedron and due to the fact that rigid materials undergo negligible deformations, rigid particles could be modeled with a single finite element [272], as illustrated in Figure 7.1. Alternatively, the rigid particles could be implemented as variational constraints [112]. Additionally, if the mesh was required to be periodic (to account for periodic boundary conditions), instead of generating a periodic mesh, paired nodes could simply be added on opposing faces of the model and the element connectivity updated to account for the additional hanging nodes.

To model fracture using polyhedral meshes, one would also need to implement compatible cohesive elements. The cohesive elements would have an arbitrary number of sides, and would use shape functions and Gauss quadrature rules appropriate for the two-dimensional, polygonal nature of the element, as illustrated in Figure 7.2.

This is a multi-staged problem that would involve the development of a polyhedral mesh

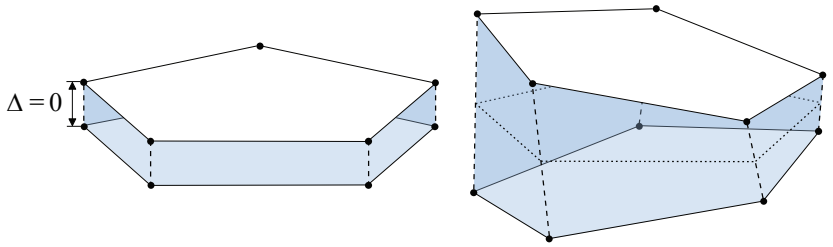

Figure 7.2: A sample cohesive element compatible with polyhedral elements.

generator, the implementation of a polyhedral finite (or virtual) element code, and the development of a library of compatible cohesive elements. While the problem is large, the resulting solution could significantly improve our ability to accurately capture the finite deformation response of this important class of materials.

7.2.2 Considering multiphysics in particle reinforced composites

While this thesis focuses on the mechanical behavior of particle reinforced composites, there has been a lot of research done on the multiphysics attributes of these composite materials. Materials with electrostrictive properties have been an exciting research topic of late; leading to applications in artificial muscles, energy harvesters and drug delivery systems [275, 276]. Recent investigations have shown that, by including particles with a high dielectric constant in polymers with a low dielectric constant, the resulting composite material can exhibit an order of magnitude increase in its electrostrictive deformations [277, 278, 279, 280, 281].

Another area in which multiphysics of particle reinforced composites is pertinent, is in the recent development of patchy particles. Patchy particles are particles which are only partially coated (see Figure 7.3), or the coating on the particle has two or more distinct zones with different properties. These composites have garnered significant attention in the past few years due to their applications in magnetic storage devices, drug delivery systems, electronics and robotics [284, 285, 286, 287].

Much of the computational framework presented in this thesis could serve as a baseline for investigating these new material composites. Extensions to account for different bulk material constituents, loading conditions and failure conditions would need to be accounted for. However, the new computational framework could significantly improve our quantitative understanding and design of such materials; and potentially spur a surge of innovation in the engineering industry.

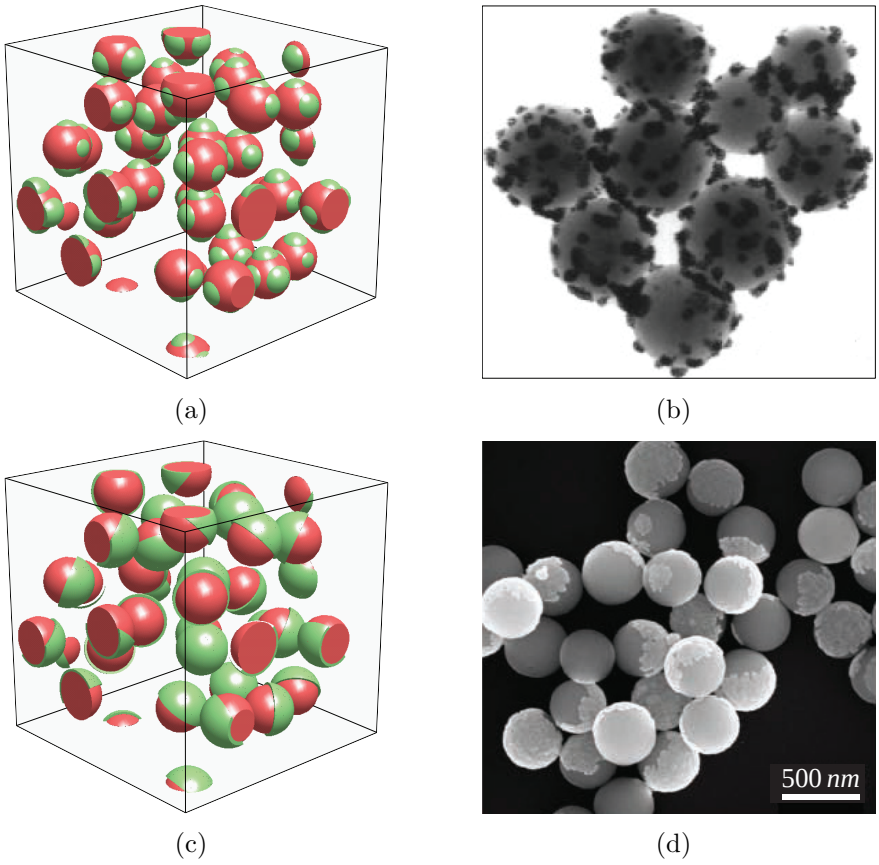

Figure 7.3: Various sample configurations of (a)-(b) patchy particles (experimental image extracted from Perro [282]), and (c)-(d) Janus particles (experimental image extracted from Taylor et al. [283]).

7.2.3 Nanoparticle reinforced adhesives for gels

Nanoparticle reinforced solutions have recently shown to be excellent adhesives for gels and biological tissue [288, 289]. Typical polymer based adhesives require chemical reactions, heating, pH changes, or other measures, to effectively bond two soft materials together [290, 291]. The addition of particles to the adhesive, however, capitalizes on the gel-chains natural inclination to adsorb (or anchor) onto the surface of the particles; forming a strong bridge between the two gels being glued together, as illustrated in Figure 7.4. In contrast to alternative approaches, nanoparticle reinforced solutions can adhere at room temperature with only a small applied pressure.

In addition to the presence of the particles, the surface treatment of the particles can have an influence on the strength and toughness of the bond [288]. By controlling the surface treatment, the effectiveness and zone of influence of the bonded region could be controlled, setting up the possibility of tailored, high strength, high toughness adhesives. This could pave the way for advancements in the fields of nanotechnology and biological materials

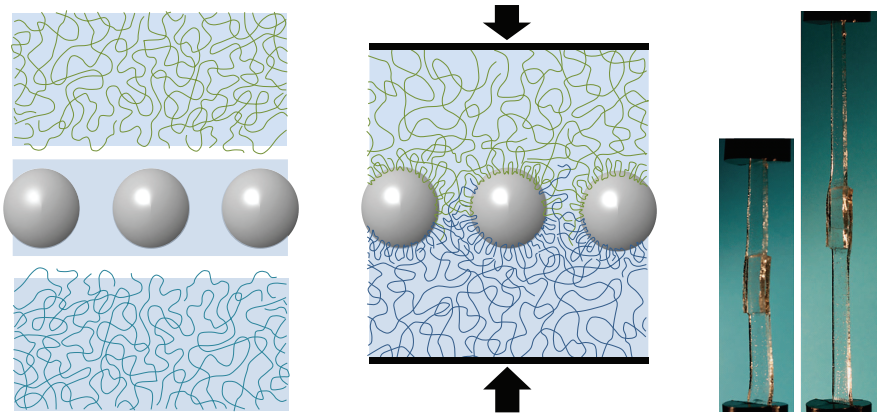

Figure 7.4: Schematic of (a) a nanoparticle reinforced adhesive between two gel layers, and (b) the gel-chains adsorbing onto the particles embedded in the adhesive. (c) Experimental testing of two gels, bonded through a nanoparticle reinforced adhesive, being stretched to large deformations. Images extracted from Rose et al. [288].

science.

7.2.4 Enhancing the Park-Paulino-Roesler cohesive model

Throughout this thesis, we make reference to the Park-Paulino-Roesler (PPR) cohesive model. This is the model we choose to capture the failure behavior of our materials. In Chapters 3 and 6 we discuss the use of the PPR model in functionally graded materials, and in Chapter 4 we coupled the model with a frictional relation. While these extensions of the PPR model have allowed us to investigate a wide variety of materials and loading scenarios, further enhancing, or extending the model to account for additional physical behavior could allow for a wider range of insight. For example, the model could be extended to account for thermodynamically consistent, rate-dependent, self healing, or electromechanically coupled materials. Below, we outline a potential path for extending the PPR model to account for electromechanical behavior. This could allow for the investigation of failure in ferroelectric, piezoelectric, or electrostrictive materials [292, 293, 294].

The first thing to consider, when designing a coupled electromechanical cohesive zone model, is the crack face boundary conditions. Permeable boundary conditions assume that the normal component of the electric displacement is continuous across the crack [295]; whereas impermeable boundary conditions assume that the normal component of the electric displacement is zero across the crack [296]. These classic boundary conditions have come under scrutiny of late, and have widely been superseded by the energetically consistent

boundary conditions proposed by Landis [297, 298]. The energetically consistent boundary conditions assign an electrical enthalpy, h_c, to the crack; where the change in the enthalpy with crack opening displacement is an applied traction, and the change in the enthalpy with respect to the potential drop is an applied charge. Thus, the new crack face boundary conditions normal to the crack face are:

$$q^+ = D_c = -\frac{dh_c}{dE_c} \quad \text{on} \quad \Gamma^+_{coh}, \qquad q^- = -D_c = \frac{dh_c}{dE_c} \quad \text{on} \quad \Gamma^-_{coh}, \tag{7.1}$$

$$T^+_n = (h_c + E_c D_c)\, n^+ \quad \text{on} \quad \Gamma^+_{coh}, \qquad T^-_n = (h_c + E_c D_c)\, n^- \quad \text{on} \quad \Gamma^-_{coh} \tag{7.2}$$

where

$$E_c = -\frac{\Delta\phi}{\Delta_n}. \tag{7.3}$$

Here, Γ^+_{coh} and Γ^-_{coh} denote the top and bottom faces of the crack; q^+ and q^- are the surface charge densities applied to the faces; T^+_n and T^-_n are the surface tractions applied to the faces; n^+ and n^- are the unit normals along the crack faces; D_c is the normal component of the electric displacement; E_c is the electric field in the crack gap; and $\Delta\phi$ is the potential drop across the crack.

In general, the electrical enthalpy is intended to model the nonlinear electrical response of the crack gap [298]. If the dielectric constant, κ_0, of the medium within the crack gap is much lower than that of the bulk material, high electric fields are generated in the crack. These high electric fields within the crack can lead to a corona discharge (electrical breakdown). To account for this behavior, Landis [297] proposed a phenomenological model which incorporates a critical electrical discharge level, E_d. Below the critical discharge level, the crack gap behaves in a linear dielectric manner, but beyond this level, charge flows between the crack surfaces, maintaining an electric field at this bounding level. The revised model is defined as:

$$h_c = -\frac{1}{2}\kappa_0 E_c^2, \quad D_c = \kappa_0 E_c \quad \Rightarrow \quad (h_c + E_c D_c) = \frac{1}{2}\kappa_0 E_c^2, \tag{7.4}$$

if $|D_c| \leq \kappa_0 E_d$, and:

$$h_c = -\frac{1}{2}\kappa_0 E_c^2, \quad D_c = \operatorname{sgn}(\omega_d)\,\kappa_0 E_d + \omega_d, \quad E_c = \operatorname{sgn}(\omega_d)\, E_d$$
$$\Rightarrow \quad (h_c + E_c D_c) = E_d\,|\omega_d| + \frac{1}{2}\kappa_0 E_d^2, \tag{7.5}$$

if $|D_c| \geq \kappa_0 E_d$. Here, ω_d is the amount of charge per unit area transferred between the crack faces. If it is not necessary to account for the breakdown strength, E_d could simply be set as infinite. By plugging Equation 7.4 (7.5) into 7.2, the additional components of force, acting

on the fracture surfaces, can be computed. Similarly, by plugging D_c from Equation 7.4 (7.5) into 7.1, the surface charge density on the fracture surfaces can be computed.

7.2.5 Rate-dependent constitutive relations

The influence of rate-dependent material properties has not been investigated in this thesis, however, this is a topic with broad applicability to the problems investigated. For example, the stiffness of elastomers is rate-dependent. Rate dependence in elastomers may be captured through the use of strain amplification factors [85]; which include experimentally determined fitting parameters to adjust the model to the specific material being investigated. However, a more rigorous approach would be to incorporate the rate dependence directly into the stored-energy function. Additionally, the stiffness of elastomers is known to be strain history dependent [178], wherein the global response of the elastomer irreversibly softens during cyclic loading. Incorporating the influence of history and rate dependence into the computational framework developed in Chapters 2 to 4, could enable a new avenue for the analysis and design of elastomeric bearings and dampers.

Additionally, rate dependency is an important topic in the dynamic fracture of materials. The cohesive relations selected in this thesis are inspired by the initial rate-independent cohesive model introduced by Dugdale [2] and Barenblatt [1]; namely, the tractions within the cohesive zone are dependent only on the opening between the cohesive surfaces, not on the rate at which the surfaces open. Nevertheless, these rate-independent cohesive models have successfully captured a wide range of fracture behavior. However, a more robust approach could be taken, which incorporates the influence of rate into the problem by considering the combined influence of rate in the bulk material and in the fracture process zone. The rate dependency of materials introduces a competition between the rate hardening of the bulk zone, which tends to enhance crack growth and the rate strengthening of the fracture process zone, which resists crack propagation [299]. Often, however, this competition is omitted in the investigation of rate-dependent materials. Gaining further insight into this competition may allow for a more complete failure analysis of materials demonstrating rate dependence.

7.2.6 Rate-dependent friction model

In Chapter 4, a new, coupled cohesive-friction model was presented for use with the PPR cohesive model. The model, as presented, does not incorporate the influence of rate, however, frictional effects are known to depend on the rate of slippage [300, 301]. To incorporate rate-

dependence into the coupled cohesive-friction model, one could modify the friction relation such that it depends on the rate of sliding between the two surfaces under contact. One of the most common rate- and state-dependent friction models takes the following form [302]:

$$\tau = \tau_0 + A\ln\left(\frac{V}{V_l}\right) + B\theta \tag{7.6}$$

where V_l is the long-term slip rate, τ_0 is a constant proportional to the effective normal stress and to the steady state coefficient of friction; and the constants A and B are proportional to the effective normal stress and to the temperature [302]. Moreover, θ is an evolving state variable described by:

$$\frac{\partial\theta}{\partial t} = -\left(\frac{V}{L}\right)\left[\theta + \ln\left(\frac{V}{V_l}\right)\right] \tag{7.7}$$

where L is a characteristic distance for exponential decay [302, 303].

Additionally, the rate-dependent friction model could be extended to consider the influence of contact between two dissimilar substrates. In this scenario, it has been shown that Coulomb friction is ill-posed for a wide range of material parameters and friction coefficients [304, 305, 306]. To overcome this, the problem could be regularized by incorporating a simple monotonic memory dependence of shear strength on the compressive normal stress; which causes the stability problem to be well-posed [307, 308].

7.2.7 Advanced cost saving procedures for fully three-dimensional dynamic cohesive fracture simulations

In terms of cost, the three-dimensional dynamic fracture framework presented in this thesis has significant room for improvement. Even the smallest simulation presented in this thesis took on the order of 20 hours. There are; however, multiple avenues which could be explored to help resolve this issue. One idea would be to implement an adaptive mesh refinement and coarsening scheme [20]. It was demonstrated in Chapter 5 that employing adaptive mesh refinement can yield significant cost savings over comparably accurate, uniformly refined meshes. The complexities in three-dimensions are much greater than those in two-dimensions, however, the potential cost savings could be significant. In addition to adaptive meshing schemes, alternative computational frameworks could be used. The current study was completed using a serial code, capable of running on only one central processing unit (CPU). Modifying the code to run not on the TopS [208] framework, but on the ParTopS (Parallel TopS) [309] framework would allow for the use of multiple CPUs and smaller wall-clock times. Alternatively, one could move away from running on CPUs

altogether, and take advantage of graphics processing units (GPUs) [310, 311] or quantum processing units (QPUs). A GPU is a powerful graphics engine that allows for large parallel applications to be run at speeds much higher than those attainable by a CPU [312, 313]. A QPU is a processor which conducts operations on qubits - the quantum analogue of the well known bit.

7.2.8 Hypervelocity impact and fragmentation

The investigation of hypervelocity impact events has seen an influx of interest in the past decade, due in large part to the increase in the amount of debris in space. The issue of space debris has become so pervasive that it poses a risk to, and must be taken into account in the design of all space craft. In 2013, NASA estimated that there are approximately 500,000 pieces of debris orbiting earth; which are equal to, or greater than, the size of a marble [314].

Alternatively, we may use hypervelocity impactors as tools for asteroid deflection. If an asteroid or comet is identified as being on a collision course with earth, with a sufficient amount of advanced warning, one option of altering its path is through the use of a hypervelocity impactor [315]. Since the experimental validation of such an event is out of this world, the investigation of these events must rely on small scale experiments (such as that illustrated in Figure 7.5) and numerical simulations.

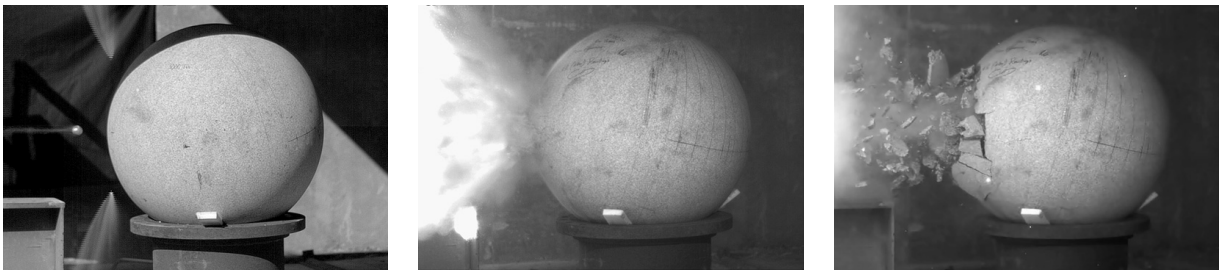

(a) (b) (c)

Figure 7.5: Fragmentation of a granite sphere under hypervelocity impact (images extracted from Walker et al. [316]).

In Chapter 6, we demonstrate the cohesive element method's ability to capture pervasive fracture and fragmentation behavior. Throughout those simulations, many cracks initiated, branched and coalesced simultaneously. Because of the cohesive element method's unique framework, this behavior was captured in a regularized manner. In a hypervelocity impact event, much of this same behavior is expected to occur; thus, the cohesive element framework may be a potential avenue for numerically simulating such an event.

Appendix A

Matlab Code to Generate Particle Reinforced Representative Unit Cell Models

```
% A model generator for randomly distributed, periodic, monodisperse,
% particle reinforced microstructures with interphases. The output is in
% the form of an input file compatible with the mesh generating software
% Netgen.

function particleRUC_3component()
clear all; close all; rng('shuffle');
for numFiles = 1:1:4 %Number of input files generated
fprintf('numFile = %d\n',numFiles);
%==============================User input==================================%
VF = 0.10;    % Volume fraction of particles
nParts = 30; % Number of particles
intT = 0.1;  % Interphase thickness (enter as a percentage of the radius)
Cedge = 100; % Length of cube edge
d1 = 0.05;    % Allowable center-to-center distance = 2*R*(1+d1)
d2 = 0.1;     % Allowable distance to boundary of the cell = R*(1+d2)
%==============================User input==================================%

pRad = ((VF*(Cedge^3)/nParts)*(3/(4*pi())))^(1/3);

FileName = strcat('vf',num2str(VF*100),'_it',num2str(intT*100),'_np',...
    num2str(nParts),'_',num2str(numFiles),'.geo');

outfile = strrep(FileName,'.geo','.inp'); foutid = fopen(outfile, 'wt');

fid = fopen(FileName,'w');
fprintf(fid,'%s %2.2f\n','# Volume fraction c =',VF);
fprintf(fid,'%s %d\n','# Radius of particles = ',pRad);
fprintf(fid,'%s\n\n','algebraic3d');

origin = [0 0 0]; %Origin of the cube

fprintf(fid,'\n%s%d%s%d%s%d%s%d%s%d%s%d%s\n','solid p1 = plane(',...
    origin(1),', ',origin(2),', ',origin(3),'; ',0,', ',0,', ',-1,');');
fprintf(fid,'%s%d%s%d%s%d%s%d%s%d%s%d%s\n','solid p2 = plane(',...
    origin(1),', ',origin(2),', ',origin(3),'; ',0,', ',-1,', ',0,');');
fprintf(fid,'%s%d%s%d%s%d%s%d%s%d%s%d%s\n','solid p3 = plane(',...
    origin(1),', ',origin(2),', ',origin(3),'; ',-1,', ',0,', ',0,');');
fprintf(fid,'%s%d%s%d%s%d%s%d%s%d%s%d%s\n','solid p4 = plane(',...
    Cedge,', ',Cedge,', ',Cedge,'; ',0,', ',0,', ',1,');');
fprintf(fid,'%s%d%s%d%s%d%s%d%s%d%s%d%s\n','solid p5 = plane(',...
```

```
    Cedge,', ',Cedge,', ',Cedge,'; ',0,', ',1,', ',0,');');
fprintf(fid,'%s%d%s%d%s%d%s%d%s%d%s%d%s\n','solid p6 = plane(',...
    Cedge,', ',Cedge,', ',Cedge,'; ',1,', ',0,', ',0,');');

fprintf(fid,'\nsolid cube = p1 and p2 and p3 and p4 and p5 and p6;\n');

% Get the centroids of the particles
[x y z] = cents(VF,Cedge,(pRad+pRad*intT),intT,d1,d2);

for i = 1:1:length(x)
  fprintf(fid,'%s%d%s%f%s%f%s%f%s%.6f%s\n','solid sph',i,...
        'a = sphere (',x(i),',',y(i),',',z(i),';',(pRad+pRad*intT),');');
  if (i ≠length(x))
    fprintf(foutid,'%f %f %f %f %f\n',x(i),y(i),z(i),pRad,pRad+pRad*intT);
  else
    fprintf(foutid,'%f %f %f %f %f',x(i),y(i),z(i),pRad,pRad+pRad*intT);
  end
end

fprintf(fid,'\n');
for i = 1:1:length(x)
    fprintf(fid,'%s%d%s%f%s%f%s%f%s%.6f%s\n','solid sph',i,...
        'b = sphere (',x(i),',',y(i),',',z(i),';',pRad,');');
end

fprintf(fid,'\nsolid int = sph1a\n');
for i = 2:1:(length(x)−1)
    fprintf(fid,'%s%d%s\n','or sph',i,'a');
end
fprintf(fid,'%s%d%s\n','or sph',length(x),'a;');

fprintf(fid,'\nsolid particles = sph1b\n');
for i = 2:1:(length(x)−1)
    fprintf(fid,'%s%d%s\n','or sph',i,'b');
end
fprintf(fid,'%s%d%s\n','or sph',length(x),'b;');

fprintf(fid,'\nsolid rest = cube and not int;');
fprintf(fid,'\nsolid interphase = int and cube and not particles;');
fprintf(fid,'\nsolid finalparticles = particles and cube;');

fprintf(fid,'\n\ntlo rest −transparent −col=[.09,.42,.96];\n');
fprintf(fid,'tlo finalparticles −col=[.93,.37,0.37];\n');
fprintf(fid,'tlo interphase −col=[.54,.83,.51];\n');

fprintf(fid,'\n"identify periodic p1 p4;"\n');
fprintf(fid,'"identify periodic p2 p5;"\n');
fprintf(fid,'"identify periodic p3 p6;"\n');

fclose(fid); fclose(foutid);
end
end

function [xFinal yFinal zFinal] = cents(vf,Lcube,r,pThick,d1,d2)

```

```
vf=vf*100; rin = r/(1+pThick); check1=2*r*(1+d1); check2=r*d2;
vcur=0; totVolSphere=0; x(1)=0; y(1)=0; z(1)=0; volCube=Lcube^3; i=2;
iter = 0;
while vcur<(vf*(1-10^(-6)))

    px=Lcube*rand; py=Lcube*rand; pz=Lcube*rand; %random seeds

    % Check the distance to the surfaces of the cube
    if ((((px-r)>=check2) || ((px-rin)<=-check2)) && (((py-r)>=check2) ...
    || ((py-rin)<=-check2)) && (((pz-r)>=check2) || ((pz-rin)<=-check2))...
    && (((px+r-Lcube)<=-check2) || ((px+rin-Lcube)>=check2)) && (((py+r...
    -Lcube)<=-check2) || ((py+rin-Lcube)>=check2)) && (((pz+r-Lcube)<=...
    -check2) || ((pz+rin-Lcube)>=check2)))
        valid=1;
    else
        continue % Start again with a new (random) position
    end

    % Check the distance to the adjacent particles
    j=1; flag=0;
    while j<i % Loop over all the particles already placed
        centDist=determineDist(j,px,py,pz,x,y,z,Lcube);
        if abs(centDist)>=check1 valid=1; j=j+1; else valid=0; j=i; end
        iter=iter+1;
        if iter >= 200000
            fprintf('Nonconvergent\n'); valid=0; j=2; i=1; flag=1;
        end
    end

    if flag==1 break; end

    if valid==1 % Particle passes the two checks

        x(i)=px; y(i)=py; z(i)=pz; % Store centroidal coordinates

        % Calculate the total volume of the particles
        volSphere=(4*pi*((r/(1+pThick))^3)/3);
        totVolSphere=totVolSphere+volSphere;
        vcur=100*(totVolSphere/volCube);
        i=i+1;
    else
        i=i;
    end
end

nP = length(x);

% Final coordinates of spheres are stored in x, y, and z arrays
xFa(1:nP-1) = x(2:nP); yFa(1:nP-1) = y(2:nP); zFa(1:nP-1) = z(2:nP);

[xFinal,yFinal,zFinal] = gParticles(xFa,yFa,zFa,Lcube,rin);
fprintf('In total, %d particle(s) are created \n',(i-2));
fprintf('Final volume fraction of the particles = %f\n',vcur);

end
```

```
152
153 function centDistMin = determineDist(j,px,py,pz,x,y,z,h)
154
155 q=[0 -h 0 0 -h -h 0 -h h 0 0 h h 0 h -h -h -h h 0 h h 0 h -h -h h];
156 r=[0 0 -h 0 -h 0 -h -h 0 h 0 h 0 h h h 0 h -h -h -h 0 h h -h h -h];
157 s=[0 0 0 -h 0 -h -h -h 0 0 h 0 h h h 0 h h 0 h h -h -h -h h -h -h];
158
159 for k=1:27
160 centDist(k)=sqrt(((px-x(j)+q(k))^2)+((py-y(j)+r(k))^2)+((pz-z(j)+s(k))^2));
161 end
162 centDistMin = min(centDist);
163 end
164
165 function [xFinal yFinal zFinal] = gParticles(x,y,z,Lc,r)
166
167 xlen=length(x); xadd=[]; yadd=[]; zadd=[];
168 M=[Lc 0 0 -Lc 0 0;0 Lc 0 0 -Lc 0;0 0 Lc 0 0 -Lc];
169
170 for i=1:1:xlen
171     lx=length(xadd); ly=length(yadd); lz=length(zadd);
172     Vadd = [x(i)<r y(i)<r z(i)<r abs(x(i)-Lc)<r abs(y(i)-Lc)<r ...
173             abs(z(i)-Lc)<r];
174
175     itr=0; st=[];
176     for j=1:6
177       if (Vadd(j)==1)
178         itr=itr+1; st(itr)=j;
179         xadd(lx+itr)=x(i)+M(1,j); yadd(ly+itr)=y(i)+M(2,j);
180         zadd(lz+itr)=z(i)+M(3,j);
181       end
182     end
183
184     if (itr==2)
185       xadd(lx+3)=x(i)+M(1,st(1))+M(1,st(2));
186       yadd(ly+3)=y(i)+M(2,st(1))+M(2,st(2));
187       zadd(lz+3)=z(i)+M(3,st(1))+M(3,st(2));
188     elseif (itr==3)
189       xadd(lx+4)=x(i)+M(1,st(1))+M(1,st(2));
190       yadd(ly+4)=y(i)+M(2,st(1))+M(2,st(2));
191       zadd(lz+4)=z(i)+M(3,st(1))+M(3,st(2));
192       xadd(lx+5)=x(i)+M(1,st(1))+M(1,st(3));
193       yadd(ly+5)=y(i)+M(2,st(1))+M(2,st(3));
194       zadd(lz+5)=z(i)+M(3,st(1))+M(3,st(3));
195       xadd(lx+6)=x(i)+M(1,st(2))+M(1,st(3));
196       yadd(ly+6)=y(i)+M(2,st(2))+M(2,st(3));
197       zadd(lz+6)=z(i)+M(3,st(2))+M(3,st(3));
198       xadd(lx+7)=x(i)+M(1,st(1))+M(1,st(2))+M(1,st(3));
199       yadd(ly+7)=y(i)+M(2,st(1))+M(2,st(2))+M(2,st(3));
200       zadd(lz+7)=z(i)+M(3,st(1))+M(3,st(2))+M(3,st(3));
201     end
202 end
203
204 xFinal = [x,xadd]; yFinal = [y,yadd]; zFinal = [z,zadd];
205
206 end
```

Appendix B

User Defined Element Subroutine of Abaqus for the Three-Dimensional PPR Cohesive Zone Model

This appendix provides the user-defined subroutine of Abaqus for the three-dimensional PPR cohesive element. The element is compatible for use with linear tetrahedral (T4) bulk elements. The electronic source files for this element and elements compatible with linear brick (B8) and quadratic tetrahedral (T10) elements are supplied through the website of Professor Glaucio H. Paulino.

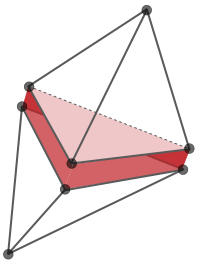

Figure B.1: Cohesive element compatible with linear tetrahedral bulk elements.

```
c 3D PPR UEL for Abaqus Code (Compatible with 4 node Tet Elements)
c Reference: DW Spring and GH Paulino, A Growing Library of Cohesive
c Elements for Use in Abaqus. Engineering Fracture Mechanics,
c Vol. 126, pp. 190–216, 2014.
c ======================================================================
      SUBROUTINE UEL (RHS, AMATRX, SVARS, ENERGY, NDOFEL, NRHS,
     1 NSVARS, PROPS, NPROPS, COORDS, MCRD, NNODE, U, DU, V, A, JTYPE,
     2 TIME, DTIME, KSTEP, KINC, JELEM, PARAMS, NDLOAD, JDLTYP,
     3 ADLMAG, PREDEF, NPREDF, LFLAGS, MLVARX, DDLMAG, MDLOAD, PNEWDT,
     4 JPROPS, NJPROP, PERIOD)
c
      INCLUDE 'ABA_PARAM.INC'
c
      DIMENSION RHS(MLVARX,*),AMATRX(NDOFEL,NDOFEL),PROPS(*),
     1 SVARS(*),ENERGY(8),COORDS(MCRD,NNODE),U(NDOFEL),
     2 DU(MLVARX,*),V(NDOFEL),A(NDOFEL),TIME(2),PARAMS(*),
     3 JDLTYP(MDLOAD,*),ADLMAG(MDLOAD,*),DDLMAG(MDLOAD,*),
     4 PREDEF(2,NPREDF,NNODE),LFLAGS(*),JPROPS(*)
c
      DIMENSION ds1(3),ds2(3),dn(3),Trac(MCRD,NRHS),
     1 Trac_Jacob(MCRD,MCRD),R(MCRD,MCRD),coord_l(MCRD,NNODE),
```

```
      2 GP_coord(2),sf(3),B(MCRD,NDOFEL),co_de_m(3,3),
      3 B_t(NDOFEL,MCRD), Transformation_M(NDOFEL,NDOFEL),
      4 Transformation_M_T(NDOFEL,NDOFEL),temp1(MCRD,NDOFEL)
C
       DIMENSION stiff_l(NDOFEL,NDOFEL),temp2(NDOFEL,NDOFEL),
      1 stiff_g(NDOFEL,NDOFEL),residual_l(NDOFEL,NRHS),
      2 residual_g(NDOFEL,NRHS),aJacob_M(2,3),delu_loc_gp(mcrd),
      3 co_de(mcrd,nnode)
C
       DOUBLE PRECISION G_fn, G_ft, f_tn, f_tt, alpha, beta, rn, rt,
      1 p_m, p_n, deln, delt, tmax, pmax, opn, opt
C
c Define inputs=============================================================
C
       G_fn=PROPS(1)
       G_ft=PROPS(2)
       f_tn=PROPS(3)
       f_tt=PROPS(4)
       alpha=PROPS(5)
       beta=PROPS(6)
       rn=PROPS(7)
       rt=PROPS(8)
       GP_n=3d0
       GP_W = 1.0d0/3.0d0
C
c Initialize matrices and vectors===========================================
C
       call k_vector_zero(ds1,3)
       call k_vector_zero(ds2,3)
       call k_vector_zero(dn,3)
       call k_matrix_zero(Trac,mcrd,nrhs)
       call k_matrix_zero(Trac_Jacob,mcrd,mcrd)
       call k_matrix_zero(R,mcrd,mcrd)
       call k_matrix_zero(coord_l,mcrd,nnode)
       call k_vector_zero(GP_coord,2)
       call k_vector_zero(sf,3)
       call k_matrix_zero(Transformation_M,ndofel,ndofel)
       call k_matrix_zero(Transformation_M_T,ndofel,ndofel)
       call k_matrix_zero(B,mcrd,ndofel)
       call k_matrix_zero(B_t,ndofel,mcrd)
       call k_matrix_zero(temp1,mcrd,ndofel)
       call k_matrix_zero(stiff_l,ndofel,ndofel)
       call k_matrix_zero(temp2,ndofel,ndofel)
       call k_matrix_zero(stiff_g,ndofel,ndofel)
       call k_matrix_zero(residual_l,ndofel,nrhs)
       call k_matrix_zero(residual_g,ndofel,nrhs)
       call k_matrix_zero(aJacob_M,2,3)
       call k_matrix_zero(rhs,ndofel,nrhs)
       call k_matrix_zero(amatrx,ndofel,ndofel)
       call k_matrix_zero(co_de,mcrd,nnode)
       a_Jacob=0.d0
C
c Do local computations=====================================================
C
       do i = 1, mcrd
```

```
77          do j = 1, nnode
78             co_de(i,j)=coords(i,j)+U(3.0*(j-1.0)+i)
79          end do
80       end do
81 C
82       call k_local_coordinates(co_de,R,coord_l,Transformation_M,
83      & Transformation_M_T,a_Jacob,aJacob_M,coords,u,ndofel,nnode,
84      & mcrd)
85 C
86 c Compute shear and normal local opening displacements===============
87 C
88       do i = 1, 3
89          ds1(i)=coord_l(1,i+3)-coord_l(1,i)
90          ds2(i)=coord_l(2,i+3)-coord_l(2,i)
91          dn(i) =coord_l(3,i+3)-coord_l(3,i)
92       end do
93 C
94 c Do calculations at the Gauss points================================
95 C
96       do i = 1, GP_n
97 C
98 c Determine the values of the shape function at each Gauss point
99 C
100         call k_shape_fun(i,sf)
101 C
102 c Determine the inputs to the cohesive model=========================
103 C
104         p_m=(alpha*(alpha-1.0)*rn**2.0)/(1.0-alpha*rn**2.0)
105         p_n=(beta*(beta-1.0)*rt**2.0)/(1.0-beta*rt**2.0)
106         deln=(G_fn/f_tn)*alpha*rn*(1.0-rn)**(alpha-1.0)
107      & *((alpha/p_m)+1.0)*((alpha/p_m)*rn+1.0)**(p_m-1.0)
108         delt=(G_ft/f_tt)*beta*rt*(1.0-rt)**(beta-1.0)
109      & *((beta/p_n)+1.0)*((beta/p_n)*rt+1.0)**(p_n-1.0)
110 C
111         call k_vector_zero(delu_loc_gp,mcrd)
112 C
113 c Determine shear and normal opening displacements at the Gauss points
114 C
115         do j = 1, 3
116            delu_loc_gp(1)=delu_loc_gp(1)+ds1(j)*sf(j)
117            delu_loc_gp(2)=delu_loc_gp(2)+ds2(j)*sf(j)
118            delu_loc_gp(3)=delu_loc_gp(3)+ dn(j)*sf(j)
119         end do
120 C
121         opn=delu_loc_gp(3)
122         opt=sqrt(delu_loc_gp(1)**2.0+delu_loc_gp(2)**2.0)
123 C
124         if ((Svars(GP_n*(i-1.0)+1.0) .LT. opt) .AND.
125      & (opt .GT. rt*delt)) then
126            Svars(GP_n*(i-1.0)+1.0)=opt
127         end if
128         if ((Svars(GP_n*(i-1.0)+2.0) .LT. opn) .AND.
129      & (opn .GT. rn*deln)) then
130            Svars(GP_n*(i-1.0)+2.0)=opn
131         end if
```

```
132           tmax=Svars(GP_n*(i-1.0)+1.0)
133           pmax=Svars(GP_n*(i-1.0)+2.0)
134 C
135 c Compute the traction vector and tangent modulus matrix
136 C
137           call k_cohesive_law(Trac,Trac_Jacob,G_fn,G_ft,deln,delt,
138      & alpha,beta,p_m,p_n,pmax,tmax,delu_loc_gp,mcrd,nrhs)
139 C
140 c Compute the B matrix and its transpose
141 C
142           call k_Bmatrix(sf,B,mcrd,ndofel)
143 C
144           call k_matrix_transpose(B,B_t,mcrd,ndofel)
145 C
146 c Compute the local stiffness matrix
147 c Local stiffness = B_t * Trac_Jacob * B
148 C
149           call k_matrix_multiply(Trac_Jacob,B,temp1,mcrd,mcrd,
150      & ndofel)
151           call k_matrix_multiply(B_t,temp1,stiff_l,ndofel,
152      & mcrd,ndofel)
153 C
154 c Compute the global stiffness matrix
155 c Global_K = Transpose(T) * K * T
156 C
157           call k_matrix_multiply(Transformation_M_T,stiff_l,
158      & temp2,ndofel,ndofel,ndofel)
159           call k_matrix_multiply(temp2,Transformation_M,stiff_g,
160      & ndofel,ndofel,ndofel)
161 C
162 c Multiply the Jacobian with the global stiffness matrix and
163 c add the contribution from each Gauss point
164 C
165           a_Mult = a_Jacob*GP_w
166           call k_matrix_plus_scalar(amatrx,stiff_g,a_Mult,
167      & ndofel,ndofel)
168 C
169 c Compute the global residual vector
170 c Local_residual = B_t * Trac
171 c Global_residual = Transpose(T) * Local_residual
172 C
173           call k_matrix_multiply(B_t,Trac,residual_l,ndofel,
174      & mcrd,nrhs)
175           call k_matrix_multiply(Transformation_M_T,residual_l,
176      & residual_g,ndofel,ndofel,nrhs)
177 C
178 c Multiply the global residual by the Jacobian and add the
179 c contribution from each point
180 C
181           call k_matrix_plus_scalar(rhs,residual_g,a_Mult,
182      & ndofel,nrhs)
183       end do
184 C
185       return
186       end
```

```
187 C=======================================================================
188 C============================SUBROUTINES================================
189 C=======================================================================
190 C
191 c Determine the global displacement-separation (B) matrix
192 C
193       subroutine k_Bmatrix(sf,B,mcrd,ndofel)
194       INCLUDE 'ABA_PARAM.INC'
195       dimension sf(3),B(mcrd,ndofel)
196       B(1,1) =  sf(1)
197       B(1,4) =  sf(2)
198       B(1,7) =  sf(3)
199       B(1,10)= -sf(1)
200       B(1,13)= -sf(2)
201       B(1,16)= -sf(3)
202       B(2,2) =  sf(1)
203       B(2,5) =  sf(2)
204       B(2,8) =  sf(3)
205       B(2,11)= -sf(1)
206       B(2,14)= -sf(2)
207       B(2,17)= -sf(3)
208       B(3,3) =  sf(1)
209       B(3,6) =  sf(2)
210       B(3,9) =  sf(3)
211       B(3,12)= -sf(1)
212       B(3,15)= -sf(2)
213       B(3,18)= -sf(3)
214 C
215       return
216       end
217 C=======================================================================
218       subroutine k_cohesive_law(T,T_d,G_fn,G_ft,deln,delt,
219      & alpha,beta,p_m,p_n,pmax,tmax,delu,mcrd,nrhs)
220       INCLUDE 'ABA_PARAM.INC'
221       dimension T(mcrd,nrhs),T_d(mcrd,mcrd),delu(mcrd)
222        DOUBLE PRECISION G_fn, G_ft, f_tn, f_tt, alpha, beta,
223      & p_m, p_n, deln, delt, tmax, pmax, popn, popt, gam_n,
224      & gam_t, Tn, Tt, Dnn, Dnt, Dtt, T_d, T, delu
225 C
226       popn=delu(3)
227       popt=sqrt(delu(1)**2.0+delu(2)**2.0)
228 C
229       call k_Mac(pM1,G_fn,G_ft)
230       call k_Mac(pM2,G_ft,G_fn)
231 C
232       if (G_fn .NE. G_ft) then
233          gam_n=(-G_fn)**(pM1/(G_fn-G_ft))*(alpha/p_m)**p_m
234          gam_t=(-G_ft)**(pM2/(G_ft-G_fn))*(beta/p_n)**p_n
235       elseif (G_fn .EQ. G_ft) then
236          gam_n=-G_fn*(alpha/p_m)**p_m
237          gam_t=(beta/p_n)**p_n
238       end if
239 C
240 c Pre-calculation of the normal cohesive traction, Tn
241 C
```

```
      if (popn .LT. 0.0) then
         popn=0.0
      elseif ((popn .GE. deln) .OR. (popt .GE. delt)) then
         Tn = 0.0
      elseif (popn .GE. pmax) then
         Tn=(gam_n/deln)*(p_m*(1.0-(popn/deln))**alpha*((p_m/alpha)
     & +(popn/deln))**(p_m-1.0)-alpha*((1.0-(popn/deln))**(alpha-1.0))
     & *((p_m/alpha)+(popn/deln))**p_m)*(gam_t*(1.0-(popt/delt))
     & **beta*((p_n/beta)+(popt/delt))**p_n+pM2)
      else
         Tn=(gam_n/deln)*(p_m*(1.0-(pmax/deln))**alpha*((p_m/alpha)
     & +(pmax/deln))**(p_m-1.0)-alpha*((1.0-(pmax/deln))**(alpha-1.0))
     & *((p_m/alpha)+(pmax/deln))**p_m)*(gam_t*(1.0-(popt/delt))
     & **beta*((p_n/beta)+(popt/delt))**p_n+pM2)
     & *popn/pmax
      end if
C
C Pre-calculation of the tangential cohesive traction, Tt
C
      if ((popn .GE. deln) .OR. (popt .GE. delt)) then
         Tt = 0.0
      elseif (popt .GE. tmax) then
         Tt=(gam_t/delt)*(p_n*(1.0-(popt/delt))**beta*((p_n/beta)
     & +(popt/delt))**(p_n-1.0)-beta*((1.0-(popt/delt))**(beta-1.0))
     & *((p_n/beta)+(popt/delt))**p_n)*(gam_n*(1.0-(popn/deln))
     & **alpha*((p_m/alpha)+(popn/deln))**p_m+pM1)
      else
         Tt=(gam_t/delt)*(p_n*(1.0-(tmax/delt))**beta*((p_n/beta)
     & +(tmax/delt))**(p_n-1.0)-beta*((1.0-(tmax/delt))**(beta-1.0))
     & *((p_n/beta)+(tmax/delt))**p_n)*(gam_n*(1.0-(popn/deln))
     & **alpha*((p_m/alpha)+(popn/deln))**p_m+pM1)
     & *popt/tmax
      end if
C
C Normal cohesive interaction
C
C (1) Contact
      if (delu(3) .LT. 0.0) then
         Dnn = -(gam_n/(deln**2))*(p_m/alpha)**(p_m-1.0)*(alpha+p_m)*
     & (gam_t*(p_n/beta)**p_n + pM2)
         Dnt = 0.0
         Tn = Dnn * delu(3)
      else if ((popn .LT. deln) .AND. (popt .LT. delt)
     & .AND. (Tn .GE. -1.0E-5)) then
         Tn = Tn
C (2) Softening condition
         if (popn .GE. pmax) then
         Dnn=(gam_n/(deln**2.0))*((p_m**2.0-p_m)*((1.0-(popn/deln))
     & **alpha)*((p_m/alpha)+(popn/deln))**(p_m-2.0)+(alpha**2.0
     & -alpha)*((1.0-(popn/deln))**(alpha-2.0))*((p_m/alpha)
     & +(popn/deln))**p_m -2.0*alpha*p_m*((1.0-(popn/deln))
     & **(alpha-1.0))*((p_m/alpha)+(popn/deln))**(p_m-1.0))*(gam_t*
     & (1.0-(popt/delt))**beta*((p_n/beta)+(popt/delt))**p_n+pM2)
         Dnt=(gam_n*gam_t/(deln*delt))*(p_m*((1.0-(popn/deln))**alpha)
     & *((p_m/alpha)+(popn/deln))**(p_m-1.0)-alpha*((1.0-(popn/deln))
```

```
297       & **(alpha-1.0))*((p_m/alpha)+(popn/deln))**p_m)*(p_n
298       & *((1.0-(popt/delt))**beta)*(((p_n/beta)+(popt/delt))
299       & **(p_n-1.0))-beta*((1.0-(popt/delt))**(beta-1.0))*((p_n/beta)
300       & +(popt/delt))**p_n)
301   c (3) Unloading/reloading condition
302             else
303             Dnn=(gam_n/deln)*(p_m*(1.0-(pmax/deln))**alpha*((p_m/alpha)
304       & +(pmax/deln))**(p_m-1.0)-alpha*((1.0-(pmax/deln))**(alpha-1.0))
305       & *((p_m/alpha)+(pmax/deln))**p_m)*(gam_t*(1.0-(popt/delt))
306       & **beta*((p_n/beta)+(popt/delt))**p_n+pM2)
307       & /pmax
308             Dnt=(gam_n*gam_t/(deln*delt))*(p_m*((1.0-(pmax/deln))**alpha)
309       & *((p_m/alpha)+(pmax/deln))**(p_m-1.0)-alpha*((1.0-(pmax/deln))
310       & **(alpha-1.0))*((p_m/alpha)+(pmax/deln))**p_m)*(p_n
311       & *((1.0-(popt/delt))**beta)*(((p_n/beta)+(popt/delt))
312       & **(p_n-1.0))-beta*((1.0-(popt/delt))**(beta-1.0))*((p_n/beta)
313       & +(popt/delt))**p_n)
314       & *popn/pmax
315             end if
316   c (4) Complete failure
317         else
318             Tn = 0.0
319             Dnn = 0.0
320             Dnt = 0.0
321         end if
322   c
323   c Tangential cohesive interaction
324   c
325         if ((popt .LT. delt) .AND. (popn .LT. deln)
326       & .AND. (Tt .GE. -1.0E-5)) then
327           Tt = Tt
328   c (1) Softening condition
329           if (popt .GE. tmax) then
330               Dtt=(gam_t/(delt**2.0))*((p_n**2.0-p_n)*((1.0-(popt/delt))
331       & **beta)*((p_n/beta)+(popt/delt))**(p_n-2.0)+(beta**2.0-beta)
332       & *((1.0-(popt/delt))**(beta-2.0))*((p_n/beta)+(popt/delt))**p_n
333       & -2.0*beta*p_n*((1.0-(popt/delt))**(beta-1.0))*((p_n/beta)
334       & +(popt/delt))**(p_n-1.0))*(gam_n*(1.0-(popn/deln))
335       & **alpha*((p_m/alpha)+(popn/deln))**p_m+pM1)
336               Dtn=(gam_n*gam_t/(deln*delt))*(p_m*((1.0-(popn/deln))
337       & **alpha)*((p_m/alpha)+(popn/deln))**(p_m-1.0)-alpha*((1.0-
338       & (popn/deln))**(alpha-1.0))*((p_m/alpha)+(popn/deln))**p_m)*(p_n
339       & *((1.0-(popt/delt))**beta)*(((p_n/beta)+(popt/delt))
340       & **(p_n-1.0))-beta*((1.0-(popt/delt))**(beta-1.0))*((p_n/beta)
341       & +(popt/delt))**p_n)
342   c (2) Unloading/reloading condition
343           else
344               Dtt=(gam_t/delt)*(p_n*(1.0-(tmax/delt))**beta*((p_n/beta)
345       & +(tmax/delt))**(p_n-1.0)-beta*((1.0-(tmax/delt))**(beta-1.0))
346       & *((p_n/beta)+(tmax/delt))**p_n)*(gam_n*(1.0-(popn/deln))
347       & **alpha*((p_m/alpha)+(popn/deln))**p_m+pM1)
348       & /tmax
349               Dtn=(gam_n*gam_t/(deln*delt))*(p_m*((1.0-(popn/deln))
350       & **alpha)*((p_m/alpha)+(popn/deln))**(p_m-1.0)-alpha*((1.0-
351       & (popn/deln))**(alpha-1.0))*((p_m/alpha)+(popn/deln))**p_m)*(p_n
```

```
352       & *((1.0-(tmax/delt))**beta)*(((p_n/beta)+(tmax/delt))
353       & **(p_n-1.0))-beta*((1.0-(tmax/delt))**(beta-1.0))*((p_n/beta)+
354       & (tmax/delt))**p_n)
355       & *popt/tmax
356           end if
357   c (3) Complete failure condition
358         else
359           Tt = 0.0
360           Dtt = 0.0
361           Dtn = 0.0
362         end if
363         if (Dtn .NE. Dnt) then
364           Dtn = 0.5*(Dtn + Dnt)
365           Dnt = Dtn
366         end if
367   c
368         if (popt .EQ. 0.0) then
369            T(1,1) = 0.0
370            T(2,1) = 0.0
371            T(3,1) = Tn
372   c
373            T_d(1,1)=Dtt
374            T_d(1,2)=Dtn
375            T_d(1,3)=0.0
376            T_d(2,1)=Dnt
377            T_d(2,2)=Dtt
378            T_d(2,3)=0.0
379            T_d(3,1)=0.0
380            T_d(3,2)=0.0
381            T_d(3,3)=Dnn
382         else
383            T(1,1)=Tt*delu(1)/popt
384            T(2,1)=Tt*delu(2)/popt
385            T(3,1)=Tn
386   c
387            T_d(1,1)=Dtt*(delu(1)/popt)**2.0+Tt*((delu(2)**2.0)
388       &     /(popt**3.0))
389            T_d(1,2)=Dtt*delu(1)*delu(2)/(popt**2.0)
390       &     -Tt*delu(1)*delu(2)/(popt**3.0)
391            T_d(1,3)=Dnt*delu(1)/popt
392   c
393            T_d(2,1)=Dtt*delu(1)*delu(2)/(popt**2.0)
394       &     -Tt*delu(1)*delu(2)/(popt**3.0)
395            T_d(2,2)=Dtt*(delu(2)/popt)**2.0+Tt*((delu(1)**2.0)
396       &     /(popt**3.0))
397            T_d(2,3)=Dnt*delu(2)/popt
398   c
399            T_d(3,1)=Dtn*delu(1)/popt
400            T_d(3,2)=Dtn*delu(2)/popt
401            T_d(3,3)=Dnn
402         end if
403   c
404         return
405         end
406   c=====================================================================
```

```
407       subroutine k_local_coordinates(co_de,R,coord_l,Transformation_M,
408      & Transformation_M_T,a_Jacob,aJacob_M,coords,u,ndofel,nnode,
409      & mcrd)
410       INCLUDE 'ABA_PARAM.INC'
411       dimension R(mcrd,mcrd),coord_l(mcrd,nnode),aJacob_M(2,3),
412      & Transformation_M(ndofel,ndofel),coords(mcrd,nnode),
413      & Transformation_M_T(ndofel,ndofel),u(ndofel),
414      & co_de(mcrd,nnode), co_de_m(3,3),SFD(2,4)
415 C
416       call k_matrix_zero(co_de_m,3,4)
417 C
418       do i = 1, 3
419          co_de_m(i,1)=(co_de(i,1)+co_de(i,4))*0.5
420          co_de_m(i,2)=(co_de(i,2)+co_de(i,5))*0.5
421          co_de_m(i,3)=(co_de(i,3)+co_de(i,6))*0.5
422       end do
423 C
424       SFD(1,1) =-1
425       SFD(1,2) = 1
426       SFD(1,3) = 0
427       SFD(2,1) =-1
428       SFD(2,2) = 0
429       SFD(2,3) = 1
430 C
431       do i = 1,2
432          do j = 1,3
433             do k =1, 3
434                aJacob_M(i,j) = aJacob_M(i,j) + SFD(i,k)*co_de_m(j,k)
435             end do
436          end do
437       end do
438
439       dum1 = aJacob_M(1,2)*aJacob_M(2,3) - aJacob_M(1,3)*aJacob_M(2,2)
440       dum2 = aJacob_M(1,3)*aJacob_M(2,1) - aJacob_M(1,1)*aJacob_M(2,3)
441       dum3 = aJacob_M(1,1)*aJacob_M(2,2) - aJacob_M(1,2)*aJacob_M(2,1)
442 C
443       a_Jacob = sqrt(dum1**2 + dum2**2 + dum3**2)/2.0d0
444       Rn1 = sqrt(dum1**2 + dum2**2 + dum3**2)
445 C
446       R(3,1) = dum1/Rn1
447       R(3,2) = dum2/Rn1
448       R(3,3) = dum3/Rn1
449 C
450       aLen=sqrt(aJacob_M(1,1)**2.0 + aJacob_M(1,2)**2.0
451      & + aJacob_M(1,3)**2.0)
452       R(1,1)=aJacob_M(1,1)/aLen
453       R(1,2)=aJacob_M(1,2)/aLen
454       R(1,3)=aJacob_M(1,3)/aLen
455 C
456       R(2,1)=R(3,2)*R(1,3)-R(3,3)*R(1,2)
457       R(2,2)=R(3,3)*R(1,1)-R(3,1)*R(1,3)
458       R(2,3)=R(3,1)*R(1,2)-R(3,2)*R(1,1)
459 C
460 C=====================================================================
461       num=nnode
```

```
C
      do i = 1, num
         dum=3.0*(i-1.0)
         Transformation_M(dum+1,dum+1)=R(1,1)
         Transformation_M(dum+1,dum+2)=R(1,2)
         Transformation_M(dum+1,dum+3)=R(1,3)
         Transformation_M(dum+2,dum+1)=R(2,1)
         Transformation_M(dum+2,dum+2)=R(2,2)
         Transformation_M(dum+2,dum+3)=R(2,3)
         Transformation_M(dum+3,dum+1)=R(3,1)
         Transformation_M(dum+3,dum+2)=R(3,2)
         Transformation_M(dum+3,dum+3)=R(3,3)
      end do
C
      call k_matrix_transpose(Transformation_M,Transformation_M_T,
     $ ndofel,ndofel)
C
      do i = 1, nnode
         coord_l(1,i)=(R(1,1)*co_de(1,i)+R(1,2)*co_de(2,i)
     & +R(1,3)*co_de(3,i))
         coord_l(2,i)=(R(2,1)*co_de(1,i)+R(2,2)*co_de(2,i)
     & +R(2,3)*co_de(3,i))
         coord_l(3,i)=(R(3,1)*co_de(1,i)+R(3,2)*co_de(2,i)
     & +R(3,3)*co_de(3,i))
      end do
C
      return
      end
C=======================================================================
      subroutine k_shape_fun(i,sf)
      INCLUDE 'ABA_PARAM.INC'
      dimension sf(3), GP_coord(2)
C
      if (i .eq. 1) then
         GP_coord(1)= 1.0d0/6.0d0
         GP_coord(2)= 2.0d0/3.0d0
      elseif (i .eq. 2) then
         GP_coord(1)= 2.0d0/3.0d0
         GP_coord(2)= 1.0d0/6.0d0
      elseif (i .eq. 3) then
         GP_coord(1)= 1.0d0/6.0d0
         GP_coord(2)= 1.0d0/6.0d0
      end if
C
      sf(1)= 1.0 - GP_coord(1) - GP_coord(2)
      sf(2)= GP_coord(1)
      sf(3)= GP_coord(2)
C
      return
      end
C=======================================================================
      subroutine k_matrix_multiply(A,B,C,l,n,m)
      INCLUDE 'ABA_PARAM.INC'
      dimension A(l,n),B(n,m),C(l,m)
C
```

```
517         call k_matrix_zero(C,l,m)
518   C
519         do i = 1, l
520            do j = 1, m
521               do k = 1, n
522                  C(i,j)=C(i,j)+A(i,k)*B(k,j)
523               end do
524            end do
525         end do
526   C
527         return
528         end
529   C=====================================================================
530         subroutine k_matrix_plus_scalar(A,B,c,n,m)
531         INCLUDE 'ABA_PARAM.INC'
532         dimension A(n,m),B(n,m)
533   C
534         do i = 1, n
535            do j = 1, m
536               A(i,j)=A(i,j)+c*B(i,j)
537            end do
538         end do
539   C
540         return
541         end
542   C=====================================================================
543         subroutine k_matrix_transpose(A,B,n,m)
544         INCLUDE 'ABA_PARAM.INC'
545         dimension A(n,m),B(m,n)
546   C
547         do i = 1, n
548            do j = 1, m
549               B(j,i)=A(i,j)
550            end do
551         end do
552   C
553         return
554         end
555   C=====================================================================
556         subroutine k_matrix_zero(A,n,m)
557         INCLUDE 'ABA_PARAM.INC'
558         dimension A(n,m)
559   C
560         do i = 1, n
561            do j = 1, m
562               A(i,j)=0.d0
563            end do
564         end do
565   C
566         return
567         end
568   C=====================================================================
569         subroutine k_vector_zero(A,n)
570         INCLUDE 'ABA_PARAM.INC'
571         dimension A(n)
```

```
572 C
573       do i = 1, n
574          A(i)=0.d0
575       end do
576 C
577       return
578       end
579 C=====================================================================
580       subroutine k_Mac(pM,a,b)
581       INCLUDE 'ABA_PARAM.INC'
582 C
583       if ((a-b) .GE. 0.0) then
584          pM=a-b
585       elseif ((a-b) .LT. 0.0) then
586          pM=0.d0
587       end if
588 C
589       return
590       end
591 C==================================END================================
```

Appendix C

Supplementary Example: Activation of Friction in a Masonry Wallette

Since the coupled cohesive-friction model presented in Chapter 4 is new, and the particular application under investigation in that chapter shows little influence due to friction (see Section 4.4.2.1), a supplementary example is selected to provide further support to the model. This supplementary example considers the shear loading of a masonry wallette, and demonstrates the influence of the coupled cohesive-friction model when a significant frictional effect is activated. The masonry wallette consists of three bricks, linked with two mortar joints, as illustrated in Figure C.1(a). During the experimental testing [317], the middle brick is supported at its top edge by two rigid blocks, and a shear load is introduced through an applied displacement on the lower edge of the outer two bricks. The vertical edges of the wallette are loaded by two load cells which control the horizontally applied pressure. The experimental investigation of this wallette was conducted by Beyer et al. [318, 317].

This problem has also been investigated numerically by Snozzi and Molinari [167]. They modeled this problem with a dynamic fracture code and adaptively inserted cohesive elements at the interface. In their simulations they used material damping to reduce the oscillations they observed in their results. Numerically, the model uses symmetric boundary conditions and only considers half the full model, as illustrated in Figure C.1(b). The domain is discretized using a uniform mesh of linear brick elements of dimension $5 \times 5 \times 5mm$. The resulting discretization contains $68,400$ elements and $75,579$ nodes. Moreover, $3,500$ cohesive elements are used to capture the failure/friction response of the interface. The bricks have an elastic modulus of $14.0GPa$, and a Poisson's ratio of 0.15. The properties of the cohesive interface are listed in Table C.1. The lower boundary of the outer brick is displaced vertically, and, as in the testing machine, the specimen is loaded with an imposed horizontal displacement with a constant normal pressure level of $0.4MPa$.

To determine the influence of frictional forces on the global response, we consider cases with and without friction included in the model. The results from our investigation are illustrated in Figure C.2. The shear force is calculated as the applied force on the lower surface of the outer brick divided by the area of the interface between the two bricks. The experimental data from Beyer et al. [317] is included, for comparison. The numerical results

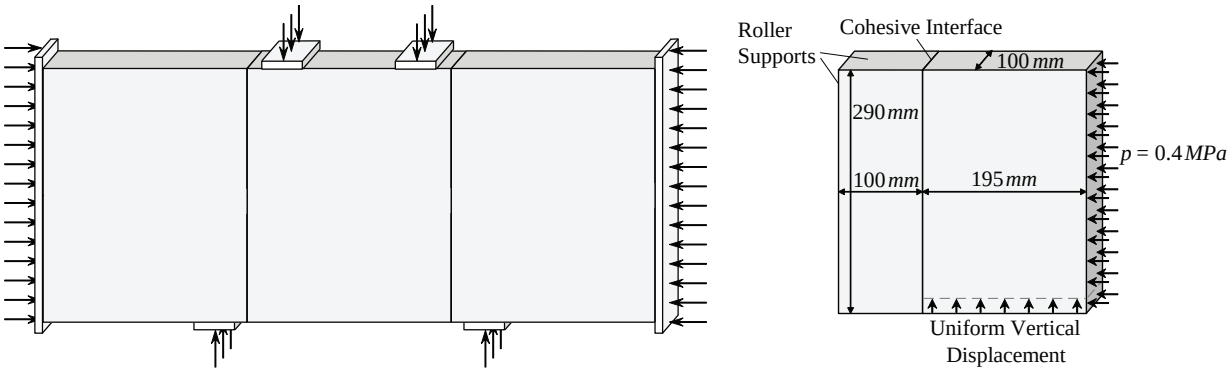

Figure C.1: Model of a masonry wallette: (a) full model, based on experimental setup, and (b) numerical model used in simulations.

Table C.1: Summary of cohesive properties used for the interface elements.

Fracture Energy (ϕ_t)	Cohesive Strength (τ)	Softening Parameter (β)	Penalty Stiffness (λ_t)	Coefficient of Friction (μ)
$750 N/m$	$0.45 MPa$	5	0.04	0.77

including friction demonstrate good agreement with the response observed experimentally. Initially, the stiffness of the composite increases in accordance with the response of the bricks. After cohesive softening initiates, the response transitions smoothly to a purely frictional regime; which the model is able to accurately capture. When friction is not included in the model, the shear stress follows the cohesive model and transitions to zero stress at a finite displacement; which is inconsistent with the response obtained experimentally.

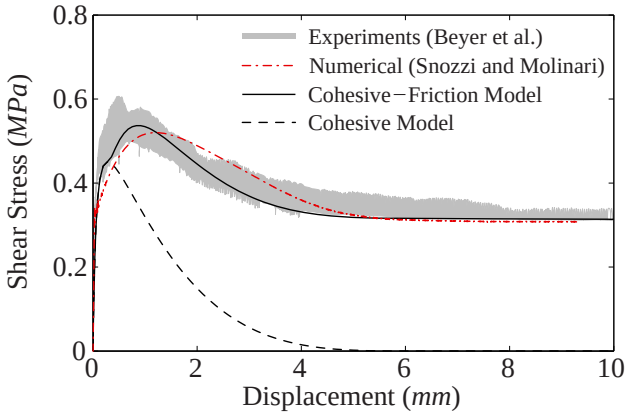

Figure C.2: Shear stress plotted as a function of applied displacement for the masonry wallette example. The experimental data is extracted from Beyer et al. [317], and the numerical results from Snozzi and Molinari [167] are included for comparison.

References

[1] G. I. Barenblatt, "The formation of equilibrium cracks during brittle fracture: General ideas and hypotheses. Axially symmetric cracks," *Journal of Applied Mathematics and Mechanics*, vol. 23, pp. 255–265, 1959.

[2] D. S. Dugdale, "Yielding of steel sheets containing slits," *Journal of the Mechanics and Physics of Solids*, vol. 8, pp. 100–104, 1960.

[3] T. L. Anderson, *Fracture Mechanics: Fundamentals and Applications*. CRC Press, Boca Raton, 1995.

[4] H. Tada, P. C. Paris, and G. R. Irwin, *The Stress Analysis of Cracks Handbook*. The American Society of Mechanical Engineers, 2000.

[5] T. J. R. Hughes, *The Finite Element Method: Linear Static and Dynamic Element Analysis*. Dover Publications, 2000.

[6] T. Belytschko, W. Liu, and B. Moran, *Nonlinear Finite Elements for Continua and Structures*. John Wiley & Sons, Inc., 2000.

[7] K. Park, G. H. Paulino, W. Celes, and R. Espinha, "Adaptive mesh refinement and coarsening for cohesive zone modeling of dynamic fracture," *International Journal for Numerical Methods in Engineering*, vol. 92, pp. 1–35, 2012.

[8] J. J. C. Remmers, R. de Borst, and A. Needleman, "The simulation of dynamic crack propagation using the cohesive segments method," *Journal of the Mechanics and Physics of Solids*, vol. 56, pp. 70–92, 2008.

[9] N. Sukumar, N. Moes, B. Moran, and T. Belytschko, "Extended finite element method for three-dimensional crack modeling," *International Journal for Numerical Methods in Engineering*, vol. 48, pp. 1549–1570, 2000.

[10] P. M. A. Areias and T. Belytschko, "Analysis of three-dimensional crack initiation and propagation using the extended finite element method," *International Journal for Numerical Methods in Engineering*, vol. 63, pp. 760–788, 2005.

[11] T. Rabczuk, S. Bordas, and G. Zi, "On three-dimensional modelling of crack growth using partition of unity methods," *Computers and Structures*, vol. 88, pp. 1391–1411, 2010.

[12] J. E. Bishop, "Simulating the pervasive fracture of materials and structures using randomly close packed Voronoi tessellations," *Computational Mechanics*, vol. 44, pp. 455–471, 2009.

[13] M. A. Jaswon, "Integral equation methods in potential theory. I," *Proceedings of the Royal Society of London. Series A: Mathematical and Physical Sciences*, vol. 275, pp. 23–32, 1963.

[14] G. T. Symm, "Integral equation methods in potential theory. II," *Proceedings of the Royal Society of London. Series A: Mathematical and Physical Sciences*, vol. 275, pp. 33–46, 1963.

[15] A. Sutradhar, G. H. Paulino, and L. J. Gray, *Symmetric Galerkin Boundary Element Method*. Springer-Verlag, Berlin, 2008.

[16] C.-Y. Wang, "Elastic fields produced by a point source in solids of general anisotropy," *Journal of Engineering Mathematics*, vol. 32, pp. 41–52, 1997.

[17] R. Radovitzky, A. Seagraves, M. Tupek, and L. Noels, "A scalable 3D fracture and fragmentation algorithm based on a hybrid, discontinuous Galerkin, cohesive element method," *Computer Methods in Applied Mechanics and Engineering*, vol. 200, pp. 326–344, 2011.

[18] D. N. . Arnold, F. Brezzi, B. Cockburn, and L. D. Marini, "Unified analysis of discontinuous Galerkin methods for elliptic problems," *SIAM Journal on Numerical Analysis*, vol. 39, pp. 1749–1779, 2002.

[19] L. Noels and R. Radovitzky, "An explicit discontinuous Galerkin method for non-linear solid dynamics: Formulation, parallel implementation and scalability properties." *International Journal for Numerical Methods in Engineering*, vol. 74, pp. 1393–1420, 2008.

[20] S. E. Leon, "Adaptive numerical simulation of fracture and failure: From plastic deformation to crack propagation," Ph.D. dissertation, University of Illinois at Urbana-Champaign, 2015.

[21] R. Abedi, S.-H. Chung, M. A. Hawker, J. Palaniappan, and R. B. Haber, "Modeling evolving discontinuities with spacetime discontinuous Galerkin methods," in *IUTAM Symposium on Discretization Methods for Evolving Discontinuities*, A. Combescure, R. de Borst, and T. Belytschko, Eds., 2007, pp. 59–87.

[22] R. Abedi, M. A. Hawker, R. B. Haber, and K. Matouš, "An adaptive spacetime discontinuous Galerkin method for cohesive models of elastodynamic fracture," *International Journal for Numerical Methods in Engineering*, vol. 81, pp. 1207–1241, 2010.

[23] R. Abedi and R. B. Haber, "Spacetime dimensional analysis and self-similar solutions of linear elastodynamics and cohesive dynamic fracture," *International Journal of Solids and Structures*, vol. 48, pp. 2076–2087, 2011.

[24] V. P. Nguyen, T. Rabczuk, S. Bordas, and M. Duflot, "Meshless methods: Review and key computer implementation aspects," *Mathematics and Computers in Simulation*, vol. 79, pp. 763–813, 2008.

[25] P. Lancaster and K. Salkauskas, "Surfaces generated by moving least squares methods," *Mathematics of Computation*, vol. 37, pp. 141–158, 1981.

[26] B. Nayroles, G. Touzot, and P. Villon, "Generalizing the finite element method: Diffuse approximation and diffuse elements," *Computational Mechanics*, vol. 10, pp. 307–318, 1992.

[27] T. Belytschko, Y. Y. Lu, and L. Gu, "Element-free Galerkin methods," *International Journal for Numerical Methods in Engineering*, vol. 37, pp. 229–256, 1994.

[28] T. Belytschko, L. Gu, and Y. Y. Lu, "Fracture and crack growth by element free Galerkin methods," *Modelling and Simulation in Materials Science and Engineering*, vol. 2, pp. 519–534, 1994.

[29] T. Belytschko and M. Fleming, "Smoothing, enrichment and contact in the element-free Galerkin method," *Computers & Structures*, vol. 71, pp. 173–195, 1999.

[30] W. K. Liu, S. Jun, and Y. F. Zhang, "Reproducing kernel particle methods," *International Journal for Numerical Methods in Fluids*, vol. 20, pp. 1081–1106, 1995.

[31] S. N. Atluri and T. Zhu, "A new Meshless Local Petrov-Galerkin (MLPG) approach in computational mechanics," *Computational Mechanics*, vol. 22, pp. 117–127, 1998.

[32] T. Rabczuk and T. Belytschko, "Cracking particles: A simplified meshfree method for arbitrary evolving cracks," *International Journal for Numerical Methods in Engineering*, vol. 61, pp. 2316–2343, 2004.

[33] D. Sulsky and L. Schreyer, "MPM simulation of dynamic material failure with a decohesion constitutive model," *European Journal of Mechanics A/Solids*, vol. 23, pp. 423–445, 2004.

[34] S. A. Silling, "Reformulation of elasticity theory for discontinuous and long-range forces," *Journal of the Mechanics and Physics of Solids*, vol. 48, pp. 175–209, 2000.

[35] Y. D. Ha and F. Bobaru, "Studies of dynamic crack propagation and crack branching with peridynamics," *International Journal of Fracture*, vol. 162, pp. 229–244, 2010.

[36] Y. D. Ha and F. Bobaru, "Characteristics of dynamic brittle fracture captured with peridynamics," *Engineering Fracture Mechanics*, vol. 78, pp. 1156–1168, 2011.

[37] Z. P. Bažant, "A note on peridynamics," Internal Technical Note, Northwestern University, 2014.

[38] S. A. Silling and F. Bobaru, "Peridynamic modeling of membranes and fibers," *International Journal for Non-Linear Mechanics*, vol. 40, pp. 395–409, 2005.

[39] W. Gerstle, N. Sau, and S. A. Silling, "Peridynamic modeling of concrete structures," *Nuclear Engineering and Design*, vol. 237, pp. 1250–1258, 2007.

[40] W. Hu, Y. D. Ha, and F. Bobaru, "Peridynamic model for dynamic fracture in unidirectional fiber-reinforced composites," *Computer Methods in Applied Mechanics and Engineering*, vol. 217-220, pp. 247–261, 2012.

[41] K. Park and G. H. Paulino, "Cohesive zone models: A critical review of traction-separation relationships across fracture surfaces," *Applied Mechanics Reviews*, vol. 64, pp. 1–20, 2013.

[42] A. Hillerborg, M. Modeer, and P. E. Petersson, "Analysis of crack formation and crack growth in concrete by means of fracture mechanics and finite elements," *Cement and Concrete Research*, vol. 6, pp. 773–781, 1976.

[43] P. E. Petersson, "Crack growth and development of fracture zones in plain concrete and similar materials," Ph.D. dissertation, Lund Institute of Technology, 1981.

[44] K. Park, G. H. Paulino, and J. Roesler, "Cohesive fracture model for functionally graded fiber reinforced concrete," *Cement and Concrete Research*, vol. 40, pp. 956–965, 2010.

[45] V. Tvergaard and J. W. Hutchinson, "The influence of plasticity on mixed mode interface toughness," *Journal of the Mechanics and Physics of Solids*, vol. 41, pp. 1119–1135, 1993.

[46] A. Needleman, "A continuum model for void nucleation by inclusion debonding," *ASME Journal of Applied Mechanics*, vol. 54, pp. 525–531, 1987.

[47] Y. Freed and L. Banks-Sills, "A new cohesive zone model for mixed mode interface fracture in bimaterials," *Engineering Fracture Mechanics*, vol. 75, pp. 4583–4593, 2008.

[48] A. Needleman, "An analysis of decohesion along an imperfect interface," *International Journal of Fracture*, vol. 42, pp. 21–40, 1990.

[49] A. Needleman, "An analysis of tensile decohesion along an interface," *Journal of the Mechanics and Physics of Solids*, vol. 38, pp. 289–324, 1990.

[50] X. P. Xu and A. Needleman, "Void nucleation by inclusion debonding in a crystal matrix," *Modelling and Simulation in Materials Science and Engineering*, vol. 1, pp. 111–132, 1993.

[51] K. Park, G. H. Paulino, and J. R. Roesler, "A unified potential-based cohesive model for mixed-mode fracture," *Journal of the Mechanics and Physics of Solids*, vol. 57, pp. 891–908, 2009.

[52] P. A. Klein, J. W. Foulk, E. P. Chen, S. A. Wimmer, and H. Gao, "Physics-based modeling of brittle fracture: Cohesive formulations and the application of meshfree methods," Sandia National Laboratories, Tech. Rep., 2000.

[53] M. L. Falk, A. Needleman, and J. R. Rice, "A critical evaluation of cohesive zone models of dynamic fracture," *Journal de Physique IV*, vol. 11, pp. 43–50, 2001.

[54] N. Blal, L. Daridon, Y. Monerie, and S. Pagano, "Artificial compliance inherent to the intrinsic cohesive zone models: Criteria and application to planar meshes," *International Journal of Fracture*, vol. 178, pp. 71–83, 2012.

[55] G. T. Camacho and M. Ortiz, "Computational modelling of impact damage in brittle materials," *International Journal of Solids and Structures*, vol. 33, pp. 2899–2938, 1996.

[56] M. Ortiz and A. Pandolfi, "Finite-deformation irreversible cohesive elements for three-dimensional crack-propagation analysis," *International Journal for Numerical Methods in Engineering*, vol. 44, pp. 1267–1282, 1999.

[57] Z. Zhang, "Extrinsic cohesive modeling of dynamic fracture and microbranching instability using a topological data structure," Ph.D. dissertation, University of Illinois at Urbana-Champaign, 2007.

[58] A. Needleman, "Some issues in cohesive surface modeling," *Procedia IUTAM*, vol. 10, pp. 221–246, 2014.

[59] J. L. Leblanc, "Rubber-filler interactions and rheological properties in filled compounds," *Progress in Polymer Science*, vol. 27, pp. 627–687, 2002.

[60] C. Heinrich, M. Aldridge, A. S. Wineman, J. Kieffer, A. M. Waas, and K. W. Shahwan, "The role of curing stresses in subsequent response, damage and failure of textile polymer composites," *Journal of the Mechanics and Physics of Solids*, vol. 61, pp. 1241–1264, 2013.

[61] J. Ramier, L. Chazeau, and C. Gauthier, "Influence of silica and its different surface treatments on the vulcanization process of silica filled SBR," *Rubber Chemistry and Technology*, vol. 80, pp. 183–193, 2007.

[62] J. Ramier, "Comportement mécanique d'élastomères chargés, influence de l'adhésion charge - polymère, influence de la morphologie," Ph.D. dissertation, L'Institut National des Sciences Appliquées de Lyon, 2004.

[63] J. Lahiri and A. Paul, "Effect of interface on the mechanical behavior of glass bead-filled PVC," *Journal of Materials Science*, vol. 20, pp. 2253–2259, 1985.

[64] A. V. Zhuk, N. N. Knunyants, V. G. Oshmyan, V. A. Topolkaraev, and A. A. Berlin, "Debonding microprocesses and interfacial strength in particle-filled polymer materials," *Journal of Materials Science*, vol. 28, pp. 4595–4606, 1993.

[65] S. L. Bai, J. Chen, Z. Huang, and Z. Yu, "The role of the interfacial strength in glass bead filled HDPE," *Journal of Materials Science Letters*, vol. 19, pp. 1587–1589, 2000.

[66] Y. S. Thio, A. S. Argon, and R. E. Cohen, "Role of interfacial adhesion strength on toughening polypropylene with rigid particles," *Polymer*, vol. 45, pp. 3139–3147, 2004.

[67] K. Renner, "Micromechanical deformation processes in polymer composites," Ph.D. dissertation, Budapest University of Technology and Economics, 2010.

[68] X. A. Zhong and W. G. Knauss, "Analysis of interfacial failure in particle-filled elastomers," *Journal of Engineering Materials and Technology*, vol. 119, pp. 198–204, 1997.

[69] X. A. Zhong and W. G. Knauss, "Effect of particle interaction and size variation on damage evolution in filled elastomers," *Mechanics of Composite Materials and Structures*, vol. 7, pp. 35–53, 2000.

[70] J. Moraleda, J. Segurado, and J. Llorca, "Effect of interface fracture on the tensile deformation of fiber reinforced elastomers," *International Journal of Solids and Structures*, vol. 46, pp. 4287–4297, 2009.

[71] H. M. Inglis, P. H. Geubelle, K. Matouš, H. Tan, and Y. Huang, "Cohesive modelling of dewetting in particulate composites: Micromechanics vs. multiscale finite element analysis," *Mechanics of Materials*, vol. 39, pp. 580–595, 2007.

[72] L. Brassart, H. M. Inglis, L. Delannay, I. Doghri, and P. H. Geubelle, "An extended Mori-Tanka homogenization scheme for finite strain modeling of debonding in particle-reinforced elastomers," *Computational Materials Science*, vol. 45, pp. 611–616, 2009.

[73] K. Matouš and P. H. Geubelle, "Multiscale modelling of particle debonding in reinforced elastomers subjected to finite deformations," *International Journal for Numerical Methods in Engineering*, vol. 65, pp. 190–223, 2006.

[74] K. Matouš and P. H. Geubelle, "Finite element formulation for modeling particle debonding in reinforced elastomers subjected to finite deformations," *Computer Methods in Applied Mechanics and Engineering*, vol. 196, pp. 620–633, 2006.

[75] T. Goudarzi, D. W. Spring, G. H. Paulino, and O. Lopez-Pamies, "Filled elastomers: A theory of filler reinforcement based on hydrodynamic and interphasial effects," *Journal of the Mechanics and Physics of Solids*, vol. 80, pp. 37–67, 2015.

[76] B. Pukánszky, "Interfaces and interphases in multicomponent materials: Past, present and future," *European Polymer Journal*, vol. 41, pp. 645–662, 2005.

[77] F. R. Eirich, "Some mechanical and molecular aspects of the performance of composites," *Applied Polymer Symposia*, vol. 39, pp. 93–102, 1984.

[78] J. Duke, W. K. Taft, and I. M. Kolthoff, "Formation of bound rubber of GR-S type polymers with carbon blacks," *Industrial and Engineering Chemistry*, vol. 43, pp. 2885–2892, 1951.

[79] G. Kraus, "Reinforcement of elastomers by carbon black." *Advances in Polymer Science*, vol. 8, pp. 155–237, 1971.

[80] G. R. Hamed and S. Hatfield, "On the role of bound rubber in carbon-black reinforcement," *Rubber Chemistry and Technology*, vol. 62, pp. 143–156, 1989.

[81] S. Wolff and M.-J. Wang, "Filler-elastomer interactions. Part IV. The effect of surface energies of fillers on elastomer reinforcement," *Rubber Chemistry and Technology*, vol. 65, pp. 329–342, 1992.

[82] J. Llorca, C. González, J. M. Molina-Aldaregula, J. Segurado, R. Seltzer, F. Sket, M. Rodriguez, S. Sádaba, R. Muñoz, and L. P. Canal, "Multiscale modeling of composite materials: A roadmap towards virtual testing," *Advanced Materials*, vol. 23, pp. 5130–5147, 2011.

[83] E. Mäder and S.-L. Gao, "Enhancing the properties of composites by controlling their interphase parameters," *Advanced Engineering Materials*, vol. 6, pp. 147–150, 2004.

[84] M. Qu, J. S. Meth, G. S. Blackman, G. M. Cohen, K. Sharp, and K. J. Van Vliet, "Tailoring and probing particle-polymer interactions in PMMA/silica nanocomposites," *Soft Matter*, vol. 7, pp. 8401–8408, 2011.

[85] J. S. Bergström and M. C. Boyce, "Mechanical behavior of particle filled elastomers," *Rubber Chemistry and Technology*, vol. 72, pp. 633–656, 1999.

[86] J. Segurado and J. Llorca, "A numerical approximation to the elastic properties of sphere-reinforced composites," *Journal of the Mechanics and Physics of Solids*, vol. 50, pp. 2107–2121, 2002.

[87] M. Galli, J. Botsis, and J. Janczak-Rusch, "An elastoplastic three dimensional homogenization model for particle reinforced composites," *Computational Materials Science*, vol. 41, pp. 312–321, 2008.

[88] O. Lopez-Pamies, T. Goudarzi, and T. Nakamura, "The nonlinear elastic response of suspensions of rigid inclusions in rubber: I - An exact result for dilute suspensions," *Journal of the Mechanics and Physics of Solids*, vol. 61, pp. 1–18, 2013.

[89] O. Lopez-Pamies, T. Goudarzi, and K. Danas, "The nonlinear elastic response of suspensions of rigid inclusions in rubber: II - A simple explicit approximation for finite concentration suspensions," *Journal of the Mechanics and Physics of Solids*, vol. 61, pp. 19–37, 2013.

[90] A. Einstein, "Eine neue bestimmung der moleküldimensionen," *Annalen der Physik*, vol. 324, pp. 289–306, 1906.

[91] E. Guth, "Theory of filler reinforcement," *Journal of Applied Physics*, vol. 16, pp. 20–25, 1945.

[92] J. D. Eshelby, "The determination of the elastic field of an ellipsoidal inclusion and related problems," *Proceedings of the Royal Society of London: A*, vol. 241, pp. 376–396, 1957.

[93] J. R. Willis, "Bounds and self-consistent estimates for the overall properties of anisotropic composites," *Journal of the Mechanics and Physics of Solids*, vol. 25, pp. 185–202, 1977.

[94] R. Hill, "On constitutive macrovariables for heterogeneous solids at finite strain," *Proceedings of the Royal Society of London A*, vol. 326, pp. 131–147, 1972.

[95] T. Goudarzi, "Iterative and variational homogenization methods for filled elastomers," Ph.D. dissertation, University of Illinois at Urbana-Champaign, 2014.

[96] M. C. Boyce and E. M. Arruda, "Constitutive models of rubber elasticity: A review," *Rubber Chemistry and Technology*, vol. 73, pp. 504–523, 2000.

[97] D. A. G. Bruggeman, "Berechnung verschiedener physikalischer Konstanten von heterogenen Substanzen. I. dielektrizitätskonstanten und leitfähigkeiten der mischkörper aus isotropen Substanzen," *Annalen der Physik*, vol. 416, pp. 636–664, 1935.

[98] R. Roscoe, "The viscosity of suspensions of rigid spheres," *British Journal of Applied Physics*, vol. 3, pp. 267–269, 1952.

[99] O. Lopez-Pamies, "An exact result for the macroscopic response of particle reinforced neo-Hookean solids," *Journal of Applied Mechanics*, vol. 77, pp. 021 016–1 – 021 016–5, 2010.

[100] O. Lopez-Pamies, "Elastic dielectric composites: Theory and application to particle-filled ideal dielectrics," *Journal of the Mechanics and Physics of Solids*, vol. 61, pp. 1–18, 2014.

[101] Z. Hashin and S. Shtrikman, "On some variational principles in anisotropic and nonhomogeneous elasticity," *Journal of the Mechanics and Physics of Solids*, vol. 10, pp. 335–342, 1962.

[102] D. R. S. Talbot and J. R. Willis, "Variational principles for inhomogeneous nonlinear media," *IMA Journal of Applied Mathematics*, vol. 35, pp. 39–54, 1985.

[103] Abaqus, *Version 6.11 Documentation, 2011. Dassault Systemes Simulia Corp. Providence, RI, USA.*

[104] W. J. Drugan and J. R. Willis, "A micromechanics-based nonlocal constitutive equation and estimates of representative volume element size for elastic composites." *Journal of the Mechanics and Physics of Solids*, vol. 44, pp. 497–524, 1996.

[105] Z. Khisaeva and M. Ostoja-Starzewski, "On the size of RVE in finite elasticity of random composites," *Journal of Elasticity*, vol. 85, pp. 153–173, 2006.

[106] M. Mosby and K. Matouš, "On mechanics and material length scales of failure in heterogeneous interfaces using a finite strain multiscale high performance solver," *Submitted*.

[107] N. Lahellec, F. Mazerolle, and J. C. Michel, "Second-order estimate of the macroscopic behavior of periodic hyperelastic composites: Theory and experimental validation," *Journal of the Mechanics and Physics of Solids*, vol. 52, pp. 27–49, 2004.

[108] N. Triantafyllidis, M. D. Nestorović, and M. W. Schraad, "Failure surfaces for finitely strained two-phase periodic solids under general in-plane loading," *Journal of Applied Mechanics*, vol. 73, pp. 506–515, 2006.

[109] J. Moraleda, J. Segurado, and J. Llorca, "Finite deformation of incompressible fiber-reinforced elastomers: A computational micromechanics approach," *Journal of the Mechanics and Physics of Solids*, vol. 57, pp. 1596–1613, 2009.

[110] J. Feder, "Random sequential adsorption," *Journal of Theoretical Biology*, vol. 87, pp. 237–254, 1980.

[111] Z. Guo, X. Shi, Y. Chen, H. Chen, X. Peng, and P. Harrison, "Mechanical modeling of incompressible particle-reinforced neo-Hookean composites based on numerical homogenization," *Mechanics of Materials*, vol. 70, pp. 1–17, 2014.

[112] H. Chi, O. Lopez-Pamies, and G. H. Paulino, "A variational formulation with rigid-body constraints for finite elasticity: Theory, finite element implementation, and applications," *Submitted*.

[113] O. Lopez-Pamies, "A new I_1-based hyperelastic model for rubber elastic materials," *Comptes Rendus Mecanique*, vol. 338, pp. 3–11, 2010.

[114] J. Schröberl, "Netgen - An advancing front 2D/3D-mesh generator based on abstract rules," *Computing and Visualization in Science*, vol. 1, pp. 41–52, 1997.

[115] O. Pierard, C. González, J. Segurado, J. Llorca, and I. Doghri, "Micromechanics of elasto-plastic materials reinforced with ellipsoidal inclusions," *International Journal of Solids and Structures*, vol. 44, pp. 6945–6962, 2007.

[116] H. M. Smallwood, "Limiting law of the reinforcement of rubber," *Journal of Applied Physics*, vol. 15, pp. 758–766, 1944.

[117] B. Omnès, S. Thuillier, P. Pilvin, Y. Grohens, and S. Gillet, "Effective properties of carbon black filled natural rubber: Experiments and modeling," *Composites: Part A*, vol. 39, pp. 1141–1149, 2008.

[118] L. Mullins and N. R. Tobin, "Stress softening in rubber vulcanizates. Part I. Use of a strain amplification factor to describe the elastic behavior of filler-reinforced vulcanized rubber," *Journal of Applied Polymer Science*, vol. 9, pp. 2993–3009, 1965.

[119] J. A. C. Harwood and A. R. Payne, "Stress softening in natural rubber vulcanizates. Part III. Carbon black-filled vulcanizates," *Journal of Applied Polymer Science*, vol. 10, pp. 315–324, 1966.

[120] V. Jha, "Carbon black filler reinforcement of elastomers," Ph.D. dissertation, Queen Mary, University of London, 2008.

[121] B. Healy, A. Gullerud, K. Koppenhoefer, A. Roy, S. RoyChowdhury, M. Walters, B. Bichon, K. Cochran, A. Carlyle, J. Sobotka, M. Messner, and R. Dodds, "WARP3D: 3-D dynamic nonlinear fracture analyses of solids using parallel computers," University of Illinois at Urbana-Champaign, Tech. Rep., 2012.

[122] A. Cerrone, P. Wawrzynek, A. Nonn, G. H. Paulino, and A. Ingraffea, "Implementation and verification of the Park-Paulino-Roesler cohesive zone model in 3D," *Engineering Fracture Mechanics*, vol. 120, pp. 26–42, 2014.

[123] K. Park and G. H. Paulino, "Computational implementation of the PPR potential-based cohesive model in Abaqus: Educational perspective," *Engineering Fracture Mechanics*, vol. 93, pp. 239–262, 2012.

[124] S. H. Song, "Fracture of asphalt concrete: A cohesive zone modeling approach considering viscoelastic effects," Ph.D. dissertation, University of Illinois at Urbana-Champaign, 2006.

[125] S. H. Song, G. H. Paulino, and W. G. Buttlar, "Cohesive zone simulation of mode I and mixed-mode crack propagation in asphalt concrete," *Geotechnical Special Publication*, vol. 130, pp. 189–198, 2005.

[126] S. H. Song, G. H. Paulino, and W. G. Buttlar, "Simulation of crack propagation in asphalt concrete using an intrinsic cohesive zone model," *ASCE Journal of Engineering Mechanics*, vol. 132, pp. 1215–1223, 2006.

[127] S. H. Song, G. H. Paulino, and W. G. Buttlar, "A bilinear cohesive zone model tailored for fracture of asphalt concrete considering viscoelastic bulk material," *Engineering Fracture Mechanics*, vol. 73, pp. 2829–2848, 2006.

[128] D. W. Spring, "Cohesive zone modeling of fracture of sustainable and functionally graded concrete," M.S. thesis, University of Illinois at Urbana-Champaign, 2011.

[129] H. D. Espinosa, P. D. Zavattieri, and S. K. Dwivedi, "A finite deformation continuum/discrete model for the description of fragmentation and damage in brittle materials," *Journal of the Mechanics and Physics of Solids*, vol. 46, pp. 1909–1942, 1998.

[130] A. Pandolfi, P. Krysl, and M. Ortiz, "Finite element simulation of ring expansion and fragmentation: The capturing of length and time scales through cohesive models of fracture," *International Journal of Fracture*, vol. 95, pp. 279–297, 1999.

[131] F. Zhou and J. F. Molinari, "Dynamic crack propagation with cohesive elements: A methodology to address mesh dependency," *International Journal for Numerical Methods in Engineering*, vol. 59, pp. 1–24, 2004.

[132] A. Mota, W. S. Klug, M. Ortiz, and A. Pandolfi, "Finite-element simulation of firearm injury to the human cranium," *Computational Mechanics*, vol. 31, pp. 115–121, 2003.

[133] A. Caballero and J. F. Molinari, "Finite element simulations of kidney stones fragmentation by direct impact: Tool geometry and multiple impacts," *International Journal of Engineering Science*, vol. 48, pp. 253–264, 2010.

[134] G. Ruiz, A. Pandolfi, and M. Ortiz, "Three-dimensional cohesive modeling of dynamic mixed-mode fracture," *International Journal for Numerical Methods in Engineering*, vol. 52, pp. 97–120, 2001.

[135] G. H. Paulino and Z. Zhang, "Dynamic fracture of functionally graded composites using an intrinsic cohesive zone model," *Materials Science Forum*, vol. 492-493, pp. 447–452, 2005.

[136] Z. Zhang and G. H. Paulino, "Cohesive zone modeling of dynamic failure in homogeneous and functionally graded materials," *Journal of Plasticity*, vol. 21, pp. 1195–1254, 2005.

[137] L. Hamitouche, M. Tarfaoui, and A. Vautrin, "An interface debonding law subject to viscous regularization for avoiding instability: Application to the delamination problems," *Engineering Fracture Mechanics*, vol. 75, pp. 3084–3100, 2008.

[138] A. Pandolfi, P. R. Guduru, M. Ortiz, and A. J. Rosakis, "Three dimensional cohesive-element analysis and experiments of dynamic fracture in C300 steel," *International Journal of Solids and Structures*, vol. 37, pp. 3733–3760, 2000.

[139] V. Tomar, J. Zhai, and M. Zhou, "Bounds for element size in a variable stiffness cohesive finite element model," *International Journal for Numerical Methods in Engineering*, vol. 61, pp. 1894–1920, 2004.

[140] H. D. Espinosa, S. Dwivedi, and H.-C. Lu, "Modeling impact induced delamination of woven fiber reinforced composites with contact/cohesive laws," *Computer Methods in Applied Mechanics and Engineering*, vol. 183, pp. 259–290, 2000.

[141] M. H. Santare and J. Lambros, "Use of graded finite elements to model the behavior of nonhomogeneous materials," *Journal of Applied Mechanics*, vol. 67, pp. 819–822, 2000.

[142] J.-H. Kim and G. H. Paulino, "Isoparametric graded finite elements for nonhomogeneous isotropic and orthotropic materials," *ASME Journal of Applied Mechanics*, vol. 69, pp. 502–514, 2002.

[143] R. W. Ogden, *Nonlinear Elastic Deformations*. Courier Dover Publications, 1997.

[144] J. R. Reeder and J. H. Crews Jr, "Mixed-mode bending method for delamination testing," *American Institute of Aeronautics and Astronautics*, vol. 28, pp. 1270–1276, 1990.

[145] C. G. Dávila, P. P. Camanho, and M. F. de Moura, "Mixed-mode decohesion elements for analyses of progressive delamination," in *42nd AIAA/ASME/ASCE/AHS/ASC Structures Structural Dynamics and Materials Conference*, 2001.

[146] P. P. Camanho, C. G. Dávila, and M. F. de Moura, "Numerical simulation of mixed-mode progressive delamination in composite materials," *Journal of Composite Materials*, vol. 37, pp. 1415–1424, 2003.

[147] D. Xie and A. M. Waas, "Discrete cohesive zone model for mixed-mode fracture using finite element analysis," *Engineering Fracture Mechanics*, vol. 73, pp. 1783–1796, 2006.

[148] Y. Mi, M. A. Crisfield, and G. A. O. Davies, "Progressive delamination using interface elements," *Journal of Composite Materials*, vol. 32, pp. 1246–1272, 1998.

[149] K. Park, "Potential-based fracture mechanics using cohesive zone and virtual internal bond modeling," Ph.D. dissertation, University of Illinois at Urbana-Champaign, 2009.

[150] G. Tagliavia, "Micromechanics of syntactic foams: Viscoelastic behavior, elastic properties, mechanics of debonding, and moisture diffusion," Ph.D. dissertation, Polytechnic Institute of New York University, 2011.

[151] T. Kawaguchi and R. A. Pearson, "The effect of particle-matrix adhesion on the mechanical behavior of glass filled epoxies. Part 2. A study on fracture toughness," *Polymer*, vol. 44, pp. 4239–4247, 2003.

[152] R. Kraus, W. Wilke, A. Zhuk, I. Luzinov, S. Minko, and A. Voronov, "Investigation of debonding processes in particle-filled polymer materials by acoustic emission: Part 1: Acoustic emission and debonding stress," *Journal of Materials Science*, vol. 32, pp. 4397–4403, 1997.

[153] C. P. Tsui, C. Y. Tang, J. P. Fan, and X. L. Xie, "Prediction for initiation of debonding damage and tensile stress-strain relation of glass-bead-filled modified polyphenylene oxide," *International Journal of Mechanical Sciences*, vol. 46, pp. 1659–1674, 2004.

[154] N. Kanetake, M. Nomura, and T. Choh, "Continuous observation of microstructural degradation during tensile loading of particle reinforced aluminum matrix composites." *Materials Science and Technology*, vol. 11, pp. 1246–1252, 1995.

[155] R. Hasemi, D. W. Spring, and G. H. Paulino, "On small deformation interfacial debonding in composite materials containing multi-coated particles," *Journal of Composite Materials*, DOI:10.1177/0021998314565431, 2015.

[156] J. L. Leblanc, *Filled Polymers: Science and Industrial Applications.* CRC Press, 2010.

[157] Y. Qiao, "Fracture toughness of composite materials reinforced by debondable particulates," *Scripta Materialia*, vol. 49, pp. 491–496, 2003.

[158] J. Segurado and J. Llorca, "A new three-dimensional interface finite element to simulate fracture in composites," *International Journal of Solids and Structures*, vol. 41, pp. 2977–2993, 2004.

[159] R. Kitey and H. V. Tippur, "Role of particle size and filler-matrix adhesion on dynamic fracture of glass-filled epoxy. I. Macromeasurements," *Acta Materialia*, vol. 53, pp. 1153–1165, 2005.

[160] N. Suzuki, M. Ito, and F. Yatsuyanagi, "Effect of rubber/filler interactions on deformation behavior of silica filled SBR systems," *Polymer*, vol. 46, pp. 193–201, 2005.

[161] F. Yatsuyanagi, N. Suzuki, M. Ito, and H. Kaidou, "Effect of surface chemistry of silica particles on the mechanical properties of silica filled Styrene-Butadiene rubber systems," *Polymer Journal*, vol. 34, pp. 332–339, 2002.

[162] M. Aldridge, A. Waas, and J. Kieffer, "Spatially resolved, in situ elastic modulus of thermoset polymer amidst carbon fibers in a polymer matrix composite," *Composites Science and Technology*, vol. 98, pp. 22–27, 2014.

[163] M. Qu, F. Deng, S. M. Kalkhoran, A. Gouldstone, A. Robisson, and K. J. Van Vliet, "Nanoscale visualization and multiscale mechanical implications of bound rubber interphases in rubber-carbon black nanocomposites," *Soft Matter*, vol. 7, pp. 1066–1077, 2011.

[164] B. Wetzel, P. Rosso, F. Haupert, and K. Friedrich, "Epoxy nanocomposites - fracture and toughening mechanisms," *Engineering Fracture Mechanics*, vol. 73, pp. 2375–2398, 2006.

[165] A. N. Gent and B. Park, "Failure processes in elastomers at or near a rigid spherical inclusion," *Journal of Materials Science*, vol. 19, pp. 1947–1956, 1984.

[166] T. Mori and K. Tanaka, "Average stress in matrix and average elastic energy of materials with misfitting inclusions," *Acta Metallurgica*, vol. 21, pp. 571–574, 1973.

[167] L. Snozzi and J. F. Molinari, "A cohesive element model for mixed mode loading with frictional contact capability," *International Journal for Numerical Methods in Engineering*, vol. 93, pp. 510–526, 2013.

[168] V. Tvergaard, "Effect of fibre debonding in a whisker-reinforced metal," *Materials Science and Engineering A*, vol. 125, pp. 203–213, 1990.

[169] J. L. Chaboche, R. Girard, and A. Schaff, "Numerical analysis of composite systems by using interphase/interface models," *Computational Mechanics*, vol. 20, pp. 3–11, 1997.

[170] V. Acary and Y. Monerie, "Nonsmooth fracture dynamics using a cohesive zone approach," Institut National de Recherche en Informatique et en Automatique, Tech. Rep., 2006.

[171] G. Alfano and E. Sacco, "Combining interface damage and friction in a cohesive-zone model," *International Journal for Numerical Methods in Engineering*, vol. 68, pp. 542–582, 2006.

[172] T. Goudarzi and O. Lopez-Pamies, "Numerical modeling of the nonlinear elastic response of filled elastomers via composite-sphere assemblages," *Journal of Applied Mechanics*, vol. 80, pp. 050 906–1 – 050 906–10, 2013.

[173] C. Heinrich, M. Aldridge, A. S. Wineman, J. Kieffer, A. M. Waas, and K. W. Shahwan, "Generation of heat and stress during the cure of polymers used in fiber composites," *International Journal of Engineering Science*, vol. 53, pp. 85–111, 2012.

[174] A. Rasool and H. J. Böhm, "Effects of particle shape on the macroscopic and microscopic linear behavior of particle reinforced composites," *International Journal of Engineering Science*, vol. 58, pp. 21–34, 2012.

[175] H. Yao and H. Gao, "Optimal shapes for adhesive binding between two elastic bodies," *Journal of Colloid and Interface Science*, vol. 298, pp. 564–572, 2006.

[176] Z. Shan and A. M. Gokhale, "Micromechanics of complex three-dimensional microstructures," *Acta Materialia*, vol. 49, pp. 2001–2015, 2001.

[177] J. J. Williams, J. Segurado, J. Llorca, and N. Chawla, "Three dimensional (3D) microstructure-based modeling of interfacial decohesion in particle reinforced metal matrix composites," *Materials Science and Engineering: A*, vol. 557, pp. 113–118, 2012.

[178] L. Mullins, "Softening of rubber by deformation," *Rubber Chemistry and Technology*, vol. 42, pp. 339–362, 1969.

[179] D. O. Potyondy, P. A. Wawrzynek, and A. R. Ingraffea, "An algorithm to generate quadrilateral or triangular element surface meshes in arbitrary domains with applications to crack propagation," *International Journal for Numerical Methods in Engineering*, vol. 38, pp. 2677–2701, 1995.

[180] M. O. Freitas, P. A. Wawrzynek, J. B. Cavalcante-Neto, C. A. Vidal, L. F. Martha, and A. R. Ingraffea, "A distributed-memory parallel technique for two-dimensional mesh generation for arbitrary domains," *Advances in Engineering Software*, vol. 59, pp. 38–52, 2013.

[181] K. D. Papoulia, S. A. Vavasis, and P. Ganguly, "Spatial convergence of crack nucleation using a cohesive finite-element model on a pinwheel-based mesh," *International Journal for Numerical Methods in Engineering*, vol. 67, pp. 1–16, 2006.

[182] C. Radin and L. Sadun, "The isoperimetric problem for pinwheel tilings," *Communications in Mathematical Physics*, vol. 177, pp. 255–263, 1996.

[183] J. J. Rimoli and J. J. Rojas, "Meshing strategies for the alleviation of mesh-induced effects in cohesive element models," *International Journal of Fracture*, vol. 193, pp. 29–42, 2015.

[184] J. Bolander and N. Sukumar, "Irregular lattice model for quasistatic crack propagation," *Physical Review B*, vol. 71, pp. 1–12, 2005.

[185] M. S. Ebeida and S. A. Mitchell, "Uniform random Voronoi meshes," in *Proceedings of the 20th International Meshing Roundtable*. Springer, 2012, pp. 273–290.

[186] S. Li and S. Ghosh, "Multiple cohesive crack growth in brittle materials by the extended Voronoi cell finite element model," *International Journal of Fracture*, vol. 141, pp. 373–393, 2006.

[187] S. Li and S. Ghosh, "Extended Voronoi cell finite element model for multiple cohesive crack propagation in brittle materials," *International Journal for Numerical Methods in Engineering*, vol. 65, pp. 1028–1067, 2006.

[188] S. Ghosh, *Micromechanical Analysis and Multi-Scale Modeling Using the Voronoi Cell Finite Element Method*. CRC Press/Taylor & Francis, 2011.

[189] E. T. Ooi, Z. J. Yang, and Z. Y. Guo, "Dynamic cohesive crack propagation modelling using the scaled boundary finite element method," *Fatigue and Fracture of Engineering Materials and Structures*, vol. 35, pp. 786–800, 2012.

[190] E. T. Ooi, C. Song, F. Tin-Loi, and Z. Yang, "Polygon scaled boundary finite elements for crack propagation modelling," *International Journal for Numerical Methods in Engineering*, vol. 91, pp. 319–342, 2012.

[191] J. E. Bishop, M. J. Martinez, and P. Newell, "A finite-element method for modeling fluid-pressure induced discrete-fracture propagation using random meshes," in *46th US Rock Mechanics/Geomechanics Symposium*, 2012.

[192] N. Sukumar and J. E. Bolander, "Voronoi-based interpolants for fracture modelling," in *Tessellations in the sciences: Virtues, Techniques and Applications of Geometric Tilings*, R. van de Weygaert, G. Vegter, J. Ritzarveld, and V. Icke, Eds. Springer-Verlag, 2008.

[193] X.-P. Xu and A. Needleman, "Numerical simulations of fast crack growth in brittle solids," *Journal of the Mechanics and Physics of Solids*, vol. 42, pp. 1397–1434, 1994.

[194] N. M. Newmark, "A method of computation for structural dynamics," *Journal of the Engineering Mechanics Division*, vol. 85, pp. 67–94, 1959.

[195] E. Hinton, T. Rock, and O. C. Zienkiewicz, "A note on mass lumping and related processes in the finite element method," *Earthquake Engineering & Structural Dynamics*, vol. 4, pp. 245–249, 1976.

[196] C. Talischi, G. H. Paulino, A. Periera, and I. F. M. Menezes, "PolyMesher: A general-purpose mesh generator for polygonal elements written in Matlab," *Journal of Structural and Multidisciplinary Optimization*, vol. 45, pp. 309–328, 2012.

[197] R. S. Thedin, A. Pereira, I. F. M. Menezes, and G. H. Paulino, "Polyhedral mesh generation and optimization for finite element computations," in *XXXV Iberian Latin American Congress on Computational Methods in Engineering*, 2014.

[198] S. P. Lloyd, "Least squares quantization in PCM," *IEEE Transactions on Information Theory*, vol. 28, pp. 129–137, 1982.

[199] S. E. Leon, D. W. Spring, and G. H. Paulino, "Reduction in mesh bias for dynamic fracture using adaptive splitting of polygonal finite elements," *International Journal for Numerical Methods in Engineering*, vol. 100, pp. 555–576, 2014.

[200] D. W. Spring, S. E. Leon, and G. H. Paulino, "Unstructured polygonal meshes with adaptive refinement for the numerical simulation of dynamic cohesive fracture," *International Journal of Fracture*, vol. 189, pp. 33–57, 2014.

[201] N. Sukumar and E. A. Malsch, "Recent advances in the construction of polygon finite element interpolants," *Archives of Computational Methods in Engineering*, vol. 13, pp. 129–163, 2006.

[202] E. L. Wachspress, *A Rational Finite Element Basis*. New York: Academic Press, 1975.

[203] N. Sukumar and A. Tabarraei, "Conforming polygonal finite elements," *International Journal for Numerical Methods in Engineering*, vol. 6, pp. 2045–2066, 2004.

[204] C. Talischi, G. H. Paulino, A. Pereira, and I. F. M. Menezes, "PolyTop: A Matlab implementation of a general topology optimization framework using unstructured polygonal finite element meshes," *Journal of Structural and Multidisciplinary Optimization*, vol. 3, pp. 329–357, 2012.

[205] S. E. Mousavi, H. Xiao, and N. Sukumar, "Generalized Gaussian quadrature rules on arbitrary polygons," *International Journal for Numerical Methods in Engineering*, vol. 82, pp. 1–26, 2009.

[206] S. Natarajan, S. Bordas, and D. Roy Mahapatra, "Numerical integration over arbitrary polygonal domains based on Schwarz-Christoffel conformal mapping," *International Journal for Numerical Methods in Engineering*, vol. 80, pp. 103–134, 2009.

[207] O. C. Zienkiewicz and J. Z. Zhu, "The superconvergent patch recovery and a posteriori error estimates. Part 1: The recovery technique," *International Journal for Numerical Methods in Engineering*, vol. 33, pp. 1331–1364, 2005.

[208] W. Celes, G. H. Paulino, and R. Espinha, "A compact adjacency-based topological data structure for finite element mesh representation," *International Journal for Numerical Methods in Engineering*, vol. 64, pp. 1529–1556, 2005.

[209] G. H. Paulino, W. Celes, R. Espinha, and Z. Zhang, "A general topology-based framework for adaptive insertion of cohesive elements in finite element meshes," *Engineering with Computers*, vol. 24, pp. 59–78, 2008.

[210] W. Celes, G. H. Paulino, and R. Espinha, "Efficient handling of implicit entities in reduced mesh representations," *Journal of Computing and Information Science in Engineering*, vol. 5, pp. 348–359, 2005.

[211] F. Erdogan and G. C. Sih, "On the crack extension in plates under plane loading and transverse shear," *Journal of Basic Engineering*, vol. 85, pp. 519–525, 1963.

[212] G. C. Sih, "Strain-energy-density factor applied to mixed mode crack problems," *International Journal of Fracture*, vol. 10, pp. 305–321, 1974.

[213] T. Belytschko, H. Chen, J. Xu, and G. Zi, "Dynamic crack propagation based on loss of hyperbolicity and a new discontinuous enrichment," *International Journal for Numerical Methods in Engineering*, vol. 58, pp. 1873–1905, 2003.

[214] C.-H. Sam, K. D. Papoulia, and S. A. Vavasis, "Obtaining initially rigid cohesive finite element models that are temporally convergent," *Engineering Fracture Mechanics*, vol. 72, pp. 2247–2267, 2005.

[215] A. Mota, W. Sun, J. T. Ostien, J. W. Foulk, and K. N. Long, "Lie-group interpolation and variational recovery for internal variables," *Computational Mechanics*, vol. 52, pp. 1281–1299, 2013.

[216] I. Babuŝka and W. C. Rheinboldt, "A-posteriori error estimates for the finite element method," *International Journal for Numerical Methods in Engineering*, vol. 12, pp. 1597–1615, 1978.

[217] G. H. Paulino, I. F. M. Menezes, J. B. C. Neto, and L. F. R. C. Martha, "A methodology for adaptive finite element analysis: Towards an integrated computational environment," *Computational Mechanics*, vol. 23, pp. 361–388, 1999.

[218] T. Grätsch and B. Klaus-Jürgen, "A posteriori error estimation techniques in practical finite element analysis," *Computers and Structures*, vol. 83, pp. 235–265, 2005.

[219] J. F. Molinari and M. Ortiz, "Three-dimensional adaptive meshing by subdivision and edge-collapse in finite-deformation dynamic-plasticity problems with application to adiabatic shear banding," *International Journal for Numerical Methods in Engineering*, vol. 53, pp. 1101–1126, 2002.

[220] A. R. Khoei, H. Azadi, and H. Moslemi, "Modeling of crack propagation via an adaptive mesh refinement based on modified superconvergent patch recovery technique," *Engineering Fracture Mechanics*, vol. 75, pp. 2921–2945, 2008.

[221] G. H. Paulino, K. Park, W. Celes, and R. Espinha, "Adaptive dynamic cohesive fracture simulations using nodal perturbation and edge-swap operators," *International Journal for Numerical Methods in Engineering*, vol. 84, pp. 1303–1343, 2010.

[222] E. W. Dijkstra, "A note on two problems in connexion with graphs," *Numerische Mathematik*, vol. 1, pp. 269–271, 1959.

[223] W. Weibull, "A statistical theory of the strength of materials," *Proceedings of the Royal Academy of Engineering Sciences*, vol. 151, pp. 1–45, 1939.

[224] J. C. Simo, P. Wriggers, K. H. Schweizerhof, and R. L. Taylor, "Finite deformation post-buckling analysis involving inelasticity and contact constraints," *International Journal for Numerical Methods in Engineering*, vol. 23, pp. 779–800, 1986.

[225] J. H. Song and T. Belytschko, "Cracking node method for dynamic fracture with finite elements," *International Journal for Numerical Methods in Engineering*, vol. 77, pp. 360–385, 2009.

[226] A. Al-Ostaz and I. Jasiuk, "Crack initiation and propagation in materials with randomly distributed holes," *Engineering Fracture Mechanics*, vol. 58, pp. 395–420, 1997.

[227] R. Becker and R. E. Smelser, "Simulation of strain localization and fracture between holes in an aluminum sheet," *Journal of the Mechanics and Physics of Solids*, vol. 42, pp. 773–796, 1994.

[228] M. Ostoja-Starzewski and G. Wang, "Particle modeling of random crack patterns in epoxy plates," *Probabilistic Engineering Mechanics*, vol. 21, pp. 267–275, 2006.

[229] J. F. Kalthoff and S. Winkler, "Failure mode transition at high rates of shear loading," *International Conference on Impact Loading and Dynamic Behavior of Materials*, vol. 1, pp. 185–195, 1987.

[230] D. Grégoire, H. Maigre, J. Réthoré, and A. Combescure, "Dynamic crack propagation under mixed-mode loading - Comparison between experiments and X-FEM simulations," *International Journal of Solids and Structures*, vol. 44, pp. 6517–6534, 2007.

[231] A. Gravouil, T. Elguedj, and H. Maigre, "An explicit dynamics extended finite element method. Part 2: Element-by-element stable-explicit/explicit dynamic scheme," *Computer Methods in Applied Mechanics and Engineering*, vol. 198, pp. 2318–2328, 2009.

[232] E. T. Ooi, M. Shi, C. Song, F. Tin-Loi, and Z. J. Yang, "Dynamic crack propagation simulation with scaled boundary polygon elements and automatic remeshing technique," *Engineering Fracture Mechanics*, vol. 106, pp. 1–21, 2013.

[233] B. Hopkinson, "A method of measuring the pressure produced in the detonation of high explosives or by the impact of bullets," *Proceedings of the Royal Society A: Mathematical, Physical and Engineering Sciences*, vol. 89, pp. 411–413, 1914.

[234] K.-J. Bathe, *Finite Element Procedures*. Prentice Hall, 1996.

[235] D. Grégoire, "Initiation, propagation, arrêt et redémarrage de fissures sous impact," Ph.D. dissertation, l'Institut National des Sciences Appliquées de Lyon, 2008.

[236] E. Sharon, S. P. Gross, and J. Fineberg, "Local crack branching as a mechanism for instability in dynamic fracture," *Physical Review Letters*, vol. 74, pp. 5096–5099, 1995.

[237] E. Sharon and J. Fineberg, "Microbranching instability and the dynamic fracture of brittle materials," *Physical Review B*, vol. 54, pp. 7128–7139, 1996.

[238] O. Miller, L. B. Freund, and A. Needleman, "Energy dissipation in dynamic fracture of brittle materials," *Modelling and Simulation in Materials Science and Engineering*, vol. 6, pp. 607–638, 1999.

[239] R. Rangarajan, M. M. Chiaramonte, M. J. Hunsweck, Y. Shen, and A. J. Lew, "Simulating curvilinear crack propagation in two dimensions with universal meshes," *International Journal for Numerical Methods in Engineering*, vol. 102, pp. 632–670, 2015.

[240] J. Mosler and M. Ortiz, "An error-estimate-free and remapping-free variational mesh refinement and coarsening method for dissipative solids at finite strains," *International Journal for Numerical Methods in Engineering*, vol. 77, pp. 437–450, 2009.

[241] Z. Zhang, G. H. Paulino, and W. Celes, "Extrinsic cohesive zone modeling of dynamic fracture and microbranching instability in brittle materials," *International Journal for Numerical Methods in Engineering*, vol. 72, pp. 893–923, 2007.

[242] Y. Kallinderis and P. Vijayant, "Adaptive refinement-coarsening scheme for three-dimensional unstructured meshes," *American Institute of Aeronautics and Astronautics Journal*, vol. 31, pp. 1440–1447, 1993.

[243] P. F. Becher, E. Y. Sun, K. P. Plucknett, K. B. Alexander, C. H. Hsueh, H. T. Lin, S. B. Waters, and C. G. Westmoreland, "Microstructural design of silicon nitride with improved fracture toughness: I, Effects of grain shape and size," *Journal of the American Ceramic Society*, vol. 81, pp. 2821–2830, 1998.

[244] E. Y. Sun, P. F. Becher, K. P. Plucknett, C. H. Hsueh, K. B. Alexander, and S. B. Waters, "Microstructural design of silicon nitride with improved fracture toughness: II, Effects of yttria and alumina additives," *Journal of the American Ceramic Society*, vol. 81, pp. 2831–2840, 1998.

[245] S. Levy, "Exploring the physics behind dynamic fragmentation through parallel simulations," Ph.D. dissertation, École Polytechnique Fédérale de Lausanne, 2010.

[246] G. Wang, A. Al-Ostaz, A. H.-D. Cheng, and P. Raju Mantena, "Particle modeling of dynamic fracture simulation of a 2D polymeric material (nylon-6,6) subject to the impact of a rigid indenter," *Computational Materials Science*, vol. 44, pp. 449–463, 2008.

[247] Z. P. Bažant and E. P. Chen, "Scaling of structural failure," Sandia National Laboratories, Tech. Rep., 1996.

[248] F. T. Peirce, "Tensile tests for cotton yarns, Part V: "The Weakest Link" Theorems on the strength of long and composite specimens," *Journal of the Textile Institute Transactions*, vol. 17, pp. 355–368, 1926.

[249] M. Fréchet, "Sur la loi de probabilité de l'écart maximum," *Annales de la Société de Mathématique*, vol. 18, pp. 93–116, 1927.

[250] R. A. Fischer and L. H. C. Tippett, "Limiting forms of the frequency distribution of the largest and smallest member of a sample," *Proceedings of the Cambridge Philosophical Society*, vol. 24, pp. 180–190, 1928.

[251] R. von Mises, "La distribution de la plus grande de n valeurs," *Reviews in Mathematics Union Interbalcanique*, vol. 1, pp. 141–160, 1936.

[252] R. Danzer, "A general strength distribution function for brittle materials," *Journal of the European Ceramic Society*, vol. 10, pp. 461–472, 1992.

[253] A. M. Freudenthal, *Statistical approach to brittle fracture.* Academic Press, 1968, ch. 6, pp. 591–616.

[254] A. D. S. Jayatilaka and K. Trustrum, "Statistical approach to brittle fracture," *Journal of Materials Science*, vol. 12, pp. 1426–1430, 1977.

[255] L. Afferrante, M. Ciavarella, and E. Valenza, "Is Weibull's modulus really a material constant? Example case with interacting collinear cracks," *International Journal of Solids and Structures*, vol. 43, pp. 5147–5157, 2006.

[256] S. H. Lo, "Volume discretization into tetrahedra - II. 3D triangulation by advancing front approach," *Computers & Structures*, vol. 39, pp. 501–511, 1991.

[257] B. Delaunay, "Sur la sphère vide. a la mémoire de Georges Voronoï," *Bulletin de l'Académie des Sciences de l'URSS. Classe des sciences mathématiques et na*, vol. 6, pp. 793–800, 1934.

[258] J. C. Cavendish, D. A. Field, and W. H. Frey, "An approach to automatic three-dimensional finite element mesh generation," *International Journal for Numerical Methods in Engineering*, vol. 21, pp. 329–347, 1985.

[259] W. J. Schroeder and M. S. Shephard, "Geometry-based fully automatic mesh generation and the Delaunay triangulation," *International Journal for Numerical Methods in Engineering*, vol. 26, pp. 2503–2515, 1988.

[260] C. Geuzaine and J.-F. Remacle, "Gmsh: a three-dimensional finite element mesh generator with built-in pre- and post-processing facilities," *International Journal for Numerical Methods in Engineering*, vol. 79, pp. 1309–1331, 2009.

[261] D. A. Field, "Laplacian smoothing and Delaunay triangulations," *Communications in Applied Numerical Methods*, vol. 4, pp. 709–712, 1988.

[262] L. R. Swank and R. M. Williams, "Correlation of static strengths and speeds of rotational failure of structural ceramics," *American Ceramic Society Bulletin*, vol. 60, pp. 830–834, 1981.

[263] R. Hashimoto, A. Ogawa, T. Morimoto, and M. Yonaiyama, "Spin test of silicon nitride disk," *The 74th JSME Annual Meeting*, vol. 2, pp. 441–442, 1996.

[264] P. Zhong, C. J. Chuong, and R. D. Goolsby, "Microhardness measurements of renal calculi: Regional differences and effects of microstructure," *Journal of Biomedical Materials Research*, vol. 26, pp. 1117–1130, 1992.

[265] P. Zhong, C. J. Chuong, and G. M. Preminger, "Characterization of fracture toughness of renal calculi using a microindentation technique," *Journal of Materials Science Letters*, vol. 12, pp. 1460–1462, 1993.

[266] G. Pittomvils, H. Vandeursen, M. Wevers, J. P. Lafaut, D. De Ridder, P. De Meester, R. Boving, and L. Baert, "The influence of internal stone structure upon the fracture behavior of urinary calculi," *Ultrasound in Medicine and Biology*, vol. 20, pp. 803–810, 1994.

[267] A. Mota, J. Knap, and M. Ortiz, "Three-dimensional fracture and fragmentation of artificial kidney stones," *Journal of Physics: Conference Series*, vol. 46, pp. 299–303, 2006.

[268] A. Caballero and J. F. Molinari, "Optimum energy on the fragmentation of kidney stones by direct impact," *International Journal for Computer-Aided Engineering and Software*, vol. 28, pp. 747–764, 2011.

[269] J. E. Bishop, "A displacement-based finite element formulation for general polyhedra using harmonic shape functions," *International Journal for Numerical Methods in Engineering*, vol. 97, pp. 1–31, 2014.

[270] A. L. Gain, C. Talischi, and G. H. Paulino, "On the virtual element method for three-dimensional linear elasticity problems on arbitrary polyhedral meshes," *Computer Methods in Applied Mechanics and Engineering*, vol. 282, pp. 132–160, 2014.

[271] A. L. Gain, G. H. Paulino, L. S. Duarte, and I. F. M. Menezes, "Topology optimization using polytopes," *Computer Methods in Applied Mechanics and Engineering*, vol. 293, pp. 411–430, 2015.

[272] H. Chi, C. Talischi, O. Lopez-Pamies, and G. H. Paulino, "Polygonal finite elements for finite elasticity," *International Journal for Numerical Methods in Engineering*, vol. 101, pp. 305–328, 2014.

[273] M. Floater, A. Gillette, and N. Sukumar, "Gradient bounds for Wachspress coordinates on polytopes," *SIAM Journal on Numerical Analysis*, vol. 52, pp. 515–532, 2014.

[274] L. Beirão da Veiga, C. Lovadina, and D. Mora, "A virtual element method for elastic and inelastic problems on polytope meshes," *arXiv preprint arXiv:1503.02042*, 2015.

[275] Y. Bar-Cohen, *Electroactive polymer (EAP) actuators and artificial muscles.* SPIE - The International Society for Optical Engineering, 2004.

[276] F. Carpi and E. Smela, *Biomedical Applications of Electroactive Polymer Actuators.* Wiley Publications, 2009.

[277] Q. M. Zhang, H. Li, M. Poh, F. Xia, Z. Y. Cheng, H. Xu, and C. Huang, "An all-organic composite actuator material with a high dielectric constant," *Nature*, vol. 419, pp. 284–287, 2002.

[278] C. Huang and Q. Zhang, "Enhanced dielectric and electromechanical responses in high dielectric constant all-polymer percolative composites," *Advanced Functional Materials*, vol. 14, pp. 501–506, 2004.

[279] C. Huang, Q. M. Zhang, J. Y. Li, and M. Rabeony, "Colossal dielectric and electromechanical responses in self-assembled polymeric nanocomposites," *Applied Physics Letters*, vol. 87, pp. 182 901–1 – 182 901–3, 2005.

[280] F. Carpi, G. Gallone, F. Galantini, and D. De Rossi, "Silicone-poly(hexylthiophene) blends as elastomers with enhanced electromechanical transduction properties," *Advanced Functional Materials*, vol. 18, pp. 235–241, 2008.

[281] O. Lopez-Pamies, T. Goudarzi, A. B. Meddeb, and Z. Ounaies, "Extreme enhancement and reduction of the dielectric response of polymer nanoparticulate composites via interphasial charges," *Applied Physics Letters*, vol. 104, pp. 242 904–1 – 242 904–5, 2014.

[282] A. Perro, "Synthèse et valorisation de particules colloïdales de morphologie et de fonctionalitè de surface contrôlées," Ph.D. dissertation, L'Université Bordeaux, 2006.

[283] R. K. Taylor, F. Seifrt, O. Zhuromskyy, U. Peschel, G. Leugering, and W. Peukert, "Painting by numbers: Nanoparticle-based colorants in the post-emperical age," *Advanced Materials*, vol. 23, pp. 2554–2570, 2011.

[284] M. Lattuada and T. Hatton, "Preparation and controlled self-assembly of Janus magnetic nanoparticles," *Journal of the American Chemical Society*, vol. 129, pp. 12 878–12 889, 2007.

[285] J. R. Howse, R. A. L. Jones, A. J. Ryan, T. Gough, R. Vafabakhsh, and R. Golestanian, "Self-motile colloidal particles: From directed propulsion to random walk," *Physical Review Letters*, vol. 99, pp. 048 102–1 – 048 102–4, 2007.

[286] A. N. Pawar and I. Kretzschmar, "Fabrication, assembly, and application of patchy particles," *Macromolecular Rapid Communications*, vol. 31, pp. 150–168, 2010.

[287] H. Bao, W. Peukert, and R. K. Taylor, "One-pot colloidal synthesis of plasmonic patchy particles," *Advanced Materials*, vol. 23, pp. 2644–2649, 2011.

[288] S. Rose, A. Prevoteau, P. Elzière, D. Hourdet, A. Marcellan, and L. Leibler, "Nanoparticle solutions as adhesives for gels and biological tissues," *Nature*, vol. 505, pp. 382–385, 2014.

[289] E. A. Appel and O. A. Scherman, "Gluing gels: A nanoparticle solution," *Nature Materials*, vol. 13, pp. 231–232, 2014.

[290] J. J. Sahlin and N. A. Peppas, "Enhanced hydrogel adhesion by polymer interdiffusion: Use of linear poly(ethylene glycol) as an adhesion promoter," *Journal of Biomaterials Science, Polymer Edition*, vol. 8, pp. 421–436, 1997.

[291] P. Techawanitchai, M. Ebara, N. Idota, T.-A. Asoh, A. Kikuchi, and T. Aoyagi, "Photo-switchable control of pH-responsive actuators via pH jump reaction," *Soft Matter*, vol. 8, pp. 2844–2851, 2012.

[292] I. Arias, S. Serebrinsky, and M. Ortiz, "A phenomenological cohesive model of ferroelectric fatigue," *Acta Materialia*, vol. 54, pp. 975–984, 2006.

[293] C. V. Verhoosel and M. A. Gutiérrez, "Modelling inter- and transgranular fracture in piezoelectric polycrystals," *Engineering Fracture Mechanics*, vol. 76, pp. 742–760, 2009.

[294] S. Kozinov, M. Kuna, and S. Roth, "A cohesive zone model for the electromechanical damage of piezoelectric/ferroelectric materials," *Smart Materials and Structures*, vol. 23, pp. 055 024–1 – 055 024–13, 2014.

[295] V. Z. Parton, "Fracture mechanics of piezoelectric materials," *Acta Astronautica*, vol. 3, pp. 671–683, 1976.

[296] W. F. Deeg, "The analysis of dislocation, crack and inclusion problems in piezoelectric solids," Ph.D. dissertation, Stanford University, 1980.

[297] C. M. Landis, "Energetically consistent boundary conditions for electromechanical fracture," *International Journal of Solids and Structures*, vol. 41, pp. 6291–6315, 2004.

[298] W. Li, R. M. McMeeking, and C. M. Landis, "On the crack face boundary conditions in electromechanical fracture and an experimental protocal for determining energy release rates," *European Journal of Mechanics A: Solids*, vol. 27, pp. 285–301, 2008.

[299] C. M. Landis, T. Pardoen, and J. W. Hutchinson, "Crack velocity dependent toughness in rate dependent materials," *Mechanics of Materials*, vol. 32, pp. 663–678, 2000.

[300] J. H. Dieterich, "Modeling of rock friction 1. Experimental results and constitutive equations," *Journal of Geophysical Research*, vol. 84, pp. 2161–2168, 1979.

[301] A. L. Ruina, "Slip instability and state variable friction laws," *Journal of Geophysical Research*, vol. 88, pp. 10 359–10 370, 1983.

[302] J. R. Rice, "Spatio-temporal complexity of slip on a fault," *Journal of Geophysical Research*, vol. 98, pp. 9885–9907, 1993.

[303] V. Prakaash and R. Clifton, "Time resolved dynamic friction measurements in pressure-shear," in *Experimental Techniques in the Dynamics of Deformable Solids, Applied Mechanics Div. Vol. 165 (AMD-Vol. 165).* American Society of Mechanical Engineers, New York., 1993.

[304] J. Weertman, "Unstable slippage across a fault that separates elastic media of different elastic constants," *Journal of Geophysical Research*, vol. 85, pp. 1455–1461, 1980.

[305] M. Renardy, "Ill-posedness at the boundary for elastic solids sliding under Coulomb frcition," *Journal of Elasticity*, vol. 27, pp. 281–287, 1992.

[306] G. G. Adams, "Self-excited oscillations of two elastic half-spaces sliding with a constant coefficient of friction," *Journal of Applied Mechanics*, vol. 62, pp. 867–872, 1995.

[307] V. Prakash, "Frictional response of sliding interfaces subjected to time varying normal pressures," *Journal of Tribology, Transactions, ASME*, vol. 1220, pp. 97–102, 1998.

[308] K. Ranjith and J. R. Rice, "Slip dynamics at an interface between dissimilar materials," *Journal of the Mechanics and Physics of Solids*, vol. 49, pp. 341–361, 2001.

[309] R. Espinha, W. Celes, N. Rodriguez, and G. H. Paulino, "ParTopS: Compact topological framework for parallel fragmentation simulations," *Engineering with Computers*, vol. 25, pp. 345–365, 2009.

[310] J. D. Owens, D. Luebke, N. Govindaraju, M. Harris, J. Krüger, A. E. Lefohn, and T. J. Purcell, "A survey of general-purpose computation on graphics hardware," *Computer Graphics Forum*, vol. 26, pp. 80–113, 2007.

[311] J. D. Owens, M. Houston, D. Luebke, S. Green, J. E. Stone, and J. C. Phillips, "GPU computing," *Proceedings of the IEEE*, vol. 96, pp. 879–899, 2008.

[312] T. Zegard and G. H. Paulino, "Toward GPU accelerated topology optimization on unstructured meshes," *Journal of Structural and Multidisciplinary Optimization*, vol. 48, pp. 473–485, 2013.

[313] A. Alhadeff, W. Celes, and G. H. Paulino, "Mapping cohesive fracture and fragmentation simulation to GPUs," *Submitted*.

[314] NASA, "Space debris and human spacecraft," September 2013. [Online]. Available: www.nasa.gov/mission_pages/station/news/orbital_debris.html

[315] NASA, "Near-earth object survey and deflection analysis of alternatives," NASA, Tech. Rep., 2007.

[316] J. D. Walker, S. Chocron, D. D. Durda, D. J. Grosch, N. Movshovitz, D. C. Richardson, and E. Asphaug, "Momentum enhancement from aluminum striking granite and the scale size effect," *International Journal of Impact Engineering*, vol. 56, pp. 12–18, 2013.

[317] K. Beyer and A. Dazio, "Quasi-static monotonic and cyclic tests on composite spadrels," *Earthquake Spectra*, vol. 28, pp. 885–906, 2012.

[318] K. Beyer, A. Abo-El-Ezz, and A. Dazio, "Quasi-static cyclic tests on different types of masonry spandrels," Report No 327, Institute of Structural Engineering, Swiss Federal Institute of Technology Zürich, Tech. Rep., 2010.